A platform for high-bandwidth, low-noise electrical nanopore sensing with thermal control

Dmytro Lomovtsev

Thesis submitted to the University of Ottawa in partial fulfillment of the requirements for the Masters of Applied Science in Mechanical Engineering

Department of Mechanical Engineering
Faculty of Engineering
University of Ottawa

Contents

Abstract

Solid-state nanopores are an emerging class of single-molecule detectors that provide information about molecular identity via the analysis of transient fluctuations in the ionic current flowing across a nanoscale pore in a thin membrane. The transport of biomolecules across a pore is a key step in nanopore-based sensing of DNA, RNA and proteins. The dynamics of biomolecular transport are complex and depend on the strength of many interactions, which can be tuned with temperature. However, temperature is rarely controlled during solid-state nanopore experiments because of the added electrical noise from the temperature control and measurement systems, greatly reducing the signal-to-noise ratio when detecting individual molecules. So far, the use of electric-based heating and cooling strategies has limited the recording bandwidth to the kHz range, restricting the studies to long polymers translocating via the pore relatively slowly. Yet, many molecules translocate through the pore orders of magnitude faster. This research presents the development and testing of an instrument to allow low-noise electrical recording of nanopore signals at MHz bandwidth as a function of temperature. Initial experiments using this custom-built instrument for the study of linear DNA polymers confirm previously observed translocation behaviours, while providing a higher temporal resolution. Overall results show that high-speed nanopore experiments are possible while controlling the temperature up to 70 °C, opening up exciting opportunities to study the unfolding of proteins toward single-molecule protein sequencing and the passage of DNA nanostructures for different bioassays. Future work will focus on realizing microfluidic flow cells and nanopore performance at higher temperature for longer recording times.

Statement of Originality and Contributions

The work presented in this thesis represents a portion of my work as a M.A.Sc student in Mechanical Engineering at the University of Ottawa under the co-supervision of Professor Vincent Tabard-Cossa (Center for Interdisciplinary Nanophysics, Department of Physics, University of Ottawa) and Professor Raphael St-Gelais (Micro and Nano Systems Lab, Department of Mechanical Engineering, University of Ottawa). I have contributed majority of the work presented in this thesis, including the literature review, instrumentation design, fabrication, experimental validation, data analysis, and manuscript writing. To the best of my knowledge, the work herein is original and copyrights have been attributed in accordance with current academic requirements and regulations.

The custom nanopore fabrication and conditioning setup used during experiments was designed by Dylan Gunn and Matthew Waugh with the later versions of the setup described in the literature review section of this thesis (Chapter 2). Mathieu Gibeault wrote the original LabView nanopore fabrication and conditioning CBD software for the hardware setup. Kyle Briggs developed internal laboratory software tools to analyze raw nanopore current data. I have made modifications and extensions to the software for the purpose of this thesis. Commercial components not designed by me and used in the instrument are described in the design and instrumentation sections (Chapter 3).

Portions of Chapter 3 and Chapter 4 describing nanopore molecular translocation experiments were written based on experiments done in partnership with Liqun He. He provided extensive practical advice and hands-on guidance in the lab on preparing the nanopores, molecular solutions, nanopore data analysis, data aggregation, and visualization tools. He has also provided direct guidance on correctly running and interpreting gel electrophoresis experiments.

Acknowledgements

First, I would like to thank Professor Vincent Tabard-Cossa for giving me the opportunity to work and study as a member of his laboratory team since my 2018 Co-op term. I have enjoyed the array of diverse and challenging projects, resulting in everyone in the lab having to sit through meetings with 50-slide engineering slide decks. Maybe that says more about my presentation skills (or lack thereof), but thank you for your patience. On this note I would like to thank the members of the lab for support, encouragement, and general wholesomeness throughout this thesis, including Dan, Erin, Kyle, Liqun, Marty, Matt, Phil, Simon, Yassine, and Zach. Matt, thanks for being a great engineering lab boss and mentor.

I would also like to thank Professor Raphael St-Gelais for his co-supervision of my thesis and occasional non-academic discussions that helped me see new perspectives. Thank you for having me in your lab, even though my contributions to its actual activity were mostly remote. I would like to thank the members of the lab for their feedback and support, specifically Albert, Alex, Chang, Kevin, Mathieu, Michel, Nikaya, Rogaya, and Tim.

A few shout-outs to all of my close friends and family who have been putting up with me during this educational endeavour. Thank you Joyce, Oliver, Vlad – I postponed our activities all too often while catching up with course and thesis work. Liqun – C&B is life. UOttawa 3° club – Alexis, JiChu, Yousef – we have survived undergraduate, and now graduate studies together. Some of you are still trying to survive, but thank you for being there nevertheless. Deep – thank you for adopting me like your own family here in Ottawa. My parents – Nina and Georgiy – thank you for always being there even though you are miles away.

Lastly, I would like to acknowledge the length of this work and your pain reading or skipping through it. A wise old tree once said:

"It is a lovely language, but it takes a very long time saying anything in it, because we do not say anything in it, unless it is worth taking a long time to say, and to listen to"

– Treebeard (J.R.R. Tolkein, Lord of The Rings: The Two Towers)

So, stay a while and listen to this tale about small holes in thin membranes.

List of Figures

List of Tables

Acronyms and Common Nomenclature

Acronyms and nomenclature defined in text close to the relevant equations or descriptions override commonly encountered acronyms in this section.

A – Ampere, and derived units fA (10^{-15} A), pA (10^{-12} A), nA (10^{-9} A), µA (10^{-6} A), mA (10^{-3} A)

A_{rms} – Ampere, root mean square value, and derived units pA_{rms} (10^{-12} A_{rms})

Å – Angstrom (10^{-10} m)

AC – alternating current

Ag / AgCl – silver / silver chloride

atm – standard atmosphere, 101 325 Pascals

bp – base pair, and derived unit of kbp (10^{3} bp)

°C – degrees Celsius

CBD – controlled breakdown

Csg – bacterial **c**urli-**s**pecific **g**ene protein complexes, of which *CsgG* and *CsgF* are subunits

DC – direct current

DNA – deoxyribonucleic acid, and derived terms ssDNA (single-stranded DNA), dsDNA (double-stranded DNA), λ-DNA (E. coli lambda bacteriophage DNA, double-stranded, usually 48,502 bp)

Hz – Hertz (1/s), and derived units kHz (10^{3} Hz), MHz (10^{6} Hz)

I – electronic or ionic current

I-V curve – nanopore ionic current vs. applied nanopore voltage curve

I-T curve – nanopore ionic current vs. nanopore temperature curve

K – Kelvin, temperature unit

KCl – potassium chloride

LiCl – lithium chloride

m – meter, and derived units of nm (10^{-9} m), µm (10^{-6} m)

M – molar (moles/L), and derived units fM (10^{-15} M), pM (10^{-12} M), nM (10^{-9} M), µM (10^{-6} M), mM (10^{-3} M)

N – Newton

nt – nucleotide

PCR – polymerase chain reaction

PDMS – polydimethylsiloxane

PSD – power spectral density

pSP65 – cloning **p**lasmid DNA that features **SP6** sequence as origin of replication, likely version **5**, discontinued therefore version coding unknown

RMS – root-mean square

SiN / SiNx – silicon nitride

SNR – signal to noise ratio

V – Volt

Chapter 1. Introduction

1.1. Motivation

Properties of molecules such as nucleic acids and proteins can be investigated by observing their capture and passage through membrane-spanning nanopores while manipulating transport conditions. Properties of interest include molecular size, shape, charge, conformation, inter- and intra-molecular binding, and aggregation. These properties can be dynamic and are often studied and manipulated by changing environmental conditions such as temperature, pressure, salt concentrations, and pH of buffered solutions solvating the molecules.

Temperature manipulation is of particular interest since thermal effects extend not only to molecular shape, transport, and interactions with the surroundings [1], [2] but also the environment itself through the changes in pH, solubility, conductance, and viscosity of buffered solutions. As such, it is necessary to develop single-molecule detection instruments with the ability to measure and carefully control the temperature of biochemical systems under investigation. Instruments utilizing membrane-spanning nanopores could enable novel contributions to the fundamental knowledge in single-molecule biophysics that eventually lead to applications in molecular diagnostics and sequencing.

1.2. Introduction to single-molecule detection using nanopores

Macroscopic investigations of aggregate molecular behaviour do not provide information on molecular heterogeneity that contributes to the average biological function [3], necessitating the application of single-molecule analysis techniques. Heterogeneous behaviour, such as transient changes in molecular conformations observed using single-molecule techniques, can reveal underlying molecular mechanisms behind biological functions and explain deviations from mean behaviour. Subsequent assessment of mean behaviour is enabled by averaging single molecule data collected via high-throughput electrical or optical interrogation methods. A wide variety of single-molecule detection methods and their applications have been summarized in the relevant literature [3], [4].

This thesis will focus on nanopore technology which provides scalable, high-throughput molecular detection methods that can be augmented with thermal control systems to enable thermal manipulation during membrane translocation experiments. Biological pores (biopores) and solid-state pores are the two main classes of nanopores defined by the types of materials that constitute them (Figure 1.1). While each has their own advantages and disadvantages, they share the defining capability to utilize electrical as opposed to optical detection strategies in a nanofluidic environment, potentially reducing instrument size and improving scalability through well-established electronic microfabrication strategies.

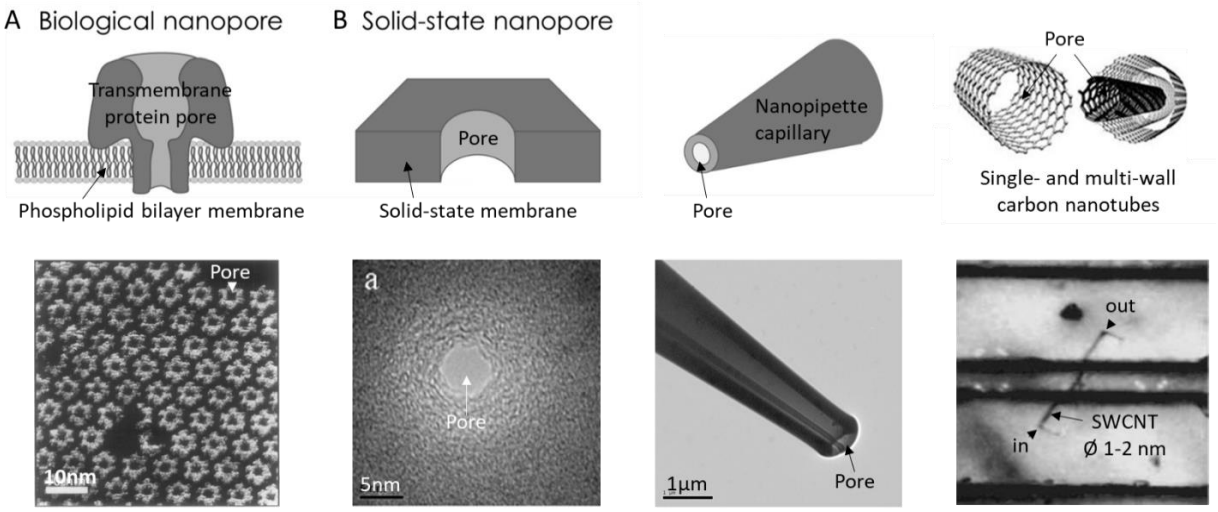

Figure 1.1. Nanopore types. Biological pores consist of a transmembrane protein channel inserted in a biological membrane (A, top) with a sample AFM image (A, bottom) [5]. Solid-state pores are apertures manufactured in solid membranes, capillaries, or nanostructures (B, top), with corresponding TEM/optical images (B, bottom) [6]–[8]. Copyright: (A, bottom) reprinted from Methods in Cell Biology (2002), Chapter 13, Figure 8, with permission from Elsevier via Copyright Clearance Center, Inc. (B, bottom right) reprinted from 'Translocation of Single-Stranded DNA Through Single-Walled Carbon Nanotubes' Fig. 1, Liu et al., Science, 327(5961), 2010, with permission from AAAS, via Copyright Clearance Center, Inc. (B, bottom left) reprinted from 'Fabrication of symmetric sub-5 nm nanopores using focused ion and electron beams' Fig. 4, Lo et al., Nanotechnology, 17, 2006, with permission from IOP Publishing, via Copyright Clearance Center, Inc. (B, bottom middle) reprinted from 'Creation of a transient vapor nanogap between two fluidic reservoirs for single molecule manipulation' Fig. 2, Polonsky et al., Review of Scientific Instruments, 85(8), 2014, with permission from AIP Publishing, via Copyright Clearance Center, Inc. (A, top) and (B, top left and middle) images from [9], distributed under Creative Commons CC BY permitting reprint. (B, top right) image from [10], distributed under Creative Commons CC BY permitting reprint.

Next generation nucleic acid sequencing capabilities with research applications have already been realized by Oxford Nanopore Technologies (UK) using biological nanopores in portable desktop instruments. Deoxyribonucleic acid (DNA) sequencing is possible with massive parallelization of 512 pore channels on the MinION and 2560 channels on the GridION devices at the cost of $1000 per 512 channel cartridge [11]. PromethION device can process up to a staggering 3000 pores per cell and up to 4 cells simultaneously. While less than 60 % of the channels may be suitable and active for operation on any given cell [12], massive parallelization with multiplexed detection ensures process results maintain statistical significance. Most recently, biopore technology has been used in high sensitivity and low cost detection of genetic mutations involved in leukemia [13], and identification of bloodstream infections using specific molecular sequencing [14].

1.3. Introduction to nanopore temperature control

While biopores have been commercially successful due to stable and predictable size, fine-tuned pore structures, low capacitance, and high molecular signal sensitivity, their biological nature could hamper applications that utilize wide-range thermal control. Main disadvantages of biopores include fixed size for all applications, manufacturing complexity using biological components, and—in the context of the current thesis—their thermal stability. Like many biomolecules, proteins that make up biopore sensing elements are stable within specific temperature ranges. For example, pores consisting of α-haemolysin (*αHL*) protein can become unstable at temperatures over 56 °C [15]–[17]. Its activity at body-like temperature of 37 °C changes over time and is reduced after 18 hours of exposure [17]. Paradoxical *αHL* stabilization has been observed at 80 °C [15], but such temperature may be too high for the stability of supporting membrane structures (phosphatidylcholine phospholipid) with melting temperatures ranging from 40 – 55 °C [18]. Bilayer modifications can facilitate elevated temperature experiments [19]. Similarly, the bacterial (*Escherichia coli*) *CsgG:CsgF* transport channel pores (**c**urli-**s**pecific **g**ene protein complexes *G* and *F*) used in the MinION are thermally stable up to 70 °C [20], precluding thermal cycling procedures that may require molecular denaturation

temperatures upwards of 95 °C as done during polymerase chain reaction (PCR). The elevated temperature experiments published for biopores have rarely used pore temperatures above 70 °C [21]–[29]. Little information is provided on temporal stability of biopores above 50 °C in those studies.

Solid-state nanopores, in contrast with biopores, are an emerging class of single-molecule detectors for a variety of biomolecules that have the advantage of being manufactured in inorganic substrates such as silicon nitride or silicon dioxide that maintain excellent thermal stability and biocompatibility in the biological temperature range [30], [31]. Recent progress in user-friendly, automated, and precise control over solid-state nanopore characteristics facilitates solid-state nanopores of tunable size [32]–[35] which allows translocation experiments of molecular complexes larger than 9 – 15 Å, the diameter of *CsgG*-based biopores [20]. Lastly, accessible methods for functionalization of solid-state nanopore substrates with different molecules provide avenues to mimic biological pore functions such as selective asymmetric transport, and molecular trapping in the sensitive pore regions [36], [37].

Temperature is rarely controlled in solid-state pore experiments despite its importance in molecular translocation dynamics. Thermal dependence of ion-binding interactions in DNA translocation as well as DNA thermophoresis through a heated nanopore have been explored in modeling studies [38]–[40]. Experimental studies have mostly limited temperature control to slowing down DNA translocations to improve molecular detection [41], [42], and enhancing DNA capture rate [43]. Only a few experimental studies have addressed fundamental translocation physics using DNA [44], [45]. To date, no studies with solid-state nanopores have taken advantage of thermal control to explore dynamics of molecules other than DNA at physiologically-relevant temperatures.

Ubiquitous methods for heating and cooling—i.e., resistive or thermoelectric—are generally incompatible with nanopore experiments requiring high bandwidth ionic current recordings due to electrical noise concerns. Any current-carrying wires can induce electromagnetic interference in the pico-Ampere (pA) nanopore recording systems even when shielded well. Such noise can limit the recording bandwidth to the kHz range, greatly reducing

the signal-to-noise ratio (SNR) when detecting individual molecules and their features. As such, studies employing thermal control have often used longer polymers (>400 nucleotides) translocating through smaller pores (<8 nm) relatively slowly, in the milliseconds range. Yet, many molecules, such as short DNA (<100 nucleotides) or small proteins (<50 kilo-Daltons), translocate through the pore orders of magnitude faster (nanoseconds to low microseconds) [46], [47]. Furthermore, faster molecular translocation at elevated temperatures [44], [45] places additional limits on the size of molecules that can conventionally be used in thermal experiments and be reliably detected using electrical methods.

As such, there is a need to develop instrumentation capable of manipulating thermal conditions around solid-state nanopores while retaining high bandwidth and SNR required for small molecule detection and characterization experiments. Such instrumentation would enable nanopore sensing experiments with high temporal resolution necessary to examine molecular translocation characteristics of small nucleic acids and proteins at physiologically-relevant temperatures, which has not been adequately studied to date using solid-state nanopores. Low temperature sensing experiments, while done previously [41], [42], could benefit from a much higher sensing bandwidth to capture data on even smaller molecules or molecular features. Lastly, it would become possible to develop practical solid-state nanopore applications taking advantage of temperature control close to the sensor itself. So far, only one study has harnessed the practical potential of thermal control, implementing a microfluidic DNA purification assay on the same microfluidic chip as the nanopore sensor [48]. However, the heated microchamber was far removed from the nanopore sensor and all current readings were done after cooling down to room temperature. Novel experiments could examine molecular product formation next to the nanopore sensor in real time during a thermally cycling polymerase chain reaction (PCR) used for nucleic acid amplification. The main challenge requiring assessment using such a sensing system would be sensor stability. While solid-state nanopore substrates (e.g. silicon oxide, silicon nitride) are generally stable in air up to very high temperatures [30], little information is available about characteristics and temporal stability of solid-state nanopores in heated electrolyte solutions. Electrochemical dissolution of nanopore substrates, more specifically material along pore walls, in alkaline solutions at room temperature is a well-known phenomenon that affects pore growth

[49]–[51]. While dissolution time scale is on the order of days, temperature elevation could expedite the process. A high-bandwidth temperature-controlled nanopore system could allow precise quantification of this phenomenon and lead to advances in material sciences by testing the performance of various membrane substrates (e.g. HfO_2).

1.4. Thesis objectives and structure

The primary objectives of this work are to present the design, fabrication, and characterization of a platform to resolve fast molecular transport through a solid-state nanopore as a function of temperature with MHz bandwidth. Proof-of-concept experiments are also carried out to demonstrate performance of the system detecting model biomolecules (linear double-stranded DNA) as a function of temperature and the potential applications that showcase how system use complexity is not significantly increased as compared to a similar room temperature setup.

This work is presented across several sections. The literature review section (Chapter 2) provides insight into the multidisciplinary topics involved in the instrument design, including solid-state nanopore physics, instrumentation, and thermal control in context of milli- and micro-fluidic devices. The instrument design section (Chapter 3) highlights the system requirements, and presents modeling, design, and device subsystem information. This section also discusses instrument characterization results in light of the design requirements. The last sections (Chapter 4 and Chapter 5) present results from proof-of-concept DNA translocation experiments, and highlight current challenges and future directions.

Chapter 2. Review of Literature

2.1. Solid state nanopore sensors

2.1.1. Overview

Operating principle of nanopores, first conceived in 1989 [52], is similar to the Coulter counter developed in the late 1940s [53] but at the nano-scale. The original counter tallied the number of blood cells in a given sample by assessing the changes in solution conductance as cells passed through an aperture filled with a conductive buffer. Similarly, a solid-state nanopore sensor detects transient ionic current blockages by molecules translocating through a nano-scale aperture in a thin membrane (Figure 2.1 A). Information about molecular identity (size, shape,

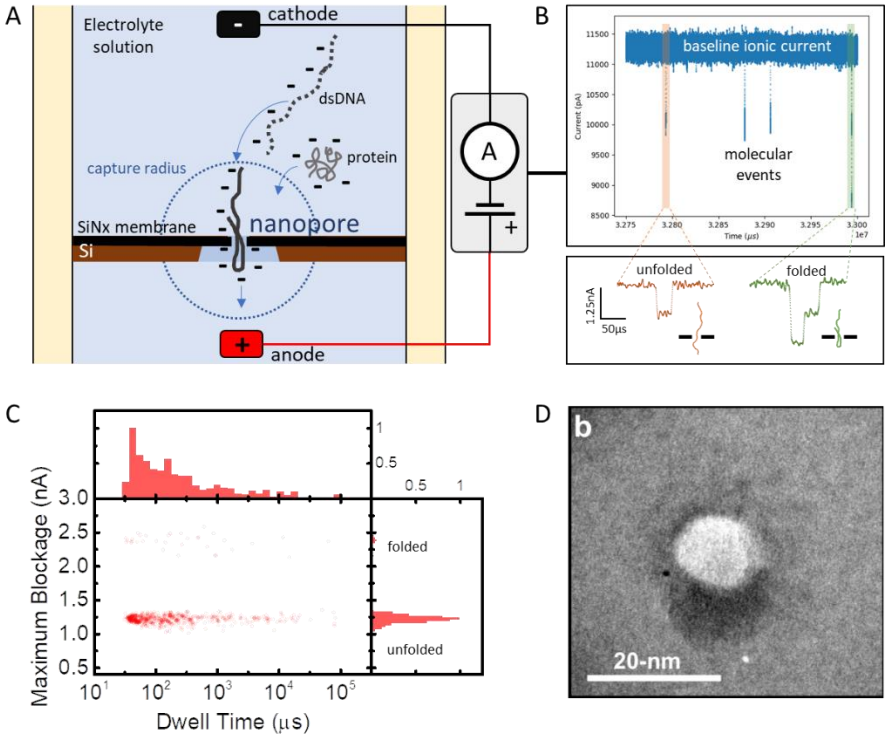

Figure 2.1. Solid-state nanopore principle. Nanopore in a silicon nitride membrane can be used to detect passage of molecules under a supplied electric field (A) while detecting ionic current blockage events that are a signature of molecular translocations (B). Experiment shown was performed using 1 kbp dsDNA at 70 °C in 3.6 M LiCl + 10 mM HEPES (pH 8) at 100 mV with a 5.5 nm diameter pore made in a 12 nm membrane. Molecules and their translocation dynamics can be fingerprinted by analyzing distributions of variables such as ionic current blockage levels during passage and dwell (passage) times (C). An example TEM image of a ~14 nm nanopore produced in a SiN substrate using controlled breakdown [34] is shown in (D). Copyright: (D) reprinted from [34], distributed under Creative Commons CC BY permitting reprint.

charge), and even molecular features, can be obtained from current blockage levels, durations, and distributions of molecular blockage event variables (Figure 2.1 B, C).

2.1.2. Nanopore materials

One of the earliest membrane substrates adopted for solid-state nanopore fabrication is silicon nitride (SiN) [54] (Figure 2.1 D) since it is relatively inexpensive and readily available as a semiconductor device and MEMS manufacturing substrate [30]. Silicon nitride offers high resistivity (10^{14} – 10^{15} Ω-cm) [55], chemical and thermal stability [56], good biocompatibility [31], and can be deposited on silicon substrates to produce relatively low residual stress membranes [30]. Such properties make SiN membranes good candidates for biochemistry-related nanopore applications at elevated temperatures. One potentially significant disadvantage is its electrochemical dissolution in alkaline solutions at room temperature that can induce unwanted pore growth over time [49]–[51]. While dissolution time scale is on the order of days, temperature elevation increases dissolution rates. Dissolution constant of the material has Arrhenius-like behavior which increases with temperature [49]. Hafnium dioxide (HfO_2) deposition has been used in our lab (unpublished work) to reduce pore growth effects at ambient temperature, but potentially introducing other issues such dwell time increases and variability, consistent with previous reports of slowing down translocations [57]. All elevated temperature experiments on solid-state nanopores have used SiN membranes [41]–[45].

Alternative materials attempt to address issues such as sensing resolution, noise, geometric control, and surface properties that allow for functionalization or specific molecular interactions. Detailed analysis of these materials is beyond the scope of this work, although the range of possibilities should be highlighted. Pores have been produced in thick planar substrates such as silicon dioxide (SiO_2) [58], glass [59], aluminum oxide (Al_3O_2) [60], zinc oxide (ZnO) [61], titanium dioxide (TiO_2) [62], hafnium dioxide (HfO_2) [57], and embedded carbon nanotubes [63]. Glass substrates generally offer low noise sensing, while metal oxides can slow down molecular translocation for detection of shorter molecules, or sensing at lower bandwidth. Pores in 2D materials (atomic-thickness membranes) have been used to improve sensitivity to molecular

features, and include graphene [64], boron nitride (BN) [65], molybdenum disulfide (MoS_2) [66], tungsten sulfide (WS_2) [67], bithmuth telluride (Bi_2Te_3) [68], and transition metal carbides (MXenes) [69]. Lastly, organic polymers have been used to produce specific pore geometries and surface properties that affect molecular transport, and include PET [70], polyurea [71], polycarbonate [72], wax [73], and polyimide [74]. Similar to SiN membranes, work on the elevated temperature behavior of wetted nanopores in these materials is scarce.

2.1.3. Nanopore fabrication

Numerous methods to manufacture solid-state nanopores for a range of substrates are well described and referenced in recent solid-state nanopore fabrication and application reviews [75]–[79]. The two most-common methods for planar substrates include ion/electron beam drilling [54], [58], and controlled dielectric breakdown [34]. Laser assisted glass pipette pulling [80] is the primary method for non-planar nanopipette pores. Other less common methods include electrical [81], atomic layer [82] or chemical vapour deposition [83], microneedle polymer perforation of plastics [84], thermal formation using metallic particles [85], and track, mask and plasma etching [86]–[88].

Controlled breakdown (CBD) is a method of choice for direct manufacturing of nanopores in SiN and SiN/SiO_2 membranes due to low cost, and process simplicity on the user side [35]. Unlike traditional focused ion/electron beam fabrication methods, CBD makes pores directly within the salt solution by applying a trans-membrane potential in multiple steps. Geometric changes related to hydration of vacuum-produced pores in beam fabrication are thus eliminated, while controllable pore size adjustment after pore formation is still achieved using a voltage pulsing protocol. Unlike beam drilling or mask etching methods, pore is randomly located on the membrane exposed to the electric field. Methods of pore localization for CBD include locally thinned membranes using ion beams [89], laser irradiation during fabrication [90], using plasmonic nanostructures [91], limiting the membrane area exposed to the electric field using microfluidic channels [92], and microscale liquid contacts [93].

The physics of dielectric breakdown [94], as well as physics of the CBD for nanopore formation have been explored in recent works [34], [95], [96]. The main idea is that voltage applied across a solid-state membrane drives tunneling current through the material to cause defect accumulation, which eventually causes breakdown and pore formation (Figure 2.2 A). The original dielectric breakdown methodology involved application of constant DC voltage across the membrane, resulting in a stochastic pore formation process with fabrication time described by Weibull distribution and related exponentially to fabrication voltage [97]. Weibull distribution process describes the weakest-link problem exemplified by random formation of hot spots with tunneling charges through the membrane until one spot has enough defects to form a conductive path for breakdown. In addition to voltage, membrane geometry and the nature of electrolyte/solvent affect pore formation time [34], [97]. Lastly, semiconductor breakdown times decrease exponentially with temperature [94], but this phenomenon has not been studied for nanopore formation specifically.

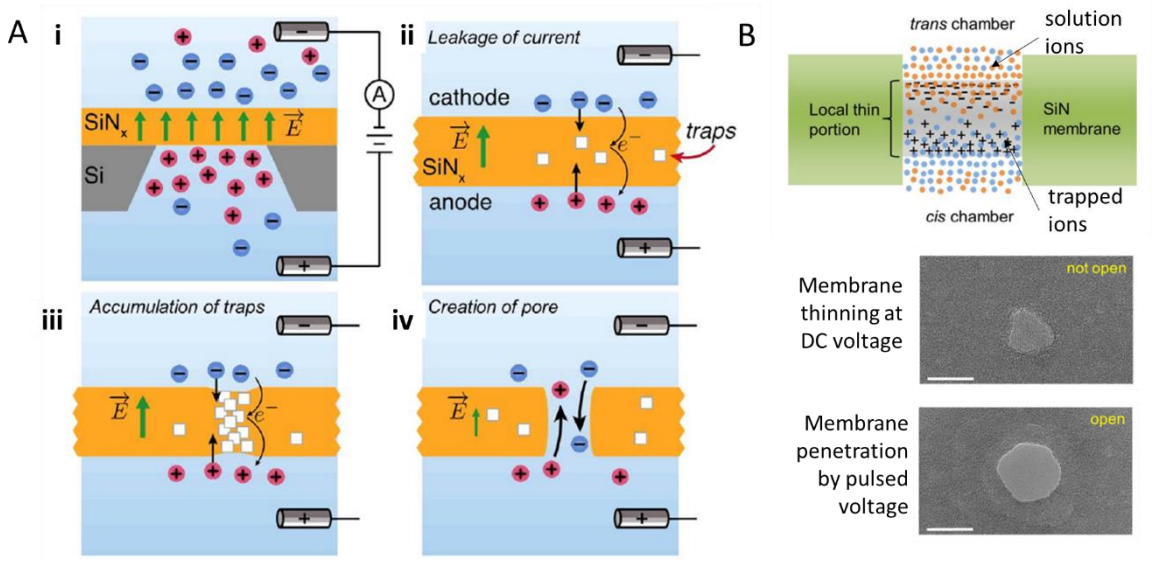

Figure 2.2. Nanopore fabrication by controlled breakdown. Membrane fabrication results from an applied DC potential across the membrane driving a tunneling current (A, i) resulting in formation and accumulation of traps/defects in weak areas (A, ii-iii), eventually forming a fluidic path as damaged material is washed out by solution (A, iv) [34]. A two-step fabrication process involves application of a high DC potential resulting in localized membrane thinning with trap accumulation (B). Subsequent application of AC potential may ease ion injection into the region and membrane weakening for pore formation [96]. Copyright: (A) reprinted from [34], distributed under Creative Commons CC BY permitting reprint. (B) reprinted from [96], distributed under Creative Commons CC BY permitting reprint.

Constant DC field fabrication methodology has been superseded by alternatives due to issues of local membrane thinning without pore formation, as well as multiple pore formation. Local membrane thinning may occur with DC fabrication resulting in detectable leakage current that mimics a pore but does not pass molecules (Figure 2.2 B) [96]. A follow-up AC pulsing has been recommended to ensure successful pore formation. Care must also be taken to prevent multiple pore formation that results from a sufficiently high localized electric field in multiple weakened membrane areas after the first pore is formed. One solution is to ensure the current feedback electronics has a fast response time to the fabrication current influx during the first pore breakdown, shutting off the electric field. Further improvements come with applying gradual voltage ramping and cycling protocol that ensures single pore formation of precisely tunable size (Figure 2.3) [35], [95]. Mechanisms of pore enlargement while using this protocol have been described by Leung et al [98].

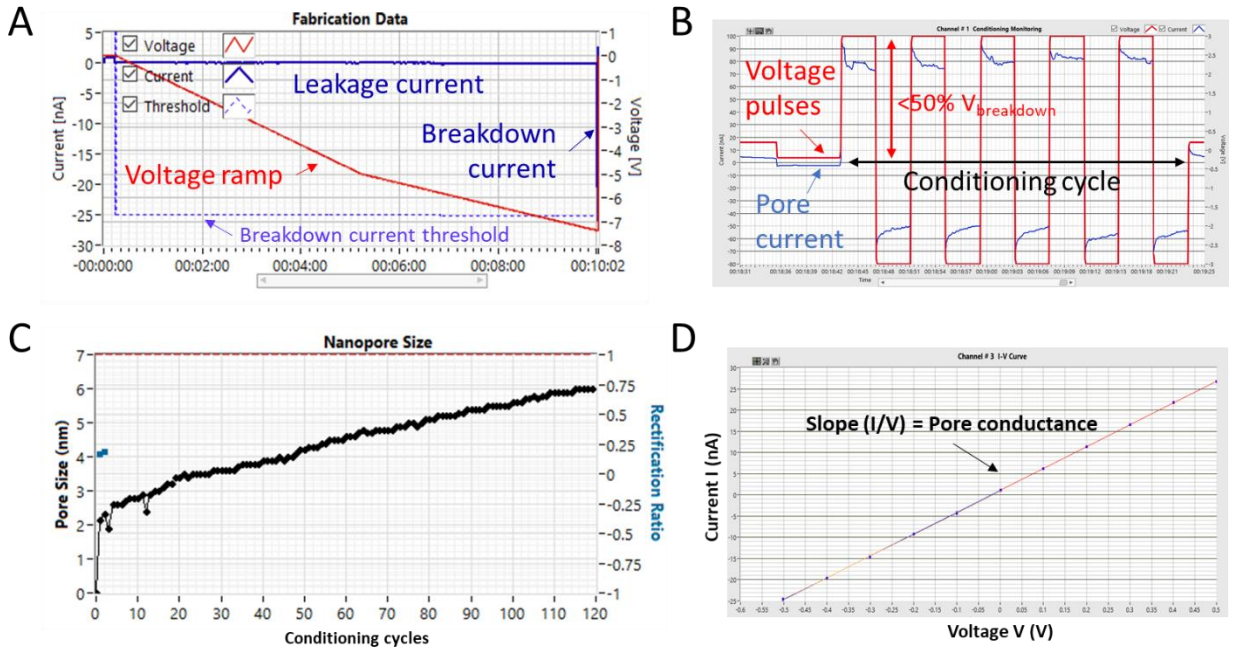

Figure 2.3. Electrical monitoring during pore fabrication. Pore fabrication protocol involves a progressive voltage ramp until material breakdown is detected by a sudden current increase that clears the fabrication threshold (A). Pore is then enlarged using multiple conditioning voltage cycles at no more than half the breakdown voltage (B) until the desired calculated pore size is achieved (C). Lastly, pore size and linearity is approximated from the characterization of pore conductance (D). Images are modified screen shots from the CBD fabrication software (Tabard-Cossa Laboratory).

2.1.4. Nanopore characterization

Molecular translocation experiments require nanopores large enough for the molecules of interest to translocate in a desired range of molecular conformations. The preferred method of determining pore diameter is an indirect electrical measurement which does not require excessive handling or changes in the pore environment. The simplest method assumes a cylindrical pore and requires measurement of only the slope of the I-V curve (Figure 2.3 D) for the following equation [35]:

$$d_{pore} = \frac{G}{2\sigma_{solution}}\left(1 + \sqrt{1 + \frac{16\sigma_{solution}L_{pore}}{\pi G}}\right) \quad \text{Eq.2.1}$$

where *d* is pore diameter, *G* is pore conductance, *σ* is solution conductivity, and *L* is pore length through the membrane. The expression in Eq.2.1 is a rearrangement and simplification of a more general cylindrical pore conductance equation which combines pore access, bulk, and surface resistance terms (Figure 2.4 A) [92], [95]. Access resistance is the resistance of an electrolyte solution just outside of the pore in the volume that converges toward the pore entrance [99]. Bulk resistance results from the resistance of the electrolyte solution present in the pore cylinder [100]. Surface resistance is a result of the charged nature of the pore substrate surface and the presence of ions in solution, forming a double layer and facilitating an electroosmotic flow [101]–[103]. Surface resistance occurs in parallel with bulk pore resistance.

For high electrolyte concentrations (e.g. 3.6 M LiCl), large pore sizes (>2 nm), and translocation of large molecules (e.g. long DNA), surface effects are often neglected in pore size determination (Figure 2.4 C) [100], [104], [105]. Assumptions and simplifications herein provide a reasonable estimate of pore size and agree with pore geometries observed following fabrication by CBD [34], [89], [106]. A further refinement of pore size can be obtained by passing DNA through the nanopore and computing pore length from current blockage as follows [33]:

$$\Delta G = G - G_{DNA} \quad \text{Eq.2.2}$$

$$L_{pore} = \frac{\sigma_{solution}\pi d_{DNA}^2}{4\Delta G} \qquad \text{Eq.2.3}$$

where ΔG is the change in pore conductance G due to blockage by DNA of diameter d_{DNA} (1.2 – 1.5 nm ssDNA, 2.2 nm dsDNA) resulting in pore conductance G_{DNA} while in solution of conductivity σ. Pore length L can then be substituted into Eq.2.1 for a refined estimate of pore diameter. This method assumes that DNA only affects the bulk conductance of the pore.

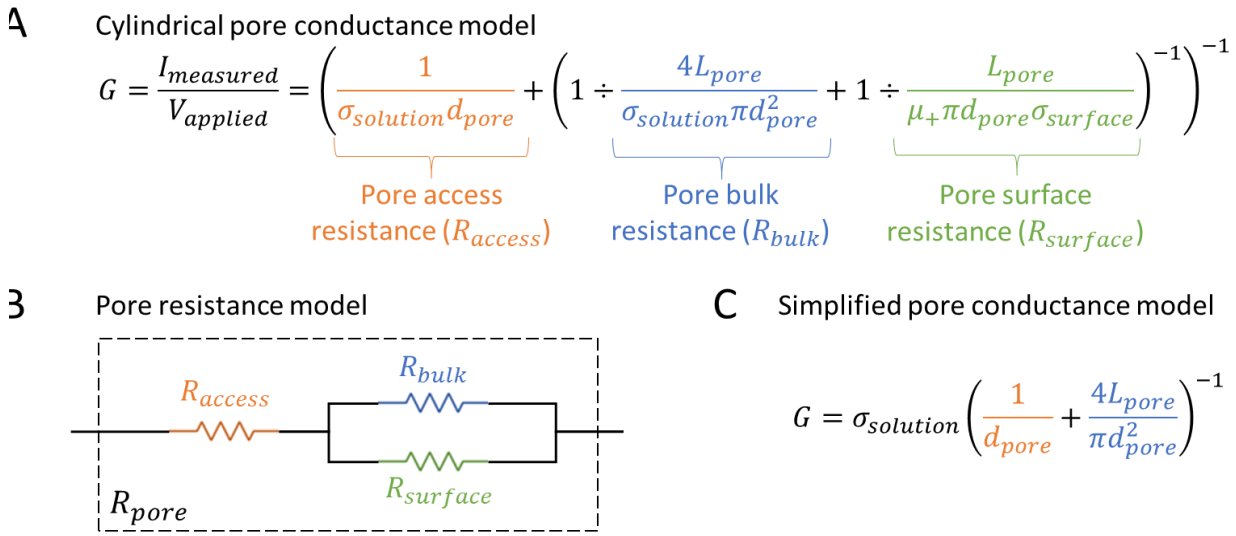

Figure 2.4. Cylindrical pore conductance model. (A) Pore conductance can be determined from the nanopore current measured at a specific applied voltage, and consists of access, bulk, and surface resistance terms. (B) Bulk and surface resistances occur in parallel within the pore, while access resistance occurs in series at pore access points. (C) Surface effects are effectively screened by high electrolyte concentrations and are less significant in larger pores, simplifying the expression.

2.1.5. Molecular sensing

Electrical nanopore sensors detect molecules and their features by recording the changes in ionic current as the molecule produces a transient blockage of the aperture during passage (Figure 2.5). Blockage levels and sublevels, durations (dwell times), and capture rates are some of the parameters that help identify the molecule and its configuration. Blockage levels are simply the differences between the open-pore baseline ionic current and the current resulting from partial occlusion of the pore by the molecule at any given time. A single molecule can feature multiple blockage sublevels resulting from geometric or electrochemical features producing

differences in occlusion during translocation. How long a molecule stays within the pore is defined by its dwell time, and is defined by its geometry as well as the interactions with the pore and other environmental factors. Lastly, frequency of translocation events can be an indicator of both the molecular concentration in solution as well as the rate of molecular capture by the pore under specific electrochemical conditions.

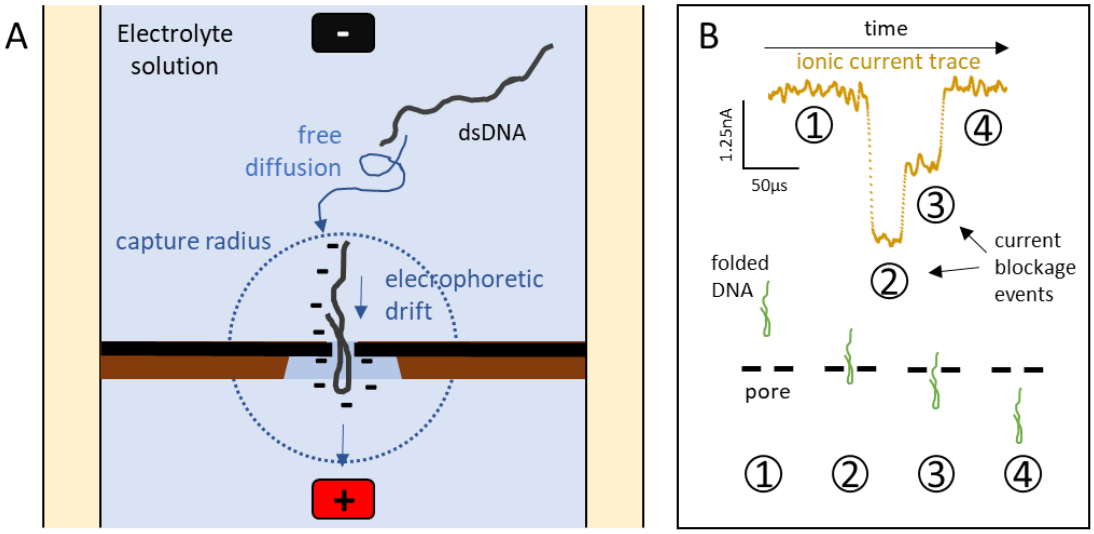

Figure 2.5. Molecular capture and translocation process. (A) The nanopore in diffusion-limited regime is initiated by a molecule diffusing within the hemispherical capture radius where the electric field becomes the dominant driver of translocation. (B) Ionic current recording at the nanopore features current blockage events of finite duration that represent the various configurations of the translocating molecule (event shown from translocation of 1 kbp dsDNA at 70 °C in 3.6 M LiCl + 10 mM HEPES (pH 8) at 100 mV with a 5.5 nm calculated diameter pore made in a 12 nm nominal thickness membrane).

The considerable complexity of polymer capture and translocation dynamics through solid-state nanopores has been discussed in a number of publications [107]–[114] and detailed analysis is beyond the scope of this work. Of note are some qualitative observations that are relevant to the experimental section in this work and the expectations of molecular translocation trends.

A molecule, such as DNA, floating far away from the pore diffuses freely in solution, primarily governed by transport and self-diffusivity with little effect from the electric field extending out of the pore (Figure 2.5 A) [108], [109]. A molecule diffusing within the pore's capture radius experiences electrophoretic drift toward the pore which is greater than its

diffusive mobility away from the pore. Capture radius *r** delineates a very small hemispherical volume around the pore [108]:

$$r^* = \Delta V \frac{d_{pore}^2 \, \mu_{molecule}}{8 \, L_{pore} \, D_{molecule}} \qquad \text{Eq.2.4}$$

and changes proportionally with applied potential ΔV, electrophoretic mobility of the molecule μ, pore length L, and molecular diffusion coefficient D. Of note is the quadratic relation with pore diameter d, whereby molecular approach toward the pore can be significantly increased with pore diameter. While molecular approach to the pore mouth is a necessary condition to start pore translocation, it is not sufficient. Molecular end has to enter the pore by overcoming the entropic barrier for orienting itself into the pore, which takes extra time [108]. It was found that large polymers such as DNA with $>10^4$ bases have diffusion-limited pore capture rate where time to capture is dominated by bulk diffusion. The entropic barrier is significantly reduced due to a large effective charge of a large molecule. Concentration-normalized capture rate R_c has similar proportionalities as capture radius [108]:

$$R_c = 2\pi \, D_{molecule} \, r^* = \Delta V \frac{\pi \, d_{pore}^2 \, \mu_{molecule}}{4 \, L_{pore}} \qquad \text{Eq.2.5}$$

Smaller molecules diffuse faster through solution but experience a greater pore entry barrier, whereby capture rate is likely exponentially related to applied potential ΔV and accounts for multiple molecular attempts to overcome the entry barrier [108], [112]. R_c (in units of m^3 / #molecules · s) provides a concentration-independent metric of capture capacity of the pore for comparison to other pores, and can be multiplied by molecular concentration in solution (#molecules / m^3) to obtain the nominal capture rate directly proportional to concentration. The takeaway is that applied voltage and solution concentration can be an effective external means of controlling capture rate. Special attention needs to be paid to the overall molecular size and charge when selecting voltage magnitude and molecular concentration.

Once a molecule has entered the pore, translocation velocity tends to be rapid and is influenced by the unraveling of initially-random molecular conformation before entry [110], [115]. Tension propagation theory has been used in an attempt to elucidate the translocation

dynamics [116], [117]. Additional complications in translocation modeling arise from molecular folding and interactions with the pores themselves [45], [107], [118]. Therefore, care must be taken when interpreting the exact meaning of variables such as capture rates and translocation times, and necessitates some form of statistical control for attributing ranges of observations to particular molecular conformations or behaviours. Use of control molecules with well-defined blockage, capture, and translocation parameters such as linear dsDNA may be necessary to standardize analysis across multiple pores with geometric and electrochemical variability.

2.1.6. Instrumentation

One of the main advantages of **c**ontrolled **b**reak**d**own (CBD) for nanopore fabrication is the low-cost and easily-accessible equipment that can be adapted to numerous fluidic cell designs independently of the sensing equipment. A conventional cost-effective fabrication setup is shown in Figure 2.6, and consists of multiple fabrication circuits mounted within a Faraday cage interfaced to a DAQ card. Nanopore membrane chips are mounted within fluidic cells providing independent fluidic access to each side of the membrane. Automated fabrication protocol can then be applied to produce a pore of desired size using readily-available CBD software as described by Waugh et al. [35] (Figure 2.3).

Molecular translocation sensing typically requires high-bandwidth (>10 kHz), ultra-low current amplification circuits (fA – nA), which are usually unable to apply voltages high enough for pore fabrication or resolve signals beyond a limited amplifier saturation current. As such, pore fabrication and molecular sensing are performed using separate hardware. Axon Instruments Axopatch 200B (Figure 2.6 E) and similar patch clamp amplifiers (HEKA EPC) have traditionally been used for molecular sensing up to 100 kHz bandwidth. Unfortunately, detection of many molecules such as short DNA (<100 nucleotides) or small proteins (<50 kilo-Daltons) require nanosecond to low microsecond temporal resolution [46], [47]. Furthermore, faster molecular translocation at elevated temperatures [44], [45] places additional restrictions on molecular sizes that can be detected by commonly-used amplifiers. Figure 2.7 demonstrates how higher temporal resolution (i.e. analog bandwidth) improves the ability to resolve ionic current details

for molecular and sub-molecular feature signals, but at the cost of higher electrical noise and lower signal-to-noise ratio.

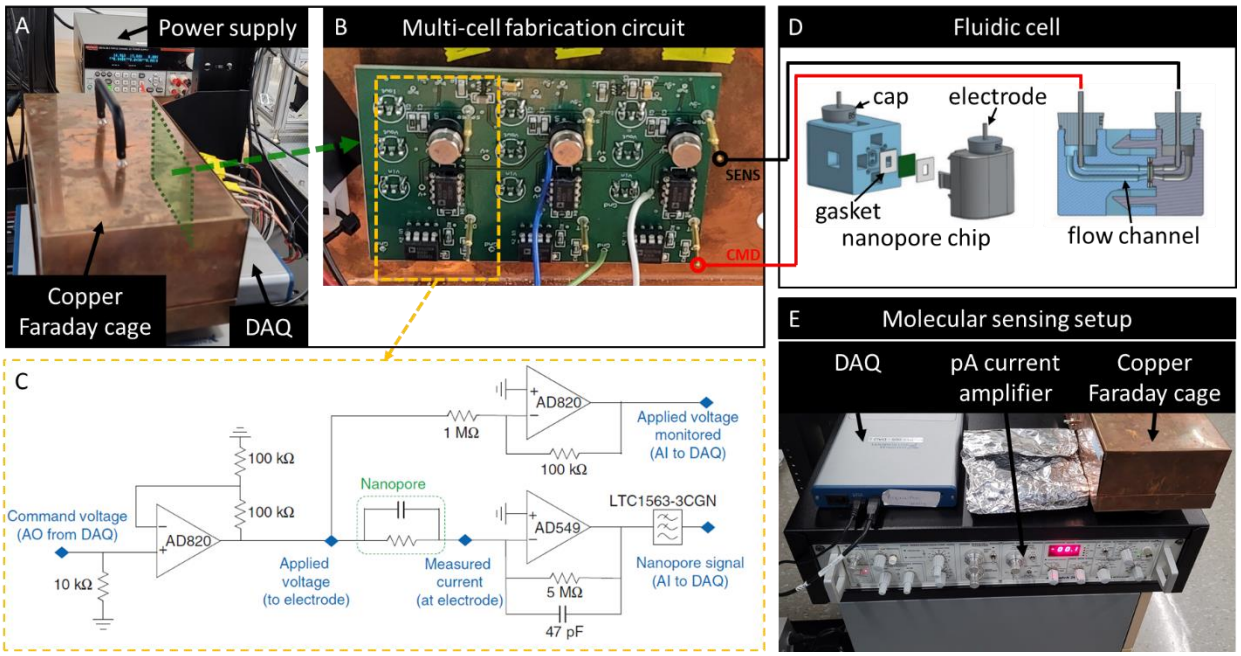

Figure 2.6. Controlled breakdown fabrication and sensing setup. A copper Faraday cage (A) with multiple inexpensive parallel fabrication circuits (B) interfaced to a DAQ card can provide a cost-effective fabrication system. Each circuit is constructed from readily available operational amplifier components for applying a voltage signal to the nanopore (AD820), reading the resultant nanopore current (AD549), feedback voltage sensing (AD820), and low-pass filtering the current signal (LTC1563) (C) [35]. An example 3D-printed fluidic cell schematic consists of the solid-state membrane chip sandwiched between fluidically sealed cavities filled with liquid electrolyte interfaced via Ag/AgCl electrodes (D) [35]. Molecular translocation sensing setup requires higher bandwidth and resolution, which is accommodated by commercial current amplifiers such as the ubiquitous Axopatch 200B (E).

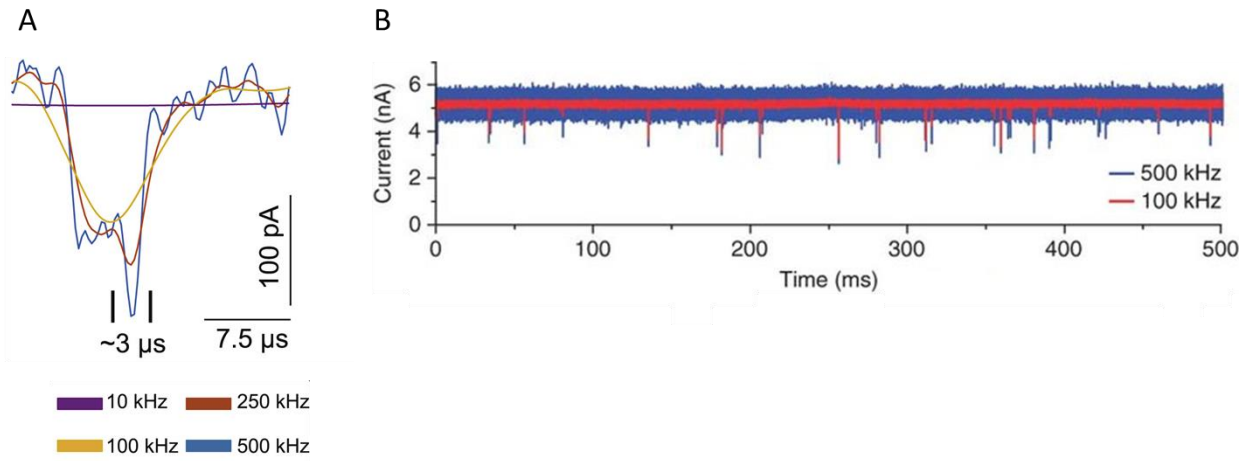

Figure 2.7. Effects of analog bandwidth on signal resolution and noise. (A) Sample ionic current signal from a molecular translocation event shows decreasing amount of detail as a function of analog signal bandwidth [119]. (B) Ionic current signal recording at higher analog bandwidth has a drawback of higher electrical noise that reduces the ability to differentiate signals from said noise [47]. Molecular signals (downward peaks) are more easily distinguishable from baseline current band at 100 kHz than at 500 kHz. Copyright: (A) reprinted with permission of Elsevier, from 'High bandwidth approaches in nanopore and ion channel recordings - A tutorial review' Fig. 6, Hartel et al., Analytica Chimica Acta, 1061, 2019, via Copyright Clearance Center, Inc. (B) reprinted with permission of Springer Nature, from 'Integrated nanopore sensing platform with sub-microsecond temporal resolution' Fig. 4, Rosenstein et al., Nature Methods, 9(5), 2012, via Copyright Clearance Center, Inc.

Transimpedance amplifier (TIA) design lies at the core of high-bandwidth, low-current, low-noise nanopore sensing. TIAs convert input current into output voltage with a specific signal gain. While detailed discussion of various TIA designs to meet the nanopore challenge is beyond the scope of this thesis, the general trend is that on-chip CMOS-process TIA designs have offered the best bandwidth and noise performance due to their minimization, reduction in parasitic capacitance, and functional integration close to the nanopores [119]. Novel CMOS-based designs have been described for solid-state and biopore sensing [47], [120]–[131]. However, CMOS-based devices require access to facilities and expertise that many nanopore researchers may not have. Discrete component TIA designs for nanopore sensing in less demanding applications are available but still require electronics assembly and testing skills [132]–[137].

Despite the many designs present in the literature, a major roadblock is the availability of commercially available amplifiers that do not require fabrication and testing by nanopore researchers, and can be interfaced with custom nanopore cells. So far the amplifier based on

[47], [128] has been commercialized in the form of the Chimera Instruments VC100, offering a 4 MHz continuous sampling rate with 1 MHz 14-bit readout within the ±20 nA range, stable with up to 100 pF capacitive loads. Unfortunately, Chimera Instruments website is down at the time of this writing. Other option includes Zurich Instruments MFLI which has recently been used in a study of wetting of MoS_2 pores [138].

2.1.7. Nanopore noise

Nanopore sensor noise can interfere with biomolecular sensing, particularly for the detection of short, rapidly translocating molecules requiring high bandwidth. Molecular translocation signals can be distorted or obfuscated when signal-to-noise ratio (SNR) is insufficient. SNR is usually defined as follows:

$$SNR = \frac{\Delta I_{blockage}}{I_{rms}} \quad \text{Eq.2.6}$$

where ΔI is the difference between open pore current and current during molecular translocation, and I_{rms} is the root mean square (RMS) noise value. RMS current noise represents the average fluctuations of ionic current from the mean. Such noise results from multiple sources which can generally be categorized into flicker, thermal, shot, dielectric, and capacitive noise (Figure 2.8 B) [139], [140], and each has a distinct relationship with frequency. The noise **p**ower **s**pectrum **d**ensity (PSD) function illustrates these frequency dependencies and can be represented as follows:

$$S(f) = a_1 f^{-1} + a_2 f^0 + a_3 f^1 + a_4 f^2 \quad \text{Eq.2.7}$$

where a_1, a_2, a_3, and a_4 represent the contributions from flicker, thermal and shot, dielectric, and capacitive noise sources, f is the frequency in Hz.

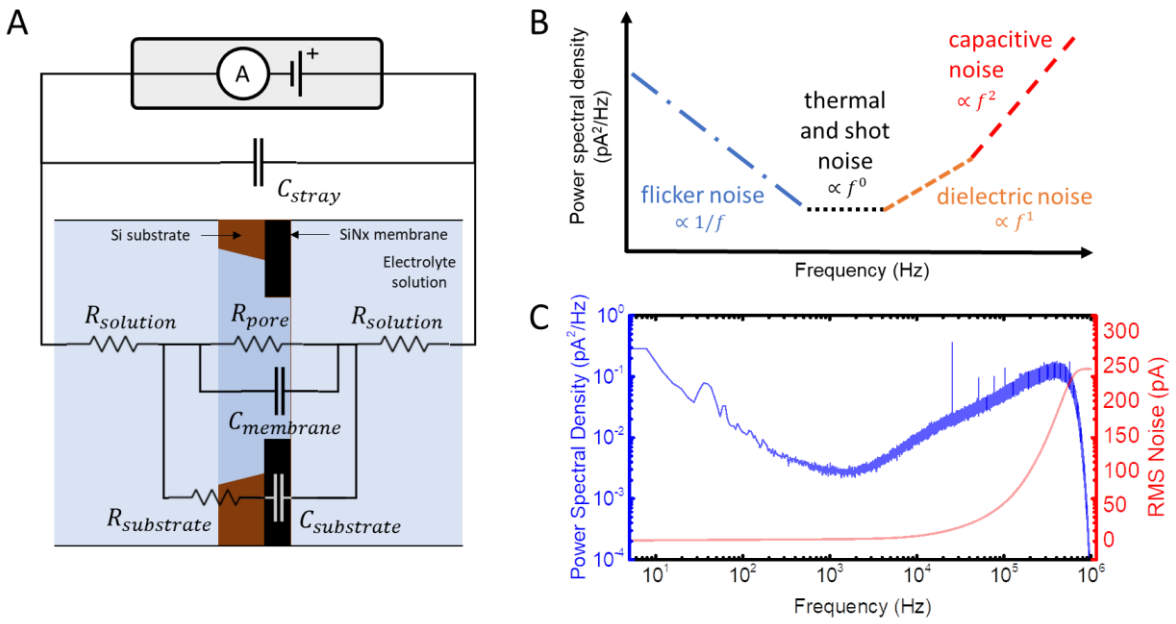

Figure 2.8. Equivalent circuit of a nanopore, and sensing noise. (A) Simplified circuit model of the nanopore sensor treats it as a system of resistors and capacitors associated with the pore and surrounding structures [47]. Membrane, substrate, and stray capacitance have a significant effect on noise at higher nanopore sensing bandwidth. (B) Power spectral density schematic representing the different noise sources as a function of frequency on a log-log scale, and (C) an example noise plot from a high-bandwidth reading of a nanopore low-pass filtered at 900 kHz.

Flicker or burst noise occurs in the low frequency range (<1 kHz) and its origins are not well understood. It may be associated with a wide range of causes such as slow fluctuations in number and mobility of charge carriers, nanobubbles, electrode noise, mechanical membrane fluctuations, flexibility and incomplete hydrophilicity of pore surfaces, and ion and contaminant adsorption [139], [140]. Hooge's formula has been used to represent flicker noise:

$$S(f) = \alpha \frac{I^2}{N_c f} \qquad \text{Eq.2.8}$$

where α is a constant quantifying the magnitude of noise, I is the ionic current, N_C is the number of charge carriers in pore volume, and f is frequency. Large flicker noise can make nanopore unusable since it can distort, obfuscate, or even mimic molecular translocation signals. Common methods of reducing this noise include improving surface hydrophilicity (metal oxide coatings,

piranha cleaning, oxygen plasma, pulsed voltage treatment), increasing pore diameter and electrolyte concentration, and improving mechanical stability of the membrane [140].

Thermal and shot noise, also referred to as white noise, are independent of frequency and have the following form [139], [140]:

$$S(f) = S_{thermal} + S_{shot} = \frac{4k_B T}{R} + 2qI \quad \text{Eq.2.9}$$

where k_B is Boltzmann constant, T is temperature, R is the pore resistance, I is pore current, and q is the charge of a single charge carrier. Thermal (Johnson-Nyquist) noise is related to thermal fluctuations of charge carriers, while shot (Poisson) noise occurs across a potential barrier such as that of the Ag/AgCl electrode [140]. White noise contribution to overall nanopore noise is negligible since pore resistance is often very high (>100 MΩ) and current is very low (pA – nA). Noise reduction can be achieved by using smaller pores, increasing TIA feedback resistor value, and cooling down the pore and the analog acquisition circuits.

Dielectric noise originates from current leakage through non-ideal dielectric membrane in which the nanopore is located [139], [140]. Thermal fluctuations in induced charge carriers in the dielectric add to noise in the 2 – 10 kHz range, which is modeled as:

$$S(f) = 8\pi k_B T C_{chip} D f \quad \text{Eq.2.10}$$

$$C_{chip} = \varepsilon A / d \quad \text{Eq.2.11}$$

where k_B is Boltzmann constant, T is temperature, C_{chip} is parasitic membrane capacitance, D is the dielectric dissipation factor of membrane, f is frequency, ε is membrane dielectric constant, A is the membrane area, and d is its thickness. Dielectric noise can be minimized by reducing the total chip capacitance, temperature, and using materials with smaller dielectric loss. PDMS coating on substrates such as glass produce some of the lowest dielectric noise [140].

Capacitive noise occurs mostly in the high-frequency spectrum since it is proportional to the square of the frequency [139], [140]:

$$S(f) = (2\pi)^2 C_{total}^2 V_{noise}^2 f^2 \quad \text{Eq.2.12}$$

where C_{total} is the total capacitance consisting nanopore chip, amplifier feedback, and parasitic capacitances, V_{noise} is the input voltage noise, and f is frequency. High bandwidth nanopore sensing is significantly limited by total system capacitance that results in capacitive noise. Noise can be reduced by using alternative materials such as glass, coating the chip with lower dielectric constant materials such as PDMS, or reducing the fluidic contact area with the membrane. CMOS-integrated nanopore amplifiers reduce both stray capacitance and voltage noise in the system as compared to the classical external amplifiers such as the Axopatch 200B [140].

The two main approaches to nanopore RMS noise measurement include time and frequency domain analyses [140]. Time domain analysis involves directly approximating the RMS noise of the nanopore from the ionic current time series data, and is analogous to the computation of a standard deviation for the ionic current trace:

$$I_{rms} = \sqrt{\frac{1}{n}\sum_{1}^{n}(X_I - i_n)^2} = \sigma_I \qquad \text{Eq.2.13}$$

where n is the number of discrete time series ionic current samples acquired by the DAQ, X_I is the mean ionic current, and i_n is the ionic current value of each individual sample. This method is simple and efficient, but does not distinguish noise contributions from different frequency domains.

Frequency domain analysis transforms the ionic current noise signal into a PSD that represents noise spectral power at particular frequencies (Figure 2.8 C). Bartlett's [141] or Welch's [142] methods can be used, where discrete Fourier transform is combined with signal windowing to compute the PSD. RMS noise can then be estimated for particular frequency ranges [140]:

$$I_{rms} = \sqrt{\int_{f1}^{f2} S(f)df} \approx \sqrt{\sum_{f1}^{f2} S(f)\Delta f} \qquad \text{Eq.2.14}$$

where *S(f)* is the PSD function integrated between lower (*f1*) and upper (*f2*) frequency bounds of interest either in continuous or discrete domains. Of interest is a unitless *L-value* approximation of *1/f* noise from frequency analysis since it can predict whether the nanopore would be usable in molecular experiments [35]:

$$L = \sqrt{\frac{1}{I^2} \sum_{1\ Hz}^{100\ Hz} S(f)\Delta f} \qquad \text{Eq.2.15}$$

The usability transition *L-value* for a 5 nm silicon nitride pores is around 10^{-2}, with a range from 10^{-4} (excellent) to 10^{-1} (unusable). L-values are likely dependent on pore size, and other operational parameters, and users are advised to verify the range for their application.

2.2. Thermal dynamics of nanopores

2.2.1. Heat transfer at the nano scale

Unlike the macro and micro scales, heat conduction on the nano scale does not follow continuum assumptions and diverges from Fourier law [143], [144]. Non-continuum heat transfer introduces phonons as discrete wave energy carriers for dielectrics, and electrons for electrically conductive materials. For semiconductors such as Si, both phonon and electron energy transfers are considered, with characteristic wavelengths on the order of 1 – 10 nm and mean free paths of energy carriers in the 40 – 300 nm range [144], i.e., the length scales of the nanopores themselves. Under these conditions quantum effects can be dominant in heat transfer and properties such as thermal conductivity may be lower than expected [145].

Likewise, fluid convection is complicated by non-equilibrium mechanisms in liquids, including electrical double layers, density layering, and interfacial solid-liquid coupling where flows diverge from classical Navier-Stokes flows at solid-liquid boundaries [146]. Electrical double layers result from interactions of liquid ions with a charged surface, resulting in two layers of charged ions over that surface. An applied electric filed can induce electroosmotic flow in these

layers, which has been harnessed in micro- and nano-fluidic pumping applications [147]. Density layering is an effect of non-charged surface interactions where liquid density has an oscillatory profile extending several nm from the surface [148]. This phenomenon can co-occur with charge oscillation for ionic liquids next to charged surfaces [149]. Lastly, unlike nanoscale gas and dilute media, liquids do not necessarily follow well-described and understood models based on molecular mean-free-path [146], [150], [151]. As such, many studies rely on empirical data and molecular dynamics (MD) simulations to describe the non-equilibrium phenomena.

Nanopore studies examining thermal behaviour have used a mixture of approaches, including numerical modeling using augmented continuum equations [40], [43], molecular dynamics simulations [38], [39], and empirical parameter fits for existing ambient-temperature models of nanopore behaviour (all other studies described in later sections, Table 2.1). Continuum equations augmented with additional terms representing thermodiffusion and electrophoretic mobilities of ions may be valid for the bulk solution behaviour in larger pores. However, their use may be questionable for small pores where near-surface effects comprise a large portion of the overall simulation volume. Molecular dynamics approaches provide valuable insight into atomic-level translocation dynamics, but may be computationally expensive if accuracy is required [152]. Empirical fits have shown agreement in trends between multiple studies but are quite far from providing an easily generalizable approach for quantitative predictions. The complexity arises from the temperature affecting the majority of the parameters involved, often in a non-linear way. Temperature influences buffer solution conductance, viscosity, and pH, as well as surface and bulk properties of molecules and pore materials. In turn, molecular translocation parameters such as nanopore conductance blockages, capture rates, translocation times, and ionic interactions change with temperature.

2.2.2. Conductance blockage and temperature

Pore conductance and conductance blockage is expected to increase with temperature (Figure 2.9) [44]. Largest contribution to pore conductance comes from bulk conductance which is easy to determine from salt solution conductivity curves. Conductivity increases approximately

linearly with temperature within the relevant range for liquid aqueous salt solutions used in nanopore research (KCl/LiCl, 0 – 100 °C) [41], [43]–[45]. Ionic double layer (DL) and electroosmotic (EOF) contributions are more difficult to estimate in practice due to the presence of temperature-dependent charge carrier mobility (μ_k), molecular charge density (σ), and Debye radius (r_D) terms. Further complications arise from their non-linear dependence on buffered solution pH, which has temperature dependence in itself [44], [153]. Nevertheless, DL and EOF contributions are usually neglected in analysis due to their relatively small contribution. Pore thermal expansion (length *l*, diameter *d*) as well as the change in pore access resistance with temperature can also be neglected due to small contributions at elevated temperatures.

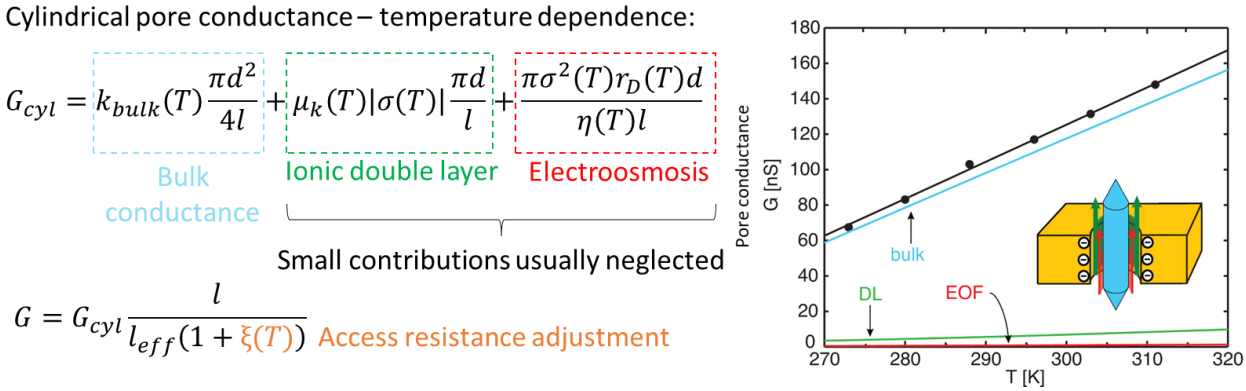

Figure 2.9. Pore conductance as a function of temperature. Bulk conductance has the greatest contribution, while ionic double layer, electroosmotic conductance, and access resistance adjustment terms are relatively small [44]. Copyright: Right figure reprinted with permission of IOP Publishing, from 'Temperature dependence of DNA translocations through solid-state nanopores' Figure 2, Verschueren et al., Nanotechnology, 26(23), 2015, via Copyright Clearance Center, Inc.

Similar to open-pore conductance, conductance blockages (ΔG) (Eq.2.2) resulting from molecular translocations scale linearly with temperature. Blockage increase depends on the salt solution and concentration used, and may double over a range of 40 K in 1 M KCl (pH 8) [44] or increase by 40 % over 35 K in 2 M LiCl (pH 8) [43]. Both global and local pore heating can enhance conductance blockage linearly [43]. Relative conductance blockage ($\Delta G/G$) changes little (<10 % drop) with temperature and can be used for normalizing molecular conduction signals across temperatures for comparison [43], [44]. Nanopore molecular dynamics simulation studies show

similar trends, and suggest the drop in relative blockage may be due to the temperature-dependent suppression of ionic mobility in the vicinity of the translocating molecule [38], [39].

2.2.3. Translocation time and temperature

Thermal control has been used to slow down DNA translocation speed for reduced detection bandwidth requirements and increased sensitivity. Fologea et al. [41] reported a 1.7x increased translocation time of a 3 kbp DNA (pSP65 plasmid) through 4 – 8 nm SiNx pores when temperature was reduced from 22 °C to 4 °C. Time increase was primarily attributed to the change in buffer viscosity, and was linearly related to viscosity. Addition of 50 % glycerol and bias voltage drop from 120 mV to 20 mV were more effective at reducing translocation times by 5.5x and 3x respectively. Zhang et al. [42] showed a similar result with 1.6x increased translocation time of λ-DNA (48.5 kbp) through 20 nm SiNx pores when temperature was reduced from 20 °C to 2 °C. Nicoli et al. [43] showed a 2.3x decreased translocation time of λ-DNA through 10 nm SiNx pores for uniform pore heating from 10 °C to 45 °C. Temperature gradients between the two sides of the nanopore did not produce any significant effects on DNA translocation [42], [43], which is consistent with theoretical results expecting weak thermophoretic effects [39], [40], and opposition of electroosmotic flow to thermophoresis within the pore [43]. Experimental results were generally consistent with a translocation time model proposed earlier [41], [154]:

$$t_d = C\,\frac{\eta_{solution}(T) L_{DNA}}{\sigma_{DNA}(T) V} \qquad \text{Eq.2.16}$$

where $\eta_{solution}(T)$ is electrolyte solution viscosity, L_{DNA} is DNA length, $\sigma_{DNA}(T)$ is its linear charge density, V is the applied voltage, and C is the proportionality constant aggregating other factors not included in the model. An alternative scaling model has similar proportionality with solution viscosity, but also includes a hydrodynamic radius of DNA (R_g) instead of its length [44], [155], [156]:

$$t_d \propto \left[R_g(T)\right]^2 \eta_{solution}(T) \qquad \text{Eq.2.17}$$

The hydrodynamic radius and viscosity decrease non-linearly with temperature (in K), resulting in non-linear reduction in translocation time, with a slower reduction at elevated temperatures. Finally, pore-DNA interactions in smaller pores (2.7 – 5 nm) amplify the slowdown of translocations at lower temperatures beyond just the effects of viscosity [45]. A ~7x slowdown due to additional pore interactions with the translocating molecule was observed from 30 °C to 0 °C as compared to ~2.7x expected with viscosity effects alone.

2.2.4. Capture rate and temperature

Molecular capture rates have been enhanced using elevated temperature conditions as well as temperature gradients in the vicinity of the pore. Negligible (~1x) [42] to moderate (~2x) [43], [44] DNA capture rate enhancements have been observed with uniform pore temperature elevation. Thermal effects can be explained by the changes in electrophoretic mobility of DNA as part of the capture rate model [44]:

$$\Gamma = c_{DNA}\Delta V \mu_{DNA}(T) \frac{\pi d_{pore}^2}{L_{pore} + \frac{1}{4}\pi d_{pore}} \quad \text{Eq.2.18}$$

$$\mu_{DNA}(T) \propto \frac{r_D(T)}{\eta_{solution}(T)} \quad \text{Eq.2.19}$$

where Γ is the capture rate, c_{DNA} is DNA concentration, μ_{DNA} is its electrophoretic mobility related to Debye length r_D and solution viscosity $\eta_{solution}$. Debye length, the distance over which a charge carrier is shielded by other charge carriers in a solution, increases with temperature. In turn, aqueous solution viscosity decreases with temperature. Thus, electrophoretic mobility increases with temperature, and results in increased capture rates.

Further improvements in capture rates have been achieved using pore temperature gradients. A 1.7x enhancement compared to uniform temperature increase was observed when translocating λ-DNA from hot (20 °C) to cold (2 °C) chambers on either side of the nanopore [42]. Thermal diffusion and its potential effect on the entropic entry barrier to the nanopore was offered as a possible explanation, although without much detail. While temperature gradients

across the entire pore length do not produce large enhancements, a localized gradient at the pore entrance can have significant effects. Nicoli et al. [43] showed how localized laser illumination and plasmonic heating using a bowtie antenna can enhance λ-DNA capture rate by an order of magnitude (10x – 20x). The overall conclusion was that thermophoresis can have a significant effect in the vicinity of the locally heated pore (over µm distances). Thermophoresis, the average tendency of particles to diffuse in the direction opposite to temperature gradients, can result from the mobility enhancement of electrolyte solution ions [43], [157]. Thermophoretic capture distance r_T can be expressed as a correlation related to the absolute temperature difference ΔT_{max}, Soret coefficient S_T, and empirically-determined constants a and b [40], [43]:

$$r_T = -\Delta T_{max} S_T a - b \qquad \text{Eq.2.20}$$

$$S_T(T) = \frac{D_T}{D} = \frac{1}{k_B T} \frac{\partial G(T)}{\partial T} \qquad \text{Eq.2.21}$$

Soret coefficient is a ratio of molecular thermodiffusion (D_T) and diffusion (D) coefficients, and depends on temperature and the change of Gibbs enthalpy ($G(T)$) of the molecule with temperature [40]. Therefore, a positive capture distance can be obtained from local positive temperature difference at the nanopore and a thermophilic (negative) Soret coefficient such as for the lithium ions [158]. Indeed, experiments showed enhanced thermophoresis using LiCl, but not KCl with a positive Soret coefficient [43], [158]. The thermophoretic capture distance for λ-DNA was predicted as 16 times the electrophoretic capture distance, and could explain significant capture rate enhancement.

Table 2.1. Summary of experimental studies on the effect of temperature in solid-state nanopores.

Source	Purpose	Method summary	Relevant takeaway
Fologea et al., 2005 [41]	Reduce DNA translocation speed using temperature, salt concentration, viscosity and bias voltage	Ion-beam milled 4 – 8 nm pores in 280 nm SiNx; sensing 10 nM 3 kBp pSP65 plasmid in 0.5-3 M KCl + TE (pH 7.5) using Axopatch 200B, 10 kHz LPF, 20-120 mV bias; 4 °C and 22 °C	• Temperature control setup not detailed • Translocation time increases linearly with viscosity • Using more viscous medium (glycerol) is more effective than reducing temperature: 5.5x vs 1.7x respectively
Wanunu et al. 2008 [45]	Investigate voltage-driven translocation dynamics of DNA through small ss-nanopores	E-beam drilled 2.7 – 5 nm pores in 10 nm SiNx; sensing 150 bp to 20 kBp dsDNA in 1 M KCl + Tris HCL (pH 8.5) using Axopatch 200B, 75 kHz LPF, 300 mV bias; 0 °C to 40 °C	• Temperature control system not detailed, thermoelectric in a faraday cage • Translocation times fit the Arrhenius model in terms of temperature dependence • Slowing down of translocation with reduced temperature is not explained fully by viscosity increase • Pore/DNA interactions may play a bigger role than viscosity changes with temperature
Nicoli et al., 2014 [43]	Investigate plasmon-induced local heating and DNA translocation in solid-state nanopores	E-beam drilled 10 nm pores in 20 nm SiNx with plasmonic nanostructures; sensing λ-DNA (48.5 kBp) in 1 – 2 M KCl, 1 – 2 M LiCl (pH 8) using Axopatch 200B, 100 mV bias; 20 °C to 60 °C via Peltier modules, 20 °C to 90 °C localized plasmonic heating	• Plasmon excitation via laser illumination of gold bowtie plasmonic antenna - hot spot at the nanopore; global Peltier module heating • Global and local heating increase conductance blockage via buffer conductance increase • Blockage event rates increased significantly by local but not global heating • Increase in localized electroosmotic flow, thermophoresis, and drag reduction implicated
Verschueren et al., 2015 [44]	Comprehensively investigate temperature dependence of DNA translocation through solid-state nanopores	E-beam drilled 8 – 16 nm pores in 20 nm SiNx; sensing λ-DNA (48.5 kBp) in 1 M KCl + TE (pH 8) using Axopatch 200B, 10 kHz LPF, 200 mV bias;	• Peltier heater/cooler via Labview+MATLAB, PID, dual faraday cage w PEEK cell • Increase with temperature: • Buffer conductance, ionic conductance of pore, ionic-

		0 °C to 50 °C via Peltier module	conductance blockages, event frequency • Decrease with temperature: • Translocation time, buffer viscosity, pH
Zhang et al., 2015 [42]	Investigate temperature changes and a temperature gradient as a means to slow down DNA translocation	Ion-beam drilled 20 nm pores in 10 nm SiNx; sensing λ-DNA (48.5 kBp) in 1 M KCl + TE (pH 8) using HEKA EPC10, 10 kHz LPF, 200 mV bias; 2 °C and 20 °C	• PTC heating and ice-water cooling, independent cis/trans chamber control • Translocation rate increases with temperature ~1.6x • Thermophoresis has no obvious effect on DNA translocation • Viscosity changes with temperature suggested as primary factor • Capture rate is enhanced, while translocation slowed by temperature gradient going from hot to cold side

2.3. Nanopore temperature control systems

Thermal control setups for experiments with solid-state nanopores have used thermoelectric heaters [43]–[45], positive temperature coefficient (PTC) heaters [42], and localized plasmonic heating via laser illumination [43]. Single or dual Faraday cages are used to isolate the setups while sensing with either Axon Instruments Axopatch 200B [41], [43]–[45] or HEKA EPC10 [42] pA current amplifiers. Most studies apply a 10 kHz low-pass filter (LPF) for sensing long DNA molecules (48.5 kbp λ-DNA), with only one study filtering at 75 kHz to detect DNA as short as 150 base pairs [45].

While the general details of the thermal control systems were mentioned, very few studies provided sufficient detail to be able to replicate the setups and predict their potential electrical and mechanical noise issues. Ubiquitous application of 10 kHz low pass filtering suggests significant noise issues above the range given a typical amplifier bandwidth of 100 kHz. Verschueren et al. [44] used dual Faraday cage setup with a Peltier heater/cooler attached in an

unspecified location (likely the external cage). External Faraday cage enclosed the Axopatch 200B head stage and the internal Faraday cage. RTDs (Pt100) provided temperature feedback from the PEEK nanopore flow cell and the inner Faraday cage. Temperature control was accomplished using a software PID via NI LAB-VIEW software. While the thermal time constant of the system is not specified, temperatures were equilibrated for 20 minutes prior to performing measurements.

Nicoli et al. [43] used an unspecified Peltier element for whole nanopore flow-cell heating with no details provided on the setup. However the plasmonic heating setup was sufficiently detailed for experiment replication. A 20 nm thick gold nanoparticle bowtie antenna with a 10 nm nanopore gap was illuminated using a 785 nm laser diode for plasmon excitation. A custom-built inverted microscope with a 60x water-immersion objective was used to expand the beam to 7 mm. Piezo stage was used to position the nanopore cell with respect to the laser beam. Localized temperature in relation to laser power was estimated from the relative nanopore conductance change [159]. Nanopore growth was considered insignificant for all but one of the experimental pores (see study SI), supporting the validity of this approach. Heating times were not specified, but likely approach the order of 10^6 °C/s for heating picoliter solution volumes [160].

Zhang et al. [42] used an unspecified PTC heater to increase the temperature using an unspecified method, and ice bath to reduce temperature. Thermal measurements were done using ultra-slender K-type thermocouples near the nanopore chip. Neither the temperature stabilization time not the system time constant were specified. Only a single Faraday cage was mentioned with locations of heating or amplifier equipment not specified. Another study used a similar resistive heating temperature control strategy for a microfluidic DNA purification assay device [48]. However, the heated microchamber was far removed from the nanopore sensor and all current readings were done after cooling down to room temperature. While the study reported more details on system performance, it was obvious that system noise would not be different from a regular non-heated setup since active heating was off during nanopore measurement and located away from the pore. Other studies [41], [45] have similarly not provided detail on their heating systems. Wanunu et al. [45] mentioned a custom-designed electromagnetically shielded chamber with thermoelectric regulation within ±0.1 °C and thermal equilibration within 5 minutes.

Biological pore studies have used similar heating methods, and have similar reporting gaps in their thermal system methods. Multiple studies reference back to the experimental methods used by Meller et al. [26], [161]. Method consists of using a custom-made copper base with a built-in thermoelectric device maintaining Teflon cell temperature. Teflon cell contains a biopore membrane in a microscale cell aperture. The whole system is enclosed in a copper Faraday cage. Temperature is maintained within ±0.01 °C to ±0.05 °C of setpoint ranging from 15 °C to 50 °C. Temperature measurement system or thermal performance is not detailed. Axon Instruments Axopatch 200B is used for sensing at the maximum available 100 kHz bandwidth. Unlike solid-state nanopores, biopore noise can be orders of magnitude lower [139]. Another study from the same time period provides no details on the thermal control system whatsoever, but uses a similar temperature range [23]. Later studies such as Payet et al. [27] presumably use Meller et al. setup based on the chain of cited references, with thermal control ranging from 20 °C to 70 °C.

Similar enclosure-based Peltier module setups have been built in other studies [24], [28], with either aluminum or copper cell heater blocks. Temperature is usually measured using thermocouples, with thermal precision of the system around 0.1 °C. Thermal performance is otherwise not detailed. Of note is the use of lower bandwidth (30 kHz) at elevated temperatures due to increased system noise [28]. Water evaporation from the electrolyte solution is also mentioned as a concern at elevated temperatures, without detailing the system used to add water back.

Alternative biological pore heating systems include the use of a refrigerated bath with a custom heat exchanger [25], Peltier devices coupled to the nanopore cell via heated/cooled liquid channels [29], and infrared laser-based heating [21], [22]. Refrigeration bath system was not well-detailed, except that it had a range from -10 °C to 20 °C, and used thermocouples for thermal monitoring with an overall temperature error of 2 °C. Liquid heating/cooling system was likewise not detailed – used water for heat transfer to the nanopore cell to achieve a temperature range from 5 °C to 45 °C. System bandwidth was limited to 10 kHz. Lastly, the infrared laser-based heating of a biological pore used intensity-modulated 1444 nm laser diode aligned by means of an inverted microscope with a 4x objective. Pore membrane located within a 50-µm hole in a

Teflon sheet was aligned using a motorized manipulator. Localized solution temperature was measured via nanopore conductance readings, which is expected to work well because of size stability of protein pores. Heating rates are comparable to picoliter volume heating on the order of 10^6 °C/s [160].

To conclude, studies controlling nanopore temperature provide few thermal control system design and performance details, and often record nanopore current signals at low analog bandwidths (not exceeding 100 kHz, with majority under 10 kHz).

2.4. Other milli- and micro-fluidic heating systems

Nanopore research has only used a subset of the known milli- and micro-fluidic heating strategies, namely Peltier and resistive thermal control for global, and laser-illumination strategies for local heating. Similarly, nanopore cooling has been achieved using Peltier or passive convection with ice water or air. This section summarizes some of the alternative approaches to microthermal heating and cooling systems. Reader is also referred to several excellent reviews on the topic [162]–[167].

Microthermal heating strategies are quite diverse, and include fluidic in-line heaters, ionic liquid Joule heating, in-situ micro-Peltier junctions, sandwich Peltier assemblies, Joule heating micro-elements, exo- and endo-thermic chemical reactions, microwave heating, acousto-fluidic heating, IR/laser, and plasmonic heating. Fluidic in-line heaters use externally heated fluids to deliver heat to the experimental apparatus [168], [169]. Ionic liquid heaters use electrical current to heat up ionic liquid in the heater channels to heat adjacent structures [170]. Micro-Peltier junctions provide both rapid heating and cooling of adjacent microfluidic volumes [171], [172]. Sandwich Peltier assemblies provide more-or-less uniform heating or cooling of larger volume microfluidic devices [173], [174]. Joule/resistive heating elements can be directly patterned within microfluidic devices for rapid and uniform heating [175]–[183]. Exo- and endo-thermal chemical reactions can change the temperature of nearby microchannels [184]. Microwave heating has emerged as a strategy for efficient heating of small volumes since it preferentially

heats aqueous solutions [185]–[188]. Acousto-fluidic heating uses high frequency surface acoustic waves to heat and mix the local microfluidic volumes [189], [190]. IR light heating is a non-contact method for fluids within optically transparent devices, and can decouple heating and cooling systems [191]–[193]. Lastly, plasmonic heating uses laser excitation on plasmonic nanostructures to heat the solutions [43], [194], [195].

Small scale cooling strategies, other than thermoelectric coolers [171], [173], [174], [196] and evaporative cooling [197] revolve around the use of micro-fins, pins, and grooves while using single- or multi-phase flows for a variety of fluids [167]. Two-phase systems require more tuning to the specific operating range of the system, but provide extra cooling performance due to the latent heat of phase change. Two-phase flows are extensively used in cooling systems that use heat pipes for example [198]. Nanofluids, or fluids that contain metallic or ceramic nanoparticles, have higher thermal conductivities than the base equivalents, improving heat transfer performance [198], [199].

Fairly accurate temperature measurement techniques are required for biological systems. Traditional techniques for localized temperature measurements in biological systems include thermocouples, thermistors, resistive temperature detectors (RTDs), and infrared (IR) thermometers [162]. Resolutions to below 0.1 °C are achievable with thermocouples, thermistors, and RTDs, with RTDs offering the highest linearity and long-term stability [200]. Thermocouples and RTDs seem to be preferentially used in microsystems discussed in the microfluidic heating studies due to their compact size, high precision, and relative ease of integration compared to other approaches. Other, more complex methods in microfluidic thermometry include liquid crystal thermometry, NMR spectroscopy, optoacoustics, interferometry, and fluorescence thermometry [162].

Chapter 3. Design and Instrumentation

3.1. Design Overview

The Design and Instrumentation chapter presents the development and fabrication of a research tool to facilitate solid-state nanopore ionic current sensing experiments in a range of temperatures and at high bandwidth. Design process follows well-established mechanical engineering design practices often taught in undergraduate mechanical engineering curricula and comprehensively detailed in [201]. Major design steps include the definition of specific system requirements, conceptual design, concept evaluation, and specific implementation of the selected concepts as a detailed design solution. During this process, the general design problem is split into an array of smaller sub-problems to solve with associated conceptual and detailed design steps. This chapter does not attempt to exhaustively describe all of the sub-problems for this project, but instead presents the steps, background and detailed reasoning behind many of the critical design decisions for the final instrument in the hopes of being a useful resource for future graduate students.

Section 3.1 covers the essential system requirements, functional assessment, possible instrument implementation approaches, and a specific hardware implementation of the selected approach with a global design overview. Subsequent sections focus on the design details and evaluation of major instrument subsystems. Section 3.2 provides details and challenges of the milli-fluidic flow cell design and fabrication, followed by Sections 3.3 and 3.4 describing the heat transfer system and noise control. Lastly, Section 3.5 presents the evaluation of instrument performance. Design sections (Sections 3.1, 3.2, 3.3, and 3.4) are written with a graduate mechanical engineering student designer in mind, providing extra background and process details. Readers with experience in the topics may find these details redundant and are encouraged to skim through sections of interest and focus on result tables and figures instead. Section subheadings are provided for rapid digital navigation.

3.1.1. Initial requirements

Initial requirements for instrument evaluation are presented in Table 3.1 and Table 3.2, and represent a projection of initial needs for molecular translocation experiments. Initial experiments would focus on molecular translocation characteristics of small nucleic acids and proteins at physiologically-relevant temperatures (ambient to 45 °C), which has not been adequately studied to date using solid-state nanopores. Initial applications work could focus on evaluation of molecular detection assay development steps that could include thermal cycling of reagents (ambient to 95 °C) in the proximity to the nanopore (i.e. PCR). Table 3.1 specifies the initial restrictions, i.e., design characteristics that must be met. Table 3.2 specifies the initial criteria, i.e., design characteristics that may be optimized through design, and prioritized by importance.

In summary, the instrument was expected to allow nanopore operation between ambient (~20 °C) and 95 °C, with a possibility to extend operation into below ambient temperature range.

Table 3.1. Initial design restrictions.

#	Restriction
1	Operate in a temperature range of 20 °C (ambient) to 95 °C
2	Maintain precise temperature to within ±1 °C around the nanopore chip
3	Provide thermal cycling capability between at least two temperature points
4	Provide an average temperature change rate of ≥0.5 °C/s
5	Accept fluidic sample volume of at least 10 µL and at most 100 µL
6	Perform molecular translocation experiments at operating temperature and volume with 1 MHz bandwidth
7	Steady-state temperature control uniform (±0.5 °C) in the buffer close to the chip
8	Material compatibility with salt buffer, DNA, and assay reagents at the operating conditions
9	Attenuate electrical noise pickup from external mechanical vibration to the system within the 1 – 1000 Hz frequency range, no specific limits provided
10	Attenuate electromagnetic interference from external electrical circuits to the levels of a no-heater setup + 15% (<75 pA rms over 1 MHz bandwidth no load Chimera amplifier reference cell, 100 MΩ, 10pF)

Table 3.2. Initial design criteria.

#	Criterion	Weight*
A	Provide real-time operation feedback, i.e. device status, temperatures, etc.	8/10, 20.51%
B	Maximize temperature change rate	5/10, 12.82%
C	Minimize temperature gradient across the solution chambers	8/10, 20.51%
D	Minimize buffer volume (10 µL minimum)	3/10, 7.69%
E	Ability to cycle to 98 °C, and below 20 °C	3/10, 7.69%
F	Maximize user friendliness	8/10, 20.51%
G	Preference for modular design with easy exchange and replacement of components, re-usability	4/10, 10.26%

***** first weight value shows the importance of the criterion to the experimental investigator on a scale from 0 to 10, second value shows the global weight of the criterion where all importance values add up to 100 %.

Biological buffers, reagents, and biomolecules (DNA, proteins) could be introduced in the vicinity of the nanopore, and brought to a specified temperature at an average rate exceeding 0.5 °C/s. Thermal precision was expected within ±1 °C of the set point based on a calibrated reference thermometer. The temperature gradient within the liquids in the fluidic cell region surrounding the nanopore chip was expected to be as symmetric and uniform as possible. The sample volume within the nanopore flow cell could be within a range of 10 to 100 µL. Flow cell material would be compatible with molecules (DNA, proteins) and reagents (salt solutions, buffers). The nanopore would be used to monitor molecular translocation events with a bandwidth of up to 1 MHz. Electromagnetic interference was to be minimized so as to be as close as possible to the noise performance of the standard non-temperature controlled system with a value below 75 pArms reference dummy cell noise (100 MΩ, 10 pF cell at 65 pArms + 15%) at the 1 MHz bandwidth recommended. Electrical noise pickup from mechanical vibrations were to be minimized within the low frequency range (1 – 1000 Hz).

3.1.2. Functional assessment

Once initial requirements are set, the design process enters the concept generation steps in which functional assessment is crucial to splitting the general problem of designing an instrument into smaller, more manageable sub-problems. A starting point is provided by the functionality of a typical ambient-temperature solid-state nanopore fabrication and sensing instrument. Such an instrument necessitates steps in preparing a thin membrane assembly, fabricating a nanopore in the membrane, and detecting the molecular translocation signals from an introduced sample solution. These steps – along with the expected process physics and additional considerations from the literature review – form the basis of the functional definition of the system (Figure 3.1). The expected operation is described in terms of functions, their inputs, and outputs without specifying an implementation. Larger functions can be broken down into smaller functions with their own associated inputs and outputs. Implementation does not have to have a 1:1 mapping of functions and physical solutions, and simply guides consideration of expected instrument behaviour.

High level functional breakdown (Figure 3.1) consists of three main functional components. The first component is preparation of membrane chip assembly by securing a silicon chip supporting a thin membrane within the device while ensuring isolated fluid electrolyte access to both sides of the membrane. The chip assembly then participates in the nanopore fabrication by **c**ontrolled **b**reak**d**own (CBD) methodology [35]. Lastly, molecular signal detection component starts with exposure of the nanopore-containing membrane to a molecular sample, replacing the nanopore fabrication buffer. Molecular translocation signals are recorded using a high-bandwidth current amplifier setup. External noise, nanopore obstruction, and temperature have to be managed during current recording. An example of further sub-functional breakdown is shown for temperature management. Temperature management in a fluidic context is responsible for temperature measurement and control, as well as the surrounding issues of evaporation, degassing, flow sealing, pressure management, dimensional stability, material chemical reactivity, operating and safety limits of all subsystems involved.

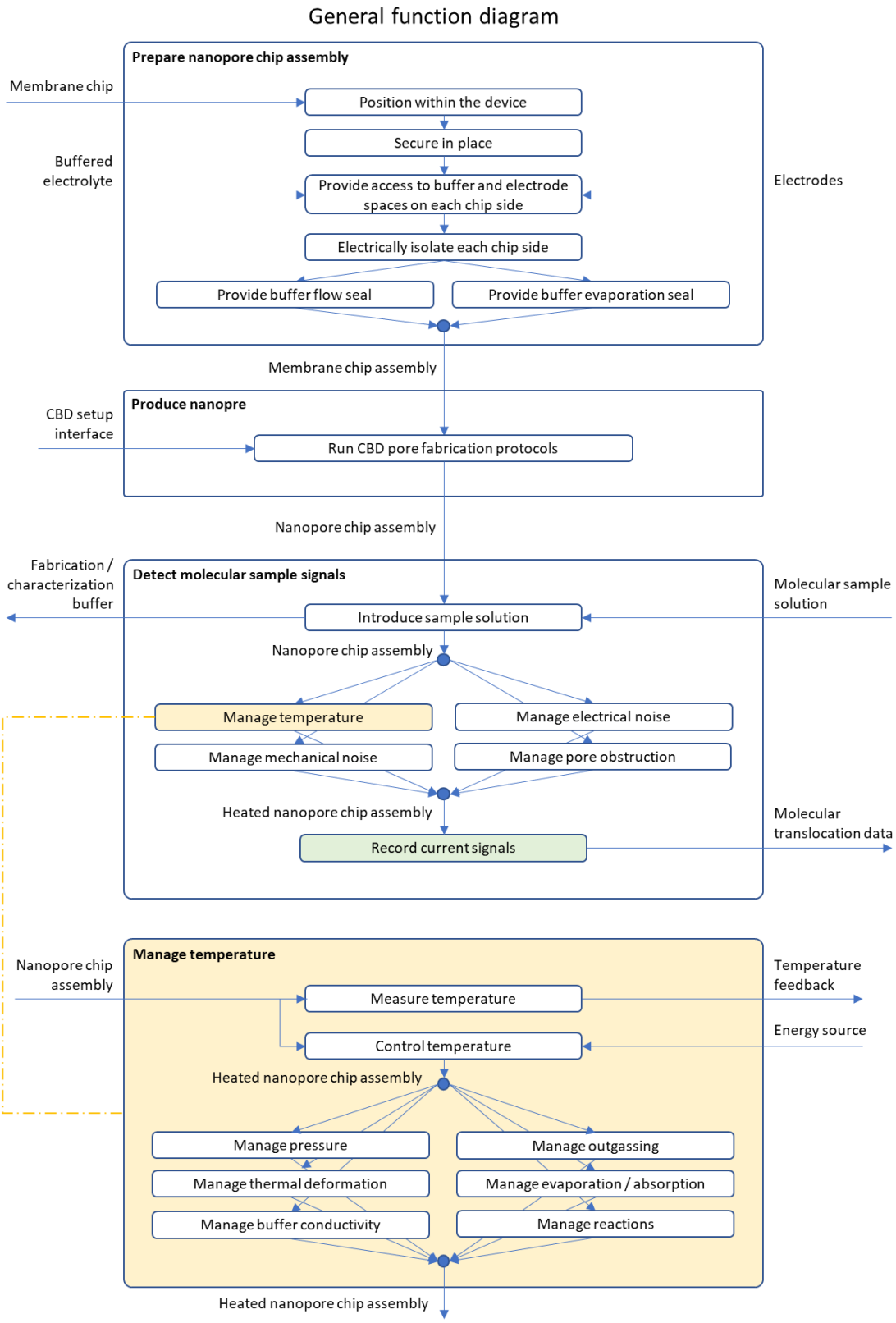

Figure 3.1. General function diagram for the nanopore thermal recording system. An example of subsystem functions for temperature management is highlighted.

3.1.3. The noise problem and how it guides implementation

While many microthermal heating and cooling strategies are described in the milli- and micro-fluidic literature [162]–[167], few of them may be appropriate for implementation in high-bandwidth electrical sensing of molecules due to potential for electrical interference. Electrical temperature measurement and heating circuits can add a significant amount of electrical noise, particularly at higher frequencies. Temperature-controlled solid-state nanopore studies have mostly limited their sensing bandwidth to 10 kHz [41]–[44], and 75 kHz [45] despite isolating their sensing circuits using one or two Faraday cages. Biological pore studies have reported 100 kHz [26], [27], [161], 20 – 30 kHz [24], [28], and 10 kHz [22], [29].

A case-in-point demonstration of the impact of electrical measurement system noise on the high-bandwidth current amplifier system can be seen in Figure 3.2. Two battery-operated thermometer sensors – VWR Temp Alert (thermistor), and OMEGA OM-EL-EH-TC (thermocouple) – were introduced next to a reference test cell (100 MΩ, 10 pF) connected to a 1 MHz Chimera VC100 amplifier within its enclosure (Appendix A – Thermometer noise test setup). This setup approximated temperature measurement in the vicinity of a chip containing a small, low-capacitance solid-state nanopore expected to have low noise. Current traces filtered at nearly full amplifier bandwidth (900 kHz) show an expectedly low baseline current noise (65 pArms), but are an order of magnitude higher when coupled with temperature measurement systems despite isolation (Figure 3.2 A, B). Low-pass filtering the signal at 20 kHz not only significantly reduces the overall noise, but also allows the use of OMEGA measurement system without detriment to the signal (Figure 3.2 C, D). Unfortunately, VWR Temp Alert thermometer demonstrated a particularly high noise coupling that was also significant at 20 kHz. This simple demonstration shows the limiting effects of electronic temperature measurement systems, even if attempts are made to isolate from external noise sources. Therefore, high-bandwidth nanopore current measurements require careful electrical isolation and the removal of the electrical temperature measurement and control equipment from the vicinity of the nanopore chip, or even use non-electrical alternatives.

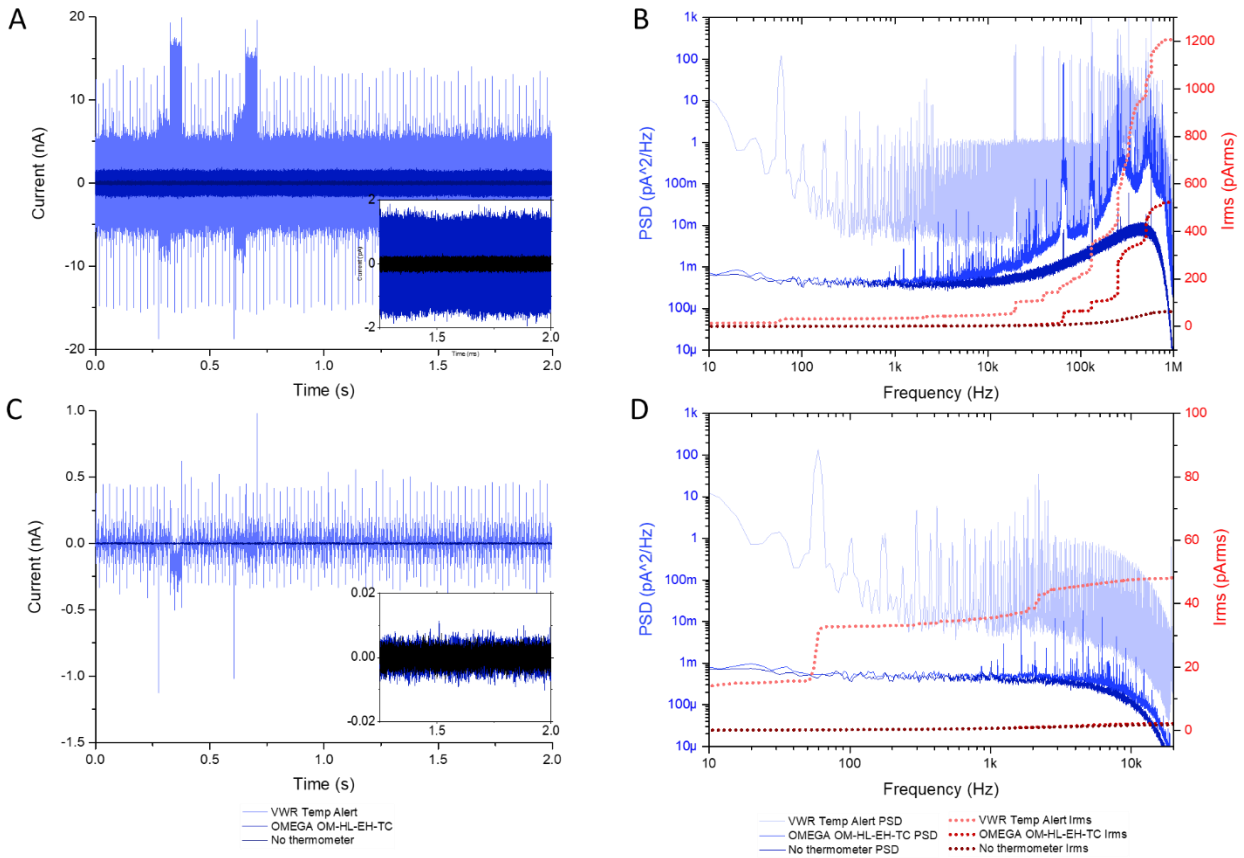

Figure 3.2. Noise associated with electrical thermal measurement systems. Current traces (A, C) and PSDs (B, D) from two battery-operated thermometer system sensors introduced next to a 100 MΩ, 10 pF reference test cell connected to a 1 MHz Chimera amplifier within a Faraday enclosure. Excessive noise density and currents are seen in signals with a 900 kHz 8-pole Bessel low-pass filter applied (A, B). When filtered at 20 kHz, the noise is much lower and barely distinguishable from baseline for the OMEGA thermometer (C, D).

3.1.4. Heating method evaluation

Electronic heating provides some of the best performance in the microfluidic context, but may be problematic for low-noise and high-bandwidth nanopore measurements. On-chip resistive microheaters provide some of the fastest response times (>20 °C/s) with precise temperature control and uniform thermal profiles in small microfluidic channels (<10 µL) [175]–[183]. Micro-Peltier junctions [171], [172] also support cooling. Unfortunately, for larger volumes targeted in the current design both the response times and uniformity would be reduced unless the volume is spread across a larger heater area, possibly increasing overall electrical capacitance

of the system. Increased heater capacitance, voltage noise from the heater circuits, and proximity to the nanopore membrane would likely be very detrimental to overall bandwidth (Eq.2.12). Macroscopic heating systems, such as Peltier modules presently used in nanopore experiments, may have a noise advantage due to isolation from the membrane chip via Faraday enclosures. One of the disadvantages of such systems is a large thermal mass, significantly reducing heating and cooling rates while requiring large electrical currents to drive. Microwave heating [185]–[188] has been used for efficiently and rapidly heating milli- and micro-fluidic volumes, but effects of strong microwaves on semiconductor membrane heating and localized nanopore currents could potentially alter ionic current and noise in an undesirable way. Lastly, acousto-fluidic heating [189], [190] provides both the heating and fluid mixing functionality, but its effects on solid-state nanopore signals are also unknown. Acousto-fluidics may face similar noise issues to other electronic strategies due to piezoelectric actuation. In addition, effects of acoustically generated fluid flows on molecular capture and translocation through the nanopore are unknown.

Non-electronic heating methods present alternatives that can potentially ensure low-noise and high-bandwidth nanopore sensing. These include exo- and endo-thermal chemical and physical reactions, fluidic in-line heaters, and optical and plasmonic heaters. The first set of alternatives uses exo- and endo-thermal chemical and physical reactions to change the temperature of nearby microchannels [184], [197]. A major disadvantage is a requirement for a constant supply of reactants, potentially non-uniform heating, and non-linearity of thermal control. Fluidic in-line heaters use externally heated or cooled fluids to deliver heat to or away from the experimental apparatus [168], [169]. While conceptually simple and modular, detailed implementation requires multiple bulky external components, increasing system size, response time, and energy requirements. Optical heating methods, such as IR light heating [191]–[193] and plasmonic heating [43], [194], [195] are the last category of non-electronic heating methods. These methods allow decoupling of heating and cooling systems while also preferentially affecting a small fluid volume of interest. The challenges in the solid-state nanopore context arise from potential excitation of stray currents (noise) in semiconductor chip frame (Si band gap ~1.1eV [202]) by light beam illumination, likely including light scattered by the fluidic medium.

An existing plasmonic heating study likely limited nanopore signal bandwidth at 10 kHz while detecting large molecules for these reasons [43].

3.1.5. Approach selection

The fluidic in-line heater approach may offer the best balance of thermal performance for a reference low-noise and high-bandwidth solid-state nanopore sensing system (Table 3.3). To meet the previously outlined minimum requirements and be on par with commercial thermocyclers [203], the preferred approach would offer a temperature range from 0 to 100 °C, thermal precision of <0.25 °C, average temperature ramping at >4 °C/s, and uniform thermal profiles across the fluidic volume between 10 and 100 µL. The approach would also ideally not introduce any electromagnetic interference with the nanopore electrical current measurement system. Out of the four winning approaches, in-line fluidic heater was chosen for high noise isolation potential as the primary deciding factor, followed by component modularity and fairly well-established design processes for the mechanical and electronic components involved. Nevertheless, many of the other presented approaches are likely viable with enough expertise, resources and troubleshooting time thrown at the problem.

3.1.6. Specific hardware implementation

A modular in-line fluidic heater system was designed and implemented, making use of ultra-high resistivity, inert heat transfer fluid (Solvay Galden HT 200 perfluoropolyether) to transfer heat to the solution inside a custom 3D-printed fluidic cell (Formlabs High Temperature resin v1) in contact with the nanopore membrane (Figure 3.3). The heat transfer fluid, stored in temperature-controlled reservoirs at different setpoint temperatures, is passed through the fluidic cell while measuring the analyte fluid temperature in real-time using a fiber-optic thermometer (Osensa FTX-200-LUX+). Ionic current is detected using a low-noise current amplifier (Chimera Instruments VC100) with 1 MHz bandwidth. Figure 3.4 shows the practical implementation of this design.

Table 3.3. General approach comparison and selection by weighted scoring.

Approach	Temperature range * [x1]	Fluid volume [x2]	Thermal ramp rate [x2]	Thermal precision [x3]	Thermal uniformity [x2]	Electromagnetic compatibility [x5]	Weighted score **
In-line fluidic heater	++++	+++	+	+++	++	+++++	50
Micro-Peltier	+++++	+	++++	+++++	++++	+	43
Peltier sandwich	+++++	++++	++++	+++	++++	++	48
Exo/endothermic physical and chemical processes	+++	++	++	+++	+	+++++	47
Joule heating of ionic liquids	++++	++	+	+++	++	+	28
Joule heating of metallic micro-heaters	++++	+	++++	+++++	+++++	+	44
Microwave heater	++++	+++	++++	++++	++++	++	48
Plasmonic heater	++++	+	+++	++++	++	++	38
IR heater	++++	++	+++	+++	++	++	37
Acousto-fluidic heater	++++	++	+++	++++	+++	+	37

***** The 6 criteria listed here are not exhaustive but form some of the major deciding factors that illustrate the decision tool function. Full list of restrictions and criteria is presented in Table 3.1 and Table 3.2.

****** Weighted score is the sum of products of criterion scores (indicated by number of +) and criterion weights (indicated in [brackets]). i.e. Weighted score = $\sum$ (# of +) · [criterion weight]

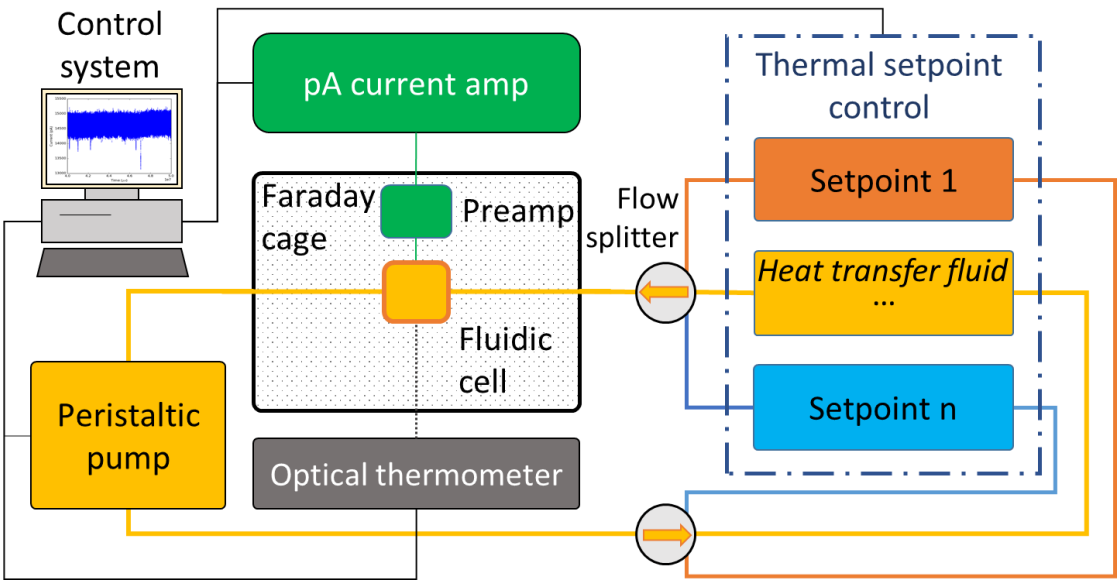

Figure 3.3. Fluidic thermal control system concept for low-noise and high-bandwidth solid-state nanopore recording. Highly electrically resistant heat transfer fluid transfers heat to and from the fluidic cell within a Faraday cage, minimizing the noise from external electrical systems.

The fluidic cell maintains a uniform thermal profile of the analyte fluid sample in the vicinity of the nanopore membrane chip using a helical geometry heat transfer channel and is described in Section 3.2. Multiple thermal setpoints, as opposed to a single flow-through heater, enable cost-effective system implementations that can rapidly ramp the cell temperature using auxiliary high or low temperature setpoints until the required temperature is reached. Peristaltic pump is used to maintain a sealed fluidic loop that simplifies maintenance and isolates the heat transfer fluid from the other system components. “Negative” pressure configuration for drawing the fluid into the cell reduces thermal losses before the fluidic cell, and ensures pulsatile forward flow from the peristaltic motion of the pump is minimized at the cell. The details of the presented thermal flow system are described in Section 3.3. Section 3.4 addresses the design of the Faraday cage to promote electrical and mechanical noise isolation while preventing the overheating of the nanopore current amplifier headstage next to the heated cell. The last design section, Section 3.5, provides experimental validation and evaluation of the instrument performance to demonstrate how it meets the requirements defined in Section 3.1.

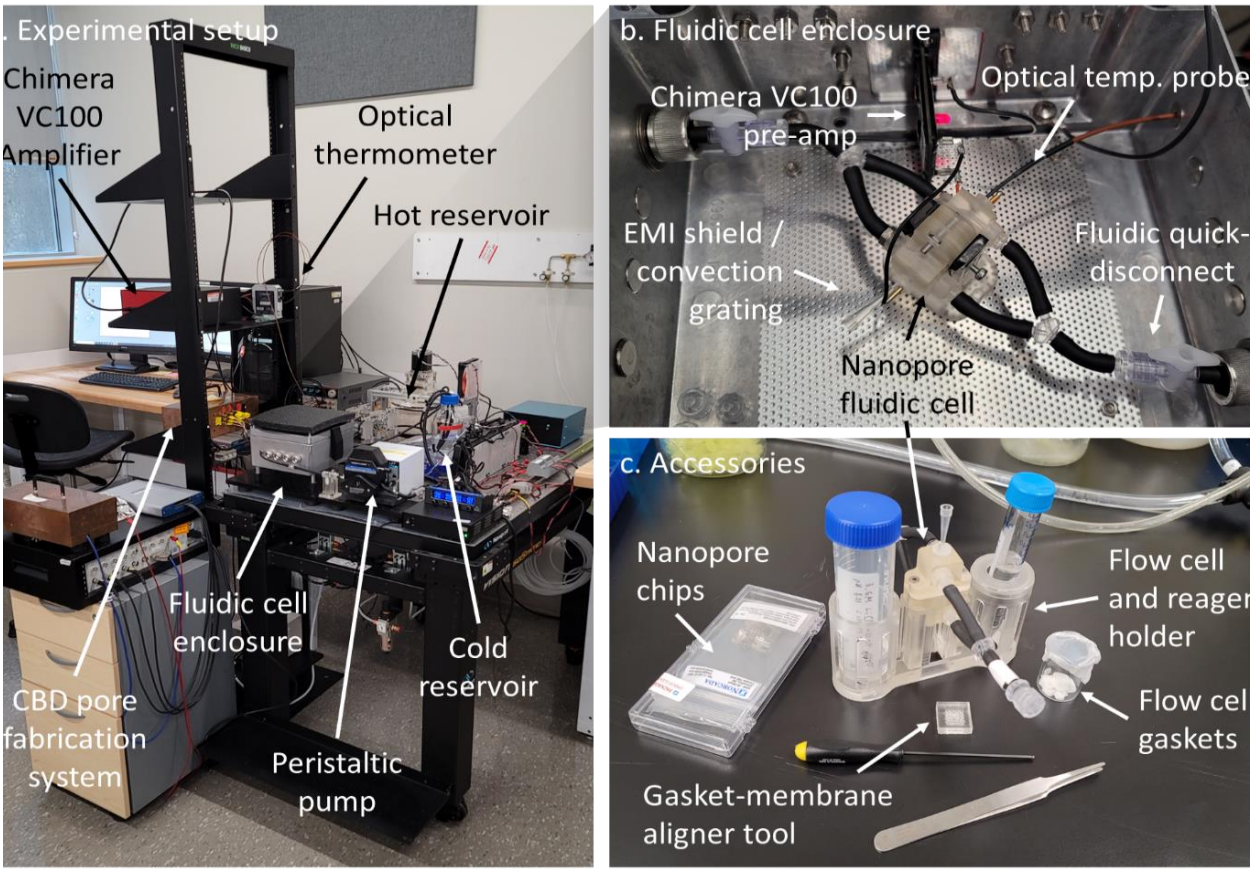

Figure 3.4. A dual-setpoint instrument featuring a hot and a cold reservoir. Experimental setup (a) shows the major system components. Fluidic cell enclosure (b) shields the nanopore cell connected to the pre-amplifier stage and the optical thermometer probe. Portability of the cell and accessory components (c) ensure low-effort usability of the system, comparable to the non-thermal CBD setups commonly used in the lab.

3.2. Fluidic Cell Design and Fabrication

3.2.1. Fluidic cell overview

Fluidic cell is the component that houses the nanopore membrane chip in liquid (e.g. salt solution with molecular analytes to be detected) while providing means to transfer heat input to the liquid surrounding the nanopore chip to maintain a relatively uniform temperature within the reservoir containing the nanopore. Figure 3.5 shows the overall design schematic and a sample fluidic cell prototype 3D-printed using a stereolithographic printer.

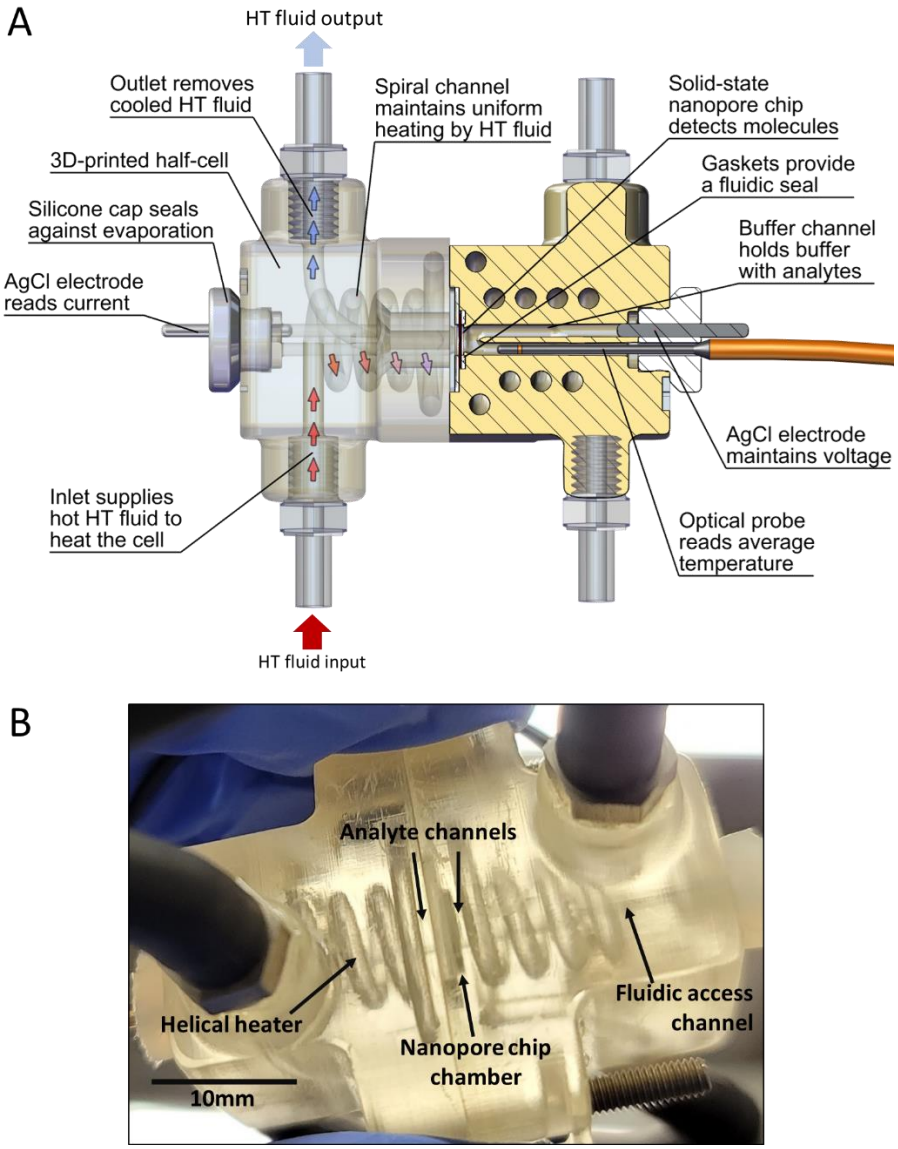

Figure 3.5. Fluidic cell design overview. (A) Fluidic cell design schematic highlights subcomponents by function. (B) Cell prototypes were 3D-printed by stereolithography using Formlabs Form 2 printer in Formlabs High Temperature (v1) resin with the manufacturer-recommended processing steps.

3.2.2. Fluidic cell geometry

3.2.2.1. Geometric considerations

The geometry of this cell is largely restricted by temperature uniformity requirements and the need to maintain precise heating of a millifluidic volume. Minimizing average thermal ramp times to achieve a steady state setpoint temperature is also desired. From a purely geometric

perspective, time to steady state is minimized by changing the effective convective area, as well as by minimizing material volume to reduce the cell's thermal capacity. This design consideration can be illustrated by the time constant expression from the lumped capacitance model of convective heat transfer into the cell [204]:

$$\tau = \frac{\rho V C}{h A_s} \qquad \text{Eq.3.1}$$

where τ is the thermal time constant, h is convective heat transfer coefficient, A_s is the effective convective surface area, ρ is cell material density, V is its volume, and C is the material heat capacitance. Increasing effective convection area and reducing cell volume reduces heating time.

Relatively uniform temperature distribution of the heated region at steady state is also a desired outcome in this design, however it is difficult to find direct and general guidelines to this question in the fluidic heat exchanger literature [205]–[209]. The heat source is a moving fluid which loses energy as it propagates across the heat exchange surfaces, therefore temperature gradients in heated regions are inevitable and expected. Microfluidic (<<10 µL) volumes are often highly thermally uniform due to large heating areas and wide scale of thermal gradients covering comparatively small fluid volumes [175]–[183]. Since current design requirements are within a larger millifluidic regime (>10 µL), temperature gradients are expected to be non-negligible, especially for materials with low to moderate thermal conductivities.

3.2.2.2. Geometry patterns

While geometry, materials, and flow parameters are all tightly linked in determining how uniform a temperature profile of a heated volume is, some common patterns derived from observations in the heat exchanger literature can be sketched out as a starting point (Figure 3.6). The most effective geometries control the location of heat sources and heat transfer barriers to enclose the heated volume (Figure 3.6 a). Once enclosed, the heat transfer from the heated volume to the external cold environment is minimized, and temperature equalizes with the heat source temperature at steady state. Since heat transfer fluid loses heat along the heat transfer

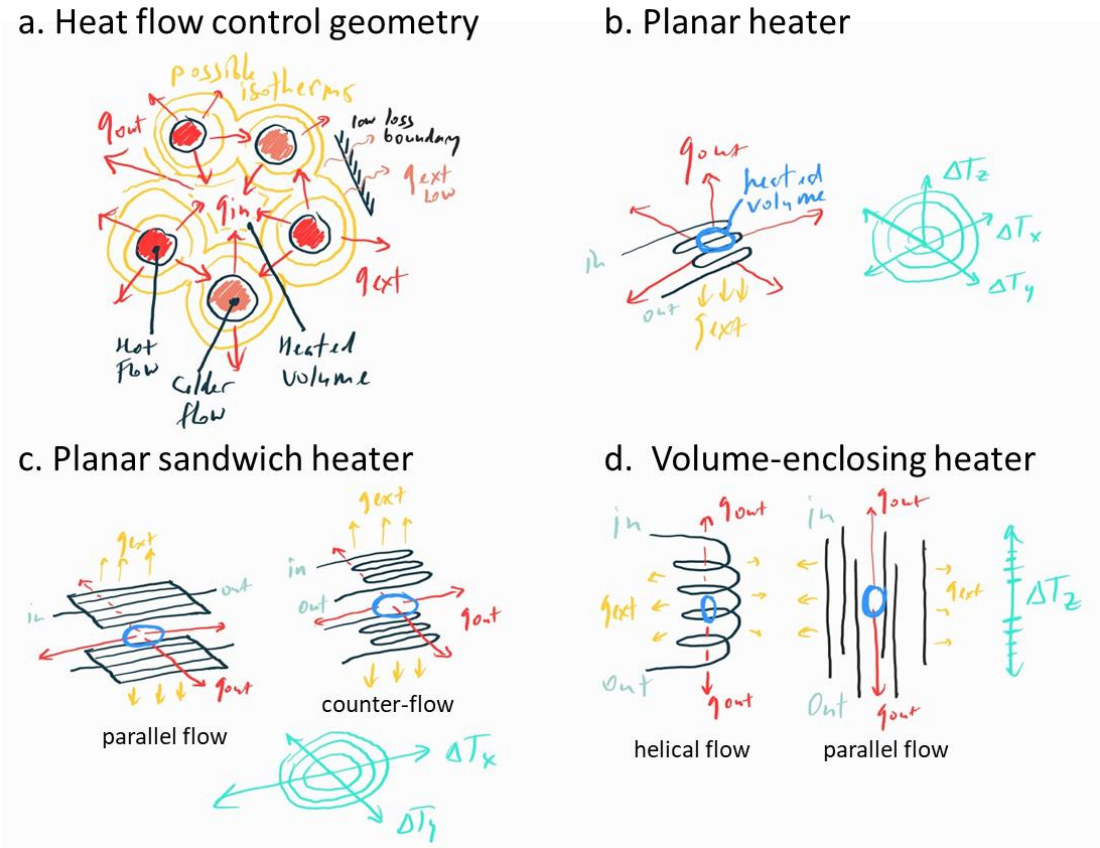

Figure 3.6. Fluidic heater geometry patterns and examples for heating a finite static volume. Temperature changes across a small heated solid or fluid volume (depicted in blue) can be minimized by controlling the location and position of the fluidic heat sources and barriers to limit energy losses and facilitate thermal equalization across flows (a). Directions of heat transfers are denoted by red arrows. Fluidic heaters can be examined according to how their geometry limits heat losses from the heated volume and prevents formation of temperature gradients in a particular coordinate system at steady state (b, c, d). I.e. volume-enclosing heater (d) limits heat losses to a single direction, potentially facilitating thermal uniformity at the cost of overall efficiency where the bulk of heat is lost to the environment if not well-insulated.

surface, a continuous channel along the heated volume will, on average, have a decreasing temperature along its path length. Steady-state temperature gradients in these channels can be minimized by using parallel-, counter-, and cross-flow geometries that force heat exchange between adjacent hot and cold channels, reducing their temperature difference.

The nanopore chip and the adjacent fluidic chambers occupy three-dimensional space and require consideration of all dimensions at the millifluidic scale. This is particularly true for higher temperatures (e.g. 90 °C), where thermal uniformity has to be within 1 % to maintain the

1 °C precision within the membrane chip and its surrounding region. As such, 3-D heater geometries can be examined according to the potential to minimize heat losses and gradients (Figure 3.6 b, c, and d). A single planar-type fluidic heater is likely to have the greatest thermal gradient problem since heat spreads in all directions (Figure 3.6 b). A planar sandwich heater configuration minimizes the gradient in the normal direction for relatively thin geometries (Figure 3.6 c). Unfortunately, large-volume heated regions require significant planar spreading of the heaters and the nanopore fluidic chambers. As such, this geometry is likely most suitable for micro- and low millifluidic volumes. Volume-enclosing heaters (Figure 3.6 d) can potentially surround the entire heated region and minimize thermal gradients to the temperature differences between the heating channels. In practice, nanopores require fluidic and electrical access with at least one access point to the surrounding cold environment, creating an opening for the heat to leave the enclosed volume.

3.2.2.3. Geometry selection

Both the planar sandwich and volume-enclosing geometries were considered for further refinement, specifically the counterflow spiral sandwich and the helical flow designs involving curved channels (Figure 3.7 a, b). Using a single curved as opposed to multiple parallel linear channels allows to generate Dean vortices that increase convective heat transfer and fluidic mixing (Figure 3.7 c) [210]–[213]. Fluidic mixing can help improve thermal uniformity within the channel, as well as between channels by increasing heat transfer coefficients. Dean vortices form when Dean number is sufficiently high for a particular geometry. Dean number for a flow is defined as:

$$De = \frac{\sqrt{0.5 * inertial\ foces * centripetal\ forces}}{viscous\ forces} = Re\sqrt{\frac{D}{2R_c}} = \frac{\rho u D}{\mu}\sqrt{\frac{D}{2R_c}} \qquad \text{Eq.3.2}$$

where *Re* is Reynolds number, ρ is fluid density, *u* is fluid velocity, *D* is the channel hydrodynamic diameter, μ is fluid's dynamic viscosity, and R_c is the radius of curvature of the channel.

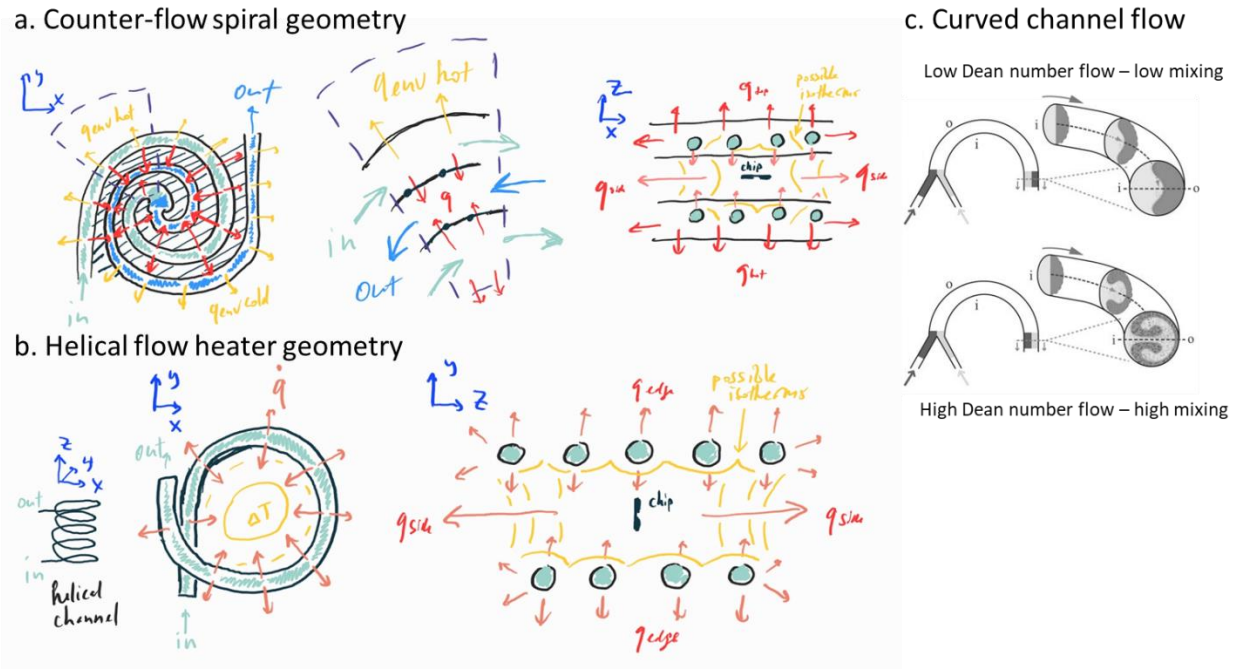

Figure 3.7. Curved-channel fluidic heating element sketches. Counter-flow spiral configuration (a) is a candidate geometry for facilitating a thermally uniform central hotspot that can be positioned on either side of a thin nanopore chip sandwich. Helical flow configuration (b) is a volume-enclosing geometry that could facilitate a thermally uniform central cylinder region and could be preferred for larger nanopore analyte volumes. Curved channel geometries (c) produce flow mixing that can improve convective heat transfer [212] and potentially reduce thermal gradients. Copyright: (c) reprinted with permission of Royal Society of Chemistry, from 'Fluid mixing in planar spiral microchannels' Fig. 1, Sudarasan & Ugaz, 6(1), 2006, via Copyright Clearance Center, Inc.

Helical heat exchanger geometry (Figure 3.7 b) was ultimately chosen for initial modeling studies and later fabrication since it potentially allows heating larger volumes in a space-efficient manner. The choice was also facilitated by the ability to manufacture complex millifluidic geometry using a stereolithographic 3D printing system and an appropriate high-temperature resin. Sandwich heater geometry would be more universally manufacturable, but is limited to flat cell designs. Helical heater is more challenging to make using traditional means, but is well-suited to heating larger volumes since it can be designed to surround the entire 3D volume in a space-efficient manner while reducing material volume and internal cell heat capacity. Counter-flow spiral heater was also modeled and prototyped as part of the development of a microfluidic cell, but is not included in this thesis, being a part of the (ongoing) future work.

3.2.3. Fluidic cell materials

3.2.3.1. Materials overview

A heated nanopore fluidic cell would ideally use a highly thermally conductive material with relatively low heat capacitance such that heat is rapidly delivered to the aqueous solution surrounding the nanopore membrane and with high thermal uniformity. Such material would have high thermal diffusivity α [214]:

$$\alpha = \frac{\lambda}{\rho C_p} \qquad \text{Eq.3.3}$$

where λ is thermal conductivity of the material, ρ is material density, and C_p is its thermal heat capacitance at constant pressure. Another way to look at thermal diffusivity is from a perspective of distance x it takes to diffuse heat in time t [214]:

$$x \approx \sqrt{2\alpha t} \qquad \text{Eq.3.4}$$

Heat can diffuse fast and wide in high thermal diffusivity materials, particularly if external convective heat losses are small relative to material's thermal conductivity (*Biot number < 0.1*). Low thermal diffusivity materials can be used to encase high diffusivity materials and prevent excessive heat losses to the external environment.

From a thermal perspective, a metal cell externally thermally shielded by polymeric foams would thus be ideal for the design (Figure 3.8) [214]. Unfortunately, a purely metallic cell would be wholly incompatible with electrical nanopore sensing due to its electrically conductive nature. Even a thin layer ceramic-coated or polymer-coated metallic cell would likely interfere with a high-bandwidth nanopore setup by providing paths for unwanted electrical noise, and parasitic capacitance coupling to the amplifier inputs. Lastly, the cell needs to be bioinert in relation to the tested molecular samples. For example, divalent metals such as Fe, Zn, Mn, and Cu affect form and function of cellular proteins [215] and therefore need to be carefully considered in the test environment such as the nanopore sensor. In turn, biochemically-active environments containing salts can facilitate corrosion even in generally corrosion resistant metals such as stainless steels, resulting in metal leaching into the biochemical environment [216].

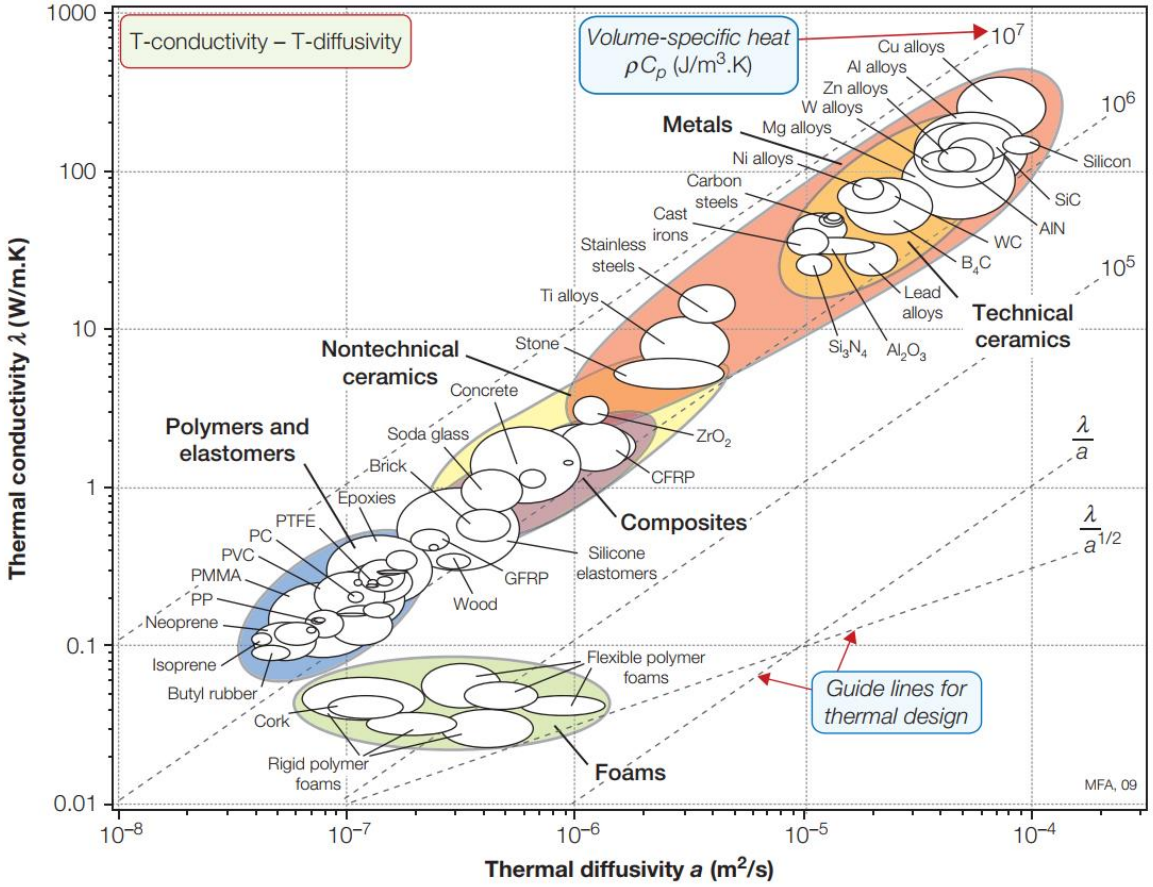

Figure 3.8. Material thermal performance as related to thermal conductivity and thermal diffusivity [214]. A heating cell requires materials with high thermal conductivity and low thermal capacitance. Thermal diffusivity ($\lambda/\rho C_p$) combines these terms along with density. Note the narrow range for volume-specific heat (ρC_p) which can be used to roughly predict thermal conductivity. Copyright: Reprinted from Materials Selection in Mechanical Design (4th ed), Figure 4.11, with permission from Elsevier via Copyright Clearance Center, Inc.

Another material class with a relatively high thermal diffusivity is ceramics. Their favourable properties include very low thermal expansions, high electrical resistivities, and a very high operating temperature ceiling [214], [217]. Silica glasses are of particular interest due to high biocompatibility, and optical transparency for hybrid (electrical and optical) nanopore detection strategies. In a way, we could not ask for a better cell material, except for the problems of brittleness, and rapid prototyping / manufacturing challenges.

Polymers are the last major structural material group and stays generally low on the thermal diffusivity spectrum. Polymers offer a range of bioinert or biocompatible materials that

feature high electrical and corrosion resistance [214], [217]–[219]. Unfortunately, generally low operating temperatures, stress relaxation, solvent swelling, and thermal creep can limit utility at elevated temperatures. Low thermal diffusivity may also necessitate a greater attention to geometric control of heat transfer. On the upside, losses to the external environment in low thermal diffusivity materials are also likely to be lower, reducing the need for meticulous thermal insulation.

Polymers are some of the most widely used materials in elevated temperature milli- and micro-fluidics, likely due to the ease of manufacturing and handling, and optical properties. Cell materials from heated microchannel studies using aqueous solutions include polydimethylsiloxane (PDMS) [168], [170], [176], [177], [184], [188], [220]–[224], polymethyl methacrylate (PMMA) [225]–[228], polyimides (PI) [180], [191], [229], polycarbonate (PC) [173], [174], [185], [230]–[232], polypropylene (PP) [233], polystyrene (PS) [234], [235], polytetrafluoroethylene (PTFE) [236], [237], and cyclic olefin copolymers (COC) [48], [238]. Commercial thermocycler test tubes (from VWR, or ThermoFisher) for biochemical reactions are usually made from polypropylene and polycarbonate, allowing rapid (>2 °C/s) temperature cycles from near 0 °C to 98 °C. While not all materials listed can be used in high temperature applications, most work well in low mechanical stress environments at physiologically relevant temperatures below 50 °C.

For the current design, plastics that can safely reach 130 °C were desired for the operation of a rapid thermal cycling scheme that involves using a very high temperature setpoint to bring the cell rapidly to a desired lower temperature setpoint. Most suitable thermoplastics that exhibit high temperature stability include polyetherimide (PEI), polyether ether ketone (PEEK), and polyoxymethylene (POM) [219] but are rarely used in milli- and micro-fluidics due to high material costs and lack of optical transparency. Thermoset plastics, such as cross-linked phenolics, esters, urethanes, polyamide-imide (PAI) and epoxy resins, are another set of potentially thermally stable plastics [219], [239]. Thermosets do not soften with increasing temperature, but are more difficult to handle in device manufacturing and maintenance. Studies have used resin-based thermosets for binding components together rather than the main structural components.

3.2.3.2. Material selection

Materials of interest for the current design were assessed for suitability based on criteria that include thermal conductivity, specific heat, heat deflection temperature, glass transition temperature, melting temperature, creep/stress deformation, thermal expansion, solvent swelling/absorption, bioinertness/biocompatibility, electrical resistivity, as well as classical stress- and strain-related properties. Information on material properties and design considerations is available in a variety of engineering textbooks [214], [240]. Manufacturability using the material was the deciding factor since a fluidic cell design is only as good as the ability to manufacture and test a number of iterations in a timely manner. A sample material parameter table and selection matrix are shown in Appendix B – Material selection tables. Ultimately, Formlabs High Temperature (FLHTAM01) photochemically-curable 3D print resin was chosen despite not scoring as high as alternatives. The availability of stereolithographic 3D-printing capacity in our lab has been vital in light of the manufacturing facility access challenges during the COVID-19 pandemic of 2020, and played an important role in a timely fabrication of not only the fluidic cell iterations but also the entire instrument.

Milli- and micro-fluidic 3D printing has been a hot topic in the past decade, particularly with increasing focus on manufacturability of devices outside of the confines of the traditional soft lithography and machining approaches [241]–[244]. Stereolithographic (SLA) 3D printing has emerged as the moderately-low-cost technique for producing complex millifluidic structures since the availability of more affordable and accessible commercially-available printing platforms (i.e. Formlabs, Asiga, EnvisionTEC, Miicraft, CADworks3D, B9Creations, Kudo3D, 3D Systems, Rapidshape, DWS, Acrea3D, Prusa Research). A simplified operating principle of an SLA system is shown in Figure 3.9. Uncured resin consisting of material monomers, photoinitiators, and photoinhibitors is exposed to a light source. The focused light has sufficient energy to only penetrate to a thin resin depth and activate the local photoinitiators that start a local polymerization reaction chain. The newly polymerizing layer is close enough to either the build platform or the previously polymerized layer to merge and bind them together. Thus, the build platform keeps shifting its height until all of the part layers are complete. System implementation challenges revolve around controlling polymerization depth, resolution, as well as the peeling

forces required to keep the part attached while moving the platform. Lastly, produced part usually requires additional post-processing steps, including an organic solvent wash and post-curing. Solvent wash removes the bulk of uncured resin from the part, while post-curing step produces further cross-linking of the internal material structure via light and heat exposure.

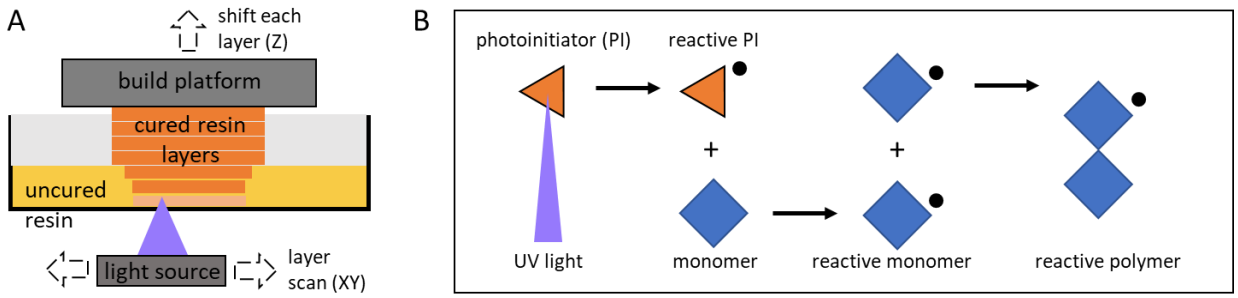

Figure 3.9. An example schematic of a stereolithographic (SLA) process. (A) SLA equipment consists of a light source scanning a local layer of uncured resin, causing its polymerization at the build platform. The build platform is constantly shifted by layer height and the layer curing process is repeated. (B) The curing process is started by the activation of local photoinitiators which facilitate resin polymerization reactions.

The defining feature of the photochemically-cured material, such as the Formlabs High Temperature (HT) resin, is the cured material's cross-linked polymeric structure, similar to thermosets. Thermosets do not tend to melt at elevated temperatures, decomposing or oxidizing instead [245]. Indeed, when subjected to a hot soldering iron, cured HT resin cracks and oxidizes instead of melting. Subjecting the material to post-curing in a UV-light enclosure (405 nm) at 60 – 80 °C after initial fabrication provides further enhancement to thermal properties. Flexural strength increases from 41 MPa to 107 MPa, heat deflection temperature increases from 42 °C to 130 °C at 1.8 MPa, and thermal expansion reduces from 121 µm/m/°C to 88 µm/m/°C [246]. One challenge is that the material becomes more brittle and susceptible to chipping on impact, requiring careful handling. Many of the material properties of the post-cured HT resin are otherwise comparable to those of polymethyl methacrylate (PMMA) (Table 3.4). This is expected given that the base resin is composed of a proprietary mixture of acrylated monomers and methacrylated oligomers [247].

Table 3.4. Comparison of PMMA and SLA 3D-print Formlabs High Temperature materials.

Parameter	PMMA*	Formlabs High Temp (v1)**
Ultimate strength (MPa)	48 – 76	51.1
Elongation at fracture (%)	2 – 10	2
Young's Modulus (MPa)	2700 – 3100	3600
Flexural modulus (MPa)	2900 – 3100	3300
Swelling (aqueous) (24hr, %)	<2	<1
Thermal expansion (linear, µm/m/°C)	$2 – 3 \cdot 10^{-4}$ (< Tg) $6 \cdot 10^{-4}$ (> Tg)	$8.8 * 10^{-5}$
Heat deflection temperature (0.25mm, °C)	51.7 – 106 (1.8 MPa) 73 – 109 (0.45 MPa)	130 (1.8 MPa) 289 (0.45 MPa)
Notched impact strength (J/m)	16 – 27	14

* [219], [248], [249]
** post-cured for 60min @ 365nm UV [246]

3.2.4. Analytical flow cell modeling

3.2.4.1. Analytical model definition

Lumped-parameter analytical models can facilitate exploration of design solutions and selection of reasonable initial design parameters since they are less computationally expensive than geometrically complex numerical models. Initial design parameters of interest include the range of heat transfer fluids, their flow speeds, and channel dimensions that result in maximum heat transfer to the cell. Flow channel pressure drops place limits on the geometric and flow parameters in the sub-millimeter thickness support geometries of the fluidic cell. The initial 3D cell design (Figure 3.10 A) includes an internal analyte channel region that is separated from the heating channel by 0.5 – 1 mm material distance, which minimizes heat transfer resistance to the analyte. External surface of the heating channel faces the square external faces of the cell across a much thicker material wall, therefore external heat transfer would likely not be as efficient.

The model is built by simplifying the 3D helical heater cell geometry to a 1D heat circuit model as shown in Figure 3.10. The complete circuit for transient heat transfer is given in Figure 3.10 A, and is then simplified to a steady state circuit in Figure 3.10 B. The steady state circuit is the one solved in this section. As such, this analytical model does not provide information on the transient response time of the system, but only on the cell temperature distribution in steady-state. The analytical model was implemented and solved in Python to account for the nonlinearity of the thermal resistances as a function of temperature. Transient analytical model was not expanded upon since results from the steady-state model described in Section 3.2.5 deviated significantly enough from numerical, experimental, and recent literature results further described in Section 3.2.7. Instead, transient behaviour was estimated numerically and characterized experimentally.

The analytic flow cell model uses the following assumptions:

1. 1D lumped parameter model (consider an axisymmetric “cylindrical cow” analogy)
2. Adiabatic internal cell boundary assuming geometric symmetry
3. Steady-state conductive, convective, and radiative heat transfer
4. Isotropic, homogeneous material properties
5. Gray and diffuse surfaces
6. Incompressible cell materials and heating fluids
7. No work done on or by the system (i.e. thermal expansion, PV work, etc.)
8. No energy generation
9. Constant external environment temperature (radiative, and convective)

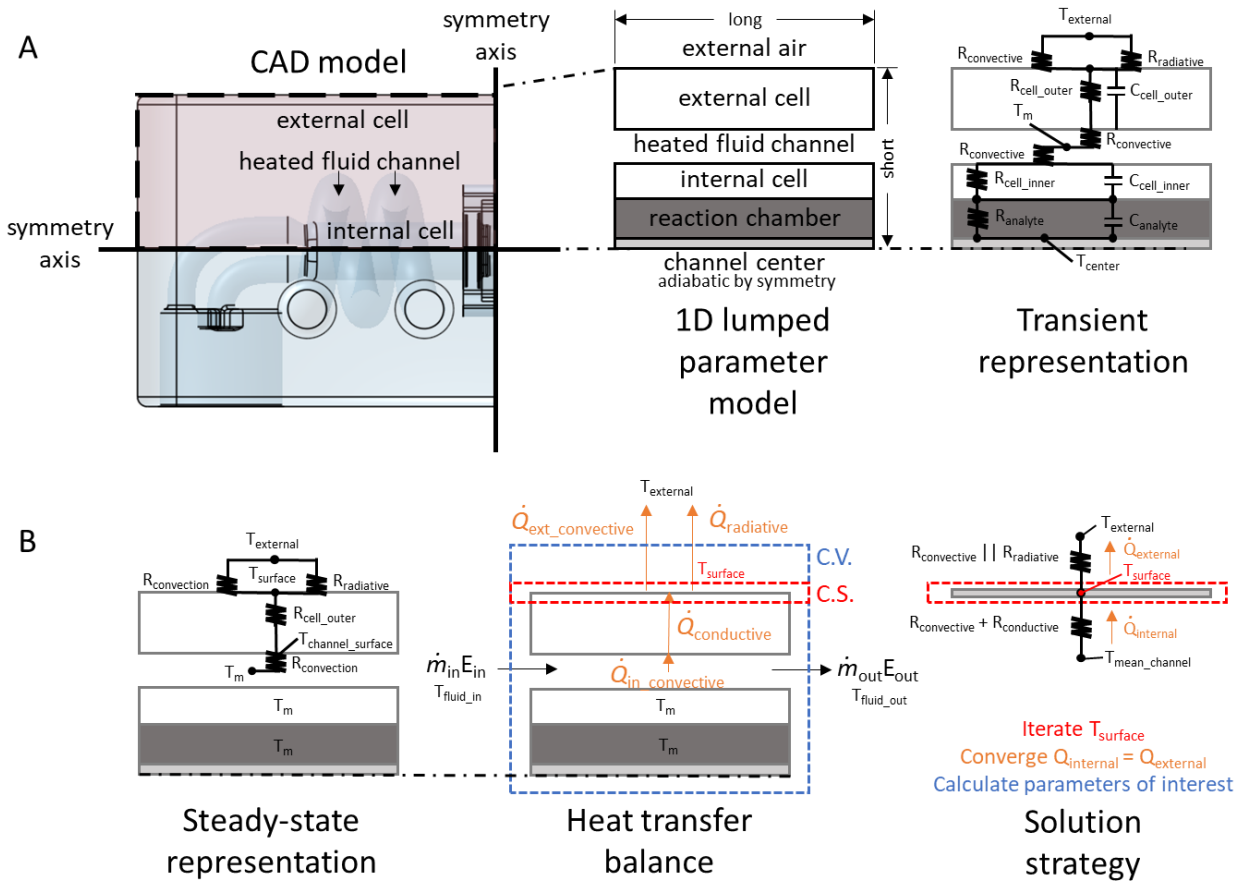

Figure 3.10. Lumped parameter model representation of the helical heater cell. 3D geometry was simplified into a lumped-parameter 1D heat circuit model (A). Steady state representation (B) was used to estimate geometric parameter range that meets initial performance goals, and determine the qualitative behaviour of the system. Energy balance across the control volume (C.V.) provides information on required flow parameters, while energy balance across the control surface (C.S.) allows to iteratively solve the non-linear problem involving radiative heat transfer and temperature-varying material parameters. Solution was implemented in Python.

The thermodynamic energy balance across the cell control volume (C.V.) (Figure 3.10 B center) defines the energy entering the system with the heat transfer fluid, and the energy leaving the system via air convection and surface radiation:

$$\dot{m}_{in}E_{in} = \dot{m}_{out}E_{out} + \dot{Q}_{ext\_convective} + \dot{Q}_{radiative} \qquad \text{Eq.3.5}$$

$$\dot{m}_{in} = \dot{m}_{out} \qquad \text{Eq.3.6}$$

where $\dot{m}_x$ represent the mass flows of heating fluid that bring with them a certain amount of energy E_x per unit of mass, and $\dot{Q}$ are the net heat transfer rates driven by temperature

differences. C.V. balance can be used to estimate the initial requirements for types of fluids, fluid flow rates, and required heater power for steady state operation. Heat transfers shown within the C.V. do not participate in this balance and are only relevant in establishing internal heat transfer mechanisms required for the problem solution based on control surface (C.S.) analysis.

The thermodynamic energy balance across the control surface (C.S.) allows the determination of cell surface temperature required for the calculation of the input-output energy balance across the C.V. The main challenge here is the non-linearity of the problem involving radiative heat transfer and temperature-varying material parameters, which can be solved using an iterative solution strategy shown on the right in Figure 3.10 B. In this strategy, heat flows across the C.V. are simplified to heat flows across the C.S. with material parameters lumped together as heat flow resistances. Given a constant mass flow rate of the heating fluid, steady-state energy losses in the fluid will depend on how much interfacial and external cell resistance there is to the transfer of heat to the external environment. The internal cell temperature is assumed to be at the mean fluid temperature since no heat losses are assumed in that compartment at steady state. The simplification itself is done using the thermal circuit analysis.

3.2.4.2. Thermal circuit analysis

A useful tool in analyzing heat transfer problems with constant properties and no internal energy generation is the thermal circuit approach. While the standard approach involves solving the appropriate form of the heat equation with the associated initial and boundary conditions, it is quite cumbersome [204]. Instead, an electrical circuit analogy of the heat transfer process defines an equivalent thermal resistance R_{eq} along which heat current Q flows due to a temperature potential ΔT:

$$Q = \frac{\Delta T}{R_{eq}} \qquad \text{Eq.3.7}$$

This method greatly simplifies the solution process by using strategies such as parallel or series circuit element reduction:

$$R_{series} = R_1 + R_2 + R_3 + \cdots \quad \text{Eq.3.8}$$

$$R_{parallel} = R_1||R_2||R_3|| \ldots = \left(\frac{1}{R_1} + \frac{1}{R_2} + \frac{1}{R_3} + \cdots\right)^{-1} \quad \text{Eq.3.9}$$

Resistances to heat transfer come in many forms and derive from conductive, convective, and radiative heat exchanges. Heat conduction is energy transport in a medium by random atomic or molecular activity due to a temperature gradient. Thermal resistance for conduction is derived from Fourier's law of thermal conduction and has the following form [204]:

$$R_{cond} = \frac{L_c}{kA_c} = \frac{1}{UA} \quad \text{Eq.3.10}$$

where L_c is the characteristic length and A_c is the characteristic area dependent on geometry, and k is the thermal conductivity of the material. Another representation of the resistor element as a conductor with conductance UA specifies an overall heat transfer coefficient. Use of UA is more common in standard heat exchanger analysis [209] and provides a more general tool to represent heat transfer terms.

Convective and radiative heat transfer resistances can also be represented in terms of heat transfer coefficients. Convective heat transfer is energy transport by conduction (random molecular motion) and advection (bulk fluid motion), while radiative heat transfer occurs without the involvement of matter as the heat transfer medium [204]. Convective and radiative resistance terms are then presented as follows:

$$R_{conv} = \frac{1}{h_c A_c} \quad \text{Eq.3.11}$$

$$R_{rad} = \frac{1}{h_r A_r} \quad \text{Eq.3.12}$$

While the expressions for both modes of heat transfer look alike, the expressions for the heat transfer coefficient term h are different and can be quite complex. In the case of convection (h_c), heat exchange involves a characterization of bulk fluid flow interacting with material boundaries (velocity, thermal, and concentration boundary layers). Simple geometries (1D, 2D orthogonal) can be solved exactly, but most other cases are represented numerically or using empirical

correlations. In the case of radiation, h_r is dependent on the third power of the temperature as well as the view factors and radiative properties of participating materials. In the simplest case of two gray (wavelength-independent), diffuse (direction-independent) surfaces, the coefficient may be approximated [204] as:

$$h_{rad} = \varepsilon_1 \sigma (T_1^2 + T_2^2)(T_1 + T_2) \qquad \text{Eq.3.13}$$

where ε is the surface emissivity, σ is the Stefan-Boltzmann constant ($5.670 \cdot 10^{-8}$ W/m^{2}K^4), and T_1 and T_2 are the temperatures of surfaces participating in radiative heat exchange. This simplified approximation is used in the analytical model.

Convective coefficient for helical channel geometries does not have an exact analytical solution, and unlike the conductive and radiative coefficients does not have a simple model to represent it. Complicating factors other than 3D geometry include possible flow types (laminar, transitional, and turbulent) as well as the formation of a consistent flow velocity and temperature profiles within the channel (developing or fully-developed velocity and thermal profiles). The fundamentals of flow types and flow profile formation are well-described in introductory heat transfer literature [204]. Of particular relevance to the current discussion are dimensionless parameters that describe fluid flows and heat transfer. These parameters include Reynolds (*Re*), Dean (*De*), Helical (*He*), Prandtl (*Pr*), Grashof (*Gr*), Rayleigh (*Ra*), and Nusselt (*Nu*) numbers.

3.2.4.3. Nusselt number for helical channels

Nusselt number (*Nu*) allows calculation of the convective heat transfer coefficient. Without going into the specifics of dimensionless derivation from Newton's cooling law and Fourier's conductive heat transfer laws, the average Nusselt number (*Nu*) is defined as the ratio of convective to conductive heat transfer across a surface boundary [204]:

$$\overline{Nu_L} = \frac{q_{convective}}{q_{conductive}} = \frac{\bar{h}\Delta T}{\frac{k_f}{L}\Delta T} = \frac{\bar{h}L}{k_f}, \qquad L = \frac{V_{channel}}{A_{chan\ surface}} \qquad \text{Eq.3.14}$$

where $\underline{h}$ is the average convection coefficient we are interested in for the model, k_f is the thermal conductivity of the fluid, and *L* is the characteristic length of the fluid channel (function of channel *V*olume and surface *A*rea). Nusselt number is analogous to the Biot number ($Bi = \underline{h}L/k_s$) that represents a similar quantity in solids. Small Nusselt number (<0.1) means heat conduction predominates relative to convection. Another way of looking at Nusselt number is locally, where it represents the non-dimensionalized temperature gradient in the *y* direction at the local point of the boundary surface:

$$Nu_x = \frac{h_x x}{k_f} = \left.\frac{\partial T^*}{\partial y^*}\right|_{y^*=0}, \qquad x = \frac{A_{chan\ section}}{P_{chan\ section}} \qquad \text{Eq.3.15}$$

Local Nusselt numbers can be integrated across the surface to determine the average Nusselt number. From definition, the local and average heat transfer coefficients are represented as:

$$h_x = \frac{k_f Nu_x}{x}, \qquad \bar{h} = \frac{k_f \overline{Nu}}{L} \qquad \text{Eq.3.16}$$

This may seem like a circular definition, except that *Nu* are often fitted empirically and usually (but not always) represented as correlations of other non-dimensional numbers:

$$Nu_x = f(x^*, Re, Pr, De), \qquad \overline{Nu} = f(Re, Pr, De), \qquad forced\ convection \qquad \text{Eq.3.17}$$

$$Nu_x = f(x^*, Gr, Pr, Ra), \qquad \overline{Nu} = f(Gr, Pr, Ra), \qquad free\ convection \qquad \text{Eq.3.18}$$

Two main conditions exist for how the Nusselt correlations are represented in the literature – constant heat flux, or constant surface temperature (Figure 3.11). Constant heat flux assumes heat flux along the channel is constant and independent of position along the channel. Mean fluid temperature in the channel then becomes a linear function. Even if heat flux is not constant but known, mean channel temperature is easy to predict. Therefore, constant heat flux condition is applicable to many general problems that do not control surface temperatures.

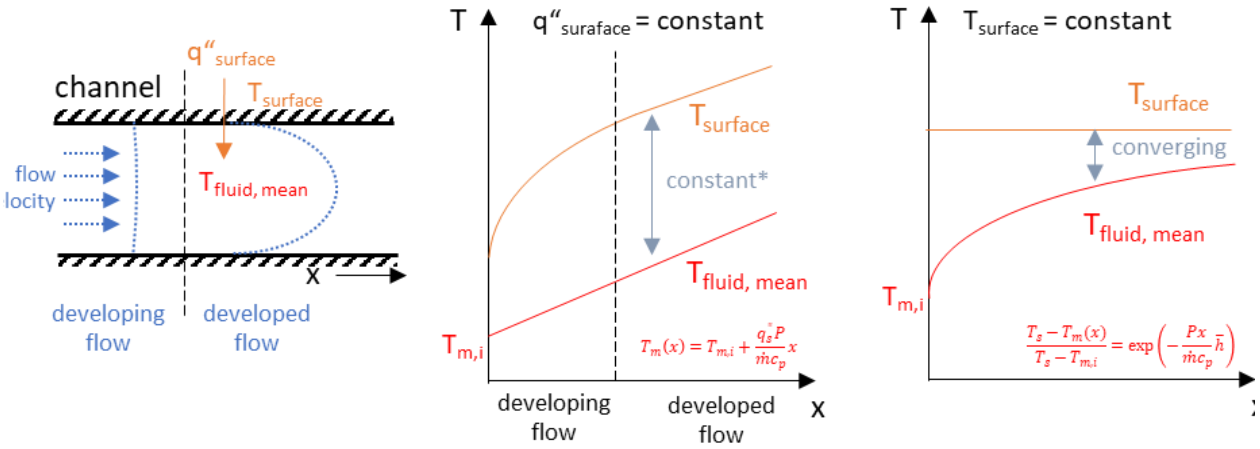

Figure 3.11. Thermal assumptions for the reported Nusselt numbers for internal flows. Constant surface heat flux (q_s'') results in a linear mean fluid temperature profile (T_m), while constant surface temperature (T_s) results in a converging mean temperature profile. Diagrams based on definitions from [204].

On the other hand, constant surface temperature condition results in mean fluid temperature that converges closer to the surface temperature. Constant surface temperature condition is appropriate when either surface or external fluid temperature is constant (i.e., temperature-controlled container). Neither condition exists perfectly in the real world, but can be a reasonable approximation to a particular situation. Constant heat flux approximation was used in the analytical flow cell model while constant temperature approximation was used in modeling the temperature-controlled heat transfer fluid reservoir.

Nusselt correlations have been proposed for both laminar and turbulent fully-developed flows in helical channels at both constant temperature (Nu_T) and constant heat flux (Nu_q) conditions [250]–[258]. Laminar flow is regular and smooth, and fluid layers do not mix. The following correlations are used in the flow cell model for laminar fully developed flows ($He < 2000$ and $Pr > 0.005$) [252], [253]:

$$\overline{Nu}_T = \left[\left(3.657 + \frac{4.343}{\left(1 + (957/Pr \cdot He^2)\right)^2}\right) + \left(1.158\left(\frac{He}{1 + 0.477/Pr}\right)^{3/2}\right)\right]^{1/3} \quad \text{Eq.3.19}$$

$$\overline{Nu}_q = \left[\left(4.364 + \frac{4.636}{\left(1 + (1342/Pr \cdot He^2)\right)^2}\right) + \left(1.816\left(\frac{He}{1 + 1.15/Pr}\right)^{3/2}\right)\right]^{1/3} \quad \text{Eq.3.20}$$

Turbulent flows are characterized by irregular fluid flow with random mixing. The following correlation is used in the flow cell model for turbulent fully developed flows (*Pr* > 1, $Re(D/2R)^{2.5}$ > 0.4) [254], [255]:

$$\overline{Nu}_{T,q} = \frac{Pr^{0.4}}{41.0} Re^{5/6} \left(\frac{D}{2R}\right)^{1/12} \left[1 + 0.061\left(Re\left(\frac{D}{2R}\right)^{2.5}\right)^{1/6}\right] \quad \text{Eq.3.21}$$

where *D* is the heating channel diameter, *R* is the planar radius of helical channel curvature, and *Pr*, *He*, and *Re* are other non-dimensional discussed in further sections.

Correlations presented are average Nusselt numbers that do not consider the distribution of heat flux along the helix. Recent experimental investigations have revealed that local Nusselt numbers for laminar flows are up to 5 times larger at the outside surface than the inside surface of the coiled pipe [259]. This means that the outer coil region potentially transfers a lot more heat than the internal one. This difference is even more pronounced for turbulent flows where local Nusselt numbers are up to 10 times larger [260]. Little information on Nusselt numbers is available on the transition region between laminar and turbulent flows which starts at the transition Reynolds number (Re_{tr}). Furthermore, inclusion of fluidic cell fittings with changing pipe diameters close to the cell is likely to interrupt flow development. No information is available on not fully-developed flows for helical channels.

3.2.4.4. Reynolds number for helical channels

Nusselt correlations are functions of other dimensionless numbers, namely *Re*, *Pr*, *De*, *He*, *Gr*, and *Ra*. A brief mention of their definition and implementation is in order to complete the

discussion of the analytical cell model. First parameter if interest is Reynolds number (*Re*) which specifies the ratio of inertial to viscous forces in a fluid flow:

$$Re = \frac{inertial\ forces}{viscous\ forces} = \frac{\rho u D_h}{\mu}, \qquad D_h = \frac{4A}{U} \qquad \text{Eq.3.22}$$

where ρ is fluid density, u is average fluid velocity, D_h is the channel hydrodynamic diameter, A is the channel cross-section area, U is the wetted channel cross-section perimeter, and μ is fluid's dynamic viscosity. Dean (*De*) and Helical (*He*) numbers can be thought of as curved channel geometric adjustments of the Reynolds number [261]:

$$De = \frac{\sqrt{0.5 * inertial\ foces * centripetal\ forces}}{viscous\ forces} = Re\sqrt{D/2R} \qquad \text{Eq.3.23}$$

$$He = Re\sqrt{D/2R_c} = De(1 + (H/2\pi R)^2)^{0.5} \qquad \text{Eq.3.24}$$

$$R_c = R(1 + (H/2\pi R)^2) \qquad \text{Eq.3.25}$$

where D is channel diameter, R is the planar radius of curvature, R_c is helical radius of curvature, and H is helix coil pitch as shown in Figure 3.12 A fluidic half-cell example.

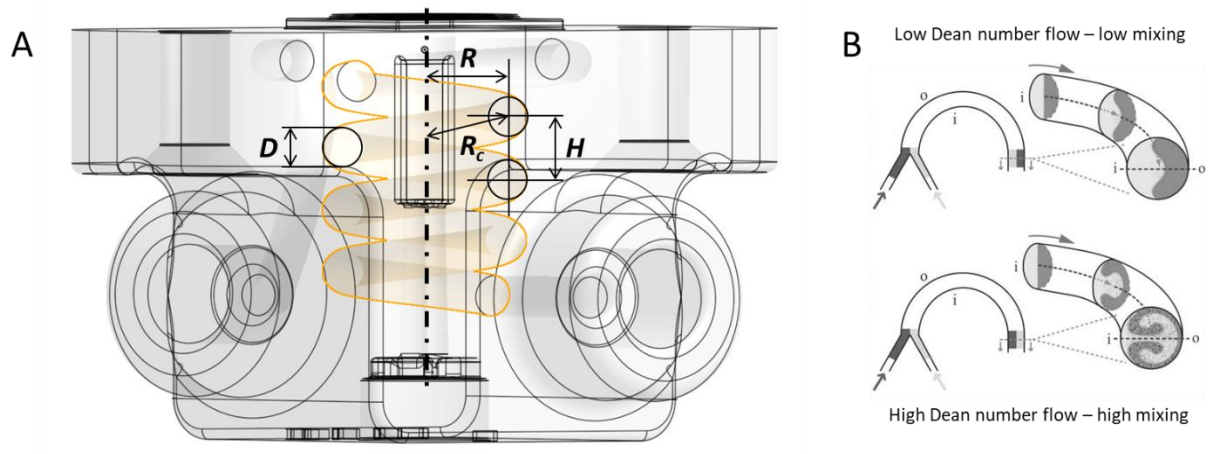

Figure 3.12. Helical channel geometry definitions within the 3D CAD model of the fluidic cell and associated curved channel flow mixing. Channel geometry (A) defines *D* as channel diameter, *H* as helical pitch, *R* as helix radius, and R_c as the channel curvature radius. Dean number affects the extent of laminar flow mixing within curved channels (B) [212]. Copyright: (B) reprinted with permission of Royal Society of Chemistry, from 'Fluid mixing in planar spiral microchannels' Fig. 1, Sudarasan & Ugaz, 6(1), 2006, via Copyright Clearance Center, Inc.

Re helps characterize the type of internal channel flow – laminar (Re < 2300), transitional (2300 < Re < 10^4), or turbulent (Re > 10^4) for straight pipes. Experimental studies have shown that flow transition is more gradual in coiled than in straight pipes [262]. Dean vortices (Figure 3.12 B) tend to suppress the onset of turbulence transition. Turbulence transition Reynolds number is adjusted for curved geometry as follows [261]:

$$Re_{tr} = 2100\left(1 + 12\sqrt{D/2R}\right), \qquad 10 < \frac{2R}{D} < \infty \qquad \text{Eq.3.26}$$

where *R* is the radius of coil curvature, and *D* is the pipe diameter. Of note, the validity range for the adjustment lies outside of the current geometric model (*2R/D* < 5), and thus the straight pipe transition is assumed (*Re* > 2300) for the current flow cell model. Unfortunately, experimental studies on the subject of helical pipes have large coil aspect ratios (curvature relative to pipe diameter), making it difficult to make well-grounded empirical predictions for compact milli- and micro-fluidic coils.

3.2.4.5. Helical pipe pressure drop

Laminar flows are generally non-mixing flows and do not provide the heat transfer enhancement inherent to chaotically mixing turbulent flows. A major disadvantage of using turbulent flows is high energy dissipation from fluid friction effects, requiring a significant pressure to sustain flow. Pressure drop in internal channels for an incompressible fluid can be estimated using the Darcy-Weisbach equation [263], [264]:

$$h_f = \frac{\Delta P}{\rho g} = f\frac{L}{D_h}\frac{u^2}{2g} \qquad \text{Eq.3.27}$$

where h_f is frictional head loss, ΔP is the frictional pressure loss, ρ is fluid density, g is the gravitational constant, f is the dimensionless Darcy or Moody friction factor, L is the pipe length, u is fluid average velocity, and D_h is hydraulic diameter. Friction factor f for laminar flow in straight pipes is simply $64/Re$, but the estimate is more involved for transitional or turbulent regimes. Moody Diagrams have been the engineering go-to methods for estimating the friction factors

before our current computing power existed. Analytical solutions for straight pipes can be obtained from the iterative Colebrook-White Equation or its direct approximations [263], [264]. Helical pipe *Fanning friction factors* for fully developed flows have been proposed for laminar flow [252], [253]:

$$f = f_{st}\left[\left(1 - \frac{0.18}{(1+(35/He)^2)^{0.5}}\right)^m + \left(1+\frac{D}{6R}\right)^2\left(\frac{He}{88.33}\right)\right]^{0.5}, \qquad f_{st} = \frac{16}{Re}, \qquad m = \begin{cases} 2, & De < 20 \\ 1, & 20 < De < 40 \\ 0, & De > 40 \end{cases} \quad \text{Eq.3.28}$$

and turbulent flow [265], [266]:

$$f = (0.079/Re^{0.25}) + \left(0.0075\sqrt{D/2R_c}\right) \quad \text{Eq.3.29}$$

Interestingly, turbulent flow approximation is independent of the Dean number, likely because this flow regime is chaotic and does not form distinct Dean vortices. Fanning friction factors are based on hydraulic radii instead of diameters, which makes Darcy friction factors four times (4x) larger than Fanning friction factors.

3.2.4.6. Prandtl number

Prandtl number (*Pr*), another parameter used in internal flow Nusselt number calculation, signifies the relative speed with which momentum and thermal energy propagate through the fluid:

$$Pr = \frac{momentum\ diffusivity}{thermal\ diffusivity} = \frac{\mu/\rho}{k/\rho c_p} = \frac{\mu c_p}{k} \quad \text{Eq.3.30}$$

where μ is the dynamic viscosity, ρ is the fluid density, c_p is the isobaric heat capacity of the fluid, and k is the fluid thermal conductivity. Momentum diffusivity is also referred to as kinematic viscosity. Thermal diffusivity was covered in Section 3.2.3 for solid materials and makes a comeback here as a relevant property of a fluid as well. A fluid with a higher *Pr* will be more effective at convective heat transfer than a fluid with a lower *Pr* where thermal conduction will

play a bigger role. Heat transfer oils feature *Pr >> 1*, which effectively makes them much better at transferring heat when not stationary. *Pr* is independent of geometry.

3.2.4.7. Free convection

Grashof (*Gr*) and Rayleigh (*Ra*) numbers are used in characterizing free convective flows such as hot external flow cell walls where fluid moves due to the fluid density gradient resulting in buoyancy forces [204]:

$$Gr = \frac{buoyancy\ forces}{viscous\ forces} = \frac{g\beta(T_s - T_\infty)L^3}{(\mu/\rho)^2}, \qquad \beta = -\frac{1}{\rho}\left(\frac{\partial\rho}{\partial T}\right)_p \qquad \text{Eq.3.31}$$

$$Ra = Gr \cdot Pr \qquad \text{Eq.3.32}$$

where *g* is the gravitational acceleration, β is the volumetric thermal expansion coefficient of the fluid, ρ is the fluid density, μ is its dynamic viscosity, and *L* is the characteristic length of the surface. Volumetric expansion depends on the difference between surface temperature T_s and external quiescent fluid temperature T_∞. Grashof number is analogous to the square of Reynolds number and plays the same role in free convection as Reynolds number in forced convection. Raleigh number, a product of *Gr* and *Pr*, is used to classify the flow regime and stability which is important in the selection of the appropriate Nusselt correlations.

Flow cell model uses free convection Nusselt correlations for vertical and horizontal cell walls associated with the simplified geometry (Figure 3.13). Walls are treated as isothermal plates. The appropriate correlation for vertical walls [267] covers laminar and turbulent regimes:

$$\overline{Nu} = \left[0.825 + \frac{0.387Ra^{1/6}}{(1 + (0.492/Pr)^{9/16})^{8/27}}\right]^2, \qquad 10^4 \le Ra \le 10^{13} \qquad \text{Eq.3.33}$$

where material properties are evaluated at film temperature $T_f = (T_s + T_\infty) / 2$, T_s is surface temperature and T_∞ is external quiescent fluid temperature.

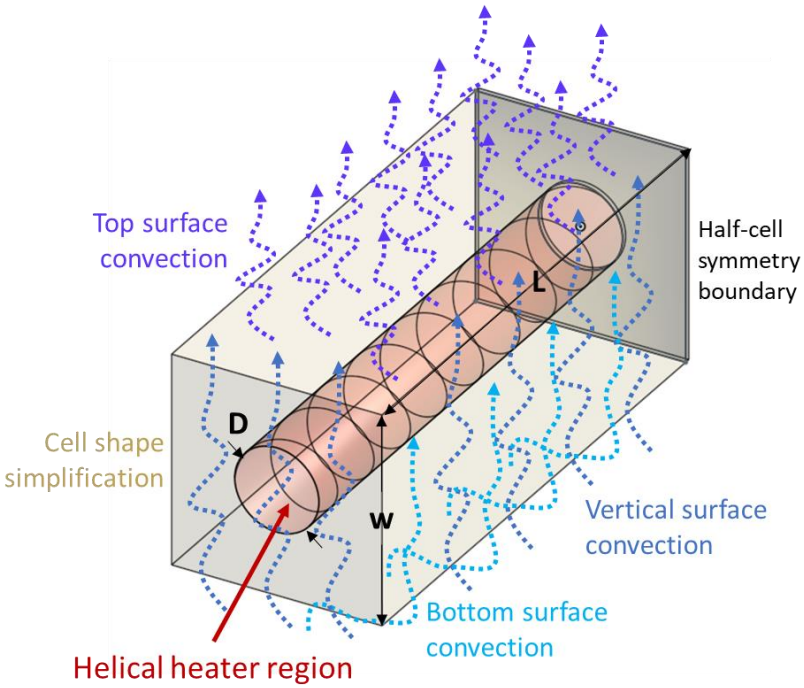

Figure 3.13. Simplified heated flow cell geometry and free convective flow of air that cools it down. Model uses the conductive thermal resistance derived from the cylinder within a rectangle shape factor (Section 3.2.4.8). Free convection considers cooling from the vertical, top, and bottom surfaces. All external surfaces, except one of the cylinder-containing surfaces at the half-cell symmetry boundary, are used in free convection due to half-cell symmetry condition. Cylinder-containing surface contributes to heat exchange and is assumed to be at the average surface temperature sharing conductive thermal resistance with the rest of the cell.

Upper surface of a hot plate correlates as follows [268]:

$$\overline{Nu} = 0.54Ra^{1/4}, \qquad 10^4 \leq Ra \leq 10^7, Pr \geq 0.7 \qquad \text{Eq.3.34}$$

$$\overline{Nu} = 0.15Ra^{1/3}, \qquad 10^7 \leq Ra \leq 10^{11} \qquad \text{Eq.3.35}$$

while lower surface of a hot plate correlates as follows [269]:

$$\overline{Nu} = 0.52Ra^{1/5}, \qquad 10^4 \leq Ra \leq 10^9, Pr \geq 0.7 \qquad \text{Eq.3.36}$$

Characteristic length for *Ra* in these correlations is defined as plate surface area divided by its perimeter ($L = A_s / P$). Substituting the described Nusselt correlations into Eq.3.16 yields convection coefficients for the appropriate surfaces, which can then be used to calculate heat transfer resistances at the solid-fluid interfaces.

3.2.4.8. Conduction resistance

The last component of the model is heat conduction resistance of the cell. While Eq.3.10 adequately describes thermal resistance in one dimension, even simplified cell geometry of the model is described by at least two dimensions (i.e., a cylinder in a box, see Figure 3.13). Existing solutions to the heat diffusion PDE are available for certain simple two- and three-dimensional geometries, and are described as shape factors [204]. Average thermal conduction resistance for the circular cylinder channel in a square solid (Figure 3.13) can then be described in terms of a shape factor as follows:

$$R_{cond,2D} = \frac{1}{Sk} \qquad \text{Eq.3.37}$$

$$S = \frac{2\pi L}{ln(1.08w/D)}, \qquad w > D, L \gg w \qquad \text{Eq.3.38}$$

where *L* is the solid depth dimension, *w* is the side dimension, *k* is the thermal conductivity of the solid, and *D* is the cylindrical channel diameter. Here flow cell *L* is not much greater than *w* and side conduction of heat will contribute to overall heat transfer. 2D approximation can be maintained by assuming the same cell resistance per cell length is maintained. Side surface area is included in the vertical surface area, and characteristic length is calculated using the expanded surface area and perimeter.

3.2.5. Analytical model results

Parameters of interest for the initial fluidic cell design were heating fluid flow speeds, channel dimensions, expected pressure drop ranges, and heat exchange at steady state for the presented CAD geometry. Among heat transfer fluids explored during the iterative design process were air, water, and vacuum pump and heat transfer oils. The relevant results are presented for the perfluoropolyether (PFPE) heat transfer oil (Solvay Galden HT200) ultimately selected for the final system implementation using PMMA for fluidic cell material properties.

The lumped parameter model demonstrated fair agreement with other models and experimental results for large volume flows (Table 3.5) despite a wide range of assumptions made. The final model half-cell average surface temperature was within 13.4 % of the experimentally measured average flow cell surface temperature, and within 17.8 % of the SolidWorks Flow Simulation finite volume analysis (FVA) model. Analytical model average surface temperature was taken directly from the converged $T_{surface}$ parameter, while experimental surface temperature was computed as an average of temperature samples collected as per Figure 3.14 sampling plan. FVA cell surface temperature was taken as an average surface temperature of the cell model (Section 3.2.6) excluding inlet and outlet tubes.

Table 3.5. Surface temperature comparison between models and experimental fluidic cells.

	Analytical model*	**Experimental***	**Finite Volume Model***
Outer Surface temperature (°C)	51.0 ($T_{surface}$)	58.8 [+]	62.0 [#]
Analyte (inner channel) temperature (°C)	90 (T_m) **	90.2 [++]	88.2 [##]
Enclosure ambient air (°C)	30 (T_∞) ***	32.2 [+++]	26.0 [###]

*half-cell heating fluid flow rate of ~200 mL/min
** equal to HT fluid mean temperature by default due to model assumptions
*** assumed parameter based on numerical and experimental results
[+] average of 24 surface measurements per Figure 3.24
[++] internal cell optical thermometer measurement
[+++] average of 8 different location measurements at steady state
[#] average cell surface temperature
[##] average HT fluid temperature at closest point to analyte channel
[###] average of horizontal cut plane air temperature

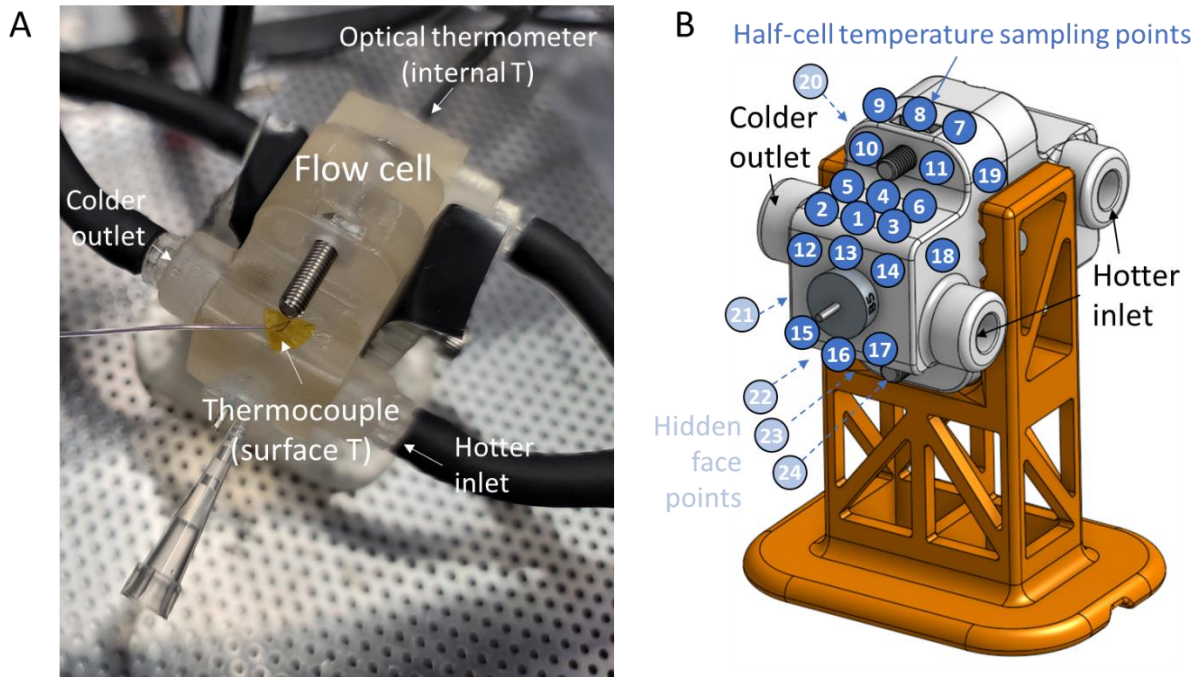

Figure 3.14. Experimental surface temperature sampling of the fluidic cell. (A) Fluidic cell setup. T-type thermocouple was secured to the cell surface via a small piece of polyimide tape, and temperature measured using OMEGA OM-HL-EH-TC temperature logger. Temperature of the cell was stabilized for 30 minutes prior, as well as an additional 3 minutes after moving the thermocouple between sampling points. Some cell surface regions were not sampled due to poor access or issues keeping the thermocouple secured. Surface sampling points are shown in (B). Measurement precision was 0.1 °C with a drift <0.5 °C over a 30 second sampling interval.

Increasing heating channel diameter at the same volumetric flow rate generally increases heat transfer from the heating channel to the cell up to a point at which flow velocity is too low to sustain sufficient convection required for effective heat transfer in oils ($Pr >> 1$) (Figure 3.15 A). This is more pronounced if using straight channel *Nu* correlations instead of helical *Nu* correlations. While heat transfer improvements offer diminishing returns with increasing channel diameter, pressure drop across the channel decreases significantly (Figure 3.15 B). This agrees with general theoretical expectations, i.e. pressure drop in laminar incompressible flow is inversely related to the square of the diameter (Hagen-Poiseuille equation). Here the flow regime is turbulent for the entire range of diameters and the geometric relationship can be fitted with a power law where channel diameter is to the inverse 5th power.

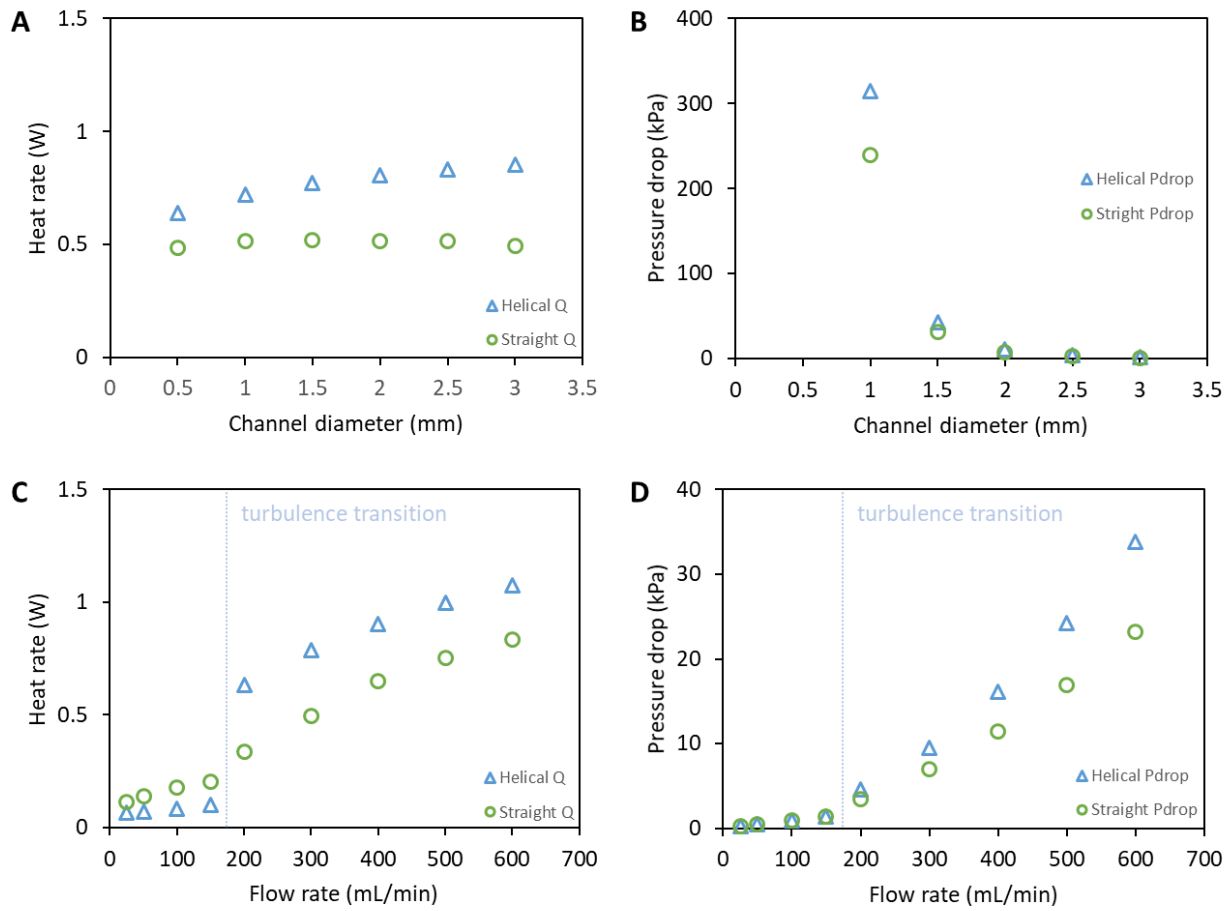

Figure 3.15. The effects of channel diameter and heating fluid flow rate on steady-state heat transfer rate to the half-cell and pressure drop in the heating channel. Models using helical vs straight channel convection correlations are compared. Flow rate is 315 mL/min for A and B. Channel diameter is 2.0 mm for C and D. Flow temperature is set to 90 °C while external enclosure environment is at 30 °C.

Channel diameter of 2.0 – 2.5 mm is in the design region which provides high heat transfer rates and low pressure drop while maintaining 3D printed cell material integrity and compactness. Figure 3.15 C shows how heat transfer fluid flow rates affect steady-state heat transfer performance for this channel size. Heat transfer rates to the half-cell remain high above 200 mL/min since flow transitions to the turbulent regime. Turbulence appears to provide more effective heat transfer in helical channels compared to straight channels at the cost of further increasing pressure requirements. Initial design flow rate of 315 mL/min was therefore chosen since it maintains a pressure drop of approximately 10 kPa and leaves sufficient “pressure drop reserve” for the connecting tubing and fittings (<50 kPa). A sufficient pressure safety margin (>2x)

is maintained on the peristaltic tubing at high temperatures. In addition, any variation in flow rate will maintain the cell in the turbulent regime, providing high heat transfer rates and acceptable pressure drops.

3.2.6. Numerical modeling

3.2.6.1. Numerical model overview

A numerical 3D fluidic cell model was built using Dessault SolidWorks 2020 Flow Simulation to corroborate thermodynamic findings from the analytical model and determine whether 3D cell geometry provided uniform thermal distributions. While the lumped-parameter model answered essential questions about the average heat transfer and fluid flow rates in the overall cell control volume, it was insufficient to determine thermal distribution within the complex 3D geometry of the cell.

In contrast to the analytical model built as a 1D lumped-parameter system of equations solved using a simple iterative method, the numerical model was built in a SolidWorks 2020 3D modeling environment defining the model geometry (Figure 3.16). Using a specialized software module (Flow Simulation), geometry was assigned materials, geometric boundary and initial conditions, and set up with parameters to solve partial differential equations on the discretized geometric domain. Resulting model was solved using the software-provided solver and represented as tabular and visual results associated with the geometry of interest. Multiple fluidic cell models (Figure 3.16 A, B, C) were simulated using different materials, heat transfer fluids, and flow and environmental conditions. This section will focus on the more recent model that uses PFPE heat transfer fluid in PMMA-like 3D print material cell within the geometrically simplified free-convection-cooled Faraday enclosure (Figure 3.16 D).

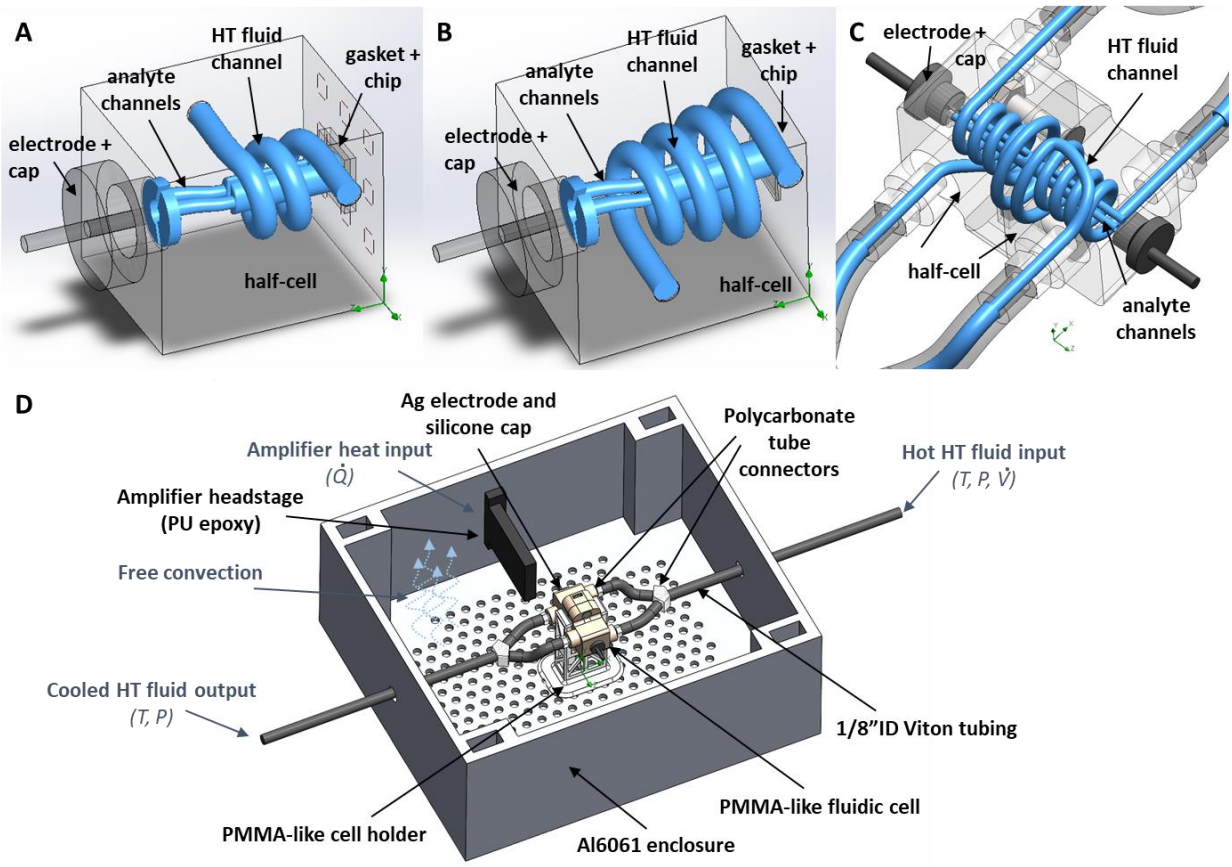

Figure 3.16. Numerical model overview. (A, B, C) Examples of the evolving numerical model geometries of the fluidic cell implemented in SolidWorks 2020 and SolidWorks Flow Simulation. (D) Most recent numeric cell model is simulated within the Faraday enclosure with the hot amplifier head stage present. The enclosure is covered from top with a convective grating lid (not shown).

3.2.6.2. Numerical modeling software

Despite its limitations, Dessault Solidworks Flow Simulation was considered sufficient for the current fluidic cell model for single-phase incompressible heat transfer flows with low speeds, transitional to low turbulence regimes, and fairly small pressure drops. Modern industrial Computer Aided Design (CAD) tools such as Dessault Solidworks or Autodesk Inventor are well-suited for semi-quantitative simulation of evolving geometric models because changes in 3D CAD model are reflected in the associated computational fluid dynamics (CFD) packages without requiring a significant time investment in rebuilding the models. While less powerful in terms of options and granularity in model set-up than dedicated Multiphysics applications such as COMSOL Multiphysics or ANSYS Fluent, integrated industrial CAD-CFD tools are the go-to

solutions for rapid prototyping. Low-hassle user interfaces bridge powerful geometry building tools with fluid and heat transfer modeling, and focus on simulation speed and automation. Nevertheless, focus on the needs of design engineers as opposed to domain specialists and academic disciplines comes at a cost of limitations on how fluid and heat transfer models are represented and solved. Current Solidworks flow simulation is largely limited to using Cartesian meshing using rectangular parallelepipeds, and solving non-reacting, laminar and turbulent flows using Favre-averaged Navier-Stokes equations and a single turbulence model [270].

3.2.6.3. Fluid flow and heat transfer model equations

Favre-averaged Navier-Stokes equations are quite versatile and can be applied for the simulation of laminar or turbulent, rotating, compressible or incompressible, and Newtonian or Non-Newtonian liquids [270]. Mass, momentum, and energy conservation equations are summarized in Figure 3.17. Mass conservation equation (Figure 3.17 A) is implemented as the general form of the mass continuity equation in Cartesian coordinates where the S^p_M distributed mass term is zero for a standard continuity equation, but Flow Simulation can also include Euler-Lagrange terms for two-phase flows (solid particle + fluid).

Both the momentum conservation (Figure 3.17 B) and energy conservation (Figure 3.17 C) equations include material stress properties accounting for fluid behaviour and turbulence. The shear stress tensor τ can have Newtonian (shear rate independent) and non-Newtonian (shear rate dependent) forms, while Reynolds stress tensor τ^R incorporates stresses related to turbulent flow using the k-ε turbulence model. External mass-distributed force terms account for buoyancy, porous media resistance, and control volume rotation if present. The combined enthalpy term H includes stagnation enthalpy (combines thermal, pressure and kinetic energy), rothalpy (rotational energy), turbulence energy, and enthalpies of fluid mixture components if present.

A. Mass conservation

$$\frac{\partial \rho}{\partial t} + \frac{\partial}{\partial x_i}(\rho u_i) = S_M^p$$

Change in distributed mass of volume over time

Distributed mass movement through volume

Multi-phase mass terms

B. Momentum conservation

$$\frac{\partial \rho u_i}{\partial t} + \frac{\partial}{\partial x_j}(\rho u_i u_j) + \frac{\partial p}{\partial x_i} = \frac{\partial}{\partial x_j}(\tau_{ij} + \tau_{ij}^R) + S_i + S_{Ii}^p$$

Change in distributed momentum over time

Distributed fluid advection

Pressure changes

Material stresses

Other forces (external mass-distributed, multi-phase)

C. Energy conservation

$$\frac{\partial \rho H}{\partial t} + \frac{\partial \rho u_i H}{\partial x_i} = \frac{\partial}{\partial x_i}(u_j(\tau_{ij} + \tau_{ij}^R) + q_i) + \frac{\partial p}{\partial t} + \left(\rho\varepsilon - \tau_{ij}^R \frac{\partial u_i}{\partial x_j}\right) + S_i u_i + S_H^p + Q_H$$

Change in distributed energy over time

Distributed energy movement through volume

Shear and diffusive heat flux

Pressure term over time (sep. from enthalpy eq)

Turbulence energy and dissipation

External energy, multi-phase energy, volume-distributed sources

$$H = stagnation\ enthalpy + rothalpy + turbulence\ enthalpy + mixture\ enthalpy$$

Figure 3.17. Favre-averaged Navier-Stokes equations in Solidworks 2020 Flow Simulation [270]. Equation terms are highlighted to present physical analogies most closely representing the terms.

This set of versatile equations is a subset of the Reynolds-Averaged Navier-Stokes (RANS) approaches that use flow averaging to greatly reduce the computational effort for turbulent flow problems [271]. The main limitation of the Solidworks implementation is the availability of a single *k-ε* turbulence model, while at least three other well-known approaches exist. In the *k-ε* model *k* is the turbulent kinetic energy and *ε* is its dissipation rate. The model is considered accurate for non-rotating free-shear-layer flows that have small pressure gradients. Free-shear-layer flows are flows that do not interact with solid boundaries. The main advantage of this model

is a fairly high solution stability. In Solidworks, the values for turbulence length and intensity must be specified by the user. Turbulence length is typically the hydraulic diameter of the channel, while turbulence intensity is a ratio of root-mean-square turbulent velocity fluctuations and mean flow velocity that can be estimated from bulk Reynolds number [272]. Rules of thumb estimate low turbulence intensity value of <1 %, medium turbulence between 1 and 5 %, and high turbulence between 5 and 20 % [273].

3.2.6.4. Solid and conjugate heat transfer model equations

Solid heat flux ($-\lambda \nabla T$) can be determined from the solutions to the temperature gradient and heat conductivity tensor (λ) in the following equation [270]:

$$\frac{\partial \rho c T}{\partial t} = \frac{\partial}{\partial x_i}\left(\lambda_i \frac{\partial T}{\partial x_i}\right) + Q_H \qquad \text{Eq.3.39}$$

where the first term describes thermal energy changes in the solid over time, the second term represents directional heat conduction and Q_H is the volume-distributed heat source. Conjugate heat transfer between fluids and solids balances the heat transfer flux around the isothermal wall boundary, where fluid heat flux is determined in part from the distributed energy movement gradient (Figure 3.17 C). Thermal contact resistances between solids are also be included in Flow Simulation by using an unspecified contact resistance term at the solid-solid boundary that results in a temperature step between the solid domains.

3.2.6.5. Radiation heat transfer model equations

Radiation heat transfer was modeled using the Solidworks Discrete Transfer model assuming gray, diffuse surfaces obeying Lambert Law, and not considering radiation transmission and scattering in semi-transparent solids such as the flow cell material. Gray surfaces have radiative properties independent of wavelength, while diffuse surface properties are independent of direction. Another model available in the software is Discrete Ordinates which approximately solves the radiative transfer equation (RTE) to account for emission, absorption,

as well as scattering of the incoming and outgoing radiation. This method covers scattering in semi-transparent media and wavelength-dependent properties. Discrete Transfer instead of the Discrete Ordinates model was used to improve computational performance with the expectation that radiative surfaces would receive more energy (i.e. no transmission through a semi-transparent flow cell).

Discrete Transfer model uses features of both Hottel zone and Monte-Carlo techniques to compute view factors that specify the proportion of the total radiative heat flux exchanged by a particular set of surfaces [270]. Both techniques are described in detail by Siegel & Howell [274]. The net radiation balance on a specific surface is the difference between the outgoing and incoming radiation energy. Solidworks defines outgoing radiative energy Q^{out} from a surface *i* as:

$$Q_i^{out} = \varepsilon_i \sigma T_i^4 A_i + (1 - \varepsilon_i) Q_i^{in} \qquad \text{Eq.3.40}$$

where the first right-hand side term is heat radiated per Stefan-Boltzmann law while the second term is the incident radiation reflected by the surface with absorptivity ε. Since surface is gray and diffuse, its absorptivity and emissivity are the same. Incoming radiative energy Q^{in} is defined as:

$$Q_i^{in} = \sum_j F_{ij}\, Q_j^{out} \qquad \text{Eq.3.41}$$

where incoming energy is the sum of energy leaving other (j^{th}) surfaces toward this (i^{th}) surface. The proportion of the total radiative energy arriving at this surface that comes from another surface is defined as a view factor F_{ij}. View factors can be determined by a Monte-Carlo simulation method where thousands of rays are traced from one surface and hit other surfaces. Hit counts compared to the total number of rays released represent the view factor. The direction at which the rays leave a random radiating point on the surface are determined from Lambert's cosine law for a diffuse surface. View factors need to be computed only once at the start of the simulation, improving computation efficiency. Once both the incoming and outgoing radiative energy is known, net radiation is simply computed as follows:

$$Q_i^{net} = Q_i^{out} - Q_i^{in} \quad \text{Eq.3.42}$$

Radiation sources considered in the model were fluidic cell surfaces, enclosure surfaces, support structure surfaces, and the ambient environment.

3.2.6.6. Domain discretization

The numerical solution is achieved using the cell-centered *finite volume* (FV) discretization of the domain into Cartesian rectangular cells (Figure 3.18) [270]. This is the only meshing method available. Cell blocks are classified as solid, fluid, and boundary cells. Boundary cells are subdivided into polyhedron volumes depending on the boundary geometry.

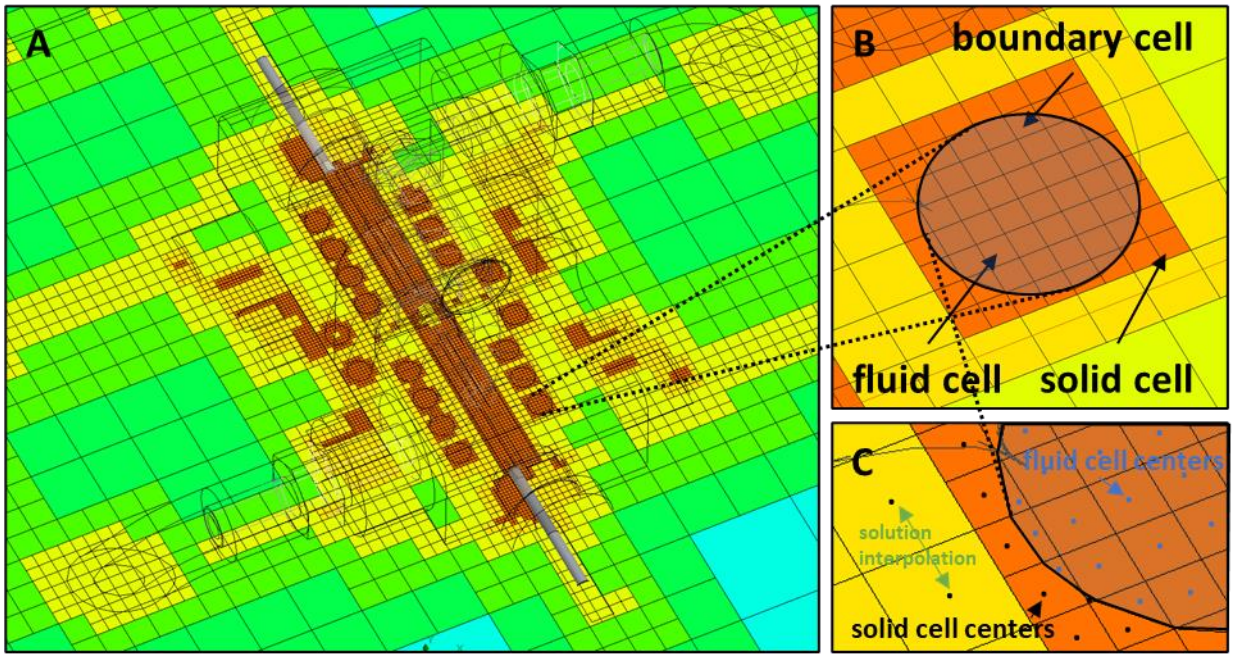

Figure 3.18. Cell-centered finite volume (FV) discretization. Fluidic cell cut plot showing different levels of mesh refinement using different colours (A). FV cells are classified as fluid, solid, or boundary cells (B). Boundary FV cells are further subdivided into fluid and solid polyhedral cells (C). In FV method, PDEs are integrated over the whole finite volume and solutions are produced at the FV cell centers. Solutions for the entire volume are then interpolated between the FV cell centers.

The cell-centered finite volume method directly integrates the PDEs based on RANS equations over the defined volumes producing an average value of a solution across that volume [275]. The

main advantage of finite volume methods compared to finite element methods is that they guarantee local conservation of mass, momentum and energy across adjacent cell boundaries, which translates into conservation across the whole domain and a stable solution. However, guaranteed conservation and stability of quantities does not necessitate solution accuracy. Solidworks implementation provides second-order accuracy spatial derivatives, which means that numerical approximation error of the solution decreases quadratically with decreasing volume element size. Decreasing volume element size can also improve accuracy by meshing better to curved geometry. Lastly, local solutions are valid for volume centers. Regions between the centers are interpolated to reconstruct the solutions for the entire volume, which can affect accuracy.

3.2.6.7. Numerical solution scheme

Solidworks flow simulation solution employs a custom iterative scheme [270] based on the popular SIMPLE and Multigrid methods [275]. While the details of these schemes are beyond the scope of this discussion, the idea behind iterative methods is essentially a guess-and-correct procedure, requiring a sufficient number of iterations to stabilize the solution. Solidworks defines a *travel* as the number of iterations required for the propagation of a numerical disturbance over the whole computational domain. At least one travel is therefore required for a solution converged across the entire model domain. When simulating fluidic cell models, two to four travels were used to ensure convergence with surface temperatures and heat fluxes specified as convergence parameters.

3.2.7. Numerical model results

Parameters explored semi-quantitatively using the numerical model included heating fluid flow rates, channel dimensions, heat exchange, pressure drops, and temperature distributions within the complex 3D geometry of the cell. For the sake of brevity only the high temperature results are shown because they represent the worst-case scenario in terms of

temperature variability. For example, thermal uniformity at steady state was expected to be within 1 °C of the membrane chip and its surrounding region based on outlined requirements. 1 °C is a much smaller fraction of 90 °C than it is of 30 °C, therefore temperature gradients at the high temperature range would be the limiting indicator of fluidic cell's performance.

3.2.7.1. Mesh independence

Mesh independence was assessed before using the constructed numerical model to ensure that the highest resolution (refinement level) and computationally efficient mesh is used (Figure 3.19). A mesh independence study collects parameter values at locations of interest while refining the mesh. Results are considered mesh-independent when further refinement produces very little (i.e. <5 %) change in parameters. A highly refined mesh theoretically results in lower numerical approximation errors up to the extent where floating point truncation errors and overall computing resources become a bigger issue. Non-monotonic simulation results are expected with Solidworks mesh refinement since it uses a combination of different computational techniques depending on mesh coarseness. Lower resolution mesh may produce a more consistent and accurate result than a higher resolution mesh if it is in the optimum range for a particular computational technique for that mesh size. A level 5 mesh with detailed channel refinement was selected for the model given low mesh dependence, and high memory and computation time costs of larger refinement.

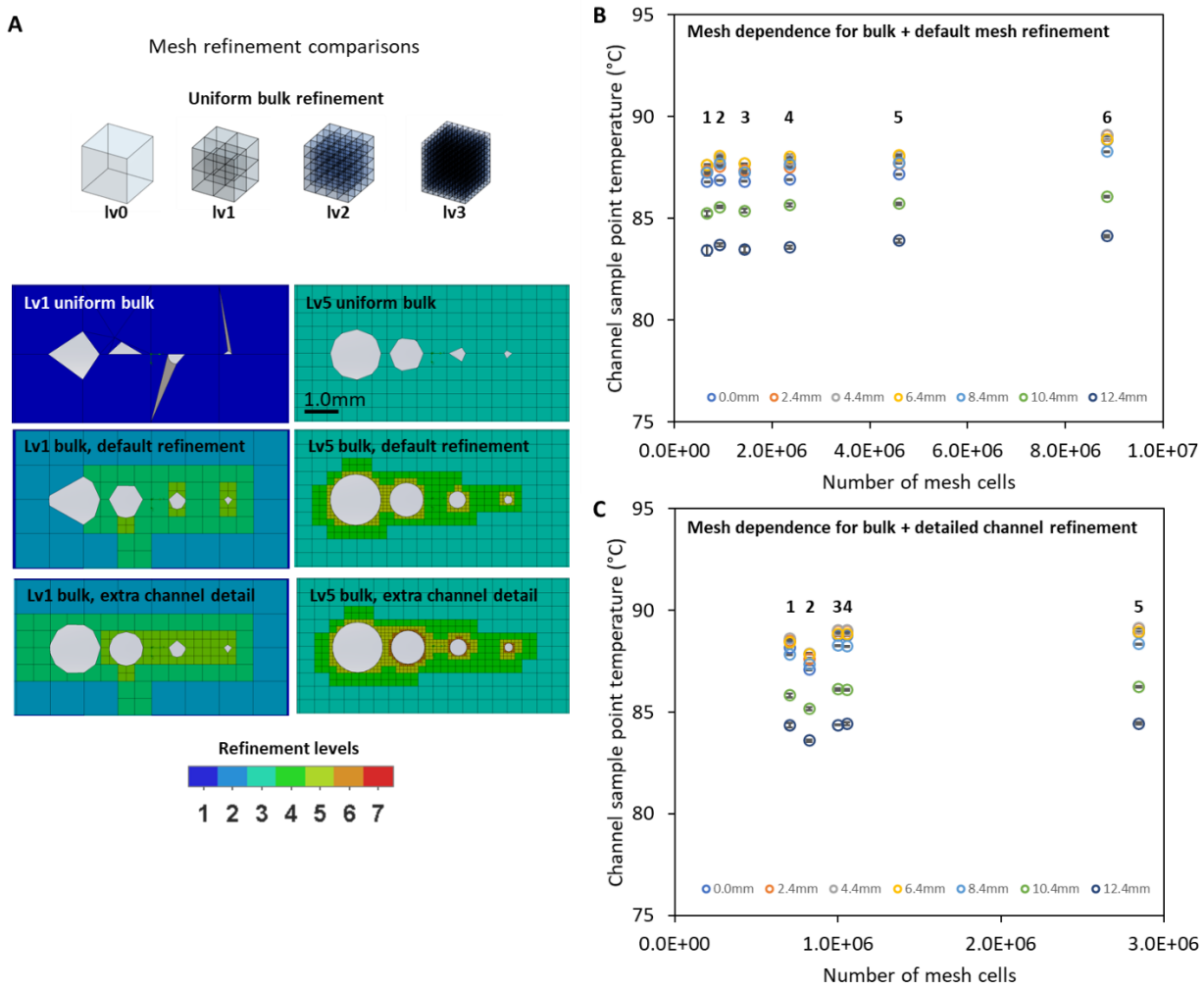

Figure 3.19. Mesh refinement in Solidworks Flow Simulation. Mesh refinement is largely automated with manual control available for small channel feature refinement. Each bulk refinement level of a specific mesh region splits each cell into eight sub-cells (A). Uniform bulk mesh, default refinement, and detailed refinement meshes shown for comparison on a sample set of channels. Interestingly, requesting a high level uniform bulk mesh does not produce the expected detail (i.e. lv5 gives lv3 refinement). Plots in B and C show mesh dependence of sample point temperatures within the fluidic cell channel for two meshing strategies. Both offer <1.5 % variability at higher mesh densities. Extra channel detail refinements offer a more efficient mesh with fewer cells that focus on regions in proximity to boundary layers.

3.2.7.2. Heat transfer results

Finite volume analysis (FVA) numerical model results show deviation from the simplified analytical model, particularly in the laminar and transitional flow regimes (Figure 3.20). As reported in Section 3.2.4, fluidic cell model geometry is outside of the empirically validated range for Nusselt correlations available in the helical channel literature. Both the channel size and

aspect ratios are located outside of the empirically validated range. Numerical results reflect the discrepancy in heat transfer coefficients, heat transfer rates, and pressure drops. Greatest agreement with the analytical model is on heat transfer rates and pressure drops within the high flow rate turbulent regions.

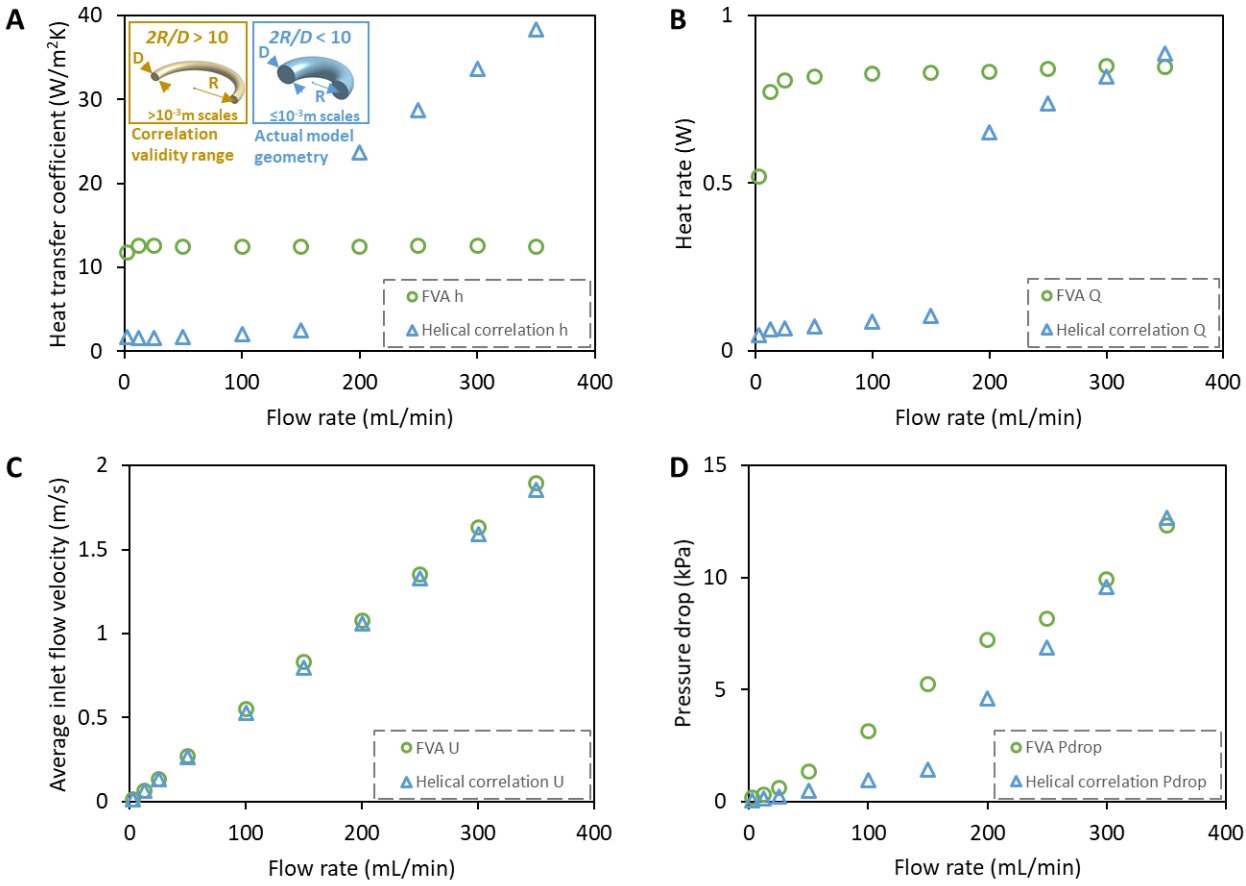

Figure 3.20. Comparison of results from the numerical (FVA) and the 1D lumped parameter (helical correlation) model. Model flow rates range from laminar to turbulent flow regimes for a 90 °C input flow of PFPE heat transfer fluid. Average internal heating fluid temperature from the FVA model is taken as the mean flow temperature (T_m) of the lumped parameter model, and average enclosure air temperatures from the FVA model are used in the lumped parameter model as the environmental temperature (T_∞). (A) Heat transfer coefficients in the lumped parameter model helical channels are based on the available Nusselt numbers derived from macroscopic helical pipe experiments with large aspect ratios ($2R/D$ > 10) and do not adequately describe the compact millifluidic helical channels ($2R/D$ < 5). (B) Heat transfer coefficient differences from the helical channels result in clear heat transfer rate differences between the models. Channel pressure drops (D) at various average flow velocities (C) in the smooth-pipe FVA model appear higher in the laminar and transitional regimes. A pressure drop rate reduction at 250 mL/min may be an artefact of the switch in numerical model behaviour as opposed to a physical phenomenon, i.e. hidden automatic change in boundary layer models.

Numerical model demonstrates better agreement with existing numerical and experimental studies of curved microfluidic channels as compared to the analytical model. Very few existing investigations confirm numerical models of milli- and micro-fluidic spiral or helical channels with experimental results, therefore it is difficult to assess their validity. Existing numerical models mostly examine spiral micro-channels in the laminar regimes [276]–[280] and attempt to leverage curvature-induced laminar flow vortices for improving heat transfer. Only one study experimentally confirmed numerical heat transfer results in a spiral microchannel heat exchanger [213]. A significant jump in Nusselt number (*Nu*) was reported for Reynolds number *Re* < 330 due to increasing Dean vortex activity. Low-magnitude laminar coefficients were not present in the micro-fluidic regime, unlike what is observed using macro-fluidic Nusselt correlations. The study also reported leveling of *Nu* for *Re* > 330 which was associated with the flow starting to gradually transition toward turbulent behaviour. This behaviour is seen in the current fluidic cell FVA model where coefficients experience a significant magnitude jump at flow rates below 25 mL/min (Re < 318), then start leveling off as flow rate increases (Figure 3.20 A). Figure 3.21 shows channel flow velocity profiles in laminar and turbulent flows where only a marginal 4.5 % heat transfer rate increase is observed (Figure 3.20 B), consistent with the leveling of the heat transfer coefficients reported in the experimentally-validated study.

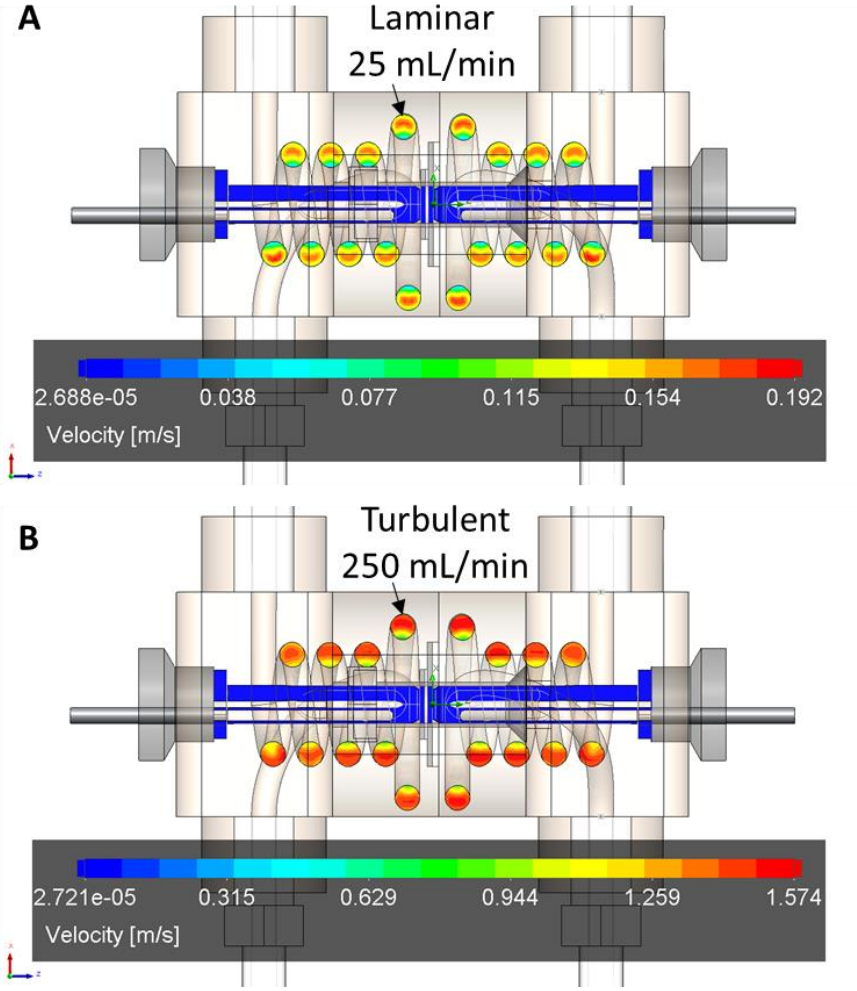

Figure 3.21. Heating channel velocity flow profiles. (A) Distinct fluid velocity layers are seen in laminar (*Re* = 318) flow. (B) Fluid mixing all the way to the solid boundary layer is seen for turbulent (*Re* = 3184) flow.

3.2.7.3. Immunity to disturbance

Low variation in heat transfer rates across flow rates (Figure 3.20 B) was leveraged for designing a system with immunity to unavoidable flow rate disturbances over time. For example, Viton fluoroelastomer peristaltic pump tubing wear was observed to reduce flow rates by as much as 30 % over three months of intermittent operation. Several industry white papers report over 20 % flow rate reduction for fluoroelastomer and EPDM tubing over 504 hours of operation [281], [282]. Selecting a design flow rate of 150 mL/min for a half-cell provides reasonable

pressure drops while keeping heat transfer rate changes under 5 % for flow rate changes of under 30 %.

3.2.7.4. Analyte temperature uniformity

Temperature uniformity within the flow cell analyte channels is not significantly impacted by the changes in flow rates within the low variability region of heat transfer (> 50 mL/min) (Figure 3.22).

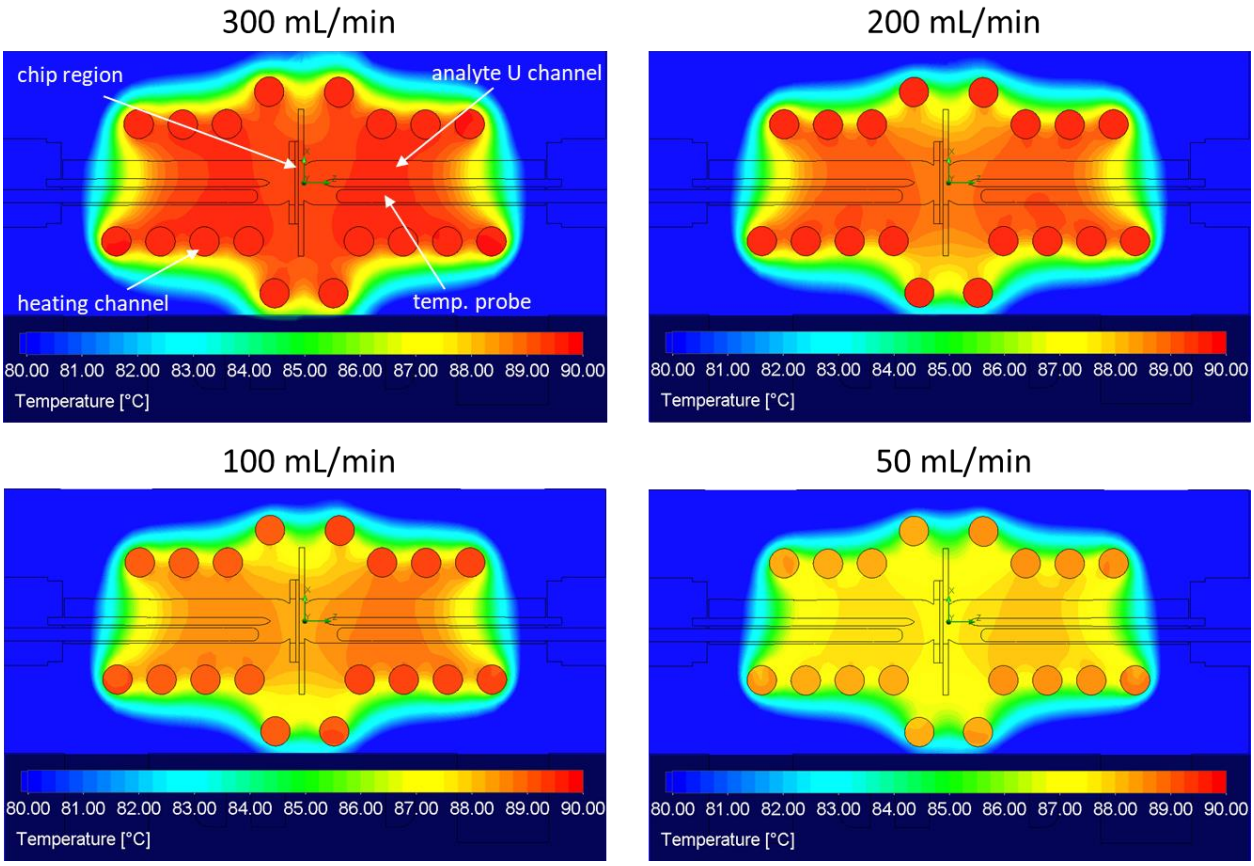

Figure 3.22. Uniformity of temperature profiles within the fluidic cell across flow rates. Analyte U channel temperature uniformity is maintained to within 1 % of the central chip region temperature for a wide heat transfer fluid flow rate range. Each isotherm designates a 0.25 °C temperature range bin. Drop in heating channel temperature with the drop in flow rates is related to higher thermal losses in the inlet tubing system (not shown) at the given flow rates. Inlet fluid temperature was maintained at a constant 90 °C.

Temperature uniformity also carries over across different heat transfer fluid flow temperatures. Analyte channel temperature is uniform to within 1 % of the chip region temperature for up to 8 mm along the central channels, shown numerically and experimentally (Figure 3.23, Figure 3.24).

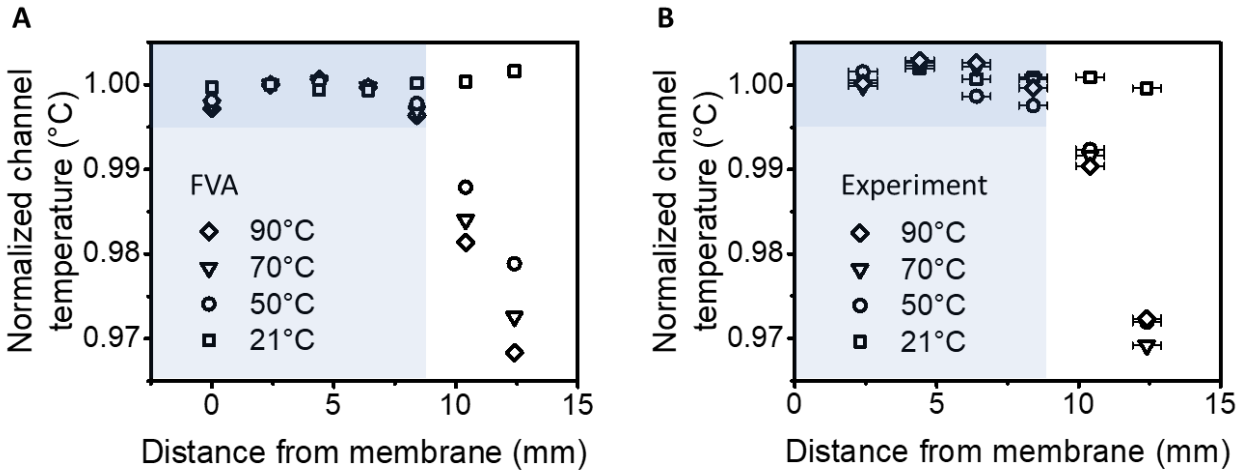

Figure 3.23. Uniformity of temperature profiles within the fluidic cell analyte channel across temperatures. Temperature uniformity is maintained to within 1 % of the central nanopore chip region temperature for the entire temperature range. Results are shown for inlet temperatures of 90, 20, 50, and 21 °C (room temperature control) Numerical FVA model (A) is in agreement with experimental results (B). 8 mm uniform temperature region is lightly shaded, while a 1 % normalized temperature range is more shaded.

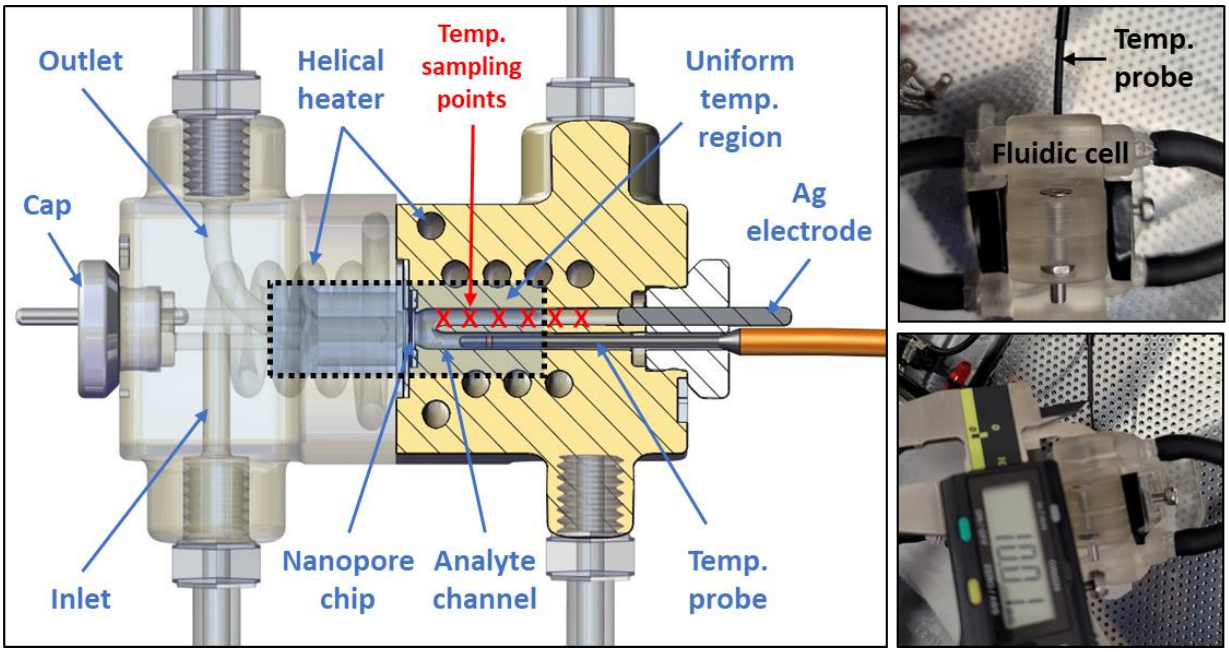

Figure 3.24. Experimental methodology for assessing temperature uniformity of the cell. Average analyte U channel temperature was measured using an optical thermometer probe of known geometry at multiple points marked by red Xs. Probe tip position within the cell was measured using a digital caliper by how much of the probe was exposed outside of the channel in reference to the cell's edge.

3.2.7.5. Heating channel pressure drop

Pressure losses across the FVA model cell are higher than expected with analytical approximations (Figure 3.20 D). Analytical results would appear more consistent if turbulent regime equations were applied to the entire flow range, suggesting secondary flows may play a more important role in small channels even at low Reynolds numbers. Interestingly, numerical model shows a reduction in pressure growth rate around 250 mL/min which is close to the theoretical turbulence transition region. This could be an artefact of the switch in numerical model behaviour for turbulent regime since friction factors are expected to increase asymptotically [213] and result in a consistent pressure increase similar to the analytical model. The main takeaway from pressure analysis is that pressure drops at design flow rates can approach 10 kPa, and model errors can be well-accounted for by using a pressure safety factor of at least 2.0.

3.2.8. Fluidic cell electrodes

3.2.8.1. Electrode type selection

Nanopore sensors use non-polarizable electrodes to transduce nanopore ionic current to electronic current at the electrode interface, minimizing distortion of both direct (DC) and alternating (AC) current components. Non-polarizable electrodes, such as the silver/silver chloride (*Ag/AgCl*) electrode, pass both DC and AC well since electrode-electrolyte reactions occur fast, often with the electrode material itself being consumed in the reduction-oxidation reactions [283]. In contrast, polarizable electrodes, such as the platinum (*Pt*) and carbon (*C*) electrodes used in other biomedical applications, behave like capacitors and do not pass DC well. Polarizable electrode reactions occur relatively slowly (if at all), and are better suited for AC transduction.

Non-polarizable *Ag/AgCl* electrodes are almost universally used in nanopore experiments with ion-matching (*Cl-*) electrolytes such as potassium chloride (*KCl*), sodium chloride (*NaCl*), and lithium chloride (*LiCl*). Ion-matching ensures nearly linear transduction of low ionic currents as per following reversible reduction-oxidation (redox) reaction [283]:

$$AgCl(s) + e^{-} \rightleftharpoons Ag(\mathrm{s}) + Cl^{-}(aq) \qquad \text{Eq.3.43}$$

where silver chloride (*AgCl*) at the cathode surface is driven toward reduction with excess electrons, producing silver metal (*Ag*), and a mobile negatively-charged chloride ion (*Cl-*) that travels toward the positively charged anode. Reaction is reversed at the anode where electrons are siphoned away from the electrode which drives the reaction toward silver metal oxidation into silver chloride. While each electrode reaction has a standard half-cell potential of ±222mV at 25 °C, inclusion of both the reducing and oxidizing electrodes in the same electrolyte at equilibrium largely cancels the potential difference (< ±40μV) [283].

3.2.8.2. Elevated temperature performance and stability

Silver chloride electrodes under non-standard (experimental) conditions have half-cell potentials dependant on concentration of *Cl-* ions and temperature, therefore residual potential difference will vary and result in measured voltage offsets at the sensor. The half-cell potential can be expressed using a modified Nernst equation [283]:

$$E_{T,c_{Cl-}} = E_{AgCl/Ag} - \frac{RT}{F}\ln(c_{Cl-}\gamma_{Cl-}) \qquad \text{Eq.3.44}$$

where $E_{AgCl/Ag}$ is the standard electrode potential at 25 °C (+222 mV), R is the universal gas constant (8.314 J/K·mol), T is the electrolyte temperature, F is the Faraday constant (96,472 C/mol), c is the concentration of ions (*molal*), and Υ is the activity coefficient that is experimentally determined and is a function of electrolyte type, temperature and pressure. The qualitative importance of this relation is that environmental variables for both electrodes have to be well controlled throughout the experiment for repeatable sensing performance.

Silver chloride electrodes are appropriate for use in the high temperature nanopore experiments since they maintain high thermal and temporal stability. Electrode standard potentials are stable up to 300 °C [284], with a drift of as little as 200 µV over 4 years within a range from 15 to 37 °C [285]. Electrodes under non-standard (experimental) use cases are usually made non-functional much sooner (several weeks) due to both passive and active depletion of the thin *AgCl* layer. Active wear includes redox reaction depletion during the experiment, as well as physical bumping and scraping of the delicate *AgCl* layer during manipulation. Passive wear includes aqueous dissolution [286], [287] and photodecomposition [288]. Photodecomposition is minimized by keeping the electrodes away from light sources. Dissolution is minimized by keeping the common halide ion (*Cl-*) concentrations as well as electrolyte temperatures low. Solubility of *AgCl* in water can increase by an order of magnitude (10^{-3} to 10^{-2} g/L) in the temperature range from 20 to 100 °C [286]. Furthermore, high concentrations of halide ions (*X = Cl, Br, I*) in aqueous solutions can paradoxically increase dissolution due to formation of AgX_2 compounds [286].

3.2.9. Aqueous electrolytes

3.2.9.1. Electrolyte selection

Aqueous electrolytes such as potassium chloride (*KCl*), sodium chloride (*NaCl*), and lithium chloride (*LiCl*) are the most frequently used electrolytes in nanopore sensing. When used at high salt concentration (i.e. 1 M KCl, 3.6 M LiCl), aqueous electrolytes suppress pore surface effects on sensor current [100], and provide higher current signal amplitude for improved spatial resolution of the sensor. Temporal resolution of the sensor can be improved by selecting electrolyte composition that slows down molecular translocations. For example, DNA translocation can be slowed down by using smaller metal ions (*Li+ < Na+ < K+*) [289]. This phenomenon can be attributed to the differences in the transient ionic bond strength between the positive metal ions and negative DNA backbone. Positive charges temporarily shield negative molecular backbone, decreasing the overall molecular charge and reducing the net electrostatic force contributing to molecular motion. Smaller ions can form stronger ionic bonds that take more time to dissociate, resulting in slower molecular motion over time. The ionic size observation does not apply to divalent ions (*Mg2+*) which seem to produce an even greater charge screening, slowdown of translocation, and molecular aggregation that can clog nanopores [289]–[291]. High concentration (3.6 M) *LiCl* is therefore an appropriate design choice for improving sensor resolution without adversely affecting sensor performance.

3.2.9.2. Electrolyte evaporation

Lithium chloride (*LiCl*) is the most appropriate aqueous electrolyte to use in the high-temperature sensing system since it reduces evaporative losses. *KCl* is frequently used in ambient room temperature experiments, but is prone to drying out even over the course of a day if not sealed well against evaporation. *LiCl* is very hygroscopic, i.e. absorbs and retains water well, widely used as a dry desiccant [292]. *LiCl* has also been used in liquid desiccant systems which require hours at temperatures as high as 80 °C with a low-humidity air flow to regenerate a high-concentration salt solution from a low-concentration salt solution [293]. Since nanopore ionic

current is directly dependent on the salt concentration, variability at elevated temperatures has to be minimized, making high-concentration (3.6 M) *LiCl* a better electrolyte from a mechanical design standpoint.

3.2.9.3. Electrolyte pH buffering

Nanopore electrolytes are pH-buffered solutions since pH – a measure of acidity or basicity of an aqueous solution – affects both the nanopore fabrication by CBD [34] and molecular stability [2]. Buffers are required to stabilize solution pH which can change as a result of gas diffusion or other reactions changing the solution's hydrogen ion balance, i.e atmospheric carbon dioxide absorption ($CO_2 + H_2O \rightarrow HCO_3^- + H^+$). pH buffers such as phosphate, Tris, glycine, and HEPES are commonly used to maintain a stable pH in molecular experiments. HEPES is a non-ionic buffer that is most often used in molecular diagnostics for its buffering capacity in the physiological pH range of 6 to 8, high water solubility, high stability, low binding affinity for metal ions, and low thermal variation (Good's buffer criteria) [153]. When compared to other Good buffers, HEPES has the smallest variation in acid-base dissociation constant (pKa) with temperature (pKa 7.55 @ 20 °C, –0.014 ΔpKa/°C), making it ideal for high-temperature applications. When pKa changes more than one pH unit from the target pH value, buffering capacity decreases significantly.

3.2.9.4. Electrolyte electrical conductivity

Lithium chloride solution has a linear electrical conductivity profile across the required temperature range (Figure 3.25) which is expected to result in linear conductivity changes in the nanopore sensor. Linear conductivity trend is consistent with monovalent metal chloride solutions used in other nanopore temperature studies that reported solution conductivity curves [43], [44].

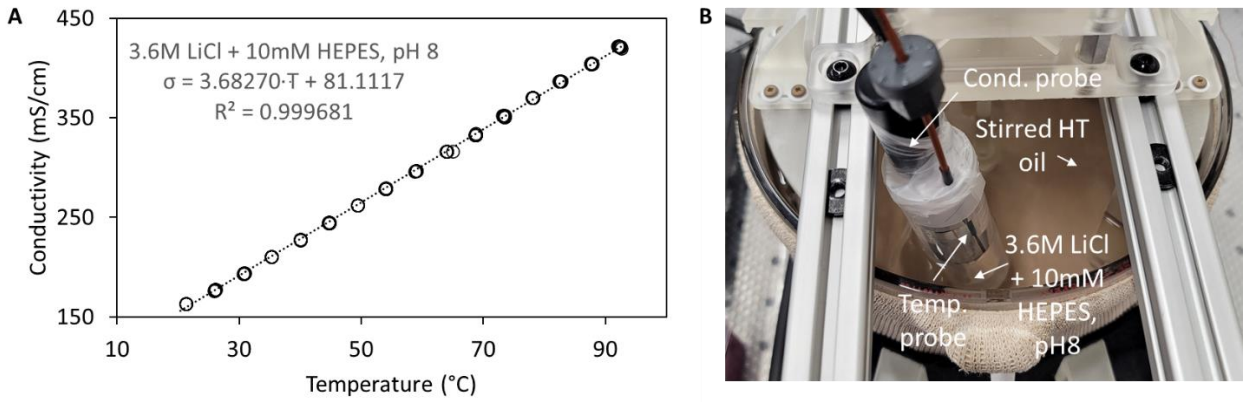

Figure 3.25. Nanopore sensor electrolyte conductivity with temperature. Linear fit (A) of 160 experimentally measured data points using VWR Symphony benchtop meter with a calibrated Orion 018020MD conductivity cell in 25 mL of 3.6 M LiCl + 10 mM HEPES, pH 8 (21 °C) test solution. Uniform temperature of a test solution was maintained by a stirred HT fluid bath (B) within 1 °C and solution temperature was equilibrated for 15 min before collecting 10 data points at each temperature.

3.2.9.5. Electrolyte material compatibility

Electrolyte compatibility with a range of cell materials was verified by subjecting 3D-printed test channels to degassed electrolytes at elevated temperatures (Figure 3.26). Deionized water (DI), isopropanol (IPA), KCl, and LiCl were compatible with FormLabs High Temperature v1 (HTv1) resin material at room temperature. DI, KCl and LiCl exposure resulted in no significant HTv1 particulate leeching (> 50 µm) and low outgassing into solution at 24 hours of exposure up to 70 °C (Table 3.6). Significant drying and salt crystallization of KCl was observed for all materials which was expected given its propensity to dry even under ambient room temperature conditions. Other PMMA-like materials tested (FormLabs High Temperature v2, and Clear v4) leech into at least one of the test solutions, which rules out their compatibility.

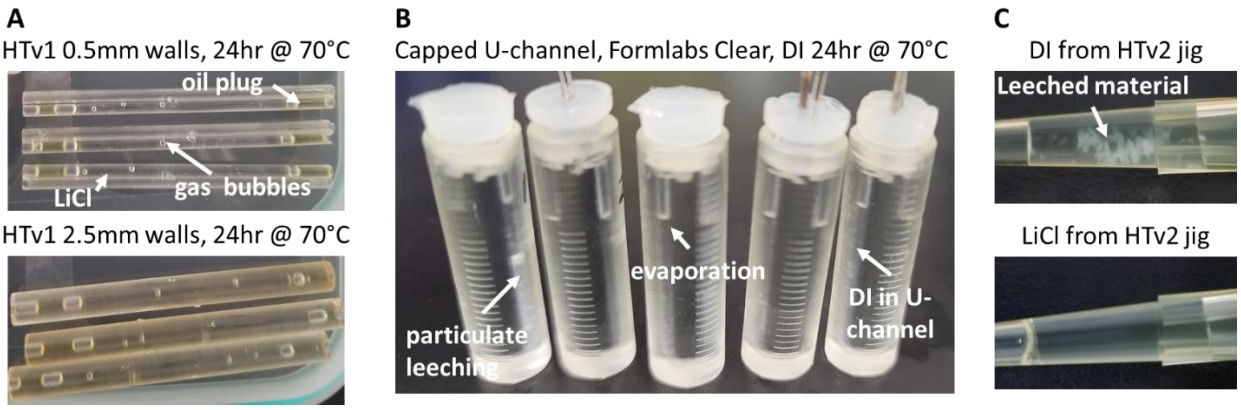

Figure 3.26. Sample 3D printed material test channels with test electrolyte solutions. Material leeching and outgassing could be assessed by filling test channels with degassed test solutions and exposing the devices (A, B) to an elevated temperature condition alongside a room temperature control. Test solutions were degassed at 45 °C, -30 kPa until no degassing was observed (>5 min) prior to loading into the test channels. Solution leeching was assessed by pipetting the fluid out of the channels and performing a visual examination under a wide-field microscope. High temperature resin v1 (FormLabs HTv1) has the best compatibility out of all the translucent PMMA-like 3D print resins tested (Formlabs HTv1, HTv2, Clear v4).

Table 3.6. Material compatibility assessment summary for 3.6 M LiCl + 10 mM HEPES, pH 8, at 70 °C for 24 hours.

Test component materials*	Fluid volume loss (%)	Particulate leeching	Outgassing
Polypropylene (ThermoFisher microcentrifuge tubes)	none	none	none
Borosilicate glass capillaries, ID 1.5-1.8	none	none	none
Clear v4, 1hr post-cure, ID 1.8, 0.5mm walls	8.3 - 8.8	yes	3-5 bubbles
Clear v4, 1hr post-cure, ID 1.0, 2.5mm walls	14 - 16	yes	1-3 bubbles
HTv1, 1hr post-cure, ID1.9, 0.5mm walls	0 - 2.4	none	1-3 bubbles
HTv1, 1hr post-cure, ID1.9, 2.5mm walls	0 - 2.4	none	2-3 bubbles
HTv2, 2hr post-cure, ID1.8, 0.5mm walls	50 - 70	yes	50-70 bubbles
HTv2, 2hr post-cure, ID1.8, 2.5mm walls	15 - 50	yes	15-50 bubbles

* Ranges based on testing N = 5 channels per material and geometric condition

3.2.10. Fluid loss management

3.2.10.1. Water loss

Water loss from the aqueous electrolyte increases salt concentration and conductivity of the electrolyte over time, which may be detrimental to nanopore sensor repeatability and long-term sensing performance. Water loss may come from absorption into fluidic cell material (i.e. polymers), and evaporation into ambient environment due to increased vapour pressure of fluid at elevated temperature. Very few studies of nanopores at elevated temperatures directly discuss fluid loss or address strategies on its management. One study reported non-negligible water loss from a Teflon fluidic cell, requiring water addition of 7 µL/hr at 25 °C and 64 µL/hr at 70 °C [28]. Investigations from Section 3.2.9 (Table 3.6) showed <2.4 % fluid volume losses over 24 hours at 70 °C using HTv1 resin material in oil-plugged channels, suggesting low material absorption or vapour conduction. Oil sealing the channels is not a user-friendly option for easily re-usable fluidic cells, therefore barrier material caps were investigated for sealing quality and re-usability.

3.2.10.2. Barrier polymeric materials

Barrier polymeric materials restrict passage of gases, vapours, and liquids through their boundaries and include a wide variety of materials which the reader is encouraged to explore via the provided references [294], [295]. Of interest are generally bioinert materials used for sealing molecular products, i.e. medication/vaccine vial stoppers. Rubbers, particularly butyl and silicone, have shown high temperature stability (i.e. autoclaving at 121 °C), and low water retention [296]. Silicone elastomers have the advantage of easy prototyping in 3D-printed molds using readily available condensation cure silicones (Dow Corning 732, 737) (Appendix C – Fluidic cell barrier cap casting system). As such, fluidic cell barrier caps were prototyped in silicone after early attempts at obtaining commercial butyl and EPDM rubber components of suitable geometry and low cost proved unsuccessful.

Thermal stability of silicone-cast barrier caps (Dow Corning 737) was assessed in comparison to 3D-printed rubber caps (Formlabs Flexible v2) used to seal existing room temperature fluidic cells (Figure 3.27). Flexible material caps provided an adequate fluidic seal with on average 0.14 mm diametral compression with no statistically significant compression set (paired t-test, n = 10, α = 0.05) after 24 hours at room temperature (~20 °C) (Figure 3.27 A). Compression set was significant at 28 % when left at 95 °C for 24 hours. In addition, Flexible material stiffened and failed likely due to hoop stresses (Figure 3.27 B). Silicone caps had a larger initial diametral compression of approximately 0.6 mm and showed compression set at both room (12 %) and elevated temperature (20 %). Nevertheless, silicone caps remained usable.

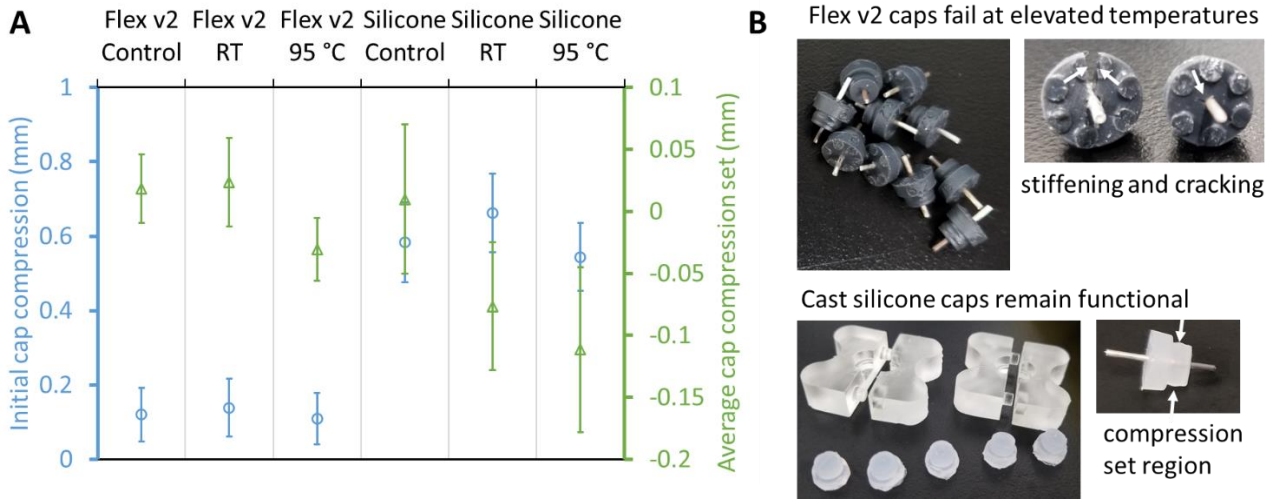

Figure 3.27. Thermal stability of fluidic cell barrier caps. Formlabs Flexible (v2) material caps designed for low temperature operation in existing nanopore fluidic cells are compared to silicone caps designed for high temperature cells with similar capping geometry. While Flexible material caps did not show significant compression set (A) at room temperature, they failed (B) after 24 hours at elevated temperature. Silicone caps showed significant compression set at room and elevated temperature, but remained functional.

3.2.10.3. Barrier cap effectiveness

Effectiveness of the HTv1 material cell with a silicone cap at containing fluid losses was assessed by measuring the conductivity of the electrolyte within the cell over time at different temperatures. Initial attempts at continuously measuring both nanopore and solution conductance within the fluidic cell at elevated temperatures had inconsistent results. First

challenge was the growth of SiNx nanopores at elevated temperatures, detailed in the later sections. The second challenge was that even without the nanopore, elevated temperature measurements produced unexpected drift dependent on temperatures. While a 200 Ω drift of electrolyte resistance over 1 hour may be negligible for a 100 MΩ nanopore sensor, it is not negligible for a 1000 – 2000 Ω fluidic cell channel used during the pore-less experiments. Given the vast number of variables affecting electrochemistry, experimentally disentangling the causes of measurement instability was beyond the scope of this work. Instead, a custom milli-fluidic conductivity cell was constructed to measure the conductivity of the electrolyte withdrawn from the cell at room temperature.

Typical high-accuracy commercial conductivity meters involve large electrodes maintaining stable and predictable electrical fields within analyte solutions while stirring to maintain uniform temperature and pH [297]. Macroscopic dimensions of commercial conductivity cells are optimized for generic use cases, where conductivity measurements become mostly independent of cell and electrode geometry for a wide range of conductivity, temperature, and pH values. Instead, a millifluidic conductivity cell (Figure 3.28) was designed for use with aqueous electrolytes in a narrow parameter range, i.e. high conductivity solutions of neutral pH at room temperature. A straight channel configuration with dual *Pt*-wire electrodes provided sufficient experimental precision (Figure 3.29) when used with the *LiCl* solution of known concentration and conductivity (Figure 3.25). Conductivity was adjusted for measured temperature variation using the modified Gaussian amplitude equation with interpolated *LiCl-H_2O* mixture constants from Wu et al. [298]. While the correlation used for temperature compensation has a reported accuracy of 1.98%, the precision of average measurements was within 0.5% and deemed sufficient. Precision, not absolute accuracy, was considered most important for comparative analysis of concentration changes within the same electrolyte solution withdrawn from the fluidic cell.

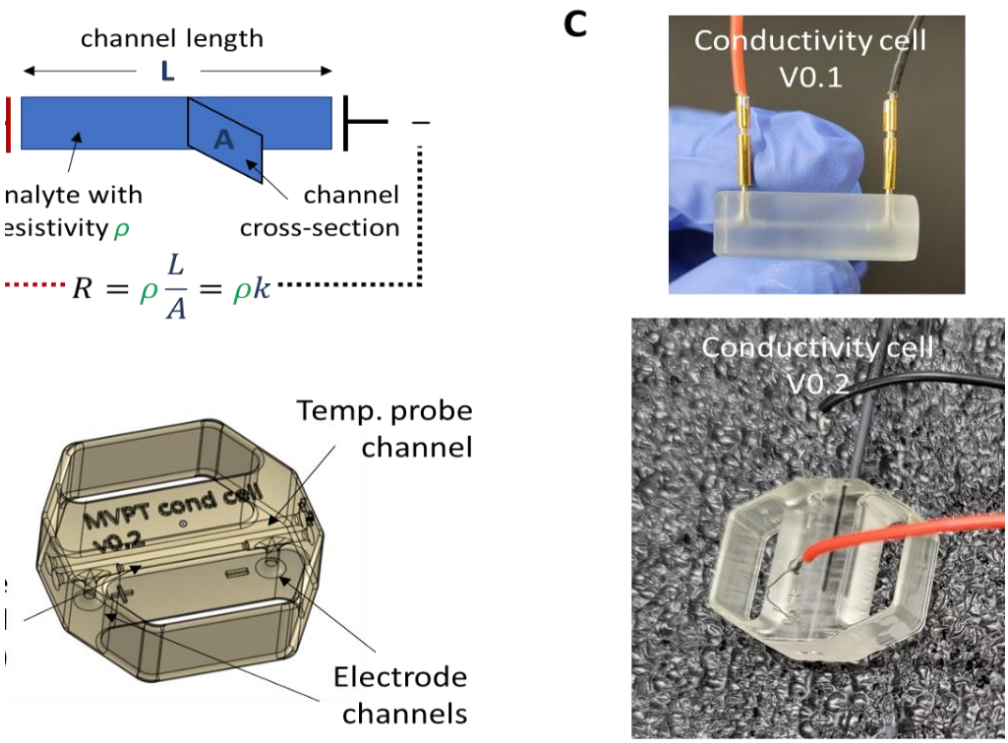

Figure 3.28. Millifluidic conductivity cell. (A) Basic principle involves measuring the electrical resistance (*R*) of a fluidic channel with known geometry (cell constant *k*) to determine the analyte resistivity (*ρ*). (B) CAD model of the latest design features a 25 µL analyte channel that draws in and retains analyte in the vicinity of the electrodes by capillary forces. (C) Several prototypes were 3D-printed, with V0.2 used in electrolyte resistivity measurement experiments at room temperature.

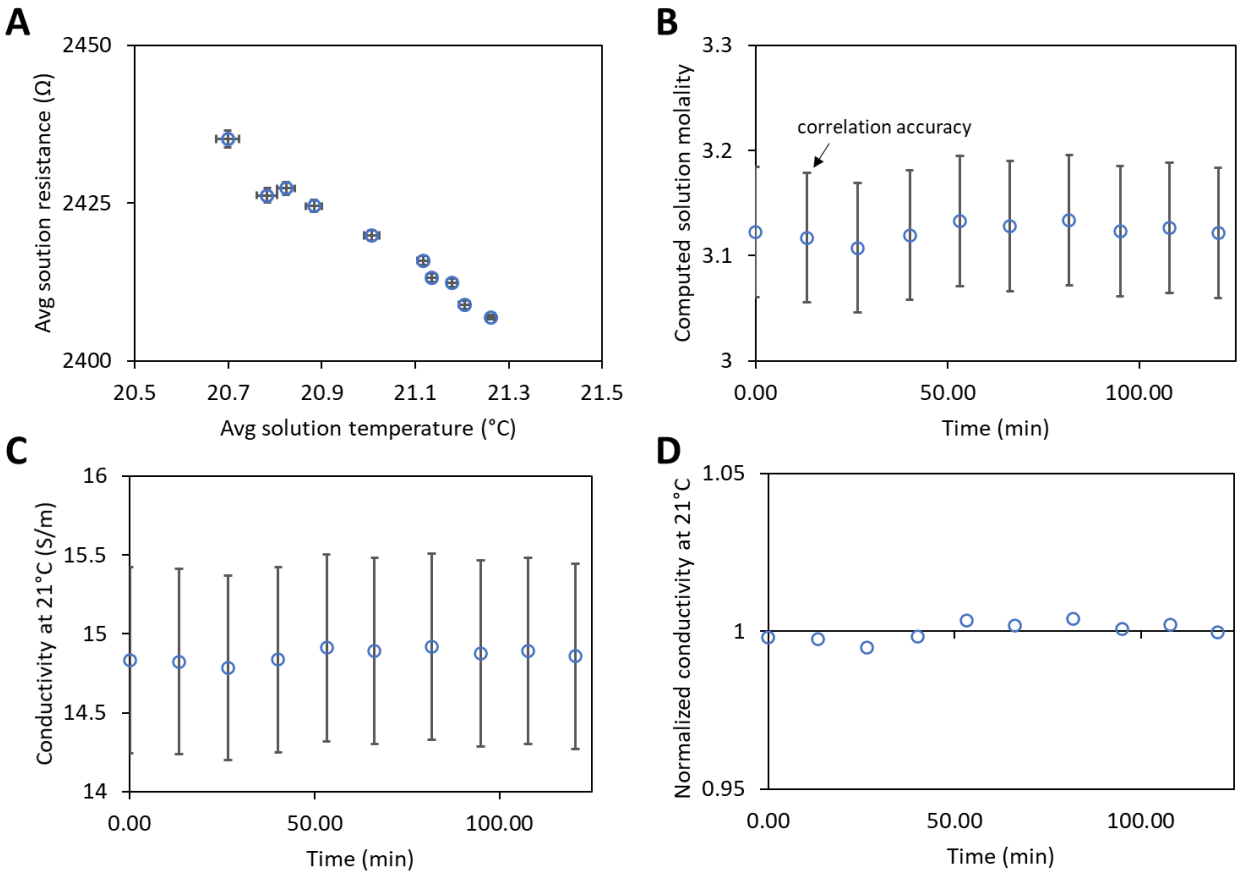

Figure 3.29. Conductivity cell validation. Conductivity cell was tested with independent 20 µL samples of 3.6 M LiCl + 10 mM HEPES, pH 8, at room temperature. Cell was thoroughly flushed with deionized water (DI) and dried between samples. Cell temperature was equilibrated for 2 minutes after sample loading, and resistance measurement was carried out for 2 minutes while also recording cell temperature. (A) Average solution resistance decreases with temperature linearly, consistent with expectations. (B) Solution concentration (molal) is recomputed per Wu et al. [298] correlations for conductivity of $LiCl+H_2O$ mixture as a function of temperature and concentration with a 1.98% accuracy error shown as error bars. (C) Solution conductivity is then normalized to 21 °C using the computed molality. (D) When normalized by average conductivity, variation in conductivity is less than 0.5 %, suggesting good precision.

The nanopore fluidic cell manufactured using HTv1 resin and using silicone barrier caps demonstrated negligible conductivity changes (<0.7 %) in 3.6 M LiCl + 10 mM HEPES, pH 8, over 1 hour up to 70 °C (Figure 3.30). The greatest conductivity increase (<4.4 %) was observed from solution degassing (60 °C, -30 kPa) prior to loading into the fluidic cell. In this context, conductivity increases are interpreted as resulting from electrolyte solution water losses, similar to elevated temperature observations during material testing (Table 3.6). Thus, the fluidic cell is considered suitable for nanopore experiments.

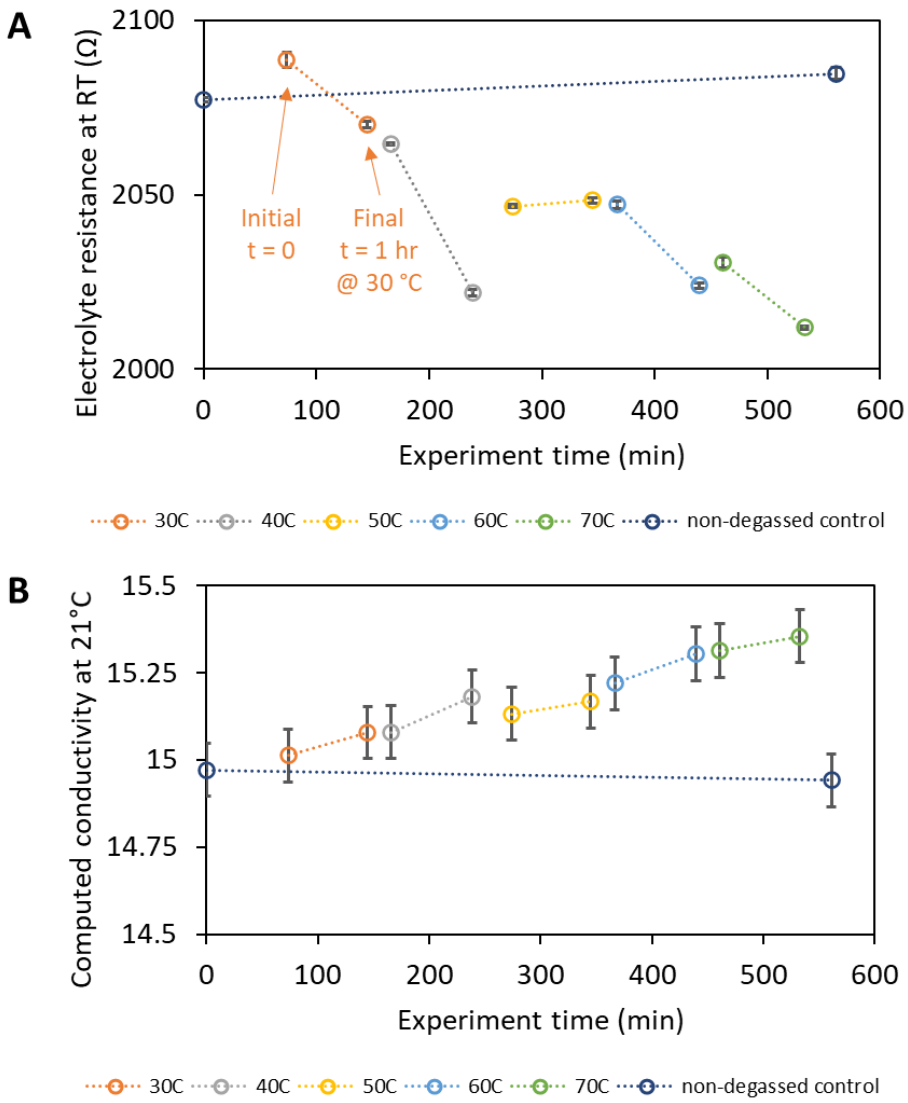

Figure 3.30. Conductivity changes in the HTv1 fluidic cell with silicone barrier caps. (A) Electrical resistance of the electrolyte (3.6 M LiCl + 10 mM HEPES, pH8) withdrawn from the HTv1 fluidic cell held at a particular temperature was measured at room temperature (RT) using the millifluidic conductivity cell. Data points for each temperature represent resistances of the initial electrolyte solution and solution after 1 hour at the specified temperature. (B) Trends in raw resistance values are not meaningful until plotted as temperature-adjusted conductivity values. Greatest conductivity increases (<4.4 %) are observed with electrolyte degassing (60 °C, -30 kPa) prior to loading into the cell, while electrolyte exposure to the cell at elevated temperature only accounts for <0.7 % of conductivity increase.

3.2.10.4. Flow cell pressure management

Sealing the fluidic cell channels against evaporation using silicone barrier caps creates pressure in the fluidic channels approaching the thin silicon nitride (SiNx) nanopore membrane

(Figure 3.31). Silicone rubber provides an airtight seal, acting like a piston during insertion. Pressure rise above 0.26 atm (or capping force >0.7 N) is sufficient to push the cap out following insertion, while pressure rise above 2 atm is sufficient to burst the SiNx nanopore membrane. Norcada chips with 40 µm x 40 µm area and 10 µm thickness SiNx membranes have burst pressure of approximately 2 atm (per information from a representative in 2020). While a sealed fluidic cell should theoretically experience the same pressure rise on both sides of the membrane due to channel symmetry, in practice channels are filled and sealed sequentially, necessitating a pressure relief mechanism. Furthermore, temperature elevation in a heated system sealed against fluid losses must consider thermal expansion of material and fluids which ultimately contributes to additional pressure rise.

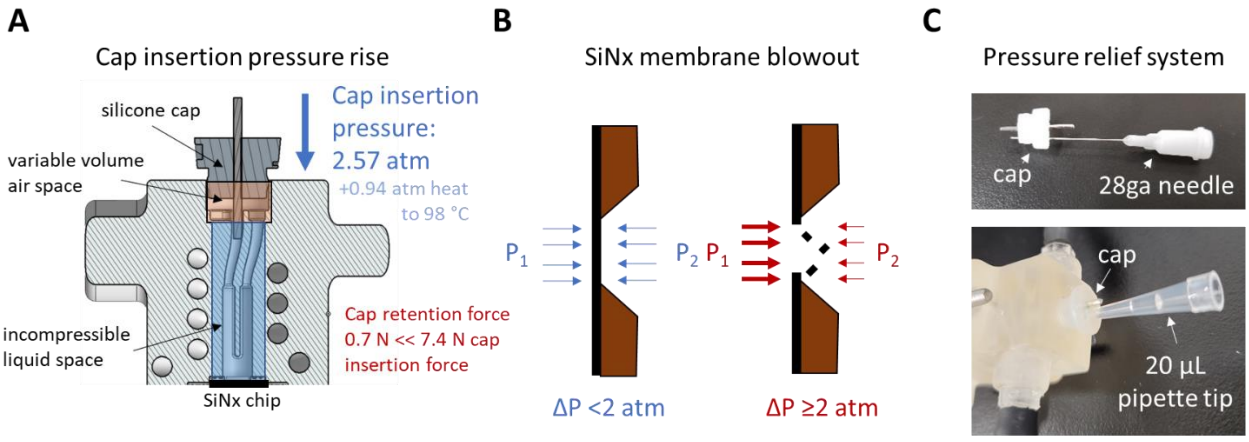

Figure 3.31. Fluidic cell sealing pressure relief. High cap insertion pressure prevents cap retention (A), and causes SiNx membrane blowout (B). Capping pressure was calculated using ideal gas law assumption and CAD geometry volumes. Membrane blowout and cap retention issues were confirmed observationally. Inexpensive pressure relief system consists of a small needle or a pipette tip (C) filled with an electrolyte solution plug to reduce internal evaporation.

A simple and inexpensive pressure relief scheme consists of a through hole in the cap in addition to the existing electrode hole (Figure 3.31 C). A needle or a pipette tip are placed within the hole to prevent electrolyte spillage on the external cap surface near the electrode connection junction. Active junction corrosion reactions adversely affect amplified current offsets during detection of pico-Ampere currents. An electrolyte solution plug within the pipette maintains an internal vapour pressure of water, reducing internal channel electrolyte evaporation.

3.3. Thermal Flow System

3.3.1. Temperature measurement

Fluidic cell temperatures are measured using a commercial optical thermometer system, while heat transfer fluid reservoir temperatures are measured using custom thermocouple circuits (Figure 3.32, Figure 3.34). Optical thermometer decouples external electromagnetic noise from the fluidic cell and the sensitive pre-amplifier circuit. Electrical decoupling is not required for other temperature-monitored flow system components, therefore significantly more cost-effective thermocouples are used for temperature feedback.

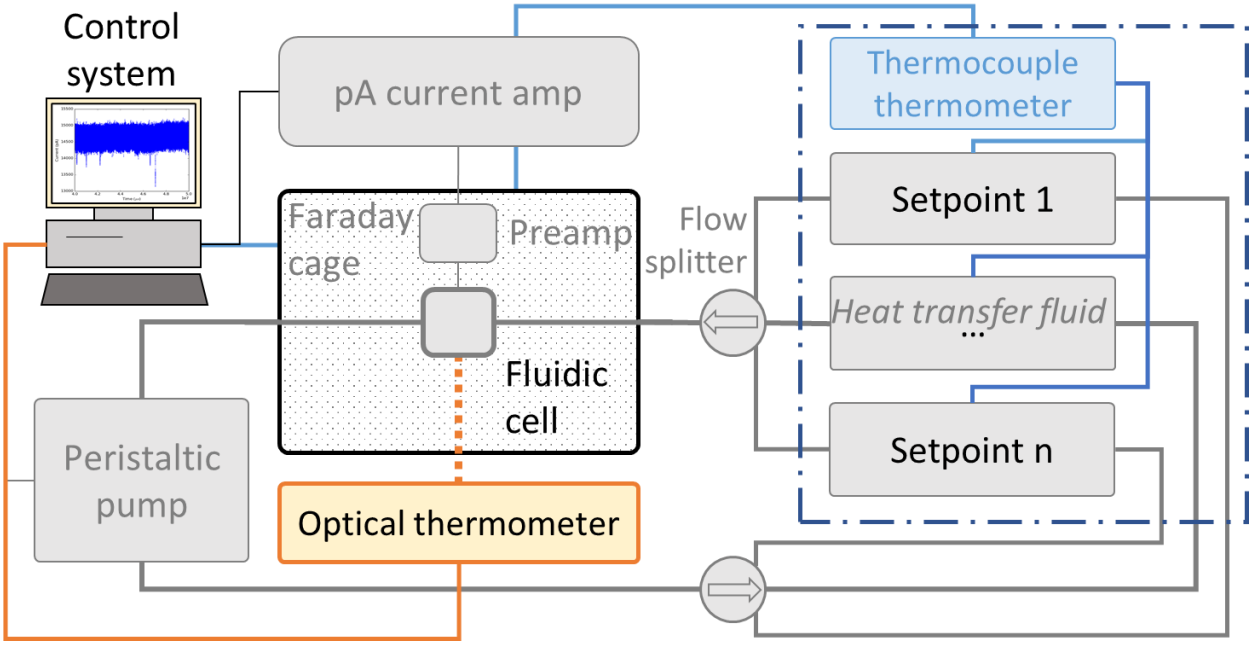

Figure 3.32. Temperature measurement systems in the instrument. Optical thermometer measures temperature within the fluidic cell's analyte channels in the vicinity of the nanopore chip, while thermocouple thermometers measure heat transfer fluid reservoir temperatures for feedback control.

While theoretically noise-free, optical thermometer systems placed in the vicinity of the nanopore membrane chip can introduce stray sensing currents from semiconductor substrate excitation (Si band gap ~1.1 eV [202]). Osensa FTX-200-LUX+, used in the current system, is a phosphorescence decay detector which uses a laser of specific wavelength to excite a phosphor crystal. Temperature-dependent light emission from the crystal is read back after excitation

ceases, with specific attention to decay time and intensity. The principles have been well described [299] and commercialized into a cost-effective package by several companies (Osensa, Advanced Energy, Optocon) for use in environments averse to metallic sensors (MRI machines, industrial power transformers). The main concern with commercial miniature optical probes is potential light leakage, which has been reported by most manufacturers contacted. Nanopore noise resulting from light leakage in the Osensa device is shown in Figure 3.33. While of low significance for a high-noise nanopore tested here, a low-noise nanopore usable for molecular experiments (pore with 10^{-1} – 10^{0} pA^2/Hz 1/f noise at +100 mV) will report false molecular events based on the low frequency spikes present. Of note, light leakage noise is reduced with increasing temperature which may be related to the shift in energy absorption spectrum of silicon toward higher photon energy excitation with temperature [300].

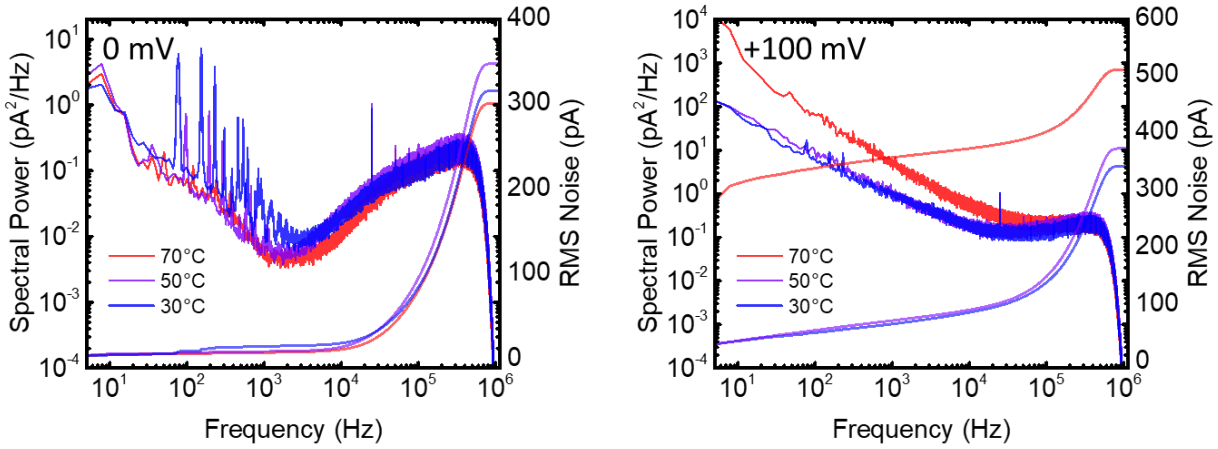

Figure 3.33. Optical temperature probe noise in a nanopore-containing fluidic cell. A noise PSD of an 8.5 nm pore in a SiNx membrane of 12 nm nominal thickness, in 3.6 M LiCl + 10 mM HEPES (pH8), is assessed at 0 and +100 mV at multiple temperatures. Shown is a high-noise nanopore that flagged the issue initially. Light leakage noise in the low frequency regime is significant and changes with temperature, therefore simple notch filters cannot be used to effectively remove the noise. While light leakage noise is not significant for this test pore at +100 mV sensing voltage, it would be for a usable low-noise nanopore (<1 pA^2/Hz under 100 Hz).

Light leakage is addressed by coating the probe in a thin layer of black polyurethane (PU) electronics potting compound (Loctite US2350) (Figure 3.34 A). First, open probe end is filled with neutral cure RTV silicone (Dow Corning 737) to tightly seal the phosphor crystal from the PU components. Once silicone is cured, the probe is dipped in a two-part PU compound. A black-

coloured, medium-hard (Shore 85A), chemically, electrically, and moisture-resistant coating significantly attenuates optical noise while adding only 0.1 – 0.2 mm thickness to the probe. PU is also in the upper range for thermal diffusivity for plastics, which should not significantly impede heat conduction from analyte solution to the probe.

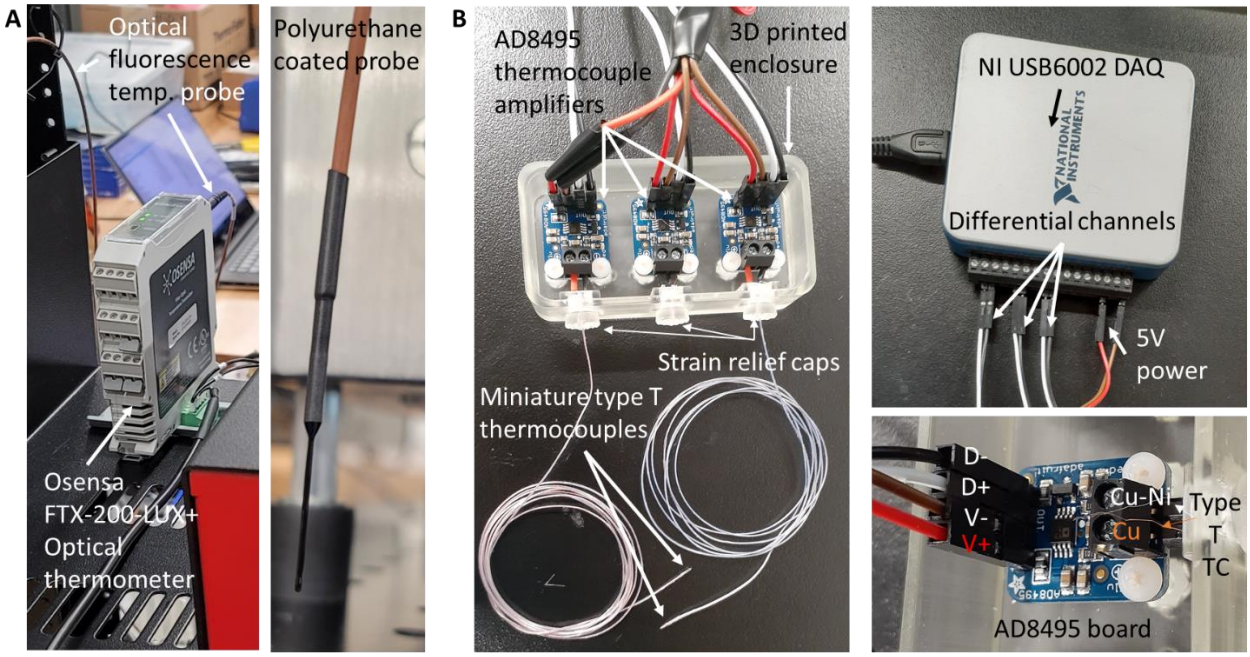

Figure 3.34. Thermometer systems. (A) Optical thermometer system (Osensa FTX-200-LUX+) consisting of the main device connected to a phosphor temperature sensor probe (PRB-400-02M-STM-20). Probe is coated in polyurethane (Loctite US2350) to significantly attenuate leakage of excitation light into the nanopore fluidic cell. (B) Thermocouple thermometer system consists of the AD8495 thermocouple amplifiers (Adafruit 1178) connected to miniature type T thermocouples (Omega Engineering 5TC-TT-T-30-36), and a NI USB6002 data acquisition system. Type T thermocouple is wired into the amplifier as shown (Cu, Cu-Ni connections), powered by a 5 V power source V+/V-, and read in differential mode from D+/D- connections.

Subsystems other than the fluidic cell within the Faraday enclosure do not require electromagnetic isolation and were implemented using an inexpensive custom-built thermocouple amplifier system (Figure 3.34 B). Reader is encouraged to explore the breadth of electrical and chemical thermometer systems in relevant reference literature [301], [302]. Thermocouple thermometers were chosen for their ease of implementation, cost effectiveness, and adequate measurement performance. With the constructed system, temperatures can be

measured to within 0.1 °C precision, 1 °C accuracy, and high bandwidth (~7 kHz) in the range of 0 to 100 °C. In practice, custom Python software limits data sampling closer to 1 kHz per multiplexed DAQ channel with a 20-point average for stable and reliable output. For further information, theoretical background and practical implementation of thermocouple circuits is well-described by academic [303], and industrial [304], [305] sources. A reference database for thermocouple electromotive force vs temperature is available as NIST ITS-90 standard [306].

3.3.2. Heat transfer fluids

Synthetic perfluoropolyether (PFPE) dielectric heat transfer fluid (Solvay Galden HT200) circulates within the fluidic heating system. It is a clear, chemically inert, non-combustible, highly electrically resistant (10^{15} Ω·cm) fluid with around three times the kinematic viscosity of water at equivalent temperatures (PFPE 2.72 cst vs. water 1 cst at 20 °C) [307]. Deionized water (DI) was the initial fluid of choice due to favourable thermal properties and cost considerations, but proved to have insufficient electrical resistivity ($18.2 \cdot 10^6$ Ω·cm), resulting in noise coupling into the nanopore system. Galden HT200 has thermal conductivity nine times lower than water, and thermal capacity four times lower than water, requiring higher flow rates for equivalent heat transfer. Recommended heating rate for HT200 is < 4 – 5 W/cm^2 for a high safety factor before fluid breaks down at approximately 14 W/cm^2. Heating beyond 200 °C upper limit for HT200 is highly frowned upon since resulting fluorinated breakdown products are bad for the general health of the researcher. Otherwise, PFPE are highly inert, safe, and compatible with a wide array of materials used in the current system (Stainless 304, 316, silicone, Viton, PC, PE, PS). The main disadvantage of PFPE is its cost which comes at 170 USD/kg, only around 330 times lower than a kilogram of gold. Approximately 4 kg of fluid is used in the system.

Other less expensive heat transfer fluids which the reader may be interested in exploring include silicone fluids (Dow SYLTHERM), mineral oils (MultiTherm IG-1), or other synthetic fluids (Eastman Therminon, Dow DOWTHERM, DuPoint Susterra). Fluids not designed for heat transfer but that may be applicable include vacuum pump oils (Solvay Fomblin, DuPont Krytox, Welch DirecTorr, Dekker Vacuum, JB Industries, etc.). A significant comparative advantage that PFPE HT

fluids have over other fluids is lower (> 2x) fluid viscosity at the required temperatures. Lower viscosity leads to lower pressure operation of the system which can facilitate the use of more compact and lower cost flow equipment. PFPE fluids also have comparatively lower vapour pressures, reducing evaporative losses from the system for long-term use. Environmentally-conscious PFPE disposal is however more challenging given the extreme chemical stability of the compounds under normal operating conditions.

3.3.3. Temperature control

3.3.3.1. Heating subsystem

Multiple temperature setpoint system, as opposed to a single flow-through heater, enable simple control and faster temperature ramp schemes for systems with large fluidic volumes and high thermal mass components (heater, tubing, pump) (Figure 3.35). An example rapid heating scheme involves using a higher temperature setpoint heater to bring the average cell temperature to the desired setpoint, then switching to the desired temperature setpoint heater. The step response scheme is sufficient for the initial temperature maintenance experiments planned using the system, requiring only two to three setpoints. In addition, limits on the recommended safe upper heating rate of the heat transfer fluid (< 7 W/cm^2, SF = 2) do not favour a single heater for rapid temperature ramping.

The main disadvantage of the multi-heater system is the cost of additional heaters, temperature controllers, and support structures when more thermal setpoints are required. However, modular system design ensures any type of heating system can be implemented at a later date to meet any new requirements. Off-the-shelf continuous fluid circulators (i.e. Julabo Forte HT) for variable temperature control can cost upward of 30,000 USD, and likely cost more to develop and test in house. A single temperature setpoint bath and associated components costs < 2500 USD (plus time to assemble). The requirement for heaters to not leach metal ions into the HT fluid to maintain high electrical resistivity places a significant limitation on the use of cheaper metal housing heating systems. Unpublished manufacturer material compatibility data

suggests metal can lose mass into Galden HT fluids at high temperatures (i.e. stainless steel, 0.02 % at 200 °C, 500 hrs). Current fluidic heater design is shown in Figure 3.36.

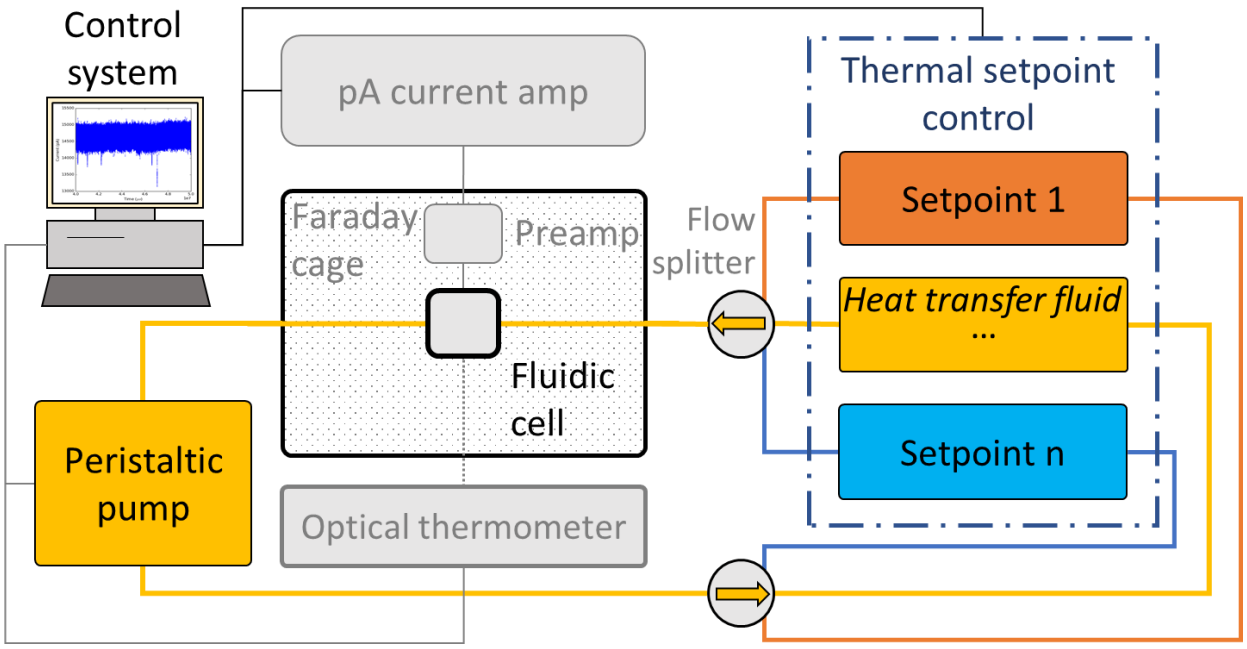

Figure 3.35. Heat transfer (HT) fluid flow distribution system. Multiple thermal setpoints can be set up to initiate step responses in fluidic cell temperatures, simplifying the control scheme and reducing the importance the thermal mass of the heating device. In addition, fluidically compatible glass/ceramic heating surfaces that do not leach metal ions into the HT fluid will not experience frequent thermal cycling that may significantly reduce their service life. Much cheaper components such as flow splitters, tubing, fittings, and the fluidic cell are easily replaceable in case of thermal fatigue failure, as well as routine maintenance schedules.

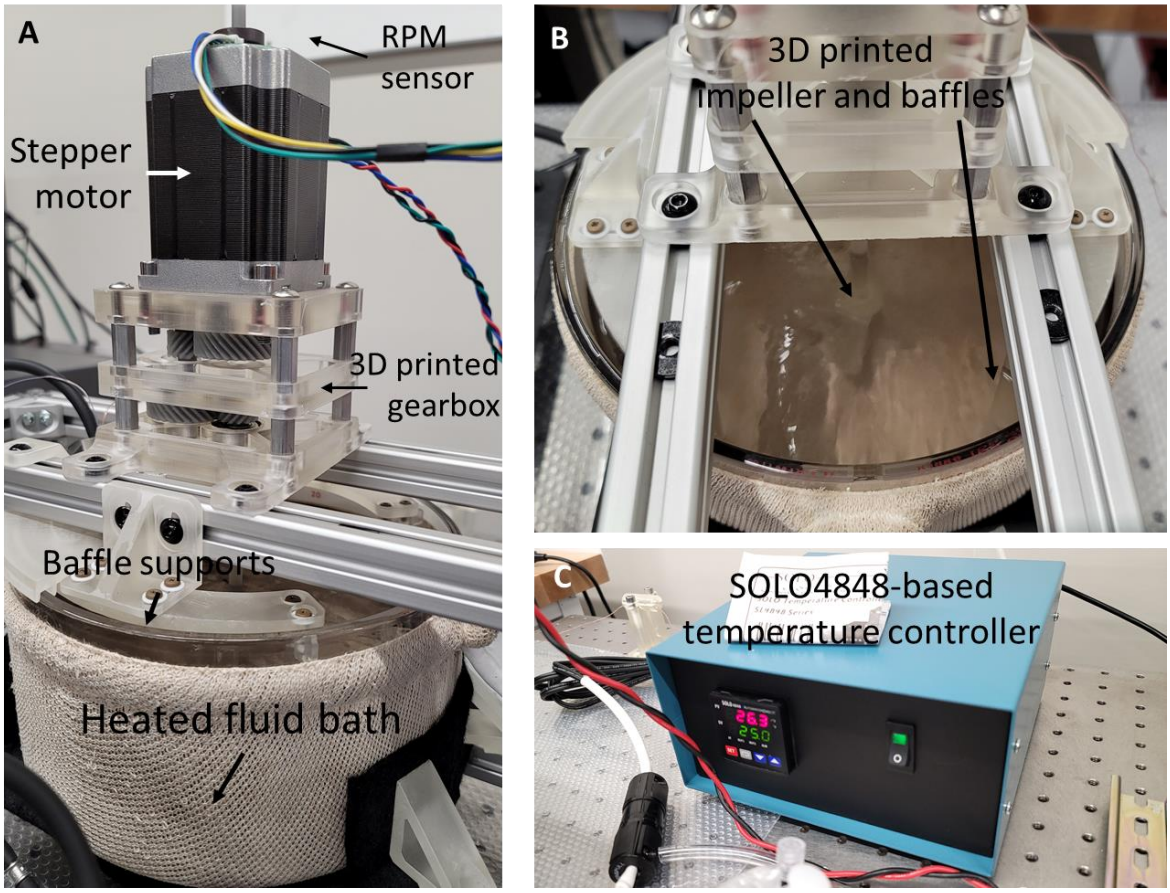

Figure 3.36. Heated fluid bath component overview. The subsystem consists of a heated glass fluid bath (Ace Glass Instatherm 9601-18) and a custom-built stirrer secured within a rigid T-slotted frame (A). Custom stirrer uses an inexpensive stepper motor system, 3D printed speed increaser gearbox, and 3D printed impeller and baffles to ensure uniform, safe, and efficient HT fluid heating (B). CSA-certified AutomationDirect SOLO4848-based temperature controller built by the University of Ottawa electronics shop provides automated temperature control tunable via a USB connection from PC. System provides up to 1200 W of PID-controlled heating power over the wide heater area of the bath, which covers both the initial transient (~750 W), as well as fluidic cell temperature maintenance requirements for up to 95 °C (~250 W) with a generous safety factor. Large heater area allows for safe (<7 W/cm^2, SF = 2) HT fluid heating**.** Appendix D – Elements of mixing fluid heater design – shows the idealized heater requirements curves.

Stirred hot tank design ensures safe and uniform HT fluid heating for precise control of fluidic cell temperature. Baffled volume with a pitched-blade impeller stirrer was designed and 3D printed in Formlabs High Temperature resin for the lack of compact and affordable commercial systems for the required design parameters. Reader can refer to a range of mixing reactor designs and mechanical design procedures in the chemical process design literature

[308]–[312]. Design practices for support structures and gearboxes can be found in the standard machine design literature [313], [314] and component manufacturer websites (McMaster-Carr, Misumi, NTN, SKF, KHK Gear, etc.).

3.3.3.2. Cooling subsystem

Cooling reservoir (Figure 3.37) provides ambient temperature HT fluid to the fluidic cell. The inexpensive implementation consists of a room temperature radiator circulating the fluid from the 'cold' HT fluid reservoir. The heat dissipation rate is typically low since the system is working with low temperature gradients even if convection coefficients and convective areas of the radiator are large. Under typical operating conditions, temperature gradients are under 5 °C and occur when hot flow is switched to a room temperature flow and around 50 mL of hot fluid mixes into the 1 L cold reservoir system. When more hot fluid is mixed into the system raising its temperature, heat dissipation is significantly lower than an equivalent water-based cooler due to the low thermal conductivity of the HT fluid combined with low fluid flow speeds within the radiator.

While this design most certainly needs optimization, the cooling system is presently sufficient for basic experimental applications that do not require rapid cycling between hot and cold setpoints. Cooling system can be significantly improved by integrating a compact Peltier cooling system to provide better heat dissipation and below-ambient temperature capability, i.e. Laird Thermal Systems SLA-400-24-02 liquid-to-air module (< 200 W at ΔT = 20 °C) or equivalent. The main disadvantage of a Peltier cooling system would be low efficiency, high power draw, high costs (> 1000 USD), and high dead volume of expensive HT fluid. Further information on heat exchanger analysis, design, and optimization is available from the following literature [209], [315]–[317].

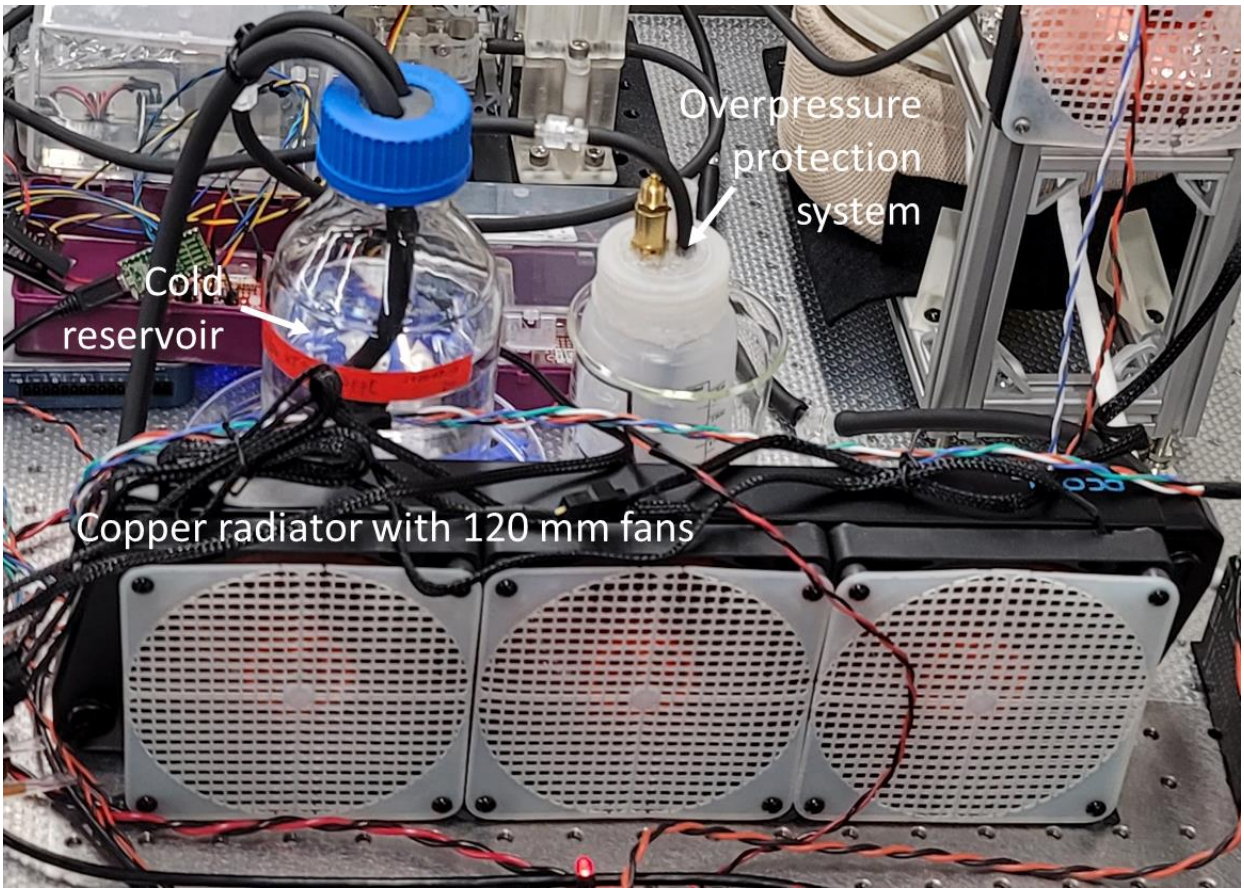

Figure 3.37. Room temperature circulator. Glass reservoir holds the room-temperature setpoint fluid, while a copper radiator from a computer watercooling system equalizes the fluid temperature with ambient room temperature. Cooling rate is variable, depending on the temperature of the incoming reservoir fluid which usually does not exceed 25 °C with alternating hot-cold switching every 5 minutes (time to ~99 % of setpoint).

3.3.4. Flow control system

3.3.4.1. Pump

The flow control system consists of the peristaltic pump and flow splitters connected to the fluidic cell and the temperature-controlled reservoirs (Figure 3.35). Peristaltic pump (Figure 3.38) maintains the HT fluid in a closed fluidic loop, simplifying design and maintenance of the system. Low volumetric flow rates with higher viscosity fluids in the system make positive displacement pumps (piston, gear, screw, peristaltic) more suitable than centrifugal pumps. Peristaltic pumps are particularly suitable, since they do not require complex and expensive high

temperature oil seals, instead relying on a single peristaltic tube that is trivial to monitor and replace with wear. Galden HT 200 fluid is too thin to be a machine lubricating oil. It is also hydrophobic which would facilitate its mixing with bearing and gasket oil films, which is undesired given its poor lubricating properties as well as eventual changes to heat transfer properties this could induce.

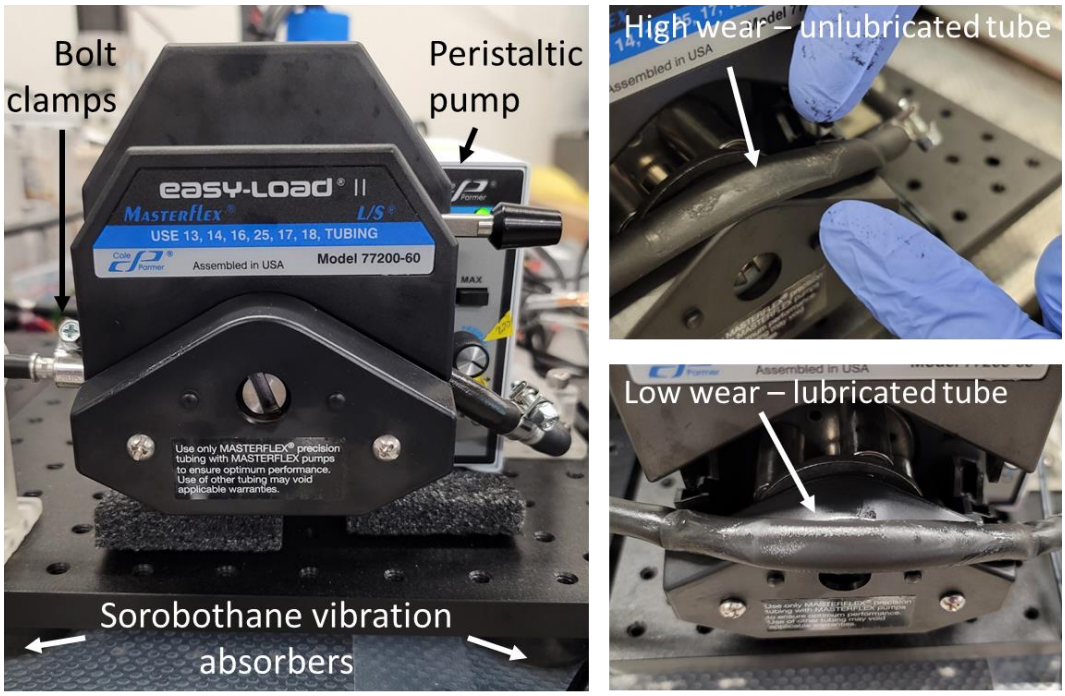

Figure 3.38. Peristaltic pump set-up. Stainless-steel roller peristaltic pump (Cole Parmer Masterflex L/S) provides high-temperature tolerant fluid displacement through the system at a constant, manually-set rate. Working tube (McMaster-Carr, high temperature Viton fluoroelastomer, 1/4" ID, 1/8" thick) is subject to wear over time with frequent temperature cycling. Silicone lubricant (Dow Corning High Vacuum Grease) extends usability from under 10 hours to months of use with re-lubrication. Pump manufacturer did not recommend tube lubrication, likely because it corrodes tube sales figures. Flow rate decreases by upward of 20 – 30 % over months of operation which was designed for and consistent with industrial reports (Section 3.2.7.3).

Steel roller peristaltic pump allows long-term high-temperature operation that would otherwise result in thermal deformation of plastic rollers typically used in such systems. The drawback is significantly increased heat conduction away from the HT fluid within the tube. As such, pump is placed downstream from the fluidic cell, drawing hot fluid through by negative

pressure gradient. An additional benefit of such arrangement is very low effect of the vibration resulting from the oscillating flow rate of the pump at the outlet on the fluidic cell located before the inlet. Tube compression by the roller at the pump inlet stores elastic compression energy which is released at the outlet, transiently accelerating the fluid.

Pulsatile flow at the outlet is reduced by a specific implementation of the overpressure protection system (Figure 3.39). Air within the HT fluid container of the overpressure system provides oscillatory flow damping, only triggering the overpressure valve when pressure exceeds ~105 kPa. Soft (Shore 60A) high temperature Viton fluoroelastomer tubing (McMaster-Carr) carrying the HT fluid provides additional viscoelastic dissipation. Other methods of addressing discontinuous flow include adjusting number of rollers and using multiple offset roller heads, which can result in rapid subsystem cost increases (> 3x).

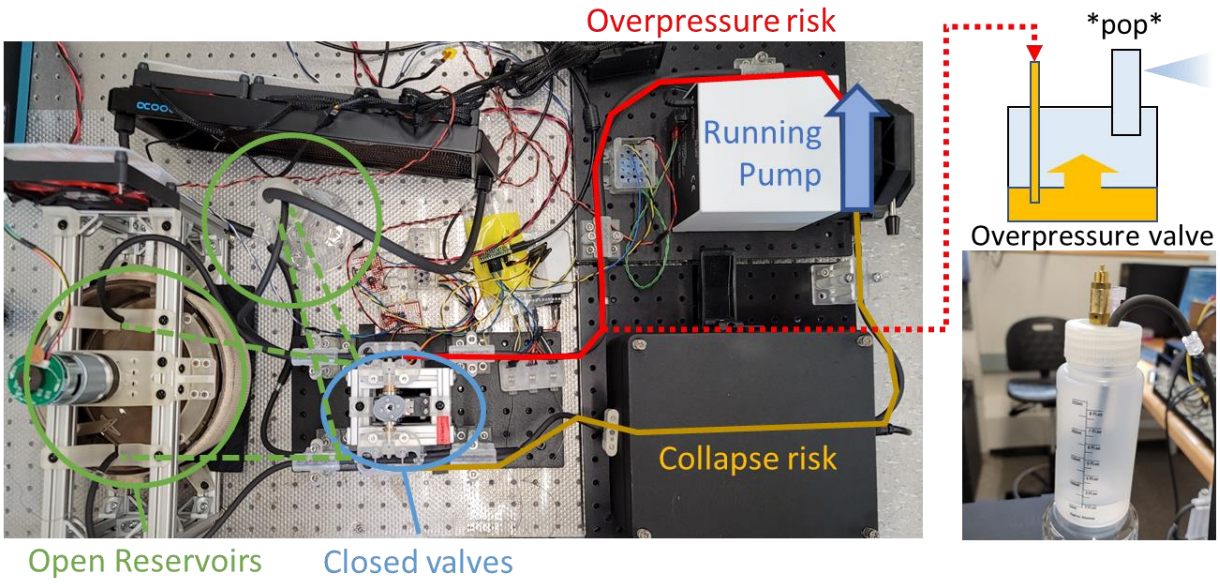

Figure 3.39. Overpressure protection system. In an accidental case where flow switching valves are closed while pump is running, forward direction pressure can unpredictably eject hot HT fluid into the environment through a failed fitting. Overpressure valve system provides immediate hardware protection and audible user notification (pop). Reverse direction is safe since it is drained of fluid and collapses, or draws cold air in. As an additional effect, air within the overpressure system acts as a pump outlet flow oscillation dampener.

3.3.4.2. Flow control valves

Flow splitters or flow control valves are responsible for directing flow between temperature-controlled reservoirs and the fluidic cell (Figure 3.40). Custom design was implemented for the dearth of affordable non-metallic commercial valves with low thermal mass, low heat conduction, and high operating temperature. Commercial isolation / pinch valves use pinch plunger materials that are likely to fail over 70 °C, requiring reinvention of the wheel. Designed valves can be considered pinch / isolation valves useful for a variety of tubes, compatible with temperatures up to 130 °C, and packaged into a stackable space-saving configuration. Appendix E – A few notes on pinch valve design – contains additional design-related details on the flow splitter.

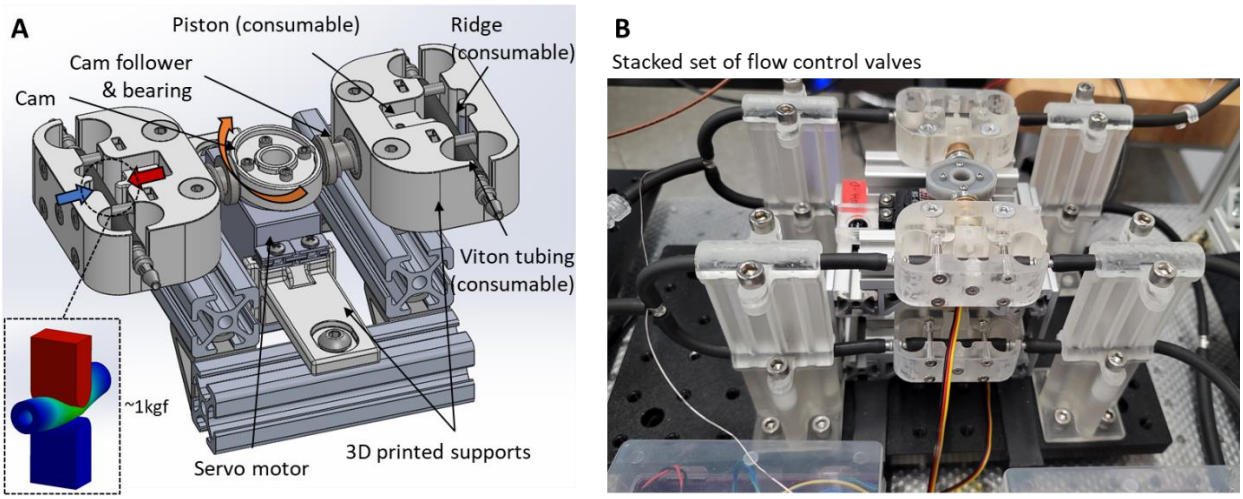

Figure 3.40. Flow control valves. HT fluid is directed between setpoint heaters using the flow control valves / flow splitters. The main principle is the symmetric pinching of both inflow and outflow tubes by cam-actuated pistons (A). Servo motor (Hitec HS-422) provides sufficient torque to pinch off the HT fluid flow in high temperature Viton fluoroelastomer tubing. Piston, ridge, and tube components are designed to be swappable high-temperature-compatible 3D print components to address eventual fatigue wear. Multiple flow control valves can be stacked (B), with Adafruit 815 PWM servo driver supporting up to 16 flow switches from a single controller.

3.3.5. Amplifier cooling

Heating the fluidic cell to a high temperature within the Faraday enclosure also heats up the internal air space, reducing the cooling of the pre-amplifier head stage. The original Chimera

VC100 Faraday cage is a sealed aluminum enclosure (Figure 3.41 A) that retains the internal temperature upward of 24 °C under normal operating conditions with main heat input from the pre-amplifier board (40 – 45 °C surface temperature). Fluidic cell and associated HT fluid tubing provide an additional heat source, with average cell surface and tubing temperatures rising close to 60 °C (measured), and contributing up to 9 W extra heat (FVA model) at 90 °C temperature setpoint. Pre-amplifier board positioned horizontally within the original enclosure is not optimum for heat dissipation, resulting temperature elevation beyond the expected range (< 50 °C). As such, the Faraday enclosure was redesigned (Figure 3.41 B) with the vertical re-orientation of the pre-amplifier, and inclusion of ventilation grating with effective electromagnetic shielding up to 1 MHz bandwidth required for nanopore sensing. The goal was to keep the pre-amplifier surface temperatures below 50 °C.

The ventilation grating provides sufficient air flow at the 90 °C fluidic cell heating setpoint for 1 hour to keep the pre-amplifier in the desired temperature range. The central pre-amplifier surface is at an average of 47.9 °C (SD 0.9, n = 3) while maintaining surrounding air temperature at an average of 32.0 °C (SD 0.7, n = 5). The temperatures are higher than predicted by the Solidworks finite volume model (41 °C central pre-amplifier surface, 26 °C air) since ventilation grating geometry was simplified with larger holes for the same total open area, while also eliminating the reflector sheet in the model. Further reductions in pre-amplifier temperature could likely be achieved by using high-absorptivity paint on the internal enclosure surfaces, and adding active external cooling. Gratings are dimensioned to accommodate standard 120 mm computer fans if required. Tubing and fluidic cell insulation with foams has been considered, but presents an impediment to the user friendliness and ease of maintenance criteria.

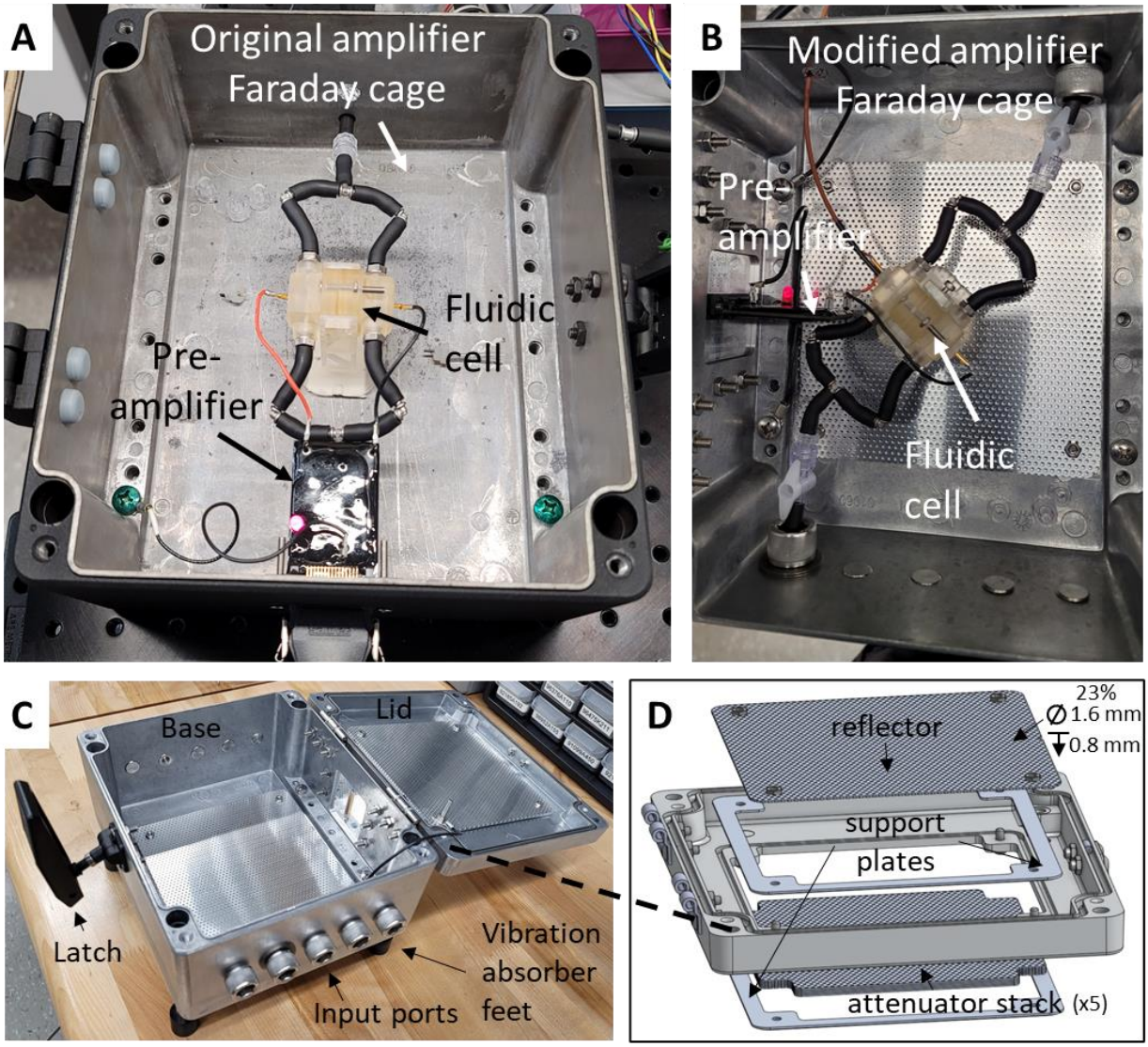

Figure 3.41. Faraday cage. Original Chimera VC100 Faraday cage enclosure (A) compared to redesigned enclosure (B). Both the base and the lid have been modified with ventilation grating (C). Component positioning flexibility has been extended by including input ports and interchangeable instrumentation connector. Ventilation grating is made from inexpensive perforated sheet metal, sufficient to facilitate air convection while attenuating and reflecting incoming electromagnetic interference (EMI) (D). Reflector and attenuator holes are staggered across a 1 mm gap, providing further EMI attenuation via reflection.

3.4. Noise Control

3.4.1. Electrical noise

Faraday cage enclosure blocks the propagation of external electromagnetic fields into the highly sensitive nanopore current amplification instrumentation (Figure 3.41). The inclusion of

ventilation gratings to manage internal heat warrants analysis of the grating aperture size that would provide high attenuation for external signals below 2.5 MHz cut-off frequency. A rule of thumb is that the cut-off wavelengths for an aperture should be less than 1/20th of the wavelength being blocked [318]. However, a better estimate can be made by considering that the grating is both a solid wall (electromagnetic wave reflector and attenuator), and a waveguide on account of aperture geometry [319], [320]. Simplifications from plane wave and waveguide theory can provide estimates for external signal attenuation, although assumptions of electrically thick materials with low intrinsic impedance have to be met:

$$Wall\ reflection, \qquad R_{wall} = 20 * \log \frac{\eta_0}{4\eta_{Al}} \qquad \text{Eq.3.45}$$

$$Wall\ absorption, \qquad A_{wall} = 20 * \log\left(\exp \frac{t}{\delta_{Al}}\right) \qquad \text{Eq.3.46}$$

$$Reduction\ in\ reflection\ effectiveness, \qquad S_r = 20 * \log\left|1 - \exp \frac{-2t}{\delta_{Al}}\right| \qquad \text{Eq.3.47}$$

$$Cylindrical\ waveguide\ attenuation,$$

$$A_{cyl} = 32 * \frac{t}{D}\sqrt{1 - \left(\frac{f}{f_c}\right)^2} - 10 * \log(\ n\ ) \qquad \text{Eq.3.48}$$

where η_0 is the intrinsic impedance of free space, η_{Al} is the intrinsic impedance of Aluminum, t is the material thickness, δ_{Al} is the skin depth of Aluminum at frequency f, n is the maximum number of material apertures lined up in straight line, D is the aperture diameter, and f_c is the specified cut-off frequency for the first electric field mode (TE_{10}). The simplifications taken do not consider the contribution from multiple wave modes and directions, instead assuming a plane wave.

Computing the waveguide relation to find aperture diameter that attenuates a 1 MHz waveform (highest sampled frequency) by 120 dB with a cut-off frequency of 2.5 MHz results in <0.97 mm aperture requirement. Producing custom gratings with these dimensions was financially impractical, therefore commercially available and affordable Aluminum perforated sheets with 1.6 mm hole diameters (McMaster-Carr 9232T311) were acquired for the initial prototype and stacked to the required thickness (Figure 3.41 D). Stacked material is thick enough

to provide > 400 dB theoretical solid wall attenuation. The limiting factor is 1.6 mm aperture diameter, resulting in approximately 60 dB expected theoretical attenuation when lined up as a grid. This was addressed by placing a staggered aperture reflector sheet in front of the attenuator across a 1 mm gap to facilitate backward reflection of already attenuated waves, and further attenuation from the gap itself (Figure 3.41 D, Figure 3.42). The original VC100 enclosure has several loosely shielded openings of up to 10 mm wide, producing theoretical attenuation of 30 dB, therefore it was expected that the modified enclosure would perform on par or better.

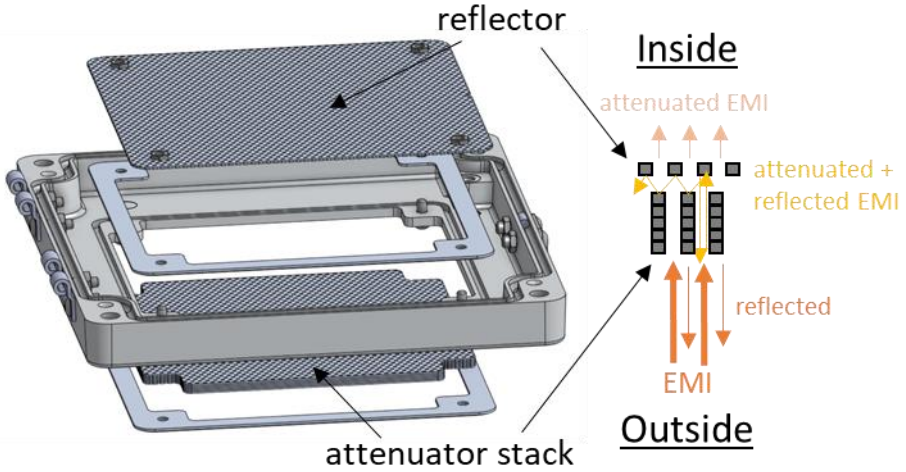

Figure 3.42. Attenuator-reflector configuration of the amplifier enclosure convection grating. CAD model and schematic of the attenuator-reflector stack designed to reduce the propagation of electromagnetic waves/interference (EMI) under 1 MHz frequency into the enclosure while still providing air flow for enclosure cooling. Externally-facing grounded perforated metal stack provides external wave reflection, and wave attenuation through the holes. Internally facing grounded metal reflector sheet has staggered holes, resulting in reflection of incoming EM waves, as well as further attenuation of scattered EM waves within the gap.

Enclosures were compared experimentally using test dummy cells of varying resistances (20 – 100 MΩ) and capacitances (10 – 200 pF) to emulate nanopores of difference sizes and material capacitance levels expected in practice. Figure 3.43 shows no significant differences in 1 MHz combined root-mean-square (RMS) noise between the enclosures across multiple trials. When enclosures were tested using a SiNx chip, ambient room light coming through the convective grating was found to have significant noise contribution for the MVPT enclosure

(Figure 3.44). Optical occlusion of light using an elevated foam cover was effective at eliminating the light-induced noise.

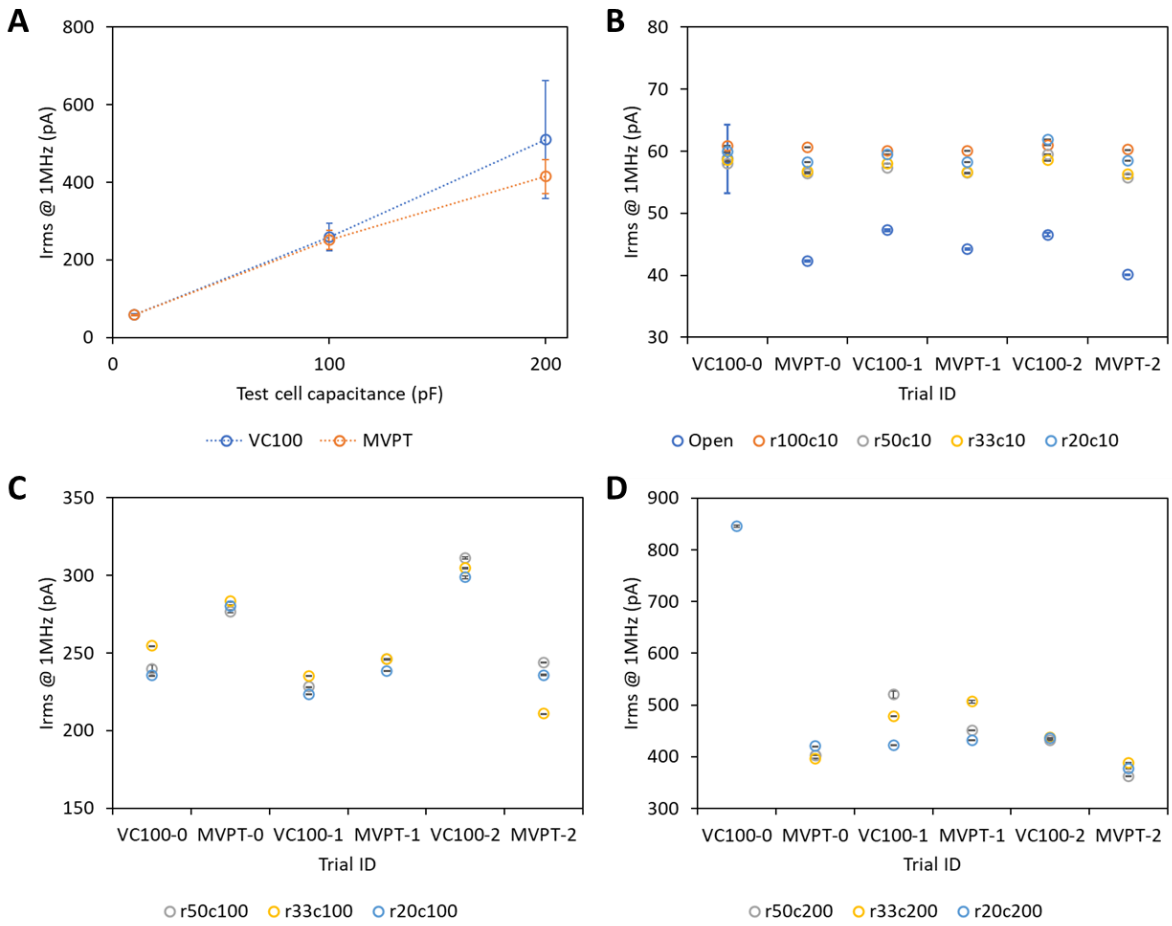

Figure 3.43. Comparison of enclosure noise performance. Average root-mean-square (RMS) noise at 1 MHz compared across all test cells between Chimera VC100 default enclosure and the re-designed MVPT enclosure (A). Test cells are described as *rXcY*, where *X* is resistance in MΩ, *Y* is capacitance in pF. No significant differences in overall noise readings across both enclosures were observed. High noise variability is seen for high capacitance test cells since Chimera amplifier does not guarantee signal stability above 100 pF capacitive load. No significant differences in combined RMS noise are observed across three amplifier trials in each enclosure using different test cells (open/no load and 10 pF in B, 100 pF in C, 200 pF in D). 200 pF test cells have highest variability and exhibited instability (i.e. VC100-0 trial). RMS noise was assessed by reading each test cell current in random order for 30s at 100 mV.

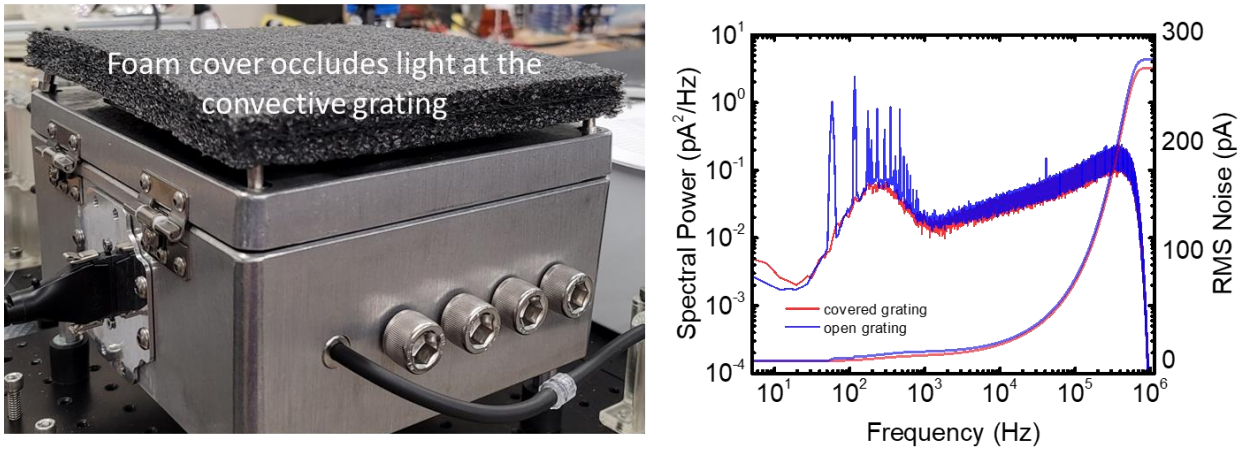

Figure 3.44. SiNx nanopore electrical noise from ambient room light. Ambient light entering the enclosure via the ventilation grating produced significant low frequency noise current spikes on a PSD for a 12 nm nominal thickness SiNx membrane on a Si backbone, assessed at 0 mV in 3.6M LiCl + 10 mM HEPES, pH8 electrolyte. The noise hump in the 10^2 – 10^3 Hz range is related to the use of high capacitance (190 pF) chip with the Chimera amplifier, and not the light source. A simple non-conductive foam cover on standoffs is effective at preventing a significant portion of external ambient light from entering the enclosure via the convective grating in the lid.

The electrical noise contribution of each of the instrument's high-current and high-noise subsystems was evaluated by activating them in turn while collecting RMS noise data from the amplifier, dummy test cells, and a low-capacitance nanopore chip (Figure 3.45). System controller activation, which is required for all other subsystems to function, contributed the most noise (< 3%). Other externally noisy subsystems (stirrer, pump, and heater) had negligible noise contributions. System controller is a microcontroller board (PJRC Teensy 4.0, ARM Cortex-M7) that interfaces to instrument subsystems and controls the extent of their activity. Unlike other subsystems, this controller connects to a computer via a USB cable that may share an internal ground connection to the USB cable of the nanopore signal amplifier. It is likely ground noise from the system controller and several non-optically coupled subsystems propagates into the amplifier. Fortunately, additional noise level is very low to warrant inductively or optically coupled USB connections, or complete opto-coupling of every controller pin to the subsystems. Currently the high-noise stirrer and pump subsystems are isolated via optocouplers (controller inputs) and mechanical relays (controller outputs).

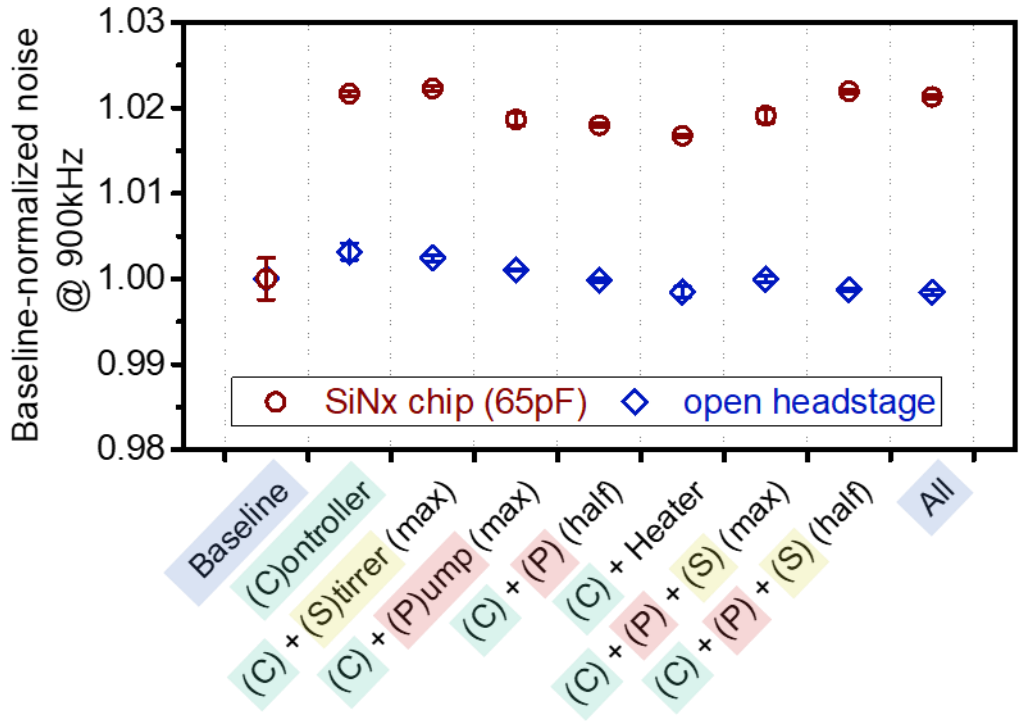

Figure 3.45. Electrical noise contribution from active subsystems. General system controller activation contributes < 3% increase in RMS noise of the system at 900 kHz when used with a low-capacitance SiNx chip. Noise magnitude was +240 pArms, with extra +7 pArms coming from control activation. Controller activation is required for other subsystems to function. Stirrer, pump, and heater are the main external noise-producing systems, effect of which is negligible within the enclosure. Noisy subsystems are electrically decoupled from the system controller using optocouplers and relays.

3.4.2. Mechanical noise

Mechanical noise isolation of the sensing systems is presently achieved globally using a vibration isolation table (Newport Vision IsoStation), and locally at component-level using optical breadboards (Thorlabs MB1012) with sorbothane vibration absorbers (Thorlabs AV5). Vibration isolation table is designed to provide high isolation of frequencies in the dominant 10 – 50 Hz range of both horizontal and vertical floor vibrations. Rated resonant frequency is ~1.5 Hz with a fairly low resonance gain (6 – 9 dB). Vibration power rejection of >30 dB for >10 Hz (20 – 30 dB/dec) ensures external floor vibration is effectively isolated from the system. Optical breadboards with foam inserts and sorbothane feet provide a secondary level of component isolation (Figure 3.46), particularly important when using a pump. Pump-related low frequency noise power is 10^{-2} pA^2/Hz at 10 Hz and 10^{-3} pA^2/Hz at 100 Hz which is at least an order of

magnitude lower than a usable low-noise SiNx nanopore (10^{-1} to 10^{0} pA^2/Hz at 10 Hz). Isolation can be optimized by using Thorlabs AV3 isolators if required.

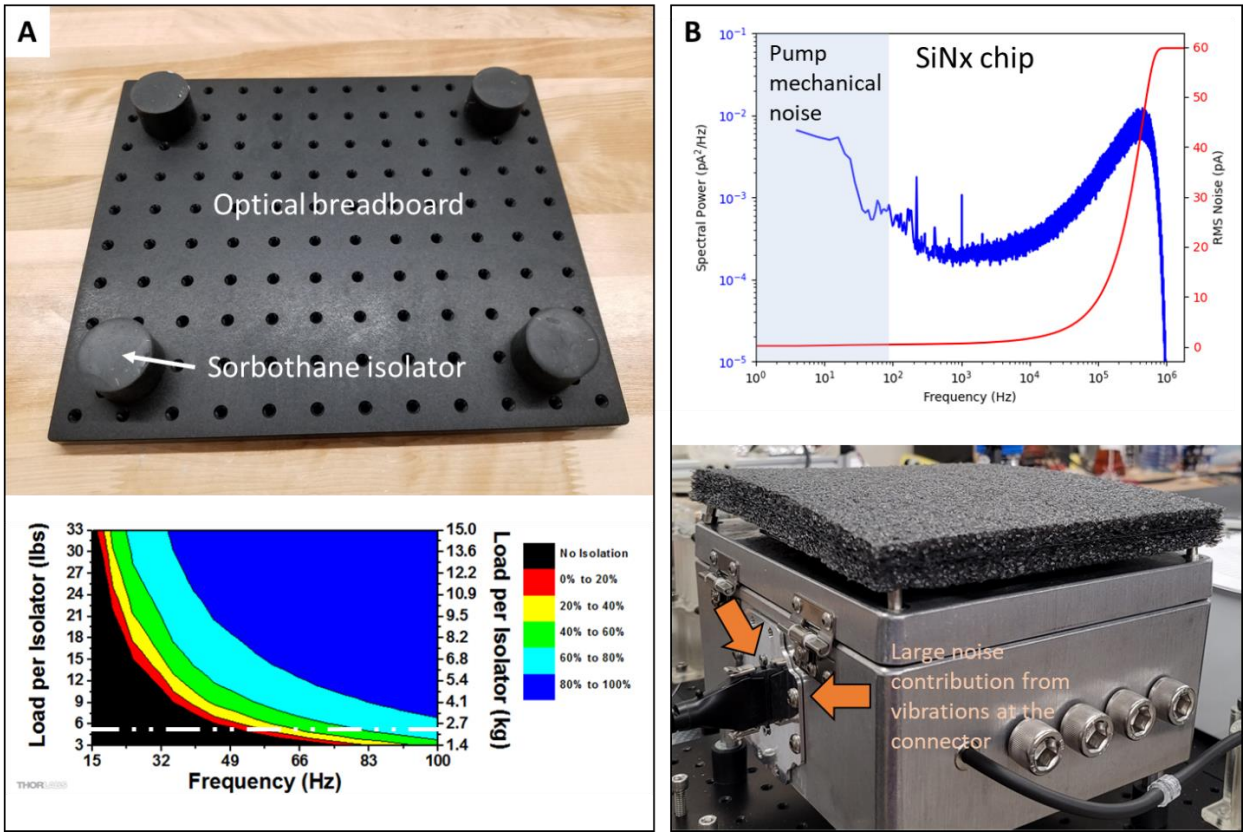

Figure 3.46. Mechanical noise isolation on component level. Optical breadboards (Thorlabs MB1012) with sorbothane damping feet (Thorlabs AV5) (A) provide modest vibration damping of the pump and enclosure at frequencies above 55 Hz (B). Dash-dot line on the isolation effectiveness plot **[321]** shows the load per isolator for the fluidic cell enclosure. Isolation can be optimized using AV3 isolators with > 80% vibration rejection > 30 Hz in this load range, but AV5 were free, readily available, and sufficient for current needs (> 1 order of magnitude above usable SiNx nanopore 1/f noise). Fully securing the external amplifier connector is by far the most important isolation strategy, since motion at the connection introduces a large portion of the noise.

3.5. Instrument performance

3.5.1. Instrument thermal performance

Thermal performance of the system was evaluated by running thermal step response trials for the entire thermal range of the system from ambient room temperature (21 °C) to 95 °C. A step response trial involves a step change in the controller output, while evaluating the change

in the process variable (PV) (Figure 3.47). Basic parameters of interest for the PV include initial state, dead time, time constant, and final state. During a step response, PV changes from initial to final state. The time it takes for PV to start responding to a controller step is dead time. Assuming a first order response, time constant is the time it takes for approximately 63 % change in PV. It takes approximately five time constants to bring PV to 99 % of final steady state value.

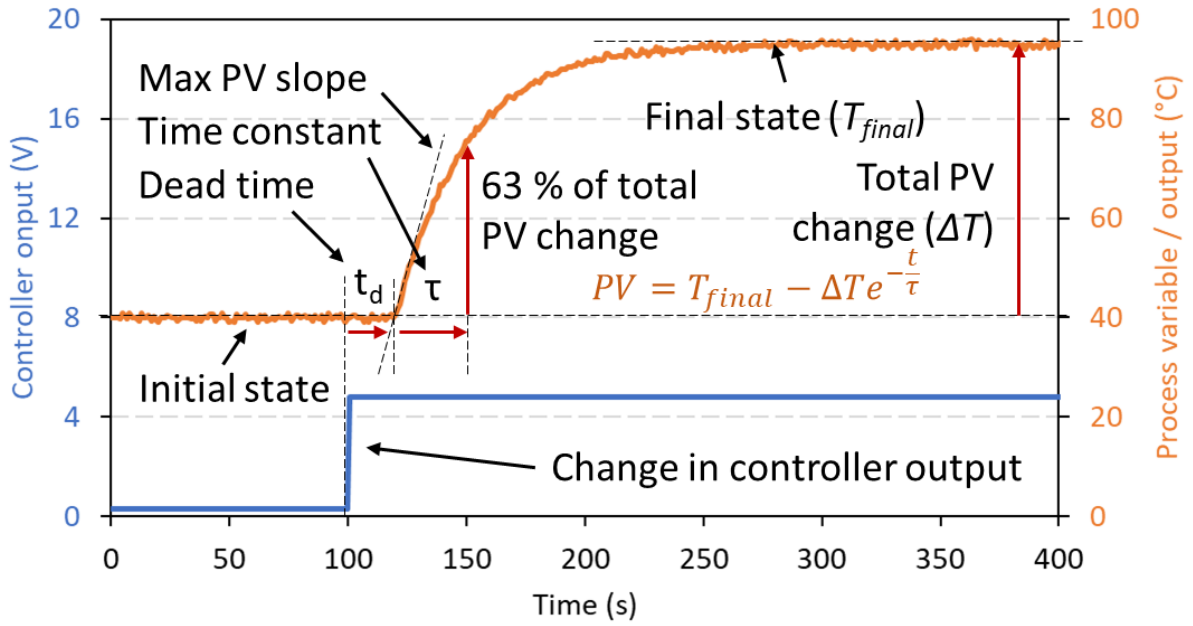

Figure 3.47. Step response parameters. In this illustrative example, change in controller output results in an exponential relaxation in process output after a dead time period. Step response curves allow time constant approximation to produce a predictive model of system response.

Additional parameters of interest are temperature measurement precision, repeatability of temperature control across multiple independent experiments, and temperature drift during each experiment. Temperature measurement precision specifies the random variation in the thermometer reading over time. Temperature control repeatability specifies how well the controller maintains requested temperature for each experiment. Temperature drift specifies how well the controller maintains requested temperature during the experiment.

An example step response curve for the system is shown in Figure 3.48. The heat transfer fluid is pumped from the hot reservoir through the fluidic cell initially at ambient room temperature, while the internal cell analyte fluid temperature is measured. Parameters averaged

from 20 step response curves across 8 different temperatures in the range from 21 °C to 95 °C are shown in Table 3.7. Time to attain what is considered thermal equilibrium (99% steady value) is under 5 minutes (τ < 60s), which is on par with other nanopore thermal system studies reporting thermal equilibration time (5 to 20 min). Measurement precision (<0.2 °C) is sufficient for general biological applications, and drift is low (<0.03 °C/min). Open-loop repeatability of measurements between experiments for a particular temperature is within 1.25 °C (95% confidence interval). For majority of cases, using a simple linear polynomial estimate of temperature loss at the fluidic cell (Figure 3.49 D) produces excellent thermal control (open loop at the fluidic cell). Using a secondary level of slow Proportional-Integral (PI) control within the Python control software is recommended for more accurate control (closed loop at the fluidic cell). This control uses readings from the cell's more accurate optical thermometer to nudge HT fluid temperature. The main downside of this control is that optical thermal probe failure could result in thermal runaway due to erroneous readings, which is why this mode should only ever be used with direct system supervision by the researcher. The primary hot bath hardware controller is more robust in that it has a failsafe in case of a thermocouple failure, shutting down the heating system.

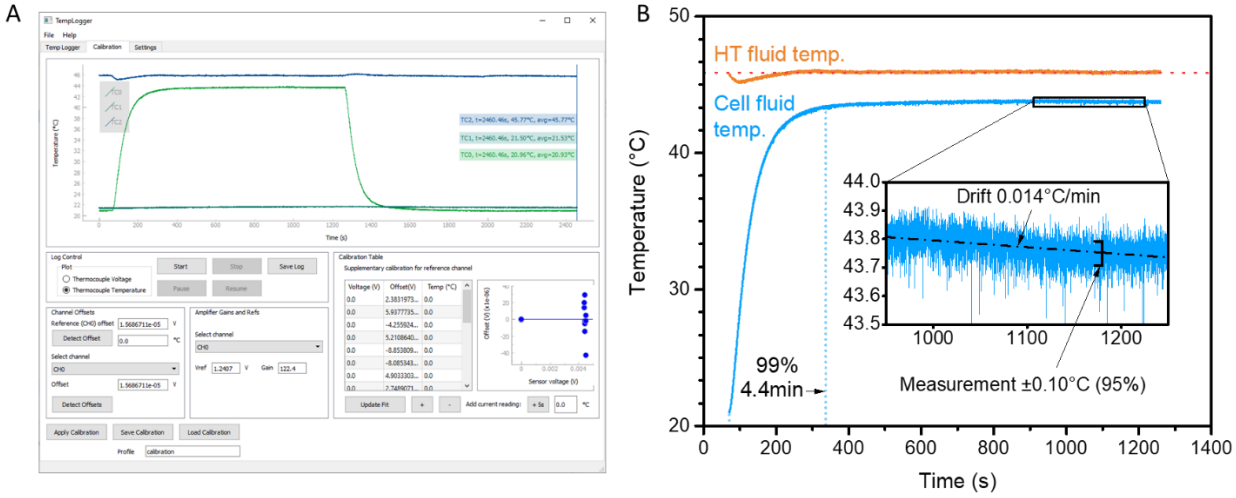

Figure 3.48. Example system step response curve. (A) Temperature logger software output showing the entire curve. (B) Curve data processed in Python to determine parameters of interest. Analysis methods are described in Appendix F – Analysis of thermal step response data.

Table 3.7. Average thermal characteristics at the fluidic cell analyte in the vicinity of the nanopore chip.

Measurement precision*	±0.16 °C (95% CI)	**Time constant***	53.2s (±5.3s, 95% CI)
Thermal repeatability*	±1.25 °C (95% CI)	**Dead time***	11.4s (±2.2s, 95% CI)
Average drift*	< 0.03 °C/min	**Thermal range**	room to 95 °C

* parameters obtained from 20 thermal step response curves at 8 different temperatures

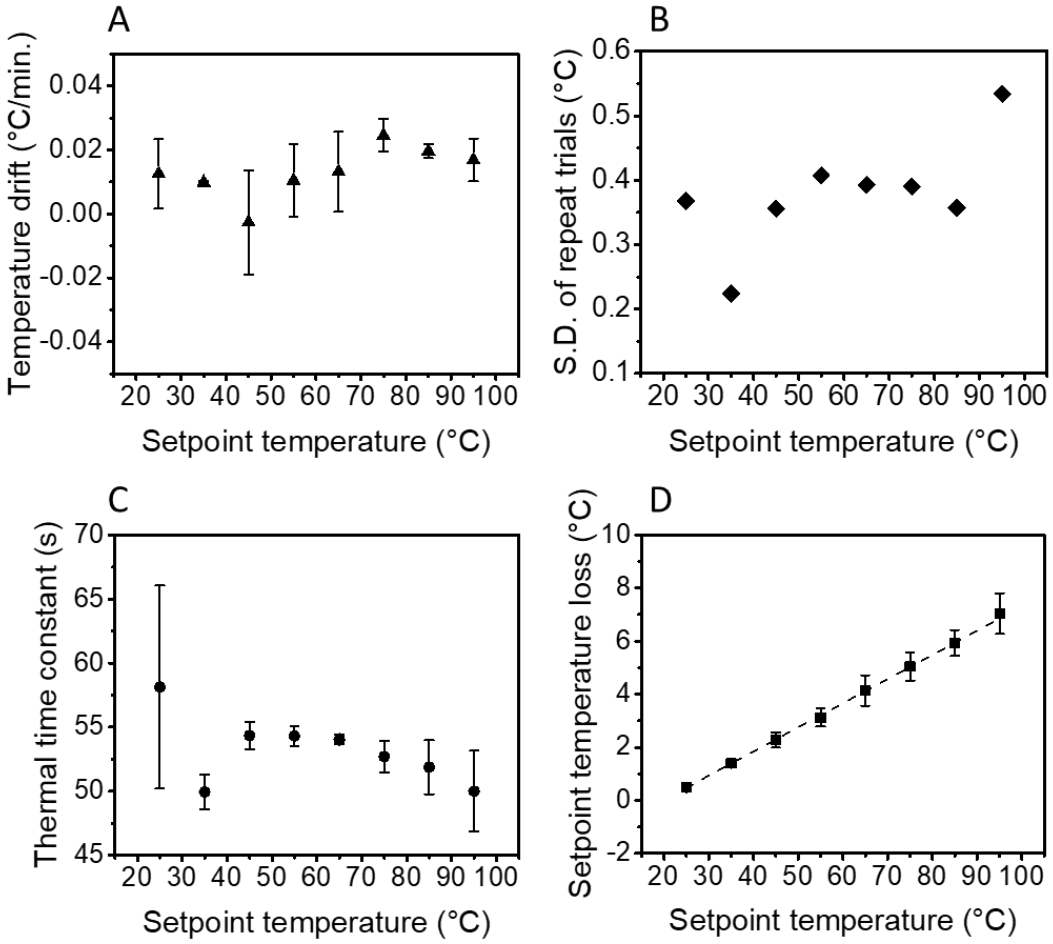

Figure 3.49. System response parameter variation with temperature. Temperature drift is low (A). Open-loop repeat trial variation is low (B). Thermal time constant is on average <60 s (C). System warm-up may have been skipped in the initial 25 °C trial, resulting in a skewed average and high variance for thermal time constant. Temperature loss at the fluidic cell is linear with hot setpoint temperature (D) and has reliably been used to set fluidic cell temperatures without closed-loop control at the fluidic cell.

3.5.2. Nanopore sensor performance

Nanopores that met size and molecular sensing requirements (<10 nm diameter, $<5 \cdot 10^1$ pA^2/Hz noise PSD scale from 1 to 100 Hz at ±100 mV in 3.6M LiCl + 10 mM HEPES, pH8, passing double-stranded DNA with at least 0.5 Hz rate) were used to quantify sensing performance with temperature. Small diameter pores were required since Chimera VC100 amplifier saturation current is 18 – 20 nA, which is rapidly reached with electrolyte temperature elevation. Performance was tested to 70 °C due to current saturation and high likelihood of SiNx pore instability above the temperature. Instability manifests as changes in pore conductance (increase, decrease, or loss) within 30 minutes of being brought to the temperature setpoint.

A total of 3 out of 12 nanopores fabricated in 10 – 15 nm nominal thickness SiNx membranes could be properly characterized since they met the RMS noise requirements, did not irreversibly clog during the DNA translocation test, and did not irreversibly lose stability up to 70 °C. Pore currents increased with voltage and stayed linear across temperatures (Figure 3.50). Current-voltage (I-V) linearity was expected since pore current is largely driven by changes in solution conductivity which is linear for *LiCl* in the ±200 mV range [43]. Current was also expected to be linear with temperature as characterized by linearity of electrolyte conductivity with temperature (Figure 3.25). Interestingly, current-temperature (I-T) linearity was lost in all SiNx pores tested following the approximate 50 °C threshold. Nanopore current increase has been attributed to enhanced SiNx nanopore growth rate at elevated temperatures.

Electrochemical dissolution of silicon in alkaline solutions at room temperature is a well-known phenomenon that can induce unwanted nanopore growth over time [49]–[51]. While dissolution time scale is on the order of days, temperature elevation increases material dissolution rate [49]. Dissolution rate is also dependent on solution-exposed surface area, which is expected to be larger for larger silicon particles. As such, exponential-like nanopore growth rate behaviour is expected with temperature elevation, and larger nanopores are expected to grow faster.

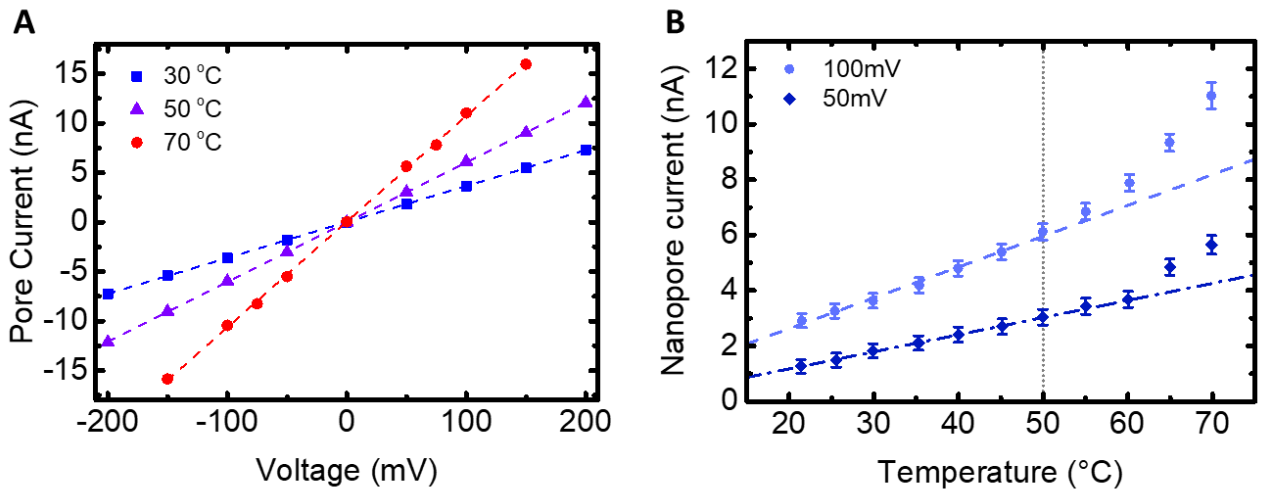

Figure 3.50. Nanopore current-voltage (IV) and current-temperature (IT) curves. (A) Sample IV curves for a 9.2 nm nanopore fabricated in 12 nm nominal thickness SiNx membrane taken in 3.6 M LiCl + 10 mM HEPES, pH8 solution. IV curves remain linear across the tested temperature range (21 °C to 70 °C). (B) Sample IT curves for the same nanopore show linear trends until at least 50 °C. Increasing nanopore growth rate at elevated temperatures is likely an important contributor to current increase.

Average growth rates for the calculated diameters of three additional nanopores are shown in Figure 3.51. While material hydrolysis may be a possible mechanism based on exponential-like growth rate increase with temperature for two of the pores (Pore 15 and 17), other growth mechanisms may be involved as evidenced by a more linear growth rate of one of the pores (Pore 18). A larger experimental sample of SiNx nanopores is required to elucidate the growth rate trends and comment on the effects of initial pore size on pore growth. We could speculate that slow pore growth at lower temperatures may not be a very significant issue for larger nanopores in excess of molecular size. Molecular detection is achieved by examining current blockages as opposed to absolute nanopore current. Current blockages should remain relatively constant at the same temperature, particularly for larger pores with fewer surface interactions. The main concern is pore growth affecting current baseline that is used for relative measurements and normalization of results between different pores.

Pore growth and instability at elevated temperatures has not been reported in the literature using SiNx membranes [41]–[45], therefore it is currently unknown if the issue is extensive or only limited to the batch of SiNx membrane chips used during the current

experiments (Norcada NBPX5005Z-AO/O-HR, L05026-03). One strategy that can potentially help address batch variability is membrane treatment with coatings. Hafnium dioxide (HfO_2) deposition has been used in our lab (unpublished data) to significantly reduce SiNx pore growth effects at ambient temperature, and could be trialed for nanopores at elevated temperatures.

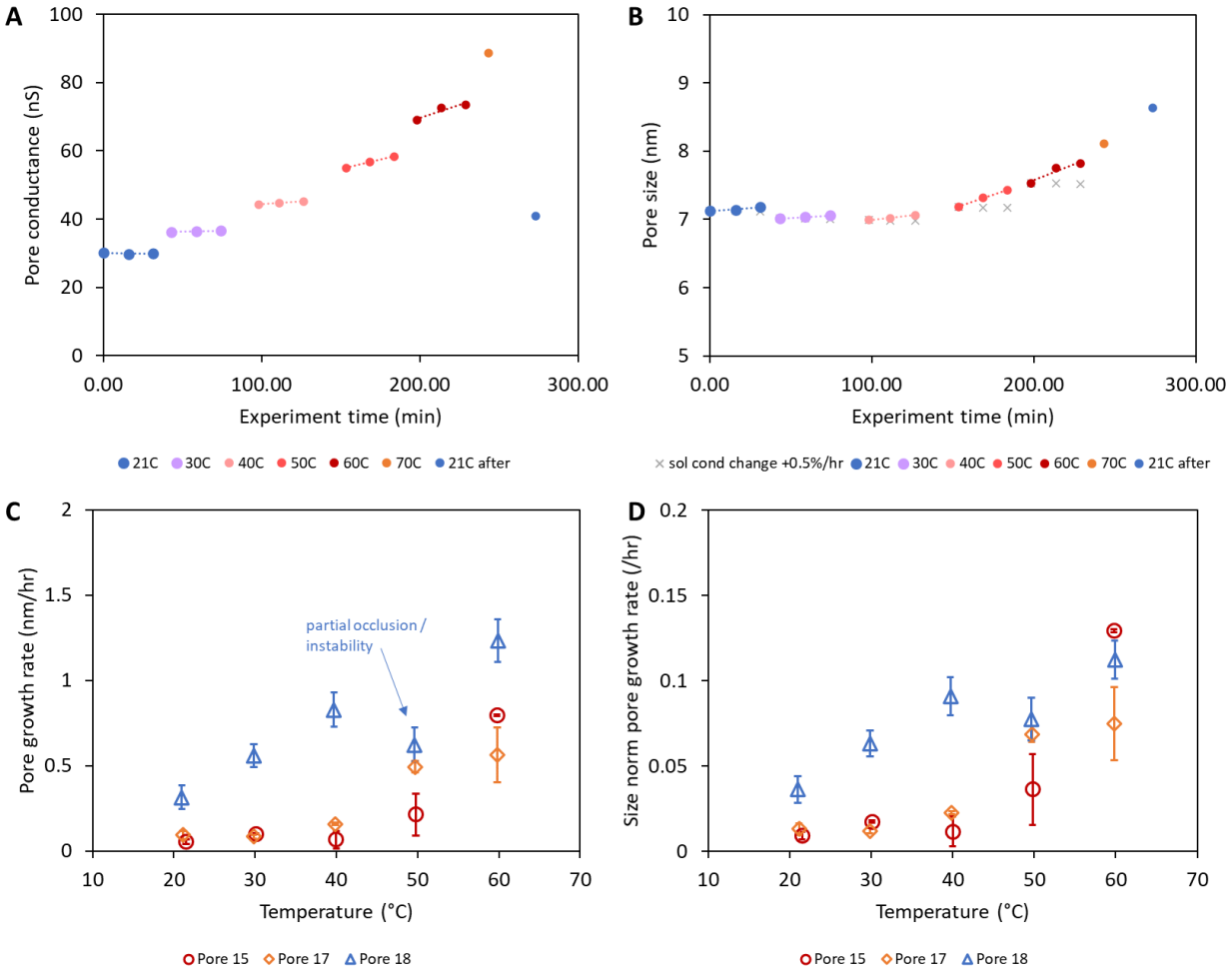

Figure 3.51. SiNx nanopore growth with temperature. Nanopore conductance with temperature (A) can be adjusted by electrolyte solution conductivity with temperature to estimate nanopore diameter using Eq.2.1 (B). Pore conductance was computed from the slope of a 9-point IV curve at each time point. Nanopore in (B) is initially 7 nm diameter in 12 nm nominal thickness SiNx, in 3.6M LiCl + 10mM HEPES, pH8. Ambient temperature measurements (B, initial and final data points in blue) show calculated pore grew to 8.6 nm during the experiment. Average growth rate for the calculated diameter of tested pores tends to increase with temperature (C, D). Pore 15 has an initial calculated diameter of 5.8 nm, Pore 17 – 7.1 nm, and Pore 18 – 8.7 nm. Size-normalization in (D) is done by the pore size during the measurement time interval.

While SiNx pore growth remains a roadbloack in the current work, a promising result not previously reported for nanopores at elevated temperatures relates to their RMS noise. Nanopore RMS noise in the low frequency range increases with temperature largely in proportion to current-squared (Figure 3.52). This result confirms expectations from nanopore noise theory that places low frequency flicker noise in current-squared dependence (Eq.2.8). Conversely, current-normalized metrics, such as the L-value (Eq.2.15), can be used to compare low frequency noise quality of different SiNx nanopores at different temperatures.

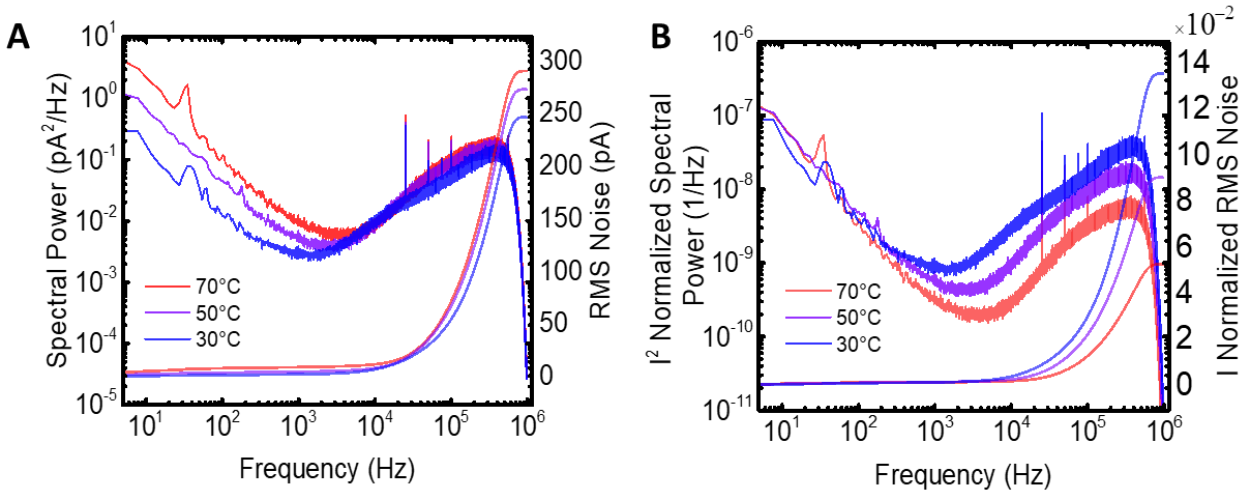

Figure 3.52. Nanopore noise at different temperatures. Sample PSD plots for a 9.2 nm nanopore fabricated in 12 nm nominal thickness SiNx membrane, monitored in 3.6 M LiCl + 10 mM HEPES, pH8, at +50 mV. Regular PSD plots in (A), current-normalized PSD plots in (B). Low frequency spectrum is confirmed to be largely scaled by square of the nanopore current, confirming nanopore noise theory and supporting the use of current-normalized pore comparison metrics across different temperatures.

3.5.3. Performance review

The constructed instrument achieves most of the requirements outlined in Table 3.1 and Table 3.2. Nanopore fluidic cells with 25 and 50 µL analyte volumes can be safely operated in a range from ambient (~20 °C) to 95 °C, with the possibility to extend operation into other temperature ranges by upgrading the fluidic heater and cooler setups. Current heating scheme provides steady state temperature precision to within ±0.16 °C, and open-loop repeatability of ±1.25 °C for the fluidic cell analyte temperature. Secondary closed-loop fluidic cell temperature feedback system can bring the temperature to within the ±1 °C outlined in initial requirements.

Temperature change rate can be approximated by first order thermal dynamics where steady state (99 % of thermal setpoint) can be achieved within 5 minutes. As such the system does not provide a uniform temperature change rate, but rather an average of ≥0.5 °C/s for a full-range jump. An additional high temperature setpoint (100 – 130 °C) can be implemented to provide rapid ramping for all setpoints before switching to the desired setpoint. Fluidic cell maintains thermal uniformity (<1 % setpoint, or <1 °C at 95 °C) within the analyte channels up to 8 mm from the chip, which is sufficiently uniform for the nanopore-interfacing volume.

Nanopore current signals can be read with bandwidth up to 1 MHz with electrical noise from the system contributing less than 3 % of the overall noise, and below 75 pA_{rms} allowable reference cell noise. Redesigned Faraday cage maintains shielding effectiveness similar to the baseline VC100 enclosure, and provides additional convective cooling to protect the expensive pre-amplifier from overheating. Mechanical noise at the fluidic cell is well-controlled ($<10^{-3}$ pA^2/Hz) above 55 Hz, and is overall sufficiently low for nanopore experiments. Improved passive vibration control down to 30 Hz can be made by upgrading the local vibration dampeners to a different model.

Main performance challenge lies within the SiNx membrane nanopore sensors themselves, whereby significant pore growth is observed above 50 °C and pores have a high chance of becoming unstable above 70 °C. Hafnium dioxide (HfO_2) deposition is recommended as a possible solution for the growth. SiNx pores are otherwise suitable for molecular translocation experiments under 50 °C, which covers a large proportion of the predicted system use cases.

Chapter 4. Molecular translocation experiments

Proof-of-concept DNA translocation experiments under temperature control demonstrated the usability and functionality of the instrument. Experiments included translocation of simple linear DNA of moderate length (1 – 2 kilo-base pairs), as well as short (up to 200 base pair length) DNA star nanostructures for room temperature to 70 °C. Linear DNA experiments compare temperature-related translocation behaviour in SiNx nanopores to what is known from the literature. DNA nanostructure experiments explore the effects of temperature on the nanopore translocation of a star-shaped DNA nanostructure component of a high-sensitivity nanopore immunoassay. Experimental results for simple DNA translocation showed consistency with expectations. Nanostructure translocation results tentatively suggest DNA stars could be used up to 50 °C in SiNx nanopores, but require further characterization and replication experiments to understand capture and tranlocation behaviour.

Parameters of interest measured during the translocation experiments include nanopore current blockage levels / sublevels, translocation durations (dwell times), and capture rates. Blockage levels (ΔG) are simply the differences between the open-pore baseline ionic current (G) and the current resulting from partial occlusion of the pore by the molecule at any given time (Figure 2.5). A single molecule can feature multiple blockage sublevels resulting from geometric or electrochemical features producing differences in occlusion during translocation. Relative blockage (ΔG/G) is a normalized metric of molecular blockage that enables comparison of blockage across different voltages used on the same pore, and blockages from large (> 5 nm) pores of different size. How long a molecule stays within the pore is defined by its dwell time, and affected by its geometry as well as the interactions with the pore, and other environmental and operational factors. Lastly, frequency of translocation events indirectly indicates the concentration of molecules in solution, and is the rate of molecular capture by the nanopore under specific electrochemical conditions.

4.1. Simple DNA translocation

DNA translocation experiments using 1 kilobase pair (kbp) double-stranded linear DNA (dsDNA) fragments showed results consistent with previous studies typically using longer DNA in SiNx membranes (Table 4.1). Nanopores were produced in SiNx membranes (Norcada, NBPX5004Z), coated with 7:1 PDMS (Dow Corning, Sylgard 184) to reduce membrane capacitance below 100 pF for high-bandwidth sensing (1 MHz, 250 kHz 8-pole Bessel low-pass filter). Moderate-length double-stranded DNA (1 kbp dsDNA, ThermoFisher NoLimits, 0.5 µg/µL) was diluted to 31 nM (1.5 µL in 38.5 µL of degassed 3.6M LiCl + 10 mM HEPES, pH 8) and translocated through the pores at ambient room (21 °C) and high temperature (70 °C) setpoint following nanopore noise characterization experiments described in Section 3.5.

Results were most consistent with previous studies translocating λ-DNA (~48.5 kbp) through SiNx nanopores in a similar size range [43], [44]. Translocation time decreased by ca. 2-fold, while relative blockage remained nearly constant over similar temperature differences. Differences in capture rates could be attributed to the differences in concentration and size of DNA used. Capture rate of 1 kbp dsDNA is enhanced in the current experiments likely due to much higher concentration, and reduction of viscous drag on the molecule with temperature (Eq.2.18, Eq.2.19), while Debye length is expected to remain nearly constant [44]. Sample current traces for an 8 nm pore (Thesis 3) for two temperatures are shown in Figure 4.1 A, while nanopore current blockage vs. dwell / translocation time distributions are shown in Figure 4.1 B. Of note is the significantly wider distribution of translocation times at elevated temperature.

Table 4.1. SiNx nanopore DNA translocation with temperature

Source	Pore size, voltage, electrolyte	DNA	Temperature range	Translocation time	Relative blockage (ΔG/G)	Capture rate
Thesis 1 *	11 nm @ 75 mV in 3.6M LiCl pH 8	ThermoFisher NoLimits 1 kbp, 31 nM	49 °C (21 to 70 °C)	↓ x2.2 (170 to 78 us)	↓ x1.1 (0.043 to 0.041)	↓ x2.6 * (0.569 to 0.216 Hz)
Thesis 2	8 nm @ 100 mV in 3.6M LiCl pH 8	ThermoFisher NoLimits 1 kbp, 31 nM	49 °C (21 to 70 °C)	↓ x2.2 (177 to 82 µs)	↓ x1.2 (0.127 to 0.109)	↑ x8.9 (0.973 to 8.62 Hz)
Thesis 3	8 nm @ 100 mV in 3.6M LiCl pH 8	ThermoFisher NoLimits 1 kbp, 31 nM	49 °C (21 to 70 °C)	↓ x2.2 (100 to 45 µs)	↓ x1.1 (0.176 to 0.155)	↑ x9.5 (0.793 to 7.54 Hz)
Verschueren et al., 2015 [44]	8 - 16 nm @ 100 mV in 1M KCl pH8	Promega λ ~48.5 kbp, 167 pM	40 °C (7 to 47 °C)	↓ x2.3 (2.1 to 0.9 ms)	↓ x1.1 (~0.013 to 0.012)	↑ x2.3 (0.2 to 0.45 Hz)
Zhang et al., 2015 [42]	20 nm @ 200 mV in 1 M KCl pH 8	Takara BIO λ ~48.5 kbp, 100 pM	18 °C (2 to 20 °C)	↓ x1.6 (2.44 to 1.55 ms)	~ constant	Not reported
Nicoli et al., 2014 [43]	10 nm @ 100 mV in 2 M LiCl pH 8	λ ~48.5 kbp, 333 pM	35 °C (10 to 45 °C)	↓ x2.1 (15 to 7 ms)	↓ x1.0 (0.051 to 0.049	↑ x2.3 (~0.06 to ~0.14 Hz plot est.)
Wanunu et al., 2008 [45] **	2.7 – 5 nm @ 300 mV in 1 M KCl pH 8.5	NoLimits 150 bp to 20 kbp, 5 nM	40 °C (0 to 40 °C)	↓ x7 (7 to 1 ms long, 0.7 to 0.1 ms short @ 1.2 kbp)	Not reported	Not reported
Fologea et al., 2005 [41]	4 – 8 nm @ 120 mV in 1.6 M KCl, 20 % glycerol, pH 7.5	3kBp pSP65 DNA plasmid, 10 nM	18 °C (4 to 22 °C)	↓ x1.7 (280 to 165 µs)	Not reported	Not reported

* low number of events recorded (<< 1000) due to hard drive space issues, results considered unreliable

** study done on small nanopores where surface interactions with the DNA slow down translocations significantly

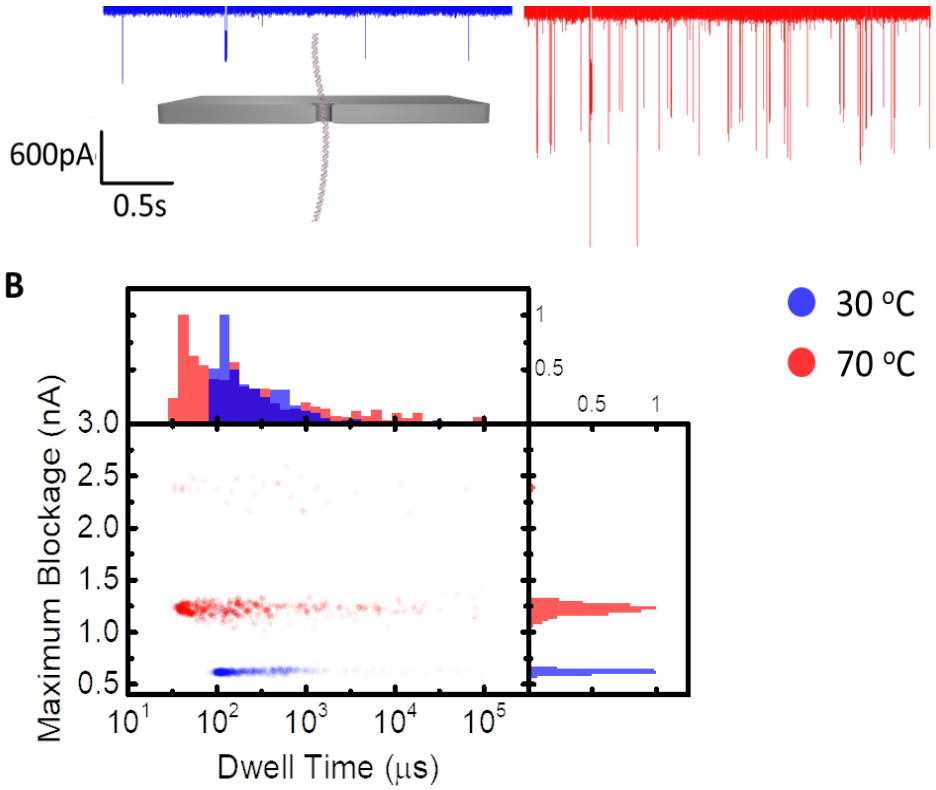

Figure 4.1. DNA translocation with temperature. (A) Current traces for 31 nM 1-kbp dsDNA translocations through an 8 nm nanopore in a 10 nm nominal thickness SiNx membrane, in 3.6 M LiCl + 10 mM HEPES (pH8) at +100 mV. Increase in nanopore current (G) at elevated temperature is associated with increase in maximum current blockage (ΔG), but the ratio (ΔG/G) remains approximately the same (↓ x1.1) since both are largely driven by solution conductivity changes. (B) Maximum current blockages show expected narrow event distributions that are largely a function of molecular size and configuration, while translocation/dwell times show wide distributions that may be related to pore surface and molecular interactions.

4.2. DNA nanostructure translocation

DNA star nanostructures [322] have recently been used in a digital nanopore immunoassay to quantify very low (femtomolar) concentrations of thyroid-stimulating hormone (TSH) from serum samples at ambient temperature (21 °C) [323]. Nanopore sensing steps of the assay involve mixing of modified star nanostructures with linker molecules to form dumbbell nanostructures (Figure 4.2). The number of linker molecules is proportional to the number of TSH molecules from the prior assay steps, and the ratio of star to dumbbell signals in the nanopore can quantify the concentration of TSH in a given sample based on signal calibration curves.

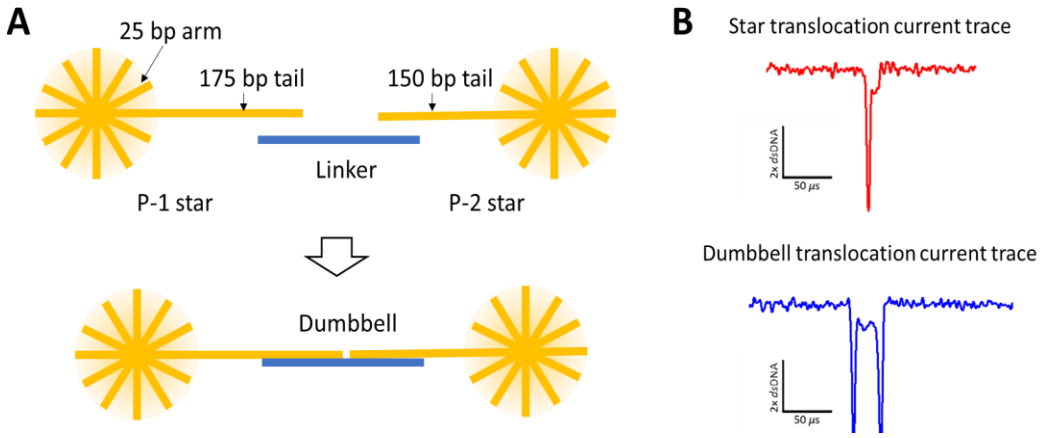

Figure 4.2. DNA star and dumbbell nanostructures. (A) DNA star are short nanostructures formed by combining 11 short (25-bp dsDNA) arms and a long (175 or 150-bp DNA) tail with and sequences corresponding to the short (50 nucleotides) DNA linker. (B) Nanostructures can be differentiated by the nanopore current trace signals (200 kHz low-pass filtered) to count the ratios of linked an unlinked stars in the quantification step of a digital immunoassay **[323]**.

While the nanopore immunoassay does not require elevated nanopore temperatures for detection of the nanostructures, temperature may add another level of control. For example, creating temperature-sensitive linkages could open the door for multiplexed detection of different molecules using the same star nanostructures, reducing the need to design and build stars of different tail sequences. Temperature control could also reduce false positives by melting weakly-bound structures. As such, the effect of temperature on nanopore translocation of DNA star nanostructures concurrently with a 2-kbp dsDNA reference was briefly investigated. Reference DNA molecules act as molecular rulers to help reduce inter-pore and inter-experiment variance in current blockage levels.

Star nanostructure translocation experiments at different temperatures were attempted on 10 nanopores produced in 12 nm nominal thickness SiNx membranes (Norcada NBPX5004Z, batch codes unknown), coated with 7:1 PDMS to reduce capacitance, and oxygen plasma cleaned prior to use. Three nanopores had reasonable 1/f noise power levels (< 10 pA^2/Hz at < 100 Hz, ±100 mV) and passed 2-kbp DNA at an acceptable translocation rate (> 0.5 Hz). One nanopore did not exhibit instability and excessive clogging at temperatures below 50 °C. DNA star

nanostructures (5 µL of 15 – 20 nM stock in 35 µL 3.6 M LiCl + 10 mM HEPES, pH8) with a 2-kbp linear dsDNA reference (2.4 nM) were introduced into the fluidic cell containing the nanopores at ambient temperature, then recorded for 10 minutes at increasing temperature setpoints. Figure 4.3 shows sample current traces and event clustering for one of the nanopores.

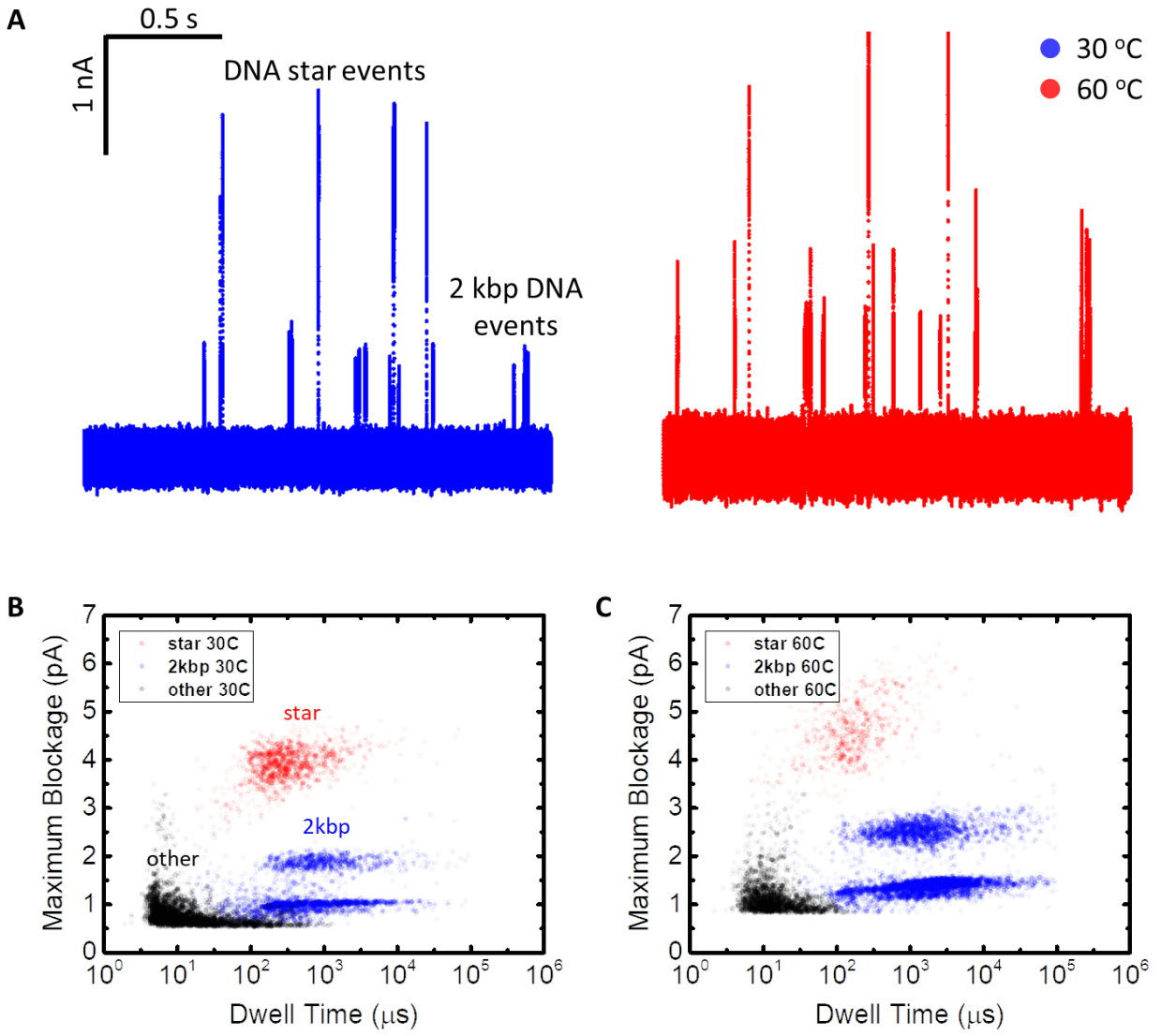

Figure 4.3. DNA nanostructure translocation current traces and events. (A) Current traces showing DNA translocations at 30 °C and 60 °C through an 8 nm pore in 12 nm nominal thickness SiNx membrane in 3.6 M LiCl + 10 mM HEPES, pH8, at -100mV, with 250 kHz low-pass filter applied. Molecular event clusters were formed based on prior expected location information [323], and event variable distributions were compared across temperatures (C, D).

Translocation events were clustered and analyzed using specialized nanopore event analysis software (NNi Nanolyzer). Events were clustered using Nanolyzer-implemented Gaussian mixtures methodology [324] by translocation time, maximum blockage, and event fit residuals axes (8 clusters showing stability over 100 clustering repetitions, merged into 3 clusters by expected average event locations [323] and residual depths).

Event rate for the 2-kbp DNA reference increased by 3.5 times from ambient to 60 °C (Figure 4.4), a trend expected from linear dsDNA experiments discussed previously. Temperatures higher than 63 °C were not attainable since pores experienced a significant increase in clog events and instability, resulting in an overall reduction in event rates. Star nanostructures show unexpected decreasing event rate trends (level to 30 °C with a slow decrease until 60 °C). The relative event ratio between the 2-kbp and the star DNA decreases by nearly eight times over the temperature range (Figure 4.4 C). Proportion of star events within the combined event pool remains stable over 1000 event mark for each temperature (Figure 4.4 D) suggesting sufficient number of events was collected for all samples.

Decreasing star event rates with temperature were unexpected. The event rates of star nanostructures could have been expected to increase at higher temperature since, in general, molecular diffusion is enhanced and viscosity is reduced. However, this behavior assumes that the capture kinetics is dominated by diffusion. A hypothesis to explain the drop in event rates of DNA nanostructures with temperature is that the system (i.e. the nanopore with its particular size and applied voltage and the molecules with their 3D shape and mobility) is not in the diffusion-limited capture region like for linear dsDNA, but instead is in the barrier-limited regime. Relatively small pore diameter (8 nm) and relatively low applied sensing voltage (100 mV) could result in a higher pore entry energy barrier and lower capture rate for the short star nanostructures, but not the long linear DNA [108], [112]. Moderate length linear DNA could be operating in the diffusion-limited capture regime where electrophoretic forces predominate, while the small star nanostructure could be operating in the barrier-limited capture regime where molecular conformations and interactions with pore material predominate. A similar behavior has been observed in [322]. Future experiments could consider detecting DNA stars

through larger low-noise pores as a function of voltage without the reference DNA to assess its baseline nanopore capture rate with temperature and molecular concentration.

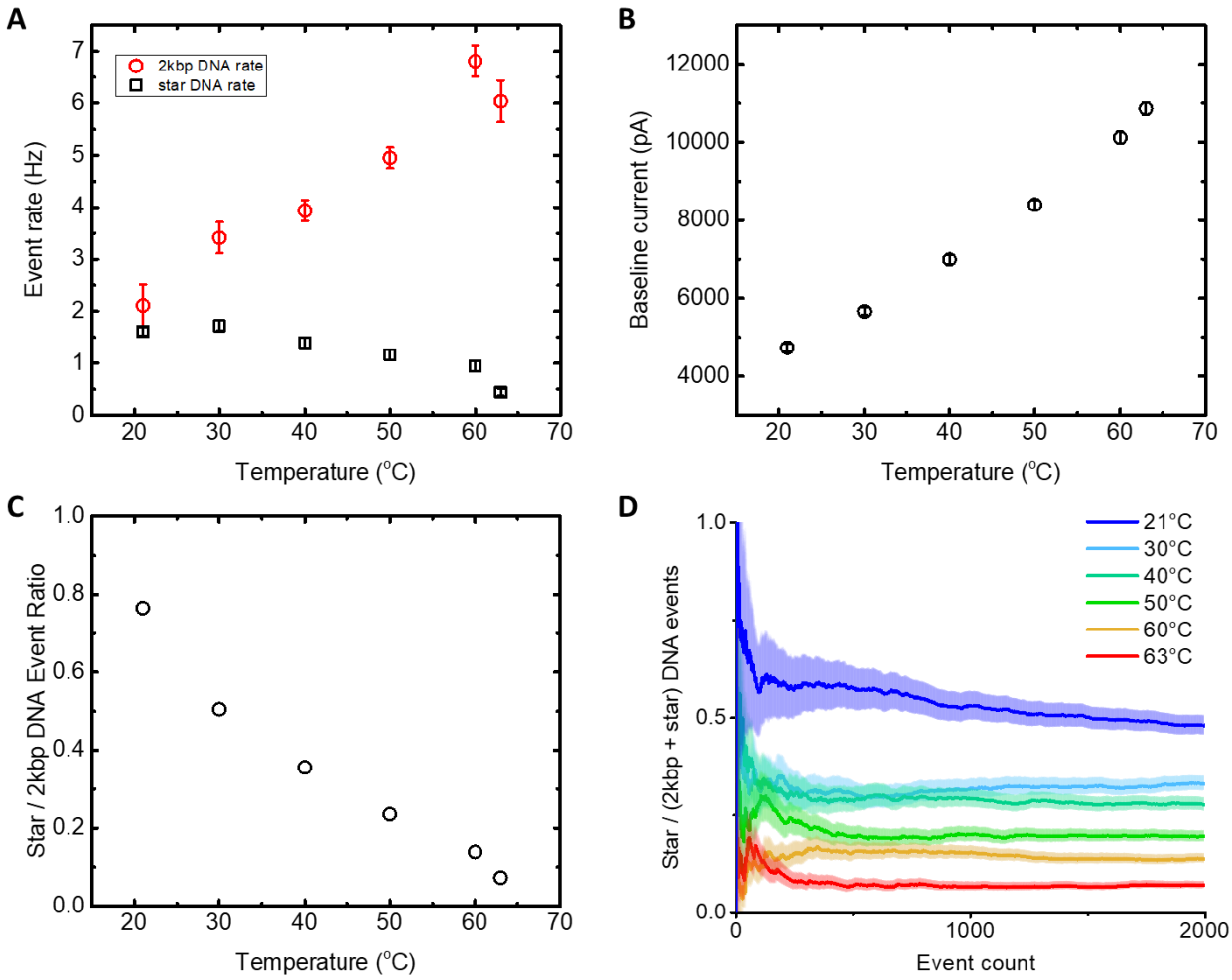

Figure 4.4. DNA translocation event rates. (A) DNA star and 2kbp reference DNA translocation event rates across temperature. Significant increase in transient pore clogging and instability at 63 °C reduces event rates. Further temperature increase permanently clogs the pore, likely with misassembled DNA star breakdown products. (B) Absolute value of nanopore baseline current with temperature shows expected trends, with slight growth at elevated temperatures as expected from SiNx nanopores. Error bars represent RMS noise at 250 kHz (C) Ratio of DNA star and 2kbp event rates used in the quantitative assay decreases with temperature. (D) As more events are recorded, the ratio of star events to the combination of star and 2kbp events remains stable. Data has a sufficient number of events for analysis.

Temperature elevation beyond 50 °C potentially affects nanostructure integrity and changes its translocation behaviour through the nanopore (Figure 4.5). The DNA star current blockage distribution normalized by 2-kbp DNA reference showed a 1.4x decrease in average blockage magnitude at 63 °C as compared to a 1.1x decrease at 50 °C (Figure 4.5 B) suggesting a change in the nanostructure and/or its interactions with the nanopore. Unfortunately, the differences are not statistically significant because of the large error bars (Figure 4.6). High spread (standard deviation) was observed in the Gaussian fits ($X^2 > 0.9$) used to estimate the average blockage levels by the Gaussian peak location. Nanostructure breakdown products (25 bp linear dsDNA) could not be differentiated from other small molecules using this pore since analysis was bandwidth-limited to 250 kHz to address fairly high capacitive noise, resulting in undetectable molecular events shorter than 4 – 5 μs.

Previous observations were verified using a different method. Experimental procedure was repeated, except DNA samples were incubated in a commercial thermocycler instead of the hot fluidic cell, and molecular migration was detected using agarose gel electrophoresis instead of the nanopore (Figure 4.7). Reader unfamiliar with gel electrophoresis is referred to an excellent open-access text on this topic [325]. Gel shows loss of the star band beyond 55 °C while smaller molecular fragment bands start appearing on the gel. Molecular integrity of the star is likely compromised, decomposing into constituent DNA fragments that likely misassemble into other structures. Complete loss of the star band, and therefore star molecular configuration, is observed at 60 °C. As temperatures increase and samples are exposed to these temperatures for longer, smaller fragment assemblies (likely 25 – 50 bp) dominate. The larger misassembled structures (~300 bp equivalent) could be responsible for permanent SiNx nanopore clogging observed at 63 °C. It is possible these structures have configurations that prevent nanopore translocation and simply block it off.

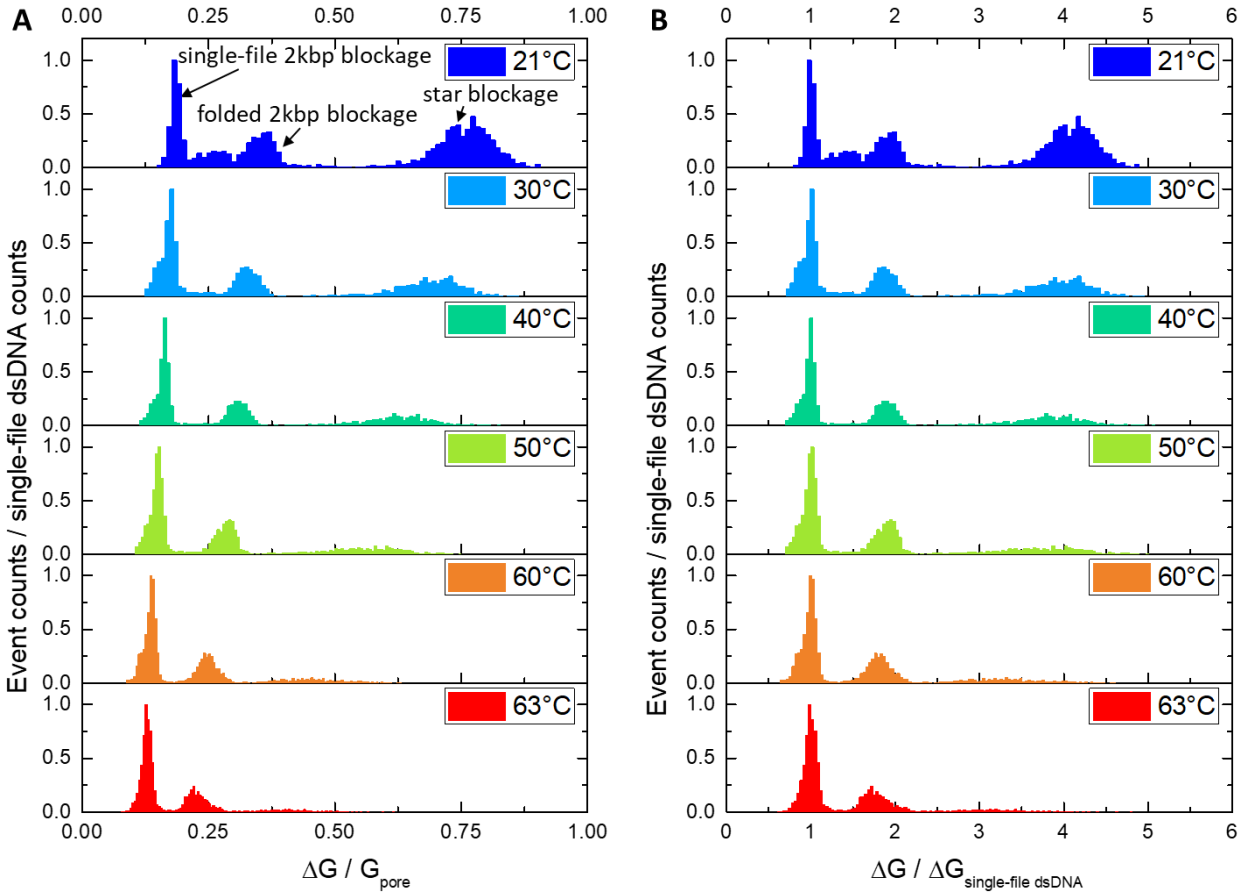

Figure 4.5. DNA translocation current blockages. (A) Baseline nanopore current-normalized blockage ($\Delta G/G_{pore}$) plotted against single-file 2kbp-normalized event counts, which are expected to decrease per Figure 4.4C. A decrease for $\Delta G/G_{pore}$ by <1.2x for single-file DNA reference over the current temperature range is expected (Section 4.1), and observed up to 50 °C. A decrease of 1.4x is observed at 63 °C suggesting more significant changes in pore-DNA interactions over the 50 – 63 °C range. (B) Using single-file 2kbp DNA as a normalization reference, average star blockage levels remain fairly unchanged up to 50 °C, with a large reduction at over 60 °C. Reduced blockage levels are consistent with partial nanostructure decomposition observed in gel electrophoresis experiments. Smaller molecular volume occludes the nanopore less, resulting in smaller blockage level.

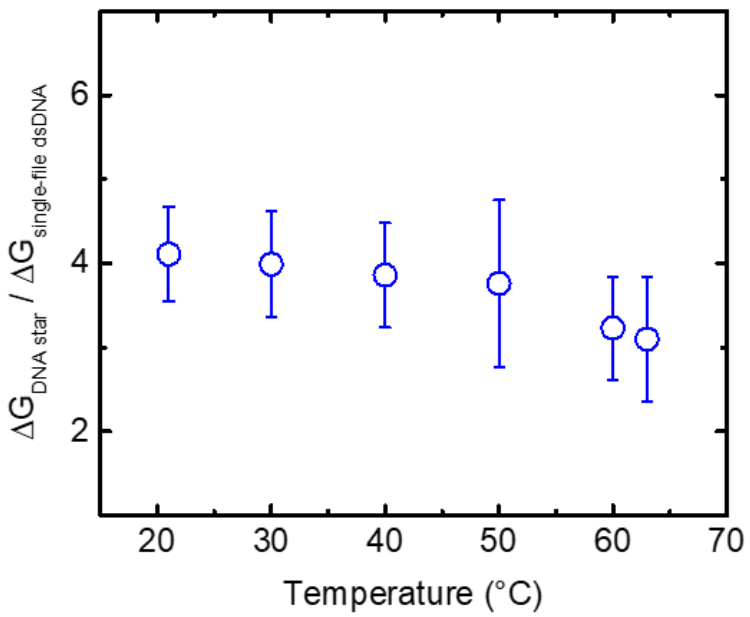

Figure 4.6. Average normalized nanopore current blockage with temperature. DNA star nanostructure and single-file 2-kbp linear dsDNA blockage distributions from Figure 4.5 were fitted in Origin 2016 using a Gaussian fit (X^2 > 0.9 all fits). Average nanopore current blockage by the DNA star nanostructures ($\Delta G_{DNA\ star}$), normalized by average 2-kbp dsDNA blockages ($\Delta G_{single\text{-}file\ dsDNA}$) show a noticeable decrease beyond 60 °C. The differences are not statistically significant due to large variation in DNA star blockages. Additional nanopore experiments with longer data collection intervals are required to further support or refute these observations.

Overall, results tentatively suggest DNA star nanostructure can be used with SiNx nanopores below 50 °C, however experimental replication and additional nanopore experiments are required to understand the effects of temperature on capture and translocation dynamics. Testing a different batch of SiNx membrane chips is recommended since experimental replication proved difficult with only 30 % (3/10) of the produced pores meeting the noise and DNA translocation rate requirements in ambient temperature conditions, and 10 % (1/10) remained thermally stable. Good SiNx chip batches used in our lab generally provide up to 80 % success rates for the ambient temperature steps.

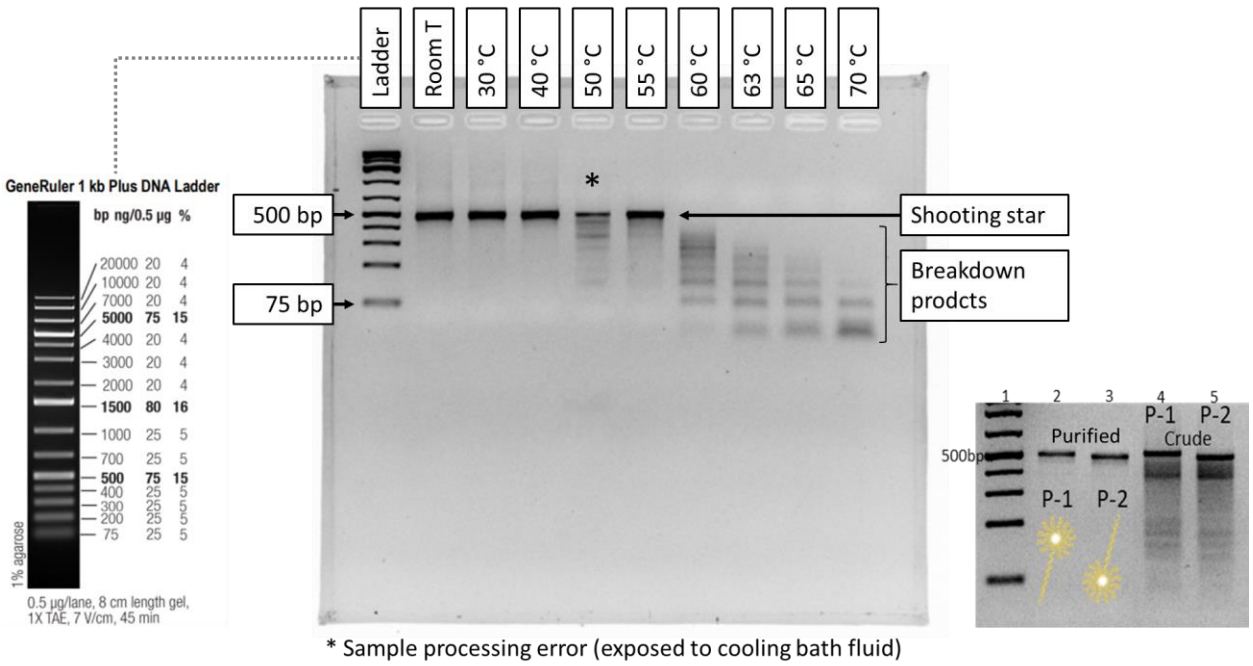

Figure 4.7. DNA nanostructure integrity with temperature. Purified DNA star (Shooting star) shows up as a 500 bp band on a 2% agarose gel in 0.5x TBE at 70 V. The star band maintains its intensity up to 55 °C, where smaller fragments start appearing under the main band. Star band disappears at 60 °C with decreasing size of disassembly products at higher temperatures. Copyright: Right gel image from Supplementary Figure 3 [323] distributed under Creative Commons CC BY permitting reprint. Left molecular ladder image from ThermoFisher SM1331 product information.

Chapter 5. Conclusions and Outlook

A research tool that can facilitate solid-state nanopore ionic current sensing experiments at a range of temperatures and high bandwidth was constructed and showed good thermal control and electrical noise performance. It is currently possible to operate a 25 µL nanopore fluidic cell in the temperature range from ambient to 95 °C, achieving steady state temperature within 5 minutes with thermal precision under ±0.2 °C and accuracy to within ±1 °C of a calibration reference thermometer with the use of closed-loop control on the fluidic cell. An additional important feature is that analyte temperature is maintained uniform to within <1 % of the thermal setpoint up to 8 mm from the nanopore chip. Analyte solution adjacent to the pore is kept at uniform environmental conditions and thermophoretic gradients across the pore are minimized. Ionic current signals from the pore can be read with a bandwidth of up to 1 MHz and a low electrical noise contribution (< 3% added noise) from the temperature control and measurement systems. Furthermore, noise characterization results were in agreement with theoretical dependence of $1/f$ pore electrical noise on the square of the pore ionic current, and supported the use of current-normalized metrics of pore quality (L-value) across temperatures. Future improvements to the temperature control system can include additional temperature setpoints with response control strategies to increase system response rate, as well as the improvements in the cooling system to allow for below-ambient temperature cooling and increased cooling rates.

Overall, this instrument opens up exciting opportunities to study the thermal unfolding of proteins toward single-molecule protein sequencing and the passage of DNA nanostructures for different bioassays. Proof-of-concept experiments using linear DNA demonstrated results consistent with previous studies in SiNx nanopores, where molecular translocation time decreased, capture rate increased, and relative ionic current blockage levels remained almost unchanged with increasing temperature. Temperature-controlled experiments using 12-arm DNA star nanostructures suggested the molecules are stable for pore translocation below 50 °C. Unfortunately, only one out of ten membranes from the batch of chips used exhibited sufficient stability to provide adequate translocation results, necessitating further replication studies.

Nevertheless, molecular capture rate observations have opened interesting questions regarding DNA star pore translocation dynamics, namely the molecular capture regimes. To elucidate some of the molecular dynamics, future experiments could explore nanostructure capture as a function of voltage, salt concentration, pore size, molecular concentration, and temperature. Solid-state nanopore performance at elevated temperatures for longer recording times can likely be addressed using different nanopore material types, and material modifications (e.g. surface coatings). Currently, SiNx nanopores show stable performance up to 50 °C, and can likely be used up to 70 °C if pore growth can be controlled. To this end, hafnium dioxide deposition on the membrane could be a potential future goal. Lastly, development of parallelized microfluidic cells for concurrent detection across multiple nanopore channels is recommended to improve system's throughput.

References

[1] R. P. C. Driessen *et al.*, “Effect of Temperature on the Intrinsic Flexibility of DNA and Its Interaction with Architectural Proteins,” *Biochemistry*, vol. 53, no. 41, pp. 6430–6438, Oct. 2014, doi: 10.1021/bi500344j.

[2] G. N. Somero, “Proteins and Temperature,” *Annu. Rev. Physiol.*, vol. 57, no. 1, pp. 43–68, Oct. 1995, doi: 10.1146/annurev.ph.57.030195.000355.

[3] H. Miller, Z. Zhou, J. Shepherd, A. J. M. Wollman, and M. C. Leake, “Single-molecule techniques in biophysics: a review of the progress in methods and applications,” *Rep. Prog. Phys.*, vol. 81, no. 2, p. 024601, Dec. 2017, doi: 10.1088/1361-6633/aa8a02.

[4] S. Goodwin, J. D. McPherson, and W. R. McCombie, “Coming of age: ten years of next-generation sequencing technologies,” *Nature Reviews Genetics*, vol. 17, no. 6, Art. no. 6, Jun. 2016, doi: 10.1038/nrg.2016.49.

[5] D. J. Müller and A. Engel, “Chapter 13 - Conformations, Flexibility, and Interactions Observed on Individual Membrane Proteins by Atomic Force Microscopy,” in *Methods in Cell Biology*, vol. 68, B. P. Jena and J. K. Heinrich Hörber, Eds. Academic Press, 2002, pp. 257–299. doi: 10.1016/S0091-679X(02)68014-8.

[6] H. Liu *et al.*, “Translocation of Single-Stranded DNA Through Single-Walled Carbon Nanotubes,” *Science*, vol. 327, no. 5961, pp. 64–67, Jan. 2010, doi: 10.1126/science.1181799.

[7] C. J. Lo, T. Aref, and A. Bezryadin, “Fabrication of symmetric sub-5 nm nanopores using focused ion and electron beams,” *Nanotechnology*, vol. 17, no. 13, pp. 3264–3267, Jun. 2006, doi: 10.1088/0957-4484/17/13/031.

[8] S. Polonsky, V. S. K. Balagurusamy, and J. A. Ott, “Creation of a transient vapor nanogap between two fluidic reservoirs for single molecule manipulation,” *Review of Scientific Instruments*, vol. 85, no. 8, p. 084301, Aug. 2014, doi: 10.1063/1.4890206.

[9] L. Reynaud, A. Bouchet-Spinelli, C. Raillon, and A. Buhot, “Sensing with Nanopores and Aptamers: A Way Forward,” *Sensors*, vol. 20, no. 16, Art. no. 16, Jan. 2020, doi: 10.3390/s20164495.

[10] R. Vidu, M. Rahman, M. Mahmoudi, M. Enachescu, T. D. Poteca, and I. Opris, “Nanostructures: a platform for brain repair and augmentation,” *Frontiers in Systems Neuroscience*, vol. 8, p. 91, 2014, doi: 10.3389/fnsys.2014.00091.

[11] “Oxford Nanopore Technologies,” 2021. https://nanoporetech.com/

[12] C. L. C. Ip *et al.*, “MinION Analysis and Reference Consortium: Phase 1 data release and analysis.” F1000Research, Oct. 15, 2015. doi: 10.12688/f1000research.7201.1.

[13] C. F. Minervini *et al.*, “Mutational analysis in BCR-ABL1 positive leukemia by deep sequencing based on nanopore MinION technology,” *Experimental and Molecular Pathology*, vol. 103, no. 1, pp. 33–37, Aug. 2017, doi: 10.1016/j.yexmp.2017.06.007.

[14] A. M. Taxt, E. Avershina, S. A. Frye, U. Naseer, and R. Ahmad, “Rapid identification of pathogens, antibiotic resistance genes and plasmids in blood cultures by nanopore sequencing,” *Sci Rep*, vol. 10, no. 1, p. 7622, May 2020, doi: 10.1038/s41598-020-64616-x.

[15] L. Z. Cooper, M. A. Madoff, and L. Weinstein, “Heat Stability and Species Range of Purified Staphylococcal α-Toxin,” *J Bacteriol*, vol. 91, no. 5, pp. 1686–1692, May 1966.

[16] S. E. JORGENSEN, E. C. SHORT, H. J. KURTZ, H. K. MUSSEN, and G. K. Y. 1976 WU, “Studies on the origin of the α-haemolysin produced by Escherichia coli,” *Journal of Medical Microbiology*, vol. 9, no. 2, pp. 173–189, 1976, doi: 10.1099/00222615-9-2-173.

[17] R. Lovell and T. A. Rees, “A Filterable Hæmolysin from Escherichia coli,” *Nature*, vol. 188, no. 4752, pp. 755–756, Nov. 1960, doi: 10.1038/188755b0.

[18] C. M. González-Henríquez, V. A. Villegas-Opazo, D. H. Sagredo-Oyarce, M. A. Sarabia-Vallejos, and C. A. Terraza, “Thermal Response Analysis of Phospholipid Bilayers Using Ellipsometric Techniques,” *Biosensors (Basel)*, vol. 7, no. 3, p. 34, Aug. 2017, doi: 10.3390/bios7030034.

[19] X. Kang, L.-Q. Gu, S. Cheley, and H. Bayley, “Single Protein Pores Containing Molecular Adapters at High Temperatures,” *Angewandte Chemie International Edition*, vol. 44, no. 10, pp. 1495–1499, 2005, doi: 10.1002/anie.200461885.

[20] S. E. Van der Verren *et al.*, “A dual constriction biological nanopore resolves homonucleotide sequences with high fidelity,” *Nat Biotechnol*, vol. 38, no. 12, pp. 1415–1420, Dec. 2020, doi: 10.1038/s41587-020-0570-8.

[21] C. E. Angevine, S. J. Seashols-Williams, and J. E. Reiner, “Infrared Laser Heating Applied to Nanopore Sensing for DNA Duplex Analysis,” *Anal. Chem.*, vol. 88, no. 5, pp. 2645–2651, Mar. 2016, doi: 10.1021/acs.analchem.5b03631.

[22] C. E. Angevine, J. W. F. Robertson, A. Dass, and J. E. Reiner, “Laser-based temperature control to study the roles of entropy and enthalpy in polymer-nanopore interactions,” *Science Advances*, vol. 7, no. 17, p. eabf5462, 2021, doi: 10.1126/sciadv.abf5462.

[23] D. W. Deamer and D. Branton, “Characterization of Nucleic Acids by Nanopore Analysis,” *Acc. Chem. Res.*, vol. 35, no. 10, pp. 817–825, Oct. 2002, doi: 10.1021/ar000138m.

[24] Y. Jung, H. Bayley, and L. Movileanu, “Temperature-Responsive Protein Pores,” *J. Am. Chem. Soc.*, vol. 128, no. 47, pp. 15332–15340, Nov. 2006, doi: 10.1021/ja065827t.

[25] D. K. Lathrop *et al.*, “Monitoring the Escape of DNA from a Nanopore Using an Alternating Current Signal,” *J. Am. Chem. Soc.*, vol. 132, no. 6, pp. 1878–1885, Feb. 2010, doi: 10.1021/ja906951g.

[26] A. Meller, L. Nivon, E. Brandin, J. Golovchenko, and D. Branton, “Rapid nanopore discrimination between single polynucleotide molecules,” *PNAS*, vol. 97, no. 3, pp. 1079–1084, Feb. 2000, doi: 10.1073/pnas.97.3.1079.

[27] L. Payet *et al.*, “Thermal Unfolding of Proteins Probed at the Single Molecule Level Using Nanopores,” *Anal. Chem.*, vol. 84, no. 9, pp. 4071–4076, May 2012, doi: 10.1021/ac300129e.

[28] L. Payet *et al.*, “Temperature Effect on Ionic Current and ssDNA Transport through Nanopores,” *Biophysical Journal*, vol. 109, no. 8, pp. 1600–1607, Oct. 2015, doi: 10.1016/j.bpj.2015.08.043.

[29] F. Piguet *et al.*, “High Temperature Extends the Range of Size Discrimination of Nonionic Polymers by a Biological Nanopore,” *Sci Rep*, vol. 6, no. 1, p. 38675, Dec. 2016, doi: 10.1038/srep38675.

[30] M. J. Madou, *Fundamentals of Microfabrication and Nanotechnology, Three-Volume Set*, 3rd ed. Boca Raton: CRC Press, 2011. [Online]. Available: https://www.taylorfrancis.com/books/mono/10.1201/9781315274164/fundamentals-microfabrication-nanotechnology-three-volume-set-marc-madou

[31] G. Voskerician *et al.*, “Biocompatibility and biofouling of MEMS drug delivery devices,” *Biomaterials*, vol. 24, no. 11, pp. 1959–1967, May 2003, doi: 10.1016/S0142-9612(02)00565-3.
[32] E. Beamish, H. Kwok, V. Tabard-Cossa, and M. Godin, “Precise control of the size and noise of solid-state nanopores using high electric fields,” *Nanotechnology*, vol. 23, no. 40, p. 405301, Sep. 2012, doi: 10.1088/0957-4484/23/40/405301.
[33] K. Briggs, H. Kwok, and V. Tabard-Cossa, “Automated Fabrication of 2-nm Solid-State Nanopores for Nucleic Acid Analysis,” *Small*, vol. 10, no. 10, pp. 2077–2086, 2014, doi: 10.1002/smll.201303602.
[34] H. Kwok, K. Briggs, and V. Tabard-Cossa, “Nanopore Fabrication by Controlled Dielectric Breakdown,” *PLOS ONE*, vol. 9, no. 3, p. e92880, Mar. 2014, doi: 10.1371/journal.pone.0092880.
[35] M. Waugh *et al.*, “Solid-state nanopore fabrication by automated controlled breakdown,” *Nat Protoc*, vol. 15, no. 1, pp. 122–143, Jan. 2020, doi: 10.1038/s41596-019-0255-2.
[36] R. Brilmayer, C. Förster, L. Zhao, and A. Andrieu-Brunsen, “Recent trends in nanopore polymer functionalization,” *Current Opinion in Biotechnology*, vol. 63, pp. 200–209, Jun. 2020, doi: 10.1016/j.copbio.2020.03.005.
[37] S. Schmid, P. Stömmer, H. Dietz, and C. Dekker, “Nanopore electro-osmotic trap for the label-free study of single proteins and their conformations,” *Nat. Nanotechnol.*, pp. 1–7, Aug. 2021, doi: 10.1038/s41565-021-00958-5.
[38] M. Belkin, S.-H. Chao, G. Giannetti, and A. Aksimentiev, “Modeling thermophoretic effects in solid-state nanopores,” *J Comput Electron*, vol. 13, no. 4, pp. 826–838, Dec. 2014, doi: 10.1007/s10825-014-0594-8.
[39] M. Belkin and A. Aksimentiev, “Molecular Dynamics Simulation of DNA Capture and Transport in Heated Nanopores,” *ACS Appl. Mater. Interfaces*, vol. 8, no. 20, pp. 12599–12608, May 2016, doi: 10.1021/acsami.6b00463.
[40] Y. He, M. Tsutsui, R. H. Scheicher, F. Bai, M. Taniguchi, and T. Kawai, “Thermophoretic Manipulation of DNA Translocation through Nanopores,” *ACS Nano*, vol. 7, no. 1, pp. 538–546, Jan. 2013, doi: 10.1021/nn304914j.
[41] D. Fologea, J. Uplinger, B. Thomas, D. S. McNabb, and J. Li, “Slowing DNA Translocation in a Solid-State Nanopore,” *Nano Lett.*, vol. 5, no. 9, pp. 1734–1737, Sep. 2005, doi: 10.1021/nl051063o.
[42] Y. Zhang *et al.*, “Temperature effect on translocation speed and capture rate of nanopore-based DNA detection,” *Sci. China Technol. Sci.*, vol. 58, no. 3, pp. 519–525, Mar. 2015, doi: 10.1007/s11431-014-5674-2.
[43] F. Nicoli, D. Verschueren, M. Klein, C. Dekker, and M. P. Jonsson, “DNA Translocations through Solid-State Plasmonic Nanopores,” *Nano Lett.*, vol. 14, no. 12, pp. 6917–6925, Dec. 2014, doi: 10.1021/nl503034j.
[44] D. V. Verschueren, M. P. Jonsson, and C. Dekker, “Temperature dependence of DNA translocations through solid-state nanopores,” *Nanotechnology*, vol. 26, no. 23, p. 234004, May 2015, doi: 10.1088/0957-4484/26/23/234004.
[45] M. Wanunu, J. Sutin, B. McNally, A. Chow, and A. Meller, “DNA Translocation Governed by Interactions with Solid-State Nanopores,” *Biophysical Journal*, vol. 95, no. 10, pp. 4716–4725, Nov. 2008, doi: 10.1529/biophysj.108.140475.

[46] C. Plesa, S. W. Kowalczyk, R. Zinsmeester, A. Y. Grosberg, Y. Rabin, and C. Dekker, "Fast Translocation of Proteins through Solid State Nanopores," *Nano Lett.*, vol. 13, no. 2, pp. 658–663, Feb. 2013, doi: 10.1021/nl3042678.

[47] J. K. Rosenstein, M. Wanunu, C. A. Merchant, M. Drndic, and K. L. Shepard, "Integrated nanopore sensing platform with sub-microsecond temporal resolution," *Nat Methods*, vol. 9, no. 5, pp. 487–492, May 2012, doi: 10.1038/nmeth.1932.

[48] N. Varongchayakul, J. S. Hersey, A. Squires, A. Meller, and M. W. Grinstaff, "A Solid-State Hard Microfluidic–Nanopore Biosensor with Multilayer Fluidics and On-Chip Bioassay/Purification Chamber," *Advanced Functional Materials*, vol. 28, no. 50, p. 1804182, 2018, doi: 10.1002/adfm.201804182.

[49] E. Laarz, B. V. Zhmud, and L. Bergström, "Dissolution and Deagglomeration of Silicon Nitride in Aqueous Medium," *Journal of the American Ceramic Society*, vol. 83, no. 10, pp. 2394–400, 2000, doi: 10.1111/j.1151-2916.2000.tb01567.x.

[50] O. Eggenberger, C. Ying, and M. Mayer, "Surface coatings for solid-state nanopores," *Nanoscale*, vol. 11, no. 42, pp. 19636–19657, 2019, doi: 10.1039/C9NR05367K.

[51] B. V. Zhmud and L. Bergström, "Dissolution Kinetics of Silicon Nitride in Aqueous Suspension," *Journal of Colloid and Interface Science*, vol. 218, no. 2, pp. 582–584, Oct. 1999, doi: 10.1006/jcis.1999.6425.

[52] D. Deamer, M. Akeson, and D. Branton, "Three decades of nanopore sequencing," *Nat Biotechnol*, vol. 34, no. 5, pp. 518–524, May 2016, doi: 10.1038/nbt.3423.

[53] M. Don. Graham, "The Coulter Principle: Foundation of an Industry," *JALA: Journal of the Association for Laboratory Automation*, vol. 8, no. 6, pp. 72–81, Dec. 2003, doi: 10.1016/S1535-5535-03-00023-6.

[54] J. Li, D. Stein, C. McMullan, D. Branton, M. J. Aziz, and J. A. Golovchenko, "Ion-beam sculpting at nanometre length scales," *Nature*, vol. 412, no. 6843, pp. 166–169, Jul. 2001, doi: 10.1038/35084037.

[55] H. S. Dow, W. S. Kim, and J. W. Lee, "Thermal and electrical properties of silicon nitride substrates," *AIP Advances*, vol. 7, no. 9, p. 095022, Sep. 2017, doi: 10.1063/1.4996314.

[56] Z. Krstic and V. D. Krstic, "Silicon nitride: the engineering material of the future," *J Mater Sci*, vol. 47, no. 2, pp. 535–552, Jan. 2012, doi: 10.1007/s10853-011-5942-5.

[57] J. Larkin, R. Henley, D. C. Bell, T. Cohen-Karni, J. K. Rosenstein, and M. Wanunu, "Slow DNA Transport through Nanopores in Hafnium Oxide Membranes," *ACS Nano*, vol. 7, no. 11, pp. 10121–10128, Nov. 2013, doi: 10.1021/nn404326f.

[58] A. J. Storm, J. H. Chen, X. S. Ling, H. W. Zandbergen, and C. Dekker, "Fabrication of solid-state nanopores with single-nanometre precision," *Nature Mater*, vol. 2, no. 8, pp. 537–540, Aug. 2003, doi: 10.1038/nmat941.

[59] C. Gao, S. Ding, Q. Tan, and L.-Q. Gu, "Method of Creating a Nanopore-Terminated Probe for Single-Molecule Enantiomer Discrimination," *Anal. Chem.*, vol. 81, no. 1, pp. 80–86, Jan. 2009, doi: 10.1021/ac802348r.

[60] B. M. Venkatesan, A. B. Shah, J.-M. Zuo, and R. Bashir, "DNA Sensing Using Nanocrystalline Surface-Enhanced Al2O3 Nanopore Sensors," *Advanced Functional Materials*, vol. 20, no. 8, pp. 1266–1275, 2010, doi: 10.1002/adfm.200902128.

[61] K.-B. Park *et al.*, “Highly reliable and low-noise solid-state nanopores with an atomic layer deposited ZnO membrane on a quartz substrate,” *Nanoscale*, vol. 9, no. 47, pp. 18772–18780, 2017, doi: 10.1039/C7NR05755E.

[62] R. Wang, T. Gilboa, J. Song, D. Huttner, M. W. Grinstaff, and A. Meller, “Single-Molecule Discrimination of Labeled DNAs and Polypeptides Using Photoluminescent-Free TiO2 Nanopores,” *ACS Nano*, vol. 12, no. 11, pp. 11648–11656, Nov. 2018, doi: 10.1021/acsnano.8b07055.

[63] T. Ito, L. Sun, and R. M. Crooks, “Observation of DNA transport through a single carbon nanotube channel using fluorescence microscopy,” *Chem. Commun.*, no. 13, pp. 1482–1483, Jun. 2003, doi: 10.1039/B302511J.

[64] M. D. Fischbein and M. Drndić, “Electron beam nanosculpting of suspended graphene sheets,” *Appl. Phys. Lett.*, vol. 93, no. 11, p. 113107, Sep. 2008, doi: 10.1063/1.2980518.

[65] S. Liu *et al.*, “Boron Nitride Nanopores: Highly Sensitive DNA Single-Molecule Detectors,” *Advanced Materials*, vol. 25, no. 33, pp. 4549–4554, 2013, doi: 10.1002/adma.201301336.

[66] K. Liu, J. Feng, A. Kis, and A. Radenovic, “Atomically Thin Molybdenum Disulfide Nanopores with High Sensitivity for DNA Translocation,” *ACS Nano*, vol. 8, no. 3, pp. 2504–2511, Mar. 2014, doi: 10.1021/nn406102h.

[67] G. Danda *et al.*, “Monolayer WS2 Nanopores for DNA Translocation with Light-Adjustable Sizes,” *ACS Nano*, vol. 11, no. 2, pp. 1937–1945, Feb. 2017, doi: 10.1021/acsnano.6b08028.

[68] Y. Shen *et al.*, “In Situ Repair of 2D Chalcogenides under Electron Beam Irradiation,” *Advanced Materials*, vol. 30, no. 14, p. 1705954, 2018, doi: 10.1002/adma.201705954.

[69] M. Mojtabavi, A. VahidMohammadi, W. Liang, M. Beidaghi, and M. Wanunu, “Single-Molecule Sensing Using Nanopores in Two-Dimensional Transition Metal Carbide (MXene) Membranes,” *ACS Nano*, vol. 13, no. 3, pp. 3042–3053, Mar. 2019, doi: 10.1021/acsnano.8b08017.

[70] Z. Siwy and A. Fuliński, “Fabrication of a Synthetic Nanopore Ion Pump,” *Phys. Rev. Lett.*, vol. 89, no. 19, p. 198103, Oct. 2002, doi: 10.1103/PhysRevLett.89.198103.

[71] H.-J. Kim *et al.*, “Translocation of DNA and protein through a sequentially polymerized polyurea nanopore,” *Nanoscale*, vol. 11, no. 2, pp. 444–453, 2019, doi: 10.1039/C8NR06229C.

[72] C. C. Harrell, Z. S. Siwy, and C. R. Martin, “Conical Nanopore Membranes: Controlling the Nanopore Shape,” *Small*, vol. 2, no. 2, pp. 194–198, 2006, doi: 10.1002/smll.200500196.

[73] S. Wu, S. R. Park, and X. S. Ling, “Lithography-Free Formation of Nanopores in Plastic Membranes Using Laser Heating,” *Nano Lett.*, vol. 6, no. 11, pp. 2571–2576, Nov. 2006, doi: 10.1021/nl0619498.

[74] A. Mara, Z. Siwy, C. Trautmann, J. Wan, and F. Kamme, “An Asymmetric Polymer Nanopore for Single Molecule Detection,” *Nano Lett.*, vol. 4, no. 3, pp. 497–501, Mar. 2004, doi: 10.1021/nl035141o.

[75] Q. Chen and Z. Liu, “Fabrication and Applications of Solid-State Nanopores,” *Sensors*, vol. 19, no. 8, Art. no. 8, Jan. 2019, doi: 10.3390/s19081886.

[76] G. Danda and M. Drndić, “Two-dimensional nanopores and nanoporous membranes for ion and molecule transport,” *Current Opinion in Biotechnology*, vol. 55, pp. 124–133, Feb. 2019, doi: 10.1016/j.copbio.2018.09.002.

[77] K. Lee *et al.*, “Recent Progress in Solid-State Nanopores,” *Advanced Materials*, vol. 30, no. 42, p. 1704680, 2018, doi: 10.1002/adma.201704680.

[78] M. Macha, S. Marion, V. V. R. Nandigana, and A. Radenovic, “2D materials as an emerging platform for nanopore-based power generation,” *Nat Rev Mater*, vol. 4, no. 9, pp. 588–605, Sep. 2019, doi: 10.1038/s41578-019-0126-z.

[79] L. Xue, H. Yamazaki, R. Ren, M. Wanunu, A. P. Ivanov, and J. B. Edel, “Solid-state nanopore sensors,” *Nat Rev Mater*, vol. 5, no. 12, pp. 931–951, Dec. 2020, doi: 10.1038/s41578-020-0229-6.

[80] L. J. Steinbock, O. Otto, C. Chimerel, J. Gornall, and U. F. Keyser, “Detecting DNA Folding with Nanocapillaries,” *Nano Lett.*, vol. 10, no. 7, pp. 2493–2497, Jul. 2010, doi: 10.1021/nl100997s.

[81] M. Ayub *et al.*, “Precise electrochemical fabrication of sub-20 nm solid-state nanopores for single-molecule biosensing,” *J. Phys.: Condens. Matter*, vol. 22, no. 45, p. 454128, Oct. 2010, doi: 10.1088/0953-8984/22/45/454128.

[82] L. Sainiemi, K. Grigoras, and S. Franssila, “Suspended nanostructured alumina membranes,” *Nanotechnology*, vol. 20, no. 7, p. 075306, Jan. 2009, doi: 10.1088/0957-4484/20/7/075306.

[83] P. Waduge *et al.*, “Direct and Scalable Deposition of Atomically Thin Low-Noise MoS2 Membranes on Apertures,” *ACS Nano*, vol. 9, no. 7, pp. 7352–7359, Jul. 2015, doi: 10.1021/acsnano.5b02369.

[84] J. Choi, C. C. Lee, and S. Park, “Scalable fabrication of sub-10 nm polymer nanopores for DNA analysis,” *Microsyst Nanoeng*, vol. 5, no. 1, pp. 1–10, Apr. 2019, doi: 10.1038/s41378-019-0050-9.

[85] L. J. de Vreede, A. van den Berg, and J. C. T. Eijkel, “Nanopore Fabrication by Heating Au Particles on Ceramic Substrates,” *Nano Lett.*, vol. 15, no. 1, pp. 727–731, Jan. 2015, doi: 10.1021/nl5042676.

[86] T. James, Y. V. Kalinin, C.-C. Chan, J. S. Randhawa, M. Gaevski, and D. H. Gracias, “Voltage-Gated Ion Transport through Semiconducting Conical Nanopores Formed by Metal Nanoparticle-Assisted Plasma Etching,” *Nano Lett.*, vol. 12, no. 7, pp. 3437–3442, Jul. 2012, doi: 10.1021/nl300673r.

[87] S. R. Park, H. Peng, and X. S. Ling, “Fabrication of Nanopores in Silicon Chips Using Feedback Chemical Etching,” *Small*, vol. 3, no. 1, pp. 116–119, 2007, doi: 10.1002/smll.200600268.

[88] I. Vlassiouk, P. Y. Apel, S. N. Dmitriev, K. Healy, and Z. S. Siwy, “Versatile ultrathin nanoporous silicon nitride membranes,” *PNAS*, vol. 106, no. 50, pp. 21039–21044, Dec. 2009, doi: 10.1073/pnas.0911450106.

[89] A. T. Carlsen, K. Briggs, A. R. Hall, and V. Tabard-Cossa, “Solid-state nanopore localization by controlled breakdown of selectively thinned membranes,” *Nanotechnology*, vol. 28, no. 8, p. 085304, Jan. 2017, doi: 10.1088/1361-6528/aa564d.

[90] J. Bustamante, “Synchronous Optical and Electrical Measurements of Single DNA Molecules Translocating Through a Solid-State Nanopore,” Thesis, Université d’Ottawa / University of Ottawa, 2015. doi: 10.20381/ruor-5739.

[91] S. Pud, D. Verschueren, N. Vukovic, C. Plesa, M. P. Jonsson, and C. Dekker, “Self-Aligned Plasmonic Nanopores by Optically Controlled Dielectric Breakdown,” *Nano Lett.*, vol. 15, no. 10, pp. 7112–7117, Oct. 2015, doi: 10.1021/acs.nanolett.5b03239.

[92] R. Tahvildari, E. Beamish, V. Tabard-Cossa, and M. Godin, “Integrating nanopore sensors within microfluidic channel arrays using controlled breakdown,” *Lab Chip*, vol. 15, no. 6, pp. 1407–1411, Mar. 2015, doi: 10.1039/C4LC01366B.

[93] C. E. Arcadia, C. C. Reyes, and J. K. Rosenstein, “In Situ Nanopore Fabrication and Single-Molecule Sensing with Microscale Liquid Contacts,” *ACS Nano*, vol. 11, no. 5, pp. 4907–4915, May 2017, doi: 10.1021/acsnano.7b01519.

[94] S. Lombardo, J. H. Stathis, B. P. Linder, K. L. Pey, F. Palumbo, and C. H. Tung, “Dielectric breakdown mechanisms in gate oxides,” *Journal of Applied Physics*, vol. 98, no. 12, p. 121301, Dec. 2005, doi: 10.1063/1.2147714.

[95] K. Briggs, “Solid-State Nanopores: Fabrication, Application, and Analysis,” Thesis, Université d’Ottawa / University of Ottawa, 2018. doi: 10.20381/ruor-22794.

[96] I. Yanagi, H. Hamamura, R. Akahori, and K. Takeda, “Two-step breakdown of a SiN membrane for nanopore fabrication: Formation of thin portion and penetration,” *Sci Rep*, vol. 8, no. 1, p. 10129, Jul. 2018, doi: 10.1038/s41598-018-28524-5.

[97] K. Briggs *et al.*, “Kinetics of nanopore fabrication during controlled breakdown of dielectric membranes in solution,” *Nanotechnology*, vol. 26, no. 8, p. 084004, Feb. 2015, doi: 10.1088/0957-4484/26/8/084004.

[98] C. Leung, K. Briggs, M.-P. Laberge, S. Peng, M. Waugh, and V. Tabard-Cossa, “Mechanisms of solid-state nanopore enlargement under electrical stress,” *Nanotechnology*, vol. 31, no. 44, p. 44LT01, Aug. 2020, doi: 10.1088/1361-6528/aba86e.

[99] J. E. Hall, “Access resistance of a small circular pore.,” *Journal of General Physiology*, vol. 66, no. 4, pp. 531–532, Oct. 1975, doi: 10.1085/jgp.66.4.531.

[100] R. M. M. Smeets, U. F. Keyser, D. Krapf, M.-Y. Wu, N. H. Dekker, and C. Dekker, “Salt Dependence of Ion Transport and DNA Translocation through Solid-State Nanopores,” *Nano Lett.*, vol. 6, no. 1, pp. 89–95, Jan. 2006, doi: 10.1021/nl052107w.

[101] T. Albrecht, T. Gibb, and P. Nuttall, “Chapter 1 - Ion Transport in Nanopores,” in *Engineered Nanopores for Bioanalytical Applications*, J. B. Edel and T. Albrecht, Eds. Oxford: William Andrew Publishing, 2013, pp. 1–30. doi: 10.1016/B978-1-4377-3473-7.00001-7.

[102] N. Di Fiori, A. Squires, D. Bar, T. Gilboa, T. D. Moustakas, and A. Meller, “Optoelectronic control of surface charge and translocation dynamics in solid-state nanopores,” *Nature Nanotech*, vol. 8, no. 12, pp. 946–951, Dec. 2013, doi: 10.1038/nnano.2013.221.

[103] R. B. Schoch, J. Han, and P. Renaud, “Transport phenomena in nanofluidics,” *Rev. Mod. Phys.*, vol. 80, no. 3, pp. 839–883, Jul. 2008, doi: 10.1103/RevModPhys.80.839.

[104] M. Firnkes, D. Pedone, J. Knezevic, M. Döblinger, and U. Rant, “Electrically Facilitated Translocations of Proteins through Silicon Nitride Nanopores: Conjoint and Competitive Action of Diffusion, Electrophoresis, and Electroosmosis,” *Nano Lett.*, vol. 10, no. 6, pp. 2162–2167, Jun. 2010, doi: 10.1021/nl100861c.

[105] O. Otto and U. F. Keyser, “Chapter 2 - DNA Translocation,” in *Engineered Nanopores for Bioanalytical Applications*, J. B. Edel and T. Albrecht, Eds. Oxford: William Andrew Publishing, 2013, pp. 31–58. doi: 10.1016/B978-1-4377-3473-7.00002-9.

[106] C. M. Frament and J. R. Dwyer, “Conductance-Based Determination of Solid-State Nanopore Size and Shape: An Exploration of Performance Limits,” *J. Phys. Chem. C*, vol. 116, no. 44, pp. 23315–23321, Nov. 2012, doi: 10.1021/jp305381j.

[107] A. T. Carlsen, O. K. Zahid, J. Ruzicka, E. W. Taylor, and A. R. Hall, “Interpreting the Conductance Blockades of DNA Translocations through Solid-State Nanopores,” *ACS Nano*, vol. 8, no. 5, pp. 4754–4760, May 2014, doi: 10.1021/nn501694n.
[108] A. Y. Grosberg and Y. Rabin, “DNA capture into a nanopore: Interplay of diffusion and electrohydrodynamics,” *J. Chem. Phys.*, vol. 133, no. 16, p. 165102, Oct. 2010, doi: 10.1063/1.3495481.
[109] J. Kärger, D. M. Ruthven, and R. Valiullin, “Diffusion in nanopores: inspecting the grounds,” *Adsorption*, vol. 27, no. 3, pp. 267–281, Apr. 2021, doi: 10.1007/s10450-020-00277-6.
[110] B. Lu, F. Albertorio, D. P. Hoogerheide, and J. A. Golovchenko, “Origins and Consequences of Velocity Fluctuations during DNA Passage through a Nanopore,” *Biophys J*, vol. 101, no. 1, pp. 70–79, Jul. 2011, doi: 10.1016/j.bpj.2011.05.034.
[111] M. Muthukumar, “Theory of capture rate in polymer translocation,” *J. Chem. Phys.*, vol. 132, no. 19, p. 195101, May 2010, doi: 10.1063/1.3429882.
[112] P. Rowghanian and A. Y. Grosberg, “Electrophoretic capture of a DNA chain into a nanopore,” *Phys. Rev. E*, vol. 87, no. 4, p. 042722, Apr. 2013, doi: 10.1103/PhysRevE.87.042722.
[113] A. N. Sohi, E. Beamish, V. Tabard-Cossa, and M. Godin, “DNA Capture by Nanopore Sensors under Flow,” *Anal. Chem.*, vol. 92, no. 12, pp. 8108–8116, Jun. 2020, doi: 10.1021/acs.analchem.9b05778.
[114] S. C. Vollmer and H. W. de Haan, “Translocation is a nonequilibrium process at all stages: Simulating the capture and translocation of a polymer by a nanopore,” *J. Chem. Phys.*, vol. 145, no. 15, p. 154902, Oct. 2016, doi: 10.1063/1.4964630.
[115] C. Plesa, N. van Loo, P. Ketterer, H. Dietz, and C. Dekker, “Velocity of DNA during Translocation through a Solid-State Nanopore,” *Nano Lett.*, vol. 15, no. 1, pp. 732–737, Jan. 2015, doi: 10.1021/nl504375c.
[116] K. Chen, I. Jou, N. Ermann, M. Muthukumar, U. F. Keyser, and N. A. W. Bell, “Dynamics of driven polymer transport through a nanopore,” *Nat. Phys.*, vol. 17, no. 9, pp. 1043–1049, Sep. 2021, doi: 10.1038/s41567-021-01268-2.
[117] P.-Y. Hsiao, “Conformation Change, Tension Propagation and Drift-Diffusion Properties of Polyelectrolyte in Nanopore Translocation,” *Polymers (Basel)*, vol. 8, no. 10, p. 378, Oct. 2016, doi: 10.3390/polym8100378.
[118] M. Mihovilovic, N. Hagerty, and D. Stein, “Statistics of DNA Capture by a Solid-State Nanopore,” *Phys. Rev. Lett.*, vol. 110, no. 2, p. 028102, Jan. 2013, doi: 10.1103/PhysRevLett.110.028102.
[119] A. J. W. Hartel, S. Shekar, P. Ong, I. Schroeder, G. Thiel, and K. L. Shepard, “High bandwidth approaches in nanopore and ion channel recordings - A tutorial review,” *Analytica Chimica Acta*, vol. 1061, pp. 13–27, Jul. 2019, doi: 10.1016/j.aca.2019.01.034.
[120] Y. Dawji *et al.*, “A 65-nm CMOS Low-Power Front-End for 3rd Generation DNA Sequencing,” in *2019 IEEE SENSORS*, Oct. 2019, pp. 1–4. doi: 10.1109/SENSORS43011.2019.8956544.
[121] G. Ferrari, F. Gozzini, A. Molari, and M. Sampietro, “Transimpedance Amplifier for High Sensitivity Current Measurements on Nanodevices,” *IEEE Journal of Solid-State Circuits*, vol. 44, no. 5, pp. 1609–1616, May 2009, doi: 10.1109/JSSC.2009.2016998.
[122] C.-L. Hsu, H. Jiang, A. G. Venkatesh, and D. A. Hall, “A Hybrid Semi-Digital Transimpedance Amplifier With Noise Cancellation Technique for Nanopore-Based DNA Sequencing,” *IEEE*

Transactions on Biomedical Circuits and Systems, vol. 9, no. 5, pp. 652–661, Oct. 2015, doi: 10.1109/TBCAS.2015.2496232.

[123] C.-L. Hsu and D. A. Hall, "A current-measurement front-end with 160dB dynamic range and 7ppm INL," in *2018 IEEE International Solid - State Circuits Conference - (ISSCC)*, Feb. 2018, pp. 326–328. doi: 10.1109/ISSCC.2018.8310316.

[124] J. Kim, "A novel input-parasitic compensation technique for a nanopore-based CMOS DNA detection sensor | SpringerLink," *Journal of the Korean Physical Society*, vol. 69, no. 11, 2016, doi: 10.3938/jkps.69.1705.

[125] J. Kim, R. Maitra, K. D. Pedrotti, and W. B. Dunbar, "A Patch-Clamp ASIC for Nanopore-Based DNA Analysis," *IEEE Transactions on Biomedical Circuits and Systems*, vol. 7, no. 3, pp. 285–295, Jun. 2013, doi: 10.1109/TBCAS.2012.2200893.

[126] J. Kim, K. Pedrotti, and W. B. Dunbar, "An area-efficient low-noise CMOS DNA detection sensor for multichannel nanopore applications," *Sensors and Actuators B: Chemical*, vol. 176, pp. 1051–1055, Jan. 2013, doi: 10.1016/j.snb.2012.08.075.

[127] Y. Park, J. Yun, and J. Kim, "Low-noise Transimpedance Amplifier Design using Chopper-stabilized Technique for Nanopore Applications," in *2018 40th Annual International Conference of the IEEE Engineering in Medicine and Biology Society (EMBC)*, Jul. 2018, pp. 1–4. doi: 10.1109/EMBC.2018.8513397.

[128] J. K. Rosenstein, S. Ramakrishnan, J. Roseman, and K. L. Shepard, "Single Ion Channel Recordings with CMOS-Anchored Lipid Membranes," *Nano Lett.*, vol. 13, no. 6, pp. 2682–2686, Jun. 2013, doi: 10.1021/nl400822r.

[129] S. Shekar *et al.*, "Measurement of DNA Translocation Dynamics in a Solid-State Nanopore at 100 ns Temporal Resolution," *Nano Lett.*, vol. 16, no. 7, pp. 4483–4489, Jul. 2016, doi: 10.1021/acs.nanolett.6b01661.

[130] M. Taherzadeh-Sani, S. M. Hussain Hussaini, H. Rezaee-Dehsorkh, F. Nabki, and M. Sawan, "A 170-dB $Ømega $ CMOS TIA With 52-pA Input-Referred Noise and 1-MHz Bandwidth for Very Low Current Sensing," *IEEE Transactions on Very Large Scale Integration (VLSI) Systems*, vol. 25, no. 5, pp. 1756–1766, May 2017, doi: 10.1109/TVLSI.2017.2654452.

[131] J.-D. Yun, J. Kim, and J.-B. Park, "An integrated potentiostat sensor with digitally-controlled input-parasitic compensation for nanopore applications," in *2015 IEEE SENSORS*, Nov. 2015, pp. 1–4. doi: 10.1109/ICSENS.2015.7370517.

[132] M. Carminati, G. Ferrari, M. Sampietro, A. P. Ivanov, and T. Albrecht, "Low-noise dual-channel current amplifier for DNA sensing with solid-state nanopores," in *2012 19th IEEE International Conference on Electronics, Circuits, and Systems (ICECS 2012)*, Dec. 2012, pp. 817–820. doi: 10.1109/ICECS.2012.6463534.

[133] P. Ciccarella, M. Carminati, G. Ferrari, R. Fraccari, and A. Bahrami, "Integrated low-noise current amplifier for glass-based nanopore sensing," in *2014 10th Conference on Ph.D. Research in Microelectronics and Electronics (PRIME)*, Jun. 2014, pp. 1–4. doi: 10.1109/PRIME.2014.6872701.

[134] C. Ciofi, F. Crupi, C. Pace, and G. Scandurra, "How to enlarge the bandwidth without increasing the noise in OP-AMP-based transimpedance amplifier," *IEEE Transactions on Instrumentation and Measurement*, vol. 55, no. 3, pp. 814–819, Jun. 2006, doi: 10.1109/TIM.2006.873782.

[135] C.-L. Hsu, “Ultra-Low Noise Current Measurement Front-Ends for Biological Applications,” UC San Diego, 2018. [Online]. Available: https://escholarship.org/uc/item/4r0185pn
[136] J. Yun, H. Choi, and J. Kim, “Low-noise wide-bandwidth DNA readout instrument for nanopore applications,” *Electronics Letters*, vol. 53, no. 11, pp. 706–708, 2017, doi: 10.1049/el.2017.0870.
[137] J.-D. Yun, J. Kim, and J.-B. Park, “A low-noise and wide-bandwidth transimpedacne amplifier design for bionanopore applications,” in *2015 International SoC Design Conference (ISOCC)*, Nov. 2015, pp. 327–328. doi: 10.1109/ISOCC.2015.7401720.
[138] S. Marion, M. Macha, S. J. Davis, A. Chernev, and A. Radenovic, “Wetting of nanopores probed with pressure,” *Phys. Chem. Chem. Phys.*, vol. 23, no. 8, pp. 4975–4987, Mar. 2021, doi: 10.1039/D1CP00253H.
[139] A. Fragasso, S. Schmid, and C. Dekker, “Comparing Current Noise in Biological and Solid-State Nanopores,” *ACS Nano*, vol. 14, no. 2, pp. 1338–1349, Feb. 2020, doi: 10.1021/acsnano.9b09353.
[140] S. Liang *et al.*, “Noise in nanopore sensors: Sources, models, reduction, and benchmarking,” *Nanotechnology and Precision Engineering*, vol. 3, no. 1, pp. 9–17, Mar. 2020, doi: 10.1016/j.npe.2019.12.008.
[141] M. S. BARTLETT, “PERIODOGRAM ANALYSIS AND CONTINUOUS SPECTRA,” *Biometrika*, vol. 37, no. 1–2, pp. 1–16, Jun. 1950, doi: 10.1093/biomet/37.1-2.1.
[142] P. Welch, “The use of fast Fourier transform for the estimation of power spectra: A method based on time averaging over short, modified periodograms,” *IEEE Transactions on Audio and Electroacoustics*, vol. 15, no. 2, pp. 70–73, Jun. 1967, doi: 10.1109/TAU.1967.1161901.
[143] J.-J. Greffet, “Laws of Macroscopic Heat Transferand Their Limits,” in *Microscale and Nanoscale Heat Transfer*, S. Volz, Ed. Berlin, Heidelberg: Springer, 2007, pp. 1–13. doi: 10.1007/11767862_1.
[144] D. W. Hahn and M. N. Özişik, “Introduction to Microscale Heat Conduction,” in *Heat Conduction*, John Wiley & Sons, Ltd, 2012, pp. 651–678. doi: 10.1002/9781118411285.ch16.
[145] M. Matsumoto, “How Can Molecular Simulations Contribute to Thermal Engineering ?
— Topics from Microbubbles and Microscale Heat Conduction —,” *Journal of Thermal Science and Technology*, vol. 3, no. 2, pp. 309–318, 2008, doi: 10.1299/jtst.3.309.
[146] G. Kalyoncu and M. Barisik, “Analytical solution of micro-/nanoscale convective liquid flows in tubes and slits,” *Microfluid Nanofluid*, vol. 21, no. 9, p. 147, Aug. 2017, doi: 10.1007/s10404-017-1985-5.
[147] Q. Yang, B. Su, Y. Wang, and W. Wu, “Low-voltage efficient electroosmotic pumps with ultrathin silica nanoporous membrane,” *ELECTROPHORESIS*, vol. 40, no. 16–17, pp. 2149–2156, 2019, doi: 10.1002/elps.201800533.
[148] M. Barisik and A. Beskok, “Equilibrium molecular dynamics studies on nanoscale-confined fluids,” *Microfluid Nanofluid*, vol. 11, no. 3, pp. 269–282, Sep. 2011, doi: 10.1007/s10404-011-0794-5.
[149] L. R. Griffin *et al.*, “Direct measurements of ionic liquid layering at a single mica–liquid interface and in nano-films between two mica–liquid interfaces,” *Phys. Chem. Chem. Phys.*, vol. 19, no. 1, pp. 297–304, Dec. 2016, doi: 10.1039/C6CP05757H.

[150] A. Agrawal, H. M. Kushwaha, and R. S. Jadhav, “Introduction to Microscale Flows and Mathematical Modelling,” in *Microscale Flow and Heat Transfer*, A. Agrawal, H. M. Kushwaha, and R. S. Jadhav, Eds. Cham: Springer International Publishing, 2020, pp. 1–23. doi: 10.1007/978-3-030-10662-1_1.

[151] S. Volz, Ed., *Microscale and Nanoscale Heat Transfer*. Berlin, Heidelberg: Springer, 2007. doi: 10.1007/11767862_1.

[152] M. Farshad and J. C. Rasaiah, “Molecular Dynamics Simulation Study of Transverse and Longitudinal Ionic Currents in Solid-State Nanopore DNA Sequencing,” *ACS Appl. Nano Mater.*, vol. 3, no. 2, pp. 1438–1447, Feb. 2020, doi: 10.1021/acsanm.9b02280.

[153] N. E. Good, G. D. Winget, W. Winter, T. N. Connolly, S. Izawa, and R. M. M. Singh, “Hydrogen Ion Buffers for Biological Research,” *Biochemistry*, vol. 5, no. 2, pp. 467–477, Feb. 1966, doi: 10.1021/bi00866a011.

[154] J. Li, M. Gershow, D. Stein, E. Brandin, and J. A. Golovchenko, “DNA molecules and configurations in a solid-state nanopore microscope,” *Nature Mater*, vol. 2, no. 9, pp. 611–615, Sep. 2003, doi: 10.1038/nmat965.

[155] S. Geggier, A. Kotlyar, and A. Vologodskii, “Temperature dependence of DNA persistence length,” *Nucleic Acids Research*, vol. 39, no. 4, pp. 1419–1426, Mar. 2011, doi: 10.1093/nar/gkq932.

[156] A. J. Storm, C. Storm, J. Chen, H. Zandbergen, J.-F. Joanny, and C. Dekker, “Fast DNA Translocation through a Solid-State Nanopore,” *Nano Lett.*, vol. 5, no. 7, pp. 1193–1197, Jul. 2005, doi: 10.1021/nl048030d.

[157] E. E. Michaelides, “Brownian movement and thermophoresis of nanoparticles in liquids,” *International Journal of Heat and Mass Transfer*, vol. 81, pp. 179–187, Feb. 2015, doi: 10.1016/j.ijheatmasstransfer.2014.10.019.

[158] T. Ikeda and M. Matsumoto, “Relative Determination of Soret Coefficients of Electrolytes. II1,” *J. Phys. Chem.*, vol. 69, no. 11, pp. 3755–3758, Nov. 1965, doi: 10.1021/j100895a018.

[159] M. P. Jonsson and C. Dekker, “Plasmonic Nanopore for Electrical Profiling of Optical Intensity Landscapes,” *Nano Lett.*, vol. 13, no. 3, pp. 1029–1033, Mar. 2013, doi: 10.1021/nl304213s.

[160] E. D. Holmstrom, N. F. Dupuis, and D. J. Nesbitt, “Pulsed IR Heating Studies of Single-Molecule DNA Duplex Dissociation Kinetics and Thermodynamics,” *Biophysical Journal*, vol. 106, no. 1, pp. 220–231, Jan. 2014, doi: 10.1016/j.bpj.2013.11.008.

[161] A. Meller, L. Nivon, and D. Branton, “Voltage-Driven DNA Translocations through a Nanopore,” *Phys. Rev. Lett.*, vol. 86, no. 15, pp. 3435–3438, Apr. 2001, doi: 10.1103/PhysRevLett.86.3435.

[162] A. Jain and K. E. Goodson, “Thermal microdevices for biological and biomedical applications,” *Journal of Thermal Biology*, vol. 36, no. 4, pp. 209–218, May 2011, doi: 10.1016/j.jtherbio.2011.02.006.

[163] L. Jasińska and K. Malecha, “Microfluidic Modules Integrated with Microwave Components—Overview of Applications from the Perspective of Different Manufacturing Technologies,” *Sensors*, vol. 21, no. 5, Art. no. 5, Jan. 2021, doi: 10.3390/s21051710.

[164] M. B. Kulkarni and S. Goel, “Advances in continuous-flow based microfluidic PCR devices—a review,” *Eng. Res. Express*, vol. 2, no. 4, p. 042001, Dec. 2020, doi: 10.1088/2631-8695/abd287.

[165] N. Y. Lee, “A review on microscale polymerase chain reaction based methods in molecular diagnosis, and future prospects for the fabrication of fully integrated portable biomedical devices,” *Microchim Acta*, vol. 185, no. 6, p. 285, May 2018, doi: 10.1007/s00604-018-2791-9.
[166] V. Miralles, A. Huerre, F. Malloggi, and M.-C. Jullien, “A Review of Heating and Temperature Control in Microfluidic Systems: Techniques and Applications,” *Diagnostics*, vol. 3, no. 1, Art. no. 1, Mar. 2013, doi: 10.3390/diagnostics3010033.
[167] J. F. Tullius, R. Vajtai, and Y. Bayazitoglu, “A Review of Cooling in Microchannels,” *Heat Transfer Engineering*, vol. 32, no. 7–8, pp. 527–541, Jun. 2011, doi: 10.1080/01457632.2010.506390.
[168] G. V. Casquillas *et al.*, “Fast microfluidic temperature control for high resolution live cell imaging,” *Lab Chip*, vol. 11, no. 3, pp. 484–489, Feb. 2011, doi: 10.1039/C0LC00222D.
[169] G. Velve-Casquillas, J. Costa, F. Carlier-Grynkorn, A. Mayeux, and P. T. Tran, “Chapter 11 - A Fast Microfluidic Temperature Control Device for Studying Microtubule Dynamics in Fission Yeast,” in *Methods in Cell Biology*, vol. 97, L. Cassimeris and P. Tran, Eds. Academic Press, 2010, pp. 185–201. doi: 10.1016/S0091-679X(10)97011-8.
[170] A. J. de Mello, M. Habgood, N. L. Lancaster, T. Welton, and R. C. R. Wootton, “Precise temperature control in microfluidic devices using Joule heating of ionic liquids,” *Lab Chip*, vol. 4, no. 5, pp. 417–419, Oct. 2004, doi: 10.1039/B405760K.
[171] G. Maltezos, A. Gomez, J. Zhong, F. A. Gomez, and A. Scherer, “Microfluidic polymerase chain reaction,” *Appl. Phys. Lett.*, vol. 93, no. 24, p. 243901, Dec. 2008, doi: 10.1063/1.3046789.
[172] G. Maltezos *et al.*, “Exploring the limits of ultrafast polymerase chain reaction using liquid for thermal heat exchange: A proof of principle,” *Appl. Phys. Lett.*, vol. 97, no. 26, p. 264101, Dec. 2010, doi: 10.1063/1.3530452.
[173] X. Qiu, M. G. Mauk, D. Chen, C. Liu, and H. H. Bau, “A large volume, portable, real-time PCR reactor,” *Lab Chip*, vol. 10, no. 22, pp. 3170–3177, Oct. 2010, doi: 10.1039/C0LC00038H.
[174] J. Yang *et al.*, “High sensitivity PCR assay in plastic micro reactors,” *Lab Chip*, vol. 2, no. 4, pp. 179–187, Nov. 2002, doi: 10.1039/B208405H.
[175] J. H. Daniel *et al.*, “Silicon microchambers for DNA amplification,” *Sensors and Actuators A: Physical*, vol. 71, no. 1, pp. 81–88, Nov. 1998, doi: 10.1016/S0924-4247(98)00158-7.
[176] M. P. Dinca, M. Gheorghe, M. Aherne, and P. Galvin, “Fast and accurate temperature control of a PCR microsystem with a disposable reactor,” *J. Micromech. Microeng.*, vol. 19, no. 6, p. 065009, May 2009, doi: 10.1088/0960-1317/19/6/065009.
[177] T.-M. Hsieh, C.-H. Luo, F.-C. Huang, J.-H. Wang, L.-J. Chien, and G.-B. Lee, “Enhancement of thermal uniformity for a microthermal cycler and its application for polymerase chain reaction,” *Sensors and Actuators B: Chemical*, vol. 130, no. 2, pp. 848–856, Mar. 2008, doi: 10.1016/j.snb.2007.10.063.
[178] A. I. K. Lao, T. M. H. Lee, I.-M. Hsing, and N. Y. Ip, “Precise temperature control of microfluidic chamber for gas and liquid phase reactions,” *Sensors and Actuators A: Physical*, vol. 84, no. 1, pp. 11–17, Aug. 2000, doi: 10.1016/S0924-4247(99)00356-8.
[179] K.-Y. Lien, S.-H. Lee, T.-J. Tsai, T.-Y. Chen, and G.-B. Lee, “A microfluidic-based system using reverse transcription polymerase chain reactions for rapid detection of aquaculture

diseases," *Microfluid Nanofluid*, vol. 7, no. 6, p. 795, Apr. 2009, doi: 10.1007/s10404-009-0438-1.

[180] E. Mavraki, D. Moschou, G. Kokkoris, N. Vourdas, S. Chatzandroulis, and A. Tserepi, "A continuous flow μPCR device with integrated microheaters on a flexible polyimide substrate," *Procedia Engineering*, vol. 25, pp. 1245–1248, Jan. 2011, doi: 10.1016/j.proeng.2011.12.307.

[181] P. Neuzil, C. Zhang, J. Pipper, S. Oh, and L. Zhuo, "Ultra fast miniaturized real-time PCR: 40 cycles in less than six minutes," *Nucleic Acids Research*, vol. 34, no. 11, p. e77, Jun. 2006, doi: 10.1093/nar/gkl416.

[182] S. Poser *et al.*, "Chip elements for fast thermocycling," *Sensors and Actuators A: Physical*, vol. 62, no. 1, pp. 672–675, Jul. 1997, doi: 10.1016/S0924-4247(97)01542-2.

[183] D. S. Yoon *et al.*, "Precise temperature control and rapid thermal cycling in a micromachined DNA polymerase chain reaction chip," *J. Micromech. Microeng.*, vol. 12, no. 6, pp. 813–823, Oct. 2002, doi: 10.1088/0960-1317/12/6/312.

[184] R. M. Guijt, A. Dodge, G. W. K. van Dedem, N. F. de Rooij, and E. Verpoorte, "Chemical and physical processes for integrated temperature control in microfluidic devices," *Lab Chip*, vol. 3, no. 1, pp. 1–4, Jan. 2003, doi: 10.1039/B210629A.

[185] A. Kempitiya, D. A. Borca-Tasciuc, H. S. Mohamed, and M. M. Hella, "Localized microwave heating in microwells for parallel DNA amplification applications," *Appl. Phys. Lett.*, vol. 94, no. 6, p. 064106, Feb. 2009, doi: 10.1063/1.3078273.

[186] T. Markovic, S. Liu, I. Ocket, and B. K. J. C. Nauwelaers, "A 20 GHz microwave heater for digital microfluidic," *International Journal of Microwave and Wireless Technologies*, vol. 9, no. 8, pp. 1591–1596, Oct. 2017, doi: 10.1017/S1759078717000563.

[187] K. Orrling, P. Nilsson, M. Gullberg, and M. Larhed, "An efficient method to perform milliliter-scale PCR utilizing highly controlled microwave thermocycling," *Chem. Commun.*, no. 7, pp. 790–791, Mar. 2004, doi: 10.1039/B317049G.

[188] J. J. Shah *et al.*, "Microwave dielectric heating of fluids in an integrated microfluidic device," *J. Micromech. Microeng.*, vol. 17, no. 11, pp. 2224–2230, Oct. 2007, doi: 10.1088/0960-1317/17/11/008.

[189] J. Kondoh, N. Shimizu, Y. Matsui, M. Sugimoto, and S. Shiokawa, "Development of temperature-control system for liquid droplet using surface Acoustic wave devices," *Sensors and Actuators A: Physical*, vol. 149, no. 2, pp. 292–297, Feb. 2009, doi: 10.1016/j.sna.2008.11.007.

[190] Y. Wang *et al.*, "A rapid and controllable acoustothermal microheater using thin film surface acoustic waves," *Sensors and Actuators A: Physical*, vol. 318, p. 112508, Feb. 2021, doi: 10.1016/j.sna.2020.112508.

[191] B. C. Giordano, J. Ferrance, S. Swedberg, A. F. R. Hühmer, and J. P. Landers, "Polymerase Chain Reaction in Polymeric Microchips: DNA Amplification in Less Than 240 Seconds," *Analytical Biochemistry*, vol. 291, no. 1, pp. 124–132, Apr. 2001, doi: 10.1006/abio.2000.4974.

[192] M.-S. Hung, C.-C. Ho, and C.-P. Chen, "Laser-induced heating integrated with a microfluidic platform for real-time DNA replication and detection," *JBO*, vol. 21, no. 8, p. 087003, Aug. 2016, doi: 10.1117/1.JBO.21.8.087003.

[193] R. P. Oda *et al.*, “Infrared-Mediated Thermocycling for Ultrafast Polymerase Chain Reaction Amplification of DNA,” *Anal. Chem.*, vol. 70, no. 20, pp. 4361–4368, Oct. 1998, doi: 10.1021/ac980452i.
[194] C. D. Ahrberg *et al.*, “Plasmonic heating-based portable digital PCR system,” *Lab Chip*, vol. 20, no. 19, pp. 3560–3568, Sep. 2020, doi: 10.1039/D0LC00788A.
[195] J. H. Son *et al.*, “Ultrafast photonic PCR,” *Light Sci Appl*, vol. 4, no. 7, pp. e280–e280, Jul. 2015, doi: 10.1038/lsa.2015.53.
[196] G. Rosengarten, S. Mutzenich, and K. Kalantar-zadeh, “Integrated microthermoelectric cooler for microfluidic channels,” *Experimental Thermal and Fluid Science*, vol. 30, no. 8, pp. 821–828, Aug. 2006, doi: 10.1016/j.expthermflusci.2006.03.011.
[197] G. Maltezos, A. Rajagopal, and A. Scherer, “Evaporative cooling in microfluidic channels,” *Appl. Phys. Lett.*, vol. 89, no. 7, p. 074107, Aug. 2006, doi: 10.1063/1.2234318.
[198] C. W. Chan, E. Siqueiros, J. Ling-Chin, M. Royapoor, and A. P. Roskilly, “Heat utilisation technologies: A critical review of heat pipes,” *Renewable and Sustainable Energy Reviews*, vol. 50, pp. 615–627, Oct. 2015, doi: 10.1016/j.rser.2015.05.028.
[199] N. K. Gupta, A. K. Tiwari, and S. K. Ghosh, “Heat transfer mechanisms in heat pipes using nanofluids – A review,” *Experimental Thermal and Fluid Science*, vol. 90, pp. 84–100, Jan. 2018, doi: 10.1016/j.expthermflusci.2017.08.013.
[200] A. S. Morris and R. Langari, “Chapter 14 - Temperature Measurement,” in *Measurement and Instrumentation*, A. S. Morris and R. Langari, Eds. Boston: Butterworth-Heinemann, 2012, pp. 347–396. doi: 10.1016/B978-0-12-381960-4.00014-0.
[201] D. G. Ullman, *The Mechanical Design Process*, 6th ed. David Ullman LLC, 2017.
[202] M. Razeghi and A. Rogalski, “Semiconductor ultraviolet detectors,” *Journal of Applied Physics*, vol. 79, no. 10, pp. 7433–7473, May 1996, doi: 10.1063/1.362677.
[203] Thermo Fisher, “Thermal cyclers: key thermal cycling concepts and ramp rates.” Thermo Fisher Scientific, 2015. Accessed: Jun. 06, 2022. [Online]. Available: https://tools.thermofisher.com/content/sfs/brochures/Thermal_Cycler_Ramp_RatesAppNote.pdf
[204] T. L. Bergman, A. Lavine, F. P. Incropera, and D. P. Dewitt, *Fundamentals of Heat and Mass Transfer*, 7th ed. John Wiley & Sons, Inc., 2011.
[205] J. E. Hesselgreaves, R. Law, and D. A. Reay, *Compact Heat Exchangers: Selection, Design and Operation*, 2nd ed. Oxford, UK: Elsevier Science & Technology, 2016.
[206] H. Lee, *Thermal Design: Heat Sinks, Thermoelectrics, Heat Pipes. Compact Heat Exchangers, and Solar Cells*. John Wiley & Sons, Inc., 2010.
[207] G. Narendran, G. Nagarajan, and Dr. A. Perumal D, “A Review on Recent Advances in Microchannel Heat Sink Configurations,” *Recent Patents on Mechanical Engineering*, vol. 11, Jul. 2018, doi: 10.2174/2212797611666180726124047.
[208] O. K. Siddiqui and S. M. Zubair, “Efficient energy utilization through proper design of microchannel heat exchanger manifolds: A comprehensive review,” *Renewable and Sustainable Energy Reviews*, vol. 74, pp. 969–1002, Jul. 2017, doi: 10.1016/j.rser.2017.01.074.
[209] K. Thulukkanam, *Heat Exchanger Design Handbook*, 2nd ed. CRC Press, 2013.

[210] P. M. Ligrani, S. Choi, A. R. Schallert, and P. Skogerboe, “Effects of Dean vortex pairs on surface heat transfer in curved channel flow,” *International Journal of Heat and Mass Transfer*, vol. 39, no. 1, pp. 27–37, Jan. 1996, doi: 10.1016/S0017-9310(96)85003-4.
[211] J. Peter B. Howell, D. R. Mott, J. P. Golden, and F. S. Ligler, “Design and evaluation of a Dean vortex-based micromixer,” *Lab Chip*, vol. 4, no. 6, pp. 663–669, Nov. 2004, doi: 10.1039/B407170K.
[212] A. Sudarsan and V. Ugaz, “Fluid mixing in planar spiral microchannels,” *Lab on a Chip*, vol. 6, no. 1, pp. 74–82, 2006, doi: 10.1039/B511524H.
[213] N. S. Virik *et al.*, “Evaluation of Heat Transfer Performance of a Spiral Microfluidic Heatsink and Heat Exchanger Device,” presented at the ASME 2018 16th International Conference on Nanochannels, Microchannels, and Minichannels, Aug. 2018. doi: 10.1115/ICNMM2018-7804.
[214] M. F. Ashby, *Materials Selection in Mechanical Design*, 4th ed. Oxford, UK: Butterworth-Heinemann, 2011.
[215] S. Barber-Zucker, B. Shaanan, and R. Zarivach, “Transition metal binding selectivity in proteins and its correlation with the phylogenomic classification of the cation diffusion facilitator protein family,” *Sci Rep*, vol. 7, no. 1, p. 16381, 2017, doi: 10.1038/s41598-017-16777-5.
[216] Y. S. Hedberg and I. O. Wallinder, “Metal release from stainless steel in biological environments: A review,” *Biointerphases*, vol. 11, no. 1, p. 018901, Mar. 2016, doi: 10.1116/1.4934628.
[217] R. J. Narayan, Ed., *Materials for Medical Devices*. ASM International, 2012. doi: 10.31399/asm.hb.v23.9781627081986.
[218] C. Batich and P. Leamy, “BIOPOLYMERS,” in *Standard Handbook of Biomedical Engineering & Design*, First edition., New York: McGraw-Hill Education, 2003. [Online]. Available: https://www.accessengineeringlibrary.com/content/book/9780071356374/chapter/chapter11
[219] J. E. Mark, *Polymer Data Handbook*. Oxford University Press, Inc., 1999.
[220] D. Han *et al.*, “MCU based real-time temperature control system for universal microfluidic PCR chip,” *Microsyst Technol*, vol. 20, no. 3, pp. 471–476, Mar. 2014, doi: 10.1007/s00542-013-1970-1.
[221] S.-J. Kim, F. Wang, M. A. Burns, and K. Kurabayashi, “Temperature-Programmed Natural Convection for Micromixing and Biochemical Reaction in a Single Microfluidic Chamber,” *Anal. Chem.*, vol. 81, no. 11, pp. 4510–4516, Jun. 2009, doi: 10.1021/ac900512x.
[222] S. Kumar *et al.*, “Microfluidic-integrated biosensors: Prospects for point-of-care diagnostics,” *Biotechnology Journal*, vol. 8, no. 11, pp. 1267–1279, 2013, doi: https://doi.org/10.1002/biot.201200386.
[223] B. Selva, P. Mary, and M.-C. Jullien, “Integration of a uniform and rapid heating source into microfluidic systems,” *Microfluid Nanofluid*, vol. 8, no. 6, pp. 755–765, Jun. 2010, doi: 10.1007/s10404-009-0505-7.
[224] J. Wu, W. Cao, W. Wen, D. C. Chang, and P. Sheng, “Polydimethylsiloxane microfluidic chip with integrated microheater and thermal sensor,” *Biomicrofluidics*, vol. 3, no. 1, p. 012005, Mar. 2009, doi: 10.1063/1.3058587.

[225] D. Curtis Saunders *et al.*, “Rapid, quantitative, reverse transcription PCR in a polymer microfluidicchip,” *Biosensors and Bioelectronics*, vol. 44, pp. 222–228, Jun. 2013, doi: 10.1016/j.bios.2013.01.019.
[226] Z. J. Jiao, X. Y. Huang, and N.-T. Nguyen, “Manipulation of a droplet in a planar channel by periodic thermocapillary actuation,” *J. Micromech. Microeng.*, vol. 18, no. 4, p. 045027, Mar. 2008, doi: 10.1088/0960-1317/18/4/045027.
[227] S. M. Torres Delgado, J. G. Korvink, and D. Mager, “The eLoaD platform endows centrifugal microfluidics with on-disc power and communication,” *Biosensors and Bioelectronics*, vol. 117, pp. 464–473, Oct. 2018, doi: 10.1016/j.bios.2018.05.056.
[228] Z. Yan, X. Huang, and C. Yang, “Deposition of colloidal particles in a microchannel at elevated temperatures,” *Microfluid Nanofluid*, vol. 18, no. 3, pp. 403–414, Mar. 2015, doi: 10.1007/s10404-014-1448-1.
[229] D. Moschou *et al.*, “All-plastic, low-power, disposable, continuous-flow PCR chip with integrated microheaters for rapid DNA amplification,” *Sensors and Actuators B: Chemical*, vol. 199, pp. 470–478, Aug. 2014, doi: 10.1016/j.snb.2014.04.007.
[230] R. H. Liu, J. Yang, R. Lenigk, J. Bonanno, and P. Grodzinski, “Self-Contained, Fully Integrated Biochip for Sample Preparation, Polymerase Chain Reaction Amplification, and DNA Microarray Detection,” *Anal. Chem.*, vol. 76, no. 7, pp. 1824–1831, Apr. 2004, doi: 10.1021/ac0353029.
[231] E. Pishbin, M. Eghbal, M. Navidbakhsh, and M. Zandi, “Localized air-mediated heating method for isothermal and rapid thermal processing on lab-on-a-disk platforms,” *Sensors and Actuators B: Chemical*, vol. 294, pp. 270–282, Sep. 2019, doi: 10.1016/j.snb.2019.05.039.
[232] D. Ross and L. E. Locascio, “Microfluidic Temperature Gradient Focusing,” *Anal. Chem.*, vol. 74, no. 11, pp. 2556–2564, Jun. 2002, doi: 10.1021/ac025528w.
[233] C. Fermér, P. Nilsson, and M. Larhed, “Microwave-assisted high-speed PCR,” *European Journal of Pharmaceutical Sciences*, vol. 18, no. 2, pp. 129–132, Feb. 2003, doi: 10.1016/S0928-0987(02)00252-X.
[234] K. Hettiarachchi, H. Kim, and G. W. Faris, “Optical manipulation and control of real-time PCR in cell encapsulating microdroplets by IR laser,” *Microfluid Nanofluid*, vol. 13, no. 6, pp. 967–975, Dec. 2012, doi: 10.1007/s10404-012-1016-5.
[235] H. Kim, S. Vishniakou, and G. W. Faris, “Petri dish PCR: laser-heated reactions in nanoliter droplet arrays,” *Lab Chip*, vol. 9, no. 9, pp. 1230–1235, May 2009, doi: 10.1039/B817288A.
[236] A. J. L. Morgan *et al.*, “Efficient microwave heating of microfluidic systems,” *Sensors and Actuators B: Chemical*, vol. 181, pp. 904–909, May 2013, doi: 10.1016/j.snb.2013.02.099.
[237] B. Shu, C. Zhang, and D. Xing, “Segmented continuous-flow multiplex polymerase chain reaction microfluidics for high-throughput and rapid foodborne pathogen detection,” *Analytica Chimica Acta*, vol. 826, pp. 51–60, May 2014, doi: 10.1016/j.aca.2014.04.017.
[238] M. Bu *et al.*, “A temperature control method for shortening thermal cycling time to achieve rapid polymerase chain reaction (PCR) in a disposable polymer microfluidic device,” *J. Micromech. Microeng.*, vol. 23, no. 7, p. 074002, Jun. 2013, doi: 10.1088/0960-1317/23/7/074002.

[239] M. Biron, “4 - Detailed Accounts of Thermoset Resins for Molding and Composite Matrices,” in *Thermosets and Composites (Second Edition)*, M. Biron, Ed. Oxford: William Andrew Publishing, 2014, pp. 145–267. doi: 10.1016/B978-1-4557-3124-4.00004-3.
[240] W. D. Callister and D. G. Rethwisch, *Materials science and engineering: an introduction*, 9th ed. John Wiley & Sons, Inc., 2014.
[241] R. Amin *et al.*, “3D-printed microfluidic devices,” *Biofabrication*, vol. 8, no. 2, p. 022001, Jun. 2016, doi: 10.1088/1758-5090/8/2/022001.
[242] A.-G. Niculescu, C. Chircov, A. C. Bîrcă, and A. M. Grumezescu, “Fabrication and Applications of Microfluidic Devices: A Review,” *International Journal of Molecular Sciences*, vol. 22, no. 4, Art. no. 4, Jan. 2021, doi: 10.3390/ijms22042011.
[243] A. V. Nielsen, M. J. Beauchamp, G. P. Nordin, and A. T. Woolley, “3D Printed Microfluidics,” *Annual Review of Analytical Chemistry*, vol. 13, no. 1, pp. 45–65, 2020, doi: 10.1146/annurev-anchem-091619-102649.
[244] S. Tasoglu and A. Folch, *3D printed microfluidic devices*. MDPI, 2019.
[245] P. J. J. Bártolo, Ed., *Stereolithography*. Boston, MA: Springer US, 2014. [Online]. Available: https://books.scholarsportal.info/uri/ebooks/ebooks2/springer/2012-05-07/1/9780387929040
[246] Formlabs, “High Temp resin for heat resistance, material data sheet FLHTAM01.” Formlabs, 2017.
[247] Formlabs, “High Temp, photoreactive resin for Form 1+, form 2, safety data sheet.” Formlabs, 2016. [Online]. Available: https://formlabs-media.formlabs.com/datasheets/Safety_Data_Sheet_EN_-_High_Temp.pdf
[248] Matweb, “Overview of materials for Acrylic, General Purpose, Molded.” http://www.matweb.com/search/DataSheet.aspx?MatGUID=3cb08da2a0054447a3790015b7214d07
[249] “PMMA.” http://www.mit.edu/~6.777/matprops/pmma.htm
[250] B. Bai, L. Guo, Z. Feng, and X. Chen, “Turbulent heat transfer in a horizontal helically coiled tube,” *Heat Transfer—Asian Research*, vol. 28, no. 5, pp. 395–403, 1999, doi: 10.1002/(SICI)1523-1496(1999)28:5<395::AID-HTJ5>3.0.CO;2-Y.
[251] V. Kubair and N. R. Kuloor, “Heat transfer to newtonian fluids in coiled pipes in laminar flow,” *International Journal of Heat and Mass Transfer*, vol. 9, no. 1, pp. 63–75, Jan. 1966, doi: 10.1016/0017-9310(66)90057-3.
[252] R. L. MANLAPAZ and S. W. CHURCHILL, “Fully Developed Laminar Flow in a Helically Coiled Tube of Finite Pitch,” *Chemical Engineering Communications*, vol. 7, no. 1–3, pp. 57–78, Jan. 1980, doi: 10.1080/00986448008912549.
[253] R. L. MANLAPAZ and S. W. CHURCHILL, “Fully Developed Laminar Convection from a Helical Coil,” *Chemical Engineering Communications*, vol. 9, no. 1–6, pp. 185–200, Jan. 1981, doi: 10.1080/00986448108911023.
[254] Y. Mori and W. Nakayama, “Study of forced convective heat transfer in curved pipes (2nd report, turbulent region),” *International Journal of Heat and Mass Transfer*, vol. 10, no. 1, pp. 37–59, Jan. 1967, doi: 10.1016/0017-9310(67)90182-2.
[255] Y. Mori and W. Nakayama, “Study on forced convective heat transfer in curved pipes: (3rd report, theoretical analysis under the condition of uniform wall temperature and practical

formulae),” *International Journal of Heat and Mass Transfer*, vol. 10, no. 5, pp. 681–695, May 1967, doi: 10.1016/0017-9310(67)90113-5.
[256] G. F. C. Rogers and Y. R. Mayhew, “Heat transfer and pressure loss in helically coiled tubes with turbulent flow,” *International Journal of Heat and Mass Transfer*, vol. 7, no. 11, pp. 1207–1216, Nov. 1964, doi: 10.1016/0017-9310(64)90062-6.
[257] R. A. Seban and E. F. McLaughlin, “Heat transfer in tube coils with laminar and turbulent flow,” *International Journal of Heat and Mass Transfer*, vol. 6, no. 5, pp. 387–395, May 1963, doi: 10.1016/0017-9310(63)90100-5.
[258] M. Yasuo and N. Wataru, “Study on forced convective heat transfer in curved pipes: (1st report, laminar region),” *International Journal of Heat and Mass Transfer*, vol. 8, no. 1, pp. 67–82, Jan. 1965, doi: 10.1016/0017-9310(65)90098-0.
[259] F. Bozzoli, L. Cattani, S. Rainieri, F. S. Viloche Bazán, and L. S. Borges, “Estimation of the local heat-transfer coefficient in the laminar flow regime in coiled tubes by the Tikhonov regularisation method,” *International Journal of Heat and Mass Transfer*, vol. 72, pp. 352–361, May 2014, doi: 10.1016/j.ijheatmasstransfer.2014.01.019.
[260] F. Bozzoli, L. Cattani, A. Mocerino, and S. Rainieri, “Turbulent flow regime in coiled tubes: local heat-transfer coefficient,” *Heat Mass Transfer*, vol. 54, no. 8, pp. 2371–2381, Aug. 2018, doi: 10.1007/s00231-017-2127-z.
[261] R. M. Manglik, “Enhancement of Convective Heat Transfer,” in *Handbook of Thermal Science and Engineering*, F. A. Kulacki, Ed. Cham: Springer International Publishing, 2017, pp. 1–31. doi: 10.1007/978-3-319-32003-8_14-1.
[262] L. Cattani, F. Bozzoli, and S. Rainieri, “Experimental study of the transitional flow regime in coiled tubes by the estimation of local convective heat transfer coefficient,” *International Journal of Heat and Mass Transfer*, vol. 112, pp. 825–836, Sep. 2017, doi: 10.1016/j.ijheatmasstransfer.2017.05.003.
[263] E. S. Menon, *Piping calculations manual*. McGraw-Hill Education, 2005.
[264] B. Silowash, *Piping systems manual*. McGraw Hill Professional, 2009.
[265] P. Mishra and S. N. Gupta, “Momentum Transfer in Curved Pipes. 1. Newtonian Fluids,” *Ind. Eng. Chem. Proc. Des. Dev.*, vol. 18, no. 1, pp. 130–137, Jan. 1979, doi: 10.1021/i260069a017.
[266] P. Mishra and S. N. Gupta, “Momentum Transfer in Curved Pipes. 2. Non-Newtonian Fluids,” *Ind. Eng. Chem. Proc. Des. Dev.*, vol. 18, no. 1, pp. 137–142, Jan. 1979, doi: 10.1021/i260069a018.
[267] S. W. Churchill and H. H. S. Chu, “Correlating equations for laminar and turbulent free convection from a vertical plate,” *International Journal of Heat and Mass Transfer*, vol. 18, no. 11, pp. 1323–1329, Nov. 1975, doi: 10.1016/0017-9310(75)90243-4.
[268] J. R. Lloyd and W. R. Moran, “Natural Convection Adjacent to Horizontal Surface of Various Planforms,” *Journal of Heat Transfer*, vol. 96, no. 4, pp. 443–447, Nov. 1974, doi: 10.1115/1.3450224.
[269] E. Radziemska and W. M. Lewandowski, “Heat transfer by natural convection from an isothermal downward-facing round plate in unlimited space,” *Applied Energy*, vol. 68, no. 4, pp. 347–366, Apr. 2001, doi: 10.1016/S0306-2619(00)00061-1.
[270] Dessault Systems, “TECHNICAL REFERENCE: SOLIDWORKS FLOW SIMULATION 2020.” Dessault Systems, 2020.

[271] J. E. Bardina, P. G. Huang, and T. J. Coakley, “Turbulence Modeling Validation, Testing, and Development,” A-976276, Apr. 1997. Accessed: Dec. 17, 2021. [Online]. Available: https://ntrs.nasa.gov/citations/19970017828
[272] N. T. Basse, “Turbulence Intensity Scaling: A Fugue,” *Fluids*, vol. 4, no. 4, Art. no. 4, Dec. 2019, doi: 10.3390/fluids4040180.
[273] CFD Online, “Turbulence intensity,” 2020. https://www.cfd-online.com/Wiki/Turbulence_intensity
[274] R. Siegel and J. R. Howell, *Thermal Radiation Heat Transfer*, 3rd ed. Hemisphere Publishing, 1992.
[275] J. Tu, G.-H. Yeoh, and C. Liu, “Chapter 5 - CFD Techniques: The Basics,” in *Computational Fluid Dynamics (Third Edition)*, J. Tu, G.-H. Yeoh, and C. Liu, Eds. Butterworth-Heinemann, 2018, pp. 155–210. doi: 10.1016/B978-0-08-101127-0.00005-2.
[276] R. Chatterjee, V. S. Duryodhan, and A. Agrawal, “Impact of aspect ratio and thermophysical properties on heat transfer behavior in spiral microchannel,” *International Journal of Thermal Sciences*, vol. 172, p. 107335, Feb. 2022, doi: 10.1016/j.ijthermalsci.2021.107335.
[277] J. C. Kurnia, A. P. Sasmito, and A. S. Mujumdar, “Laminar convective heat transfer for in-plane spiral coils of noncircular cross sections ducts: A computational fluid dynamics study,” *Thermal Science*, vol. 16, no. 1, pp. 109–118, 2012.
[278] S. D. Marshall, R. Arayanarakool, L. Balasubramaniam, B. Li, P. S. Lee, and P. C. Y. Chen, “Heat Exchanger Improvement via Curved Microfluidic Channels: Part 2 — Investigation Into Heat Transfer Enhancement due to the Dynamics of Dean Vortices,” presented at the ASME 2016 5th International Conference on Micro/Nanoscale Heat and Mass Transfer, Mar. 2016. doi: 10.1115/MNHMT2016-6406.
[279] S. D. Marshall, B. Li, R. Arayanarakool, P. Seng Lee, L. Balasubramaniam, and P. C. Y. Chen, “Heat Exchanger Improvement Via Curved Microfluidic Channels: Impacts of Cross-Sectional Geometry and Dean Vortex Strength,” *Journal of Heat Transfer*, vol. 140, no. 1, Aug. 2017, doi: 10.1115/1.4037339.
[280] K. Narrein, S. Sivasankaran, and P. Ganesan, “Two-Phase Analysis of A Helical Microchannel Heat Sink Using Nanofluids,” *Numerical Heat Transfer, Part A: Applications*, vol. 68, no. 11, pp. 1266–1279, Dec. 2015, doi: 10.1080/10407782.2015.1032017.
[281] C. Golub, L. Lei, and G. Ling, “Flow Rate Consistency of Peristaltic Pump Tubing Materials in Chemical Dispensing Applications,” Saint-Gobain Process Systems, White Paper, 2017. [Online]. Available: https://www.processsystems.saint-gobain.com/sites/imdf.processsystems.com/files/flow-rate-consistency-of-peristaltic-pump-tubing-materials_0.pdf
[282] D. Szyk, K. Dempsey, and C. Golub, “Flow Rate Stability of Medical Peristaltic Pump Tubing Materials | Medical,” Saint-Gobain Process Systems, White Paper, 2020. [Online]. Available: https://www.medical.saint-gobain.com/resources/white-papers/flow-rate-stability-medical-peristaltic-pump-tubing-materials
[283] S. Grimnes and O. G. Martinsen, *Bioimpedance and Bioelectricity Basics*, 3rd ed. Academic Press, 2015. [Online]. Available: https://www.sciencedirect.com/book/9780124114708/bioimpedance-and-bioelectricity-basics

[284] R. S. Greeley, W. T. Smith, R. W. Stoughton, and M. H. Lietzke, “ELECTROMOTIVE FORCE STUDIES IN AQUEOUS SOLUTIONS AT ELEVATED TEMPERATURES. I. THE STANDARD POTENTIAL OF THE SILVER-SILVER CHLORIDE ELECTRODE1,” *J. Phys. Chem.*, vol. 64, no. 5, pp. 652–657, May 1960, doi: 10.1021/j100834a031.

[285] I. Maksimov *et al.*, “Temporal stability of standard potentials of silver–silver chloride reference electrodes,” *Accred Qual Assur*, vol. 17, no. 5, pp. 529–533, Oct. 2012, doi: 10.1007/s00769-012-0913-3.

[286] A. Brumby *et al.*, “Silver, Silver Compounds, and Silver Alloys,” in *Ullmann’s Encyclopedia of Industrial Chemistry*, John Wiley & Sons, Ltd, 2008. doi: 10.1002/14356007.a24_107.pub2.

[287] B. J. Polk, A. Stelzenmuller, G. Mijares, W. MacCrehan, and M. Gaitan, “Ag/AgCl microelectrodes with improved stability for microfluidics,” *Sensors and Actuators B: Chemical*, vol. 114, no. 1, pp. 239–247, Mar. 2006, doi: 10.1016/j.snb.2005.03.121.

[288] G. E. F. Lundell and J. I. Hoffman, “The effect of light on silver chloride in chemical analyses.” National Institute of Standards and Technology, 1930. [Online]. Available: https://archive.org/details/effectoflightons41109lund/mode/2up

[289] S. W. Kowalczyk, D. B. Wells, A. Aksimentiev, and C. Dekker, “Slowing down DNA Translocation through a Nanopore in Lithium Chloride,” *Nano Lett.*, vol. 12, no. 2, pp. 1038–1044, Feb. 2012, doi: 10.1021/nl204273h.

[290] J. Uplinger, B. Thomas, R. Rollings, D. Fologea, D. McNabb, and J. Li, “K+, Na+, and Mg2+ on DNA translocation in silicon nitride nanopores,” *ELECTROPHORESIS*, vol. 33, no. 23, pp. 3448–3457, 2012, doi: 10.1002/elps.201200165.

[291] Y. Zhang, L. Liu, J. Sha, Z. Ni, H. Yi, and Y. Chen, “Nanopore detection of DNA molecules in magnesium chloride solutions,” *Nanoscale Res Lett*, vol. 8, no. 1, Art. no. 1, Dec. 2013, doi: 10.1186/1556-276X-8-245.

[292] U. Wietelmann and M. Steinbild, “Lithium and Lithium Compounds,” in *Ullmann’s Encyclopedia of Industrial Chemistry*, John Wiley & Sons, Ltd, 2014, pp. 1–38. doi: 10.1002/14356007.a15_393.pub2.

[293] S. Bouzenada, A. N. Kaabi, L. Frainkin, T. Salmon, and A. Léonard, “Experimental Comparative Study on Lithium Chloride and Calcium Chloride Desiccants,” *Procedia Computer Science*, vol. 83, pp. 718–725, Jan. 2016, doi: 10.1016/j.procs.2016.04.159.

[294] P. E. Keller and R. T. Kouzes, “Water vapor permeation in plastics,” Pacific Northwest National Lab.(PNNL), Richland, WA (United States), 2017.

[295] L. K. Massey, *Permeability properties of plastics and elastomers: a guide to packaging and barrier materials*. Cambridge University Press, 2003.

[296] H. R. Held and S. Landi, “Water permeability of elastomers,” *Journal of Biological Standardization*, vol. 5, no. 2, pp. 111–119, Jan. 1977, doi: 10.1016/0092-1157(77)90005-1.

[297] W. Boyes, *Instrumentation reference book*, 4th ed. Butterworth-Heinemann, 2010.

[298] X. Wu, Y. Gong, S. Xu, Z. Yan, X. Zhang, and S. Yang, “Electrical Conductivity of Lithium Chloride, Lithium Bromide, and Lithium Iodide Electrolytes in Methanol, Water, and Their Binary Mixtures,” *J. Chem. Eng. Data*, vol. 64, no. 10, pp. 4319–4329, Oct. 2019, doi: 10.1021/acs.jced.9b00405.

[299] S. W. Allison and G. T. Gillies, “Remote thermometry with thermographic phosphors: Instrumentation and applications,” *Review of Scientific Instruments*, vol. 68, no. 7, pp. 2615–2650, Jul. 1997, doi: 10.1063/1.1148174.
[300] G. G. Macfarlane, T. P. McLean, J. E. Quarrington, and V. Roberts, “Exciton and phonon effects in the absorption spectra of germanium and silicon,” *Journal of Physics and Chemistry of Solids*, vol. 8, pp. 388–392, Jan. 1959, doi: 10.1016/0022-3697(59)90372-5.
[301] C. Gosse, C. Bergaud, and P. Löw, “Molecular Probes for Thermometry in Microfluidic Devices,” in *Thermal Nanosystems and Nanomaterials*, S. Volz, Ed. Berlin, Heidelberg: Springer, 2009, pp. 301–341. doi: 10.1007/978-3-642-04258-4_10.
[302] C. Hagart-Alexander, “Chapter 21 - Temperature Measurement,” in *Instrumentation Reference Book (Fourth Edition)*, W. Boyes, Ed. Boston: Butterworth-Heinemann, 2010, pp. 269–326. doi: 10.1016/B978-0-7506-8308-1.00021-8.
[303] G. Recktenwald, “Conversion of thermocouple voltage to temperature,” *Portland: Portland State University*, vol. 23, 2010, [Online]. Available: https://web.cecs.pdx.edu/~gerry/epub/pdf/thermocouple.pdf
[304] Analog Devices, “AN-1087: Thermocouple Linearization When Using the AD8494/AD8495/AD8496/AD8497.” https://www.analog.com/en/app-notes/an-1087.html
[305] Mosaic Industries, “Using Thermocouples,” *Mosaic Documentation Web*. http://www.mosaic-industries.com/embedded-systems/microcontroller-projects/temperature-measurement/thermocouple/microcontroller
[306] NIST, “NIST ITS-90 Thermocouple Database.” National Institute of Standards and Technology, 2018. doi: 10.18434/T4S888.
[307] Solvay, “Galden® PFPE.” https://www.solvay.com/en/brands/galden-pfpe
[308] V. A. Atiemo-Obeng, S. M. Kresta, and E. L. Paul, *Handbook of Industrial Mixing*. John Wiley & Sons, Incorporated, 2004.
[309] A. K. Coker, *Modeling of chemical kinetics and reactor design*. Gulf Professional Publishing, 2001.
[310] K. Richard, J. Jason, G. Padron, and A. David, “Impeller Performance in Stirred Tanks,” *Chemical Engineering*, vol. 124, no. 8, p. 42, 2017.
[311] N. Spogis and J. Nunhez, “Optimizing a hydrofoil for industrial use,” *Procedia Engineering*, vol. 138, pp. 403–412, 2016.
[312] R. J. Weetman, B. Gigas, and others, “Mixer mechanical design-fluid forces,” 2002.
[313] R. G. Budynas and J. K. Nisbett, *Shigley’s mechanical engineering design*, 9th ed. New York: McGraw-Hill, 2011.
[314] R. C. Juvinall and K. M. Marshek, *Fundamentals of Machine Component Design*, 5th ed. Wiley, 2012. Accessed: Oct. 28, 2019. [Online]. Available: https://www.wiley.com/en-us/Fundamentals+of+Machine+Component+Design%2C+6th+Edition-p-9781118987681
[315] F. Frass, R. Hofmann, and K. Ponweiser, *Principles of finned-tube heat exchanger design for enhanced heat transfer*, 2nd ed. WSEAS Press, 2015.
[316] Y. Muzychka and M. Yovanovich, “Pressure drop in laminar developing flow in noncircular ducts: A scaling and modeling approach,” *Journal of Fluids Engineering*, vol. 131, no. 11, 2009.

[317] L. A. Sphaier, J. Su, R. M. Cotta, and F. Kulacki, “Handbook of thermal science and engineering.” Springer, 2017.
[318] H. Zumbahlen, *Basic linear design*. Analog Devices, 2007.
[319] T. Hubing, “LearnEMC - Resources for Electromagnetic Compatibility Engineers,” 2022. https://learnemc.com/emc-resources
[320] H. W. Ott, *Electromagnetic Compatibility Engineering*. Hoboken, NJ: John Wiley & Sons, Inc., 2009.
[321] Thorlabs, “Passive Benchtop Isolation Systems,” 2022. https://www.thorlabs.com/newgrouppage9.cfm?objectgroup_id=1129
[322] L. He, P. Karau, and V. Tabard-Cossa, “Fast capture and multiplexed detection of short multi-arm DNA stars in solid-state nanopores,” *Nanoscale*, vol. 11, no. 35, pp. 16342–16350, Sep. 2019, doi: 10.1039/C9NR04566J.
[323] L. He *et al.*, “Digital immunoassay for biomarker concentration quantification using solid-state nanopores,” *Nat Commun*, vol. 12, no. 1, p. 5348, Sep. 2021, doi: 10.1038/s41467-021-25566-8.
[324] Scikit learn, “2.1. Gaussian mixture models,” *scikit-learn*, 2021. https://scikit-learn/stable/modules/mixture.html
[325] S. Magdeldin, *Gel Electrophoresis - Principles and Basics*. IntechOpen, 2012. doi: 10.5772/2205.

Appendix A – Thermometer noise test setup

Example thermometer noise test setup attaches a temperature probe on top of the 100MΩ 10pF amplifier reference test cell in the native amplifier enclosure, akin to placing a temperature probe close to the nanopore membrane. Thermometers tested in this manner were VWR Temp Alert and OMEGA OM-HL-EH-TC, and compared to baseline trace with the cell alone. Both thermometers are battery-powered, not connected to any external circuits, therefore additional electrical noise is introduced by the thermometer systems themselves being present within the original Chimera VC100 Faraday cage.

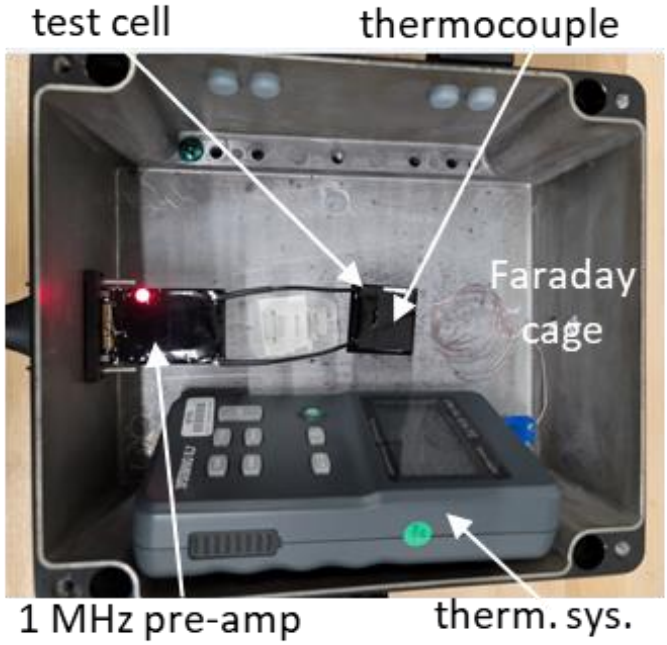

Alternative test setup includes the thermometer outside of the Faraday cage with the thermocouple or thermistor probe threaded inside. In this case, noise is significantly higher, and precipitated by the placement of the probe inside the enclosure. It is therefore reasonable to say that designing and building a secondary internal Faraday cage will not reduce the thermometer noise as long as the electrically-conductive probe is near the R-C element of the dummy test cell where temperature is being measured (i.e. next to the nanopore in the actual fluidic cell).

Appendix B – Material selection tables

Material selection table for the heated nanopore fluidic cell is presented. High-resolution image can be zoomed in. Table is not split into many many pages because it would be just as difficult to follow.

Material	Thermal conductivity (W/m*K)	Specific heat Cp (kJ/kg*K)	Heat deflection (0.25mm) (°C)	Glass transition Tg (°C)	Melting (°C)	Creep/stress deformation	Thermal expansion (um/m) (linear, 1/K)	Swelling/humidity absorption	Optical features/ transparency	Biocompatibility/ bioinertness	Hydrophobicity	Electrical resistivity (Ohm*m)	Mass density (g/cm3)	Young's Modulus (MPa)	Fracture toughness (MPa m$^{1/2}$)	Elongation (%)	Ultimate strength (MPa)	Part manufacturing	Comments
Cured PDMS (Sylgard 184)[1]	0.16 (50°C) 0.15 (80°C)	1.46 (25°C) 1.625 (77°C)	-	-	None for cross-linked. Thermal decomposition > 200°C	10% set (22hr, >23°C) 20% (3 years, 23°C)	9.06*10^{-4}(20° C) 9.61* 10^{-4}(207°C)	Hydrophobic, <1% with no effect on properties	n = 1.4 Somewhat transluscent IR absorption 2900-2100, ~ 1000-1100 (/cm)	Good, physiologically inert	Hydrophobic, 90-120° contact angle	4x10^{13}	0.95-1.20 0.97 (20°C) 0.81 (207°C)	0.360-0.870 1.32-2.97 (Compressive 3.51-7.65)	Soft elastomer	430-725	3.51-7.65 (Compressive 28.4-51.7GPa)	Mold casting, soft lithography	Thermoset. Properties depend on curing conditions, higher moduli for higher crosslink temperature
PMMA (acrylic)[2]	0.187 - 0.216	1.25 - 1.7	68 (1.82MPa) 51.7-106 (1.8MPa) 73-109(0.46MPa)	>106 (atactic) >50 (isotactic) >120 (syndio)	160	>84°C on-recoverable creep; Creep modulus 1200-1800MPa	6*10^{-5} (>Tg) 2-3*10^{-4} (< Tg)	<2% (24hr)	T = 92% Little UV Absorbance <260nm IT absorption ~ 3000 n = 1.49	Good, physiologically inert	?	1-1.6*10^{14}	1.17-1.20	2700-3100	1.21 (23°C air) 1.76 (37°C, water)	2-10	48-76 (60% reduction to 100°C)	Batch or continuous Polymerization; Machining; Laser cutting	Tensile strength decreases with water absorption
Glass (borosilicate)[3]	1.14	0.83	>Tg	536	1070	>Tg	3.5*10^{-6}	-	transparent n = 1.473	Good, inert	Hydrophilic surface when untreated, 32° contact angle	10^{14}	2.235	65000		-	7 (tensile) 100 (compr)	Pre-made pipette tubes? Glass forming	Borosilicate glass has very low thermal expansion coefficients
Polyimide (PAI, Torlon)[4]	0.259 - 0.533	1	178-279 (1.8MPa)	275-276	-	<2% (1000hrs, 103.4MPa)	3.6*10^{-5}	<0.6% (24hr) <4.6% (eq)	Typically opaque, can have translucency	Good, cell compatible		3*10^{13}	1.38	5200	3.68-4.48	10-18	117.2 (tensile) 241.4 (compr)	Injection mold; Machine	Thermoplastic. Hygroscopic High temperature and wear resistance
Polyimide (PEI, Ultem 1000)[5]	0.220	2	209-210 (0.46MPa) 200-201 (1.8MPa)	217	-	<1% (28MPa, 21°C) 4% (28MPa, 121°C)	5.6*10^{-5}	<0.25% (24hr) <1.3% (eq)	Amber-transparent	Good, cell compatible	?	1*10^{15}	1.27	3000	1.99-4.03	7-60	105 (tensile) 150 (compr)	Easy machining; Ultem 9085 PEI FDM 3D print filament available	Thermoplastic. Related to PEEK, lower temp and impact strength.
Polyimide (ODA-PMDA, Kapton, Vespel)[6]	0.35	1.13	360	360-410	-	0.14% (13.8MPa)	4.5*10^{-5} (<23° C) 5.4*10^{-5} (>23° C)	0.24% (24hr) 0.72% (48hr, 50°C) 1-1.3 (eq, 50% RH)	Transparency possible n = 1.70-1.80 >2500nm absorption of 70+%	Possible local tissue toxicity, No DNA damage in mammalian cell cultures	?	10$^{14-15}$	1.42	2413 (compr)		6-7.5	86.2(tensile) 41.4(260°C tensile)	Easy machining	Kapton tape, Vespel rods and sheets - data presented for Vespel PEEK superior for chemical resistance. Vespel superior for wear resistance and toughness. Vespel does not outgas
Parylene (coating) [7]	0.084-0.125	0.711756	-	13	427		3.5-3.8*10^{-5}	<0.1% (24hr)	Transparent coating?	Biocompatible, medical implants	?	2*10^{14}	1.1-1.4	600-1400 (isotropic)		18-330	25-62 (isotropic) 45-76 (tensile)	coating	Coatings, thin features. No thick bars or rods or sheets
Polypropelene (PP, isotactic)[8]	0.11-0.22	1.920	72-107	2.5-10.7	186	5% (50% of breaking load) <0.5% (10% of breaking load)	6.5*10^{-5} (-30-0°C) 1.05*10^{-4} (0-30°C) 1.4*10^{-4} (30-57°C) 6.6-6.7*10^{-4} (>175°C)	<0.1% (eq)	Transparent	Biocompatible, lab tubes etc		10-10^{16}	0.9-0.91 (25° C, commercial)	8 - 8250 (tensile) 1380 (compr)	?high	3-900	9-80	Injection molding, extrusion, spinning	Thermoplastic Inexpensive, widely available
PETG[9]	0.29	1.2	63 (1.82MPa) 71 (0.46MPa)	80	265	<2.5% (80% tensile str, 11hr fail) <1% (60% tensile str, 27 +hr)	9.1*10^{-5}	0.5% (24hr)	Transparent	Food grade biocompatibility		10^{13}	1.41	1700 (tensile)		18	50 (tensile)	FDM 3D print, machining	Thermoplastic Inexpensive, widely available
Polystyrene (solid not styrofoam)[10]	0.116 (50°C) 0.128 (100°C) 0.13 (200°C)	1.3-1.5	85 (1.82MPa) 95 (0.46MPa	100	240	2% (18MPa, 1000hr) 20MPa breaks after 790hr	6-8*10^{-5}(< Tg)	<0.15% 0.1% (eq)	Transparent n = 1.59-1.6	Cell compatible		10$^{18-20}$	1.04-1.127 (change ~2.65 *10^{-4} < Tg; ~6.05* 10^{-4} > Tg)	3200-3400 (tensile) 3000 (compr)		1-4	30-60 (tensile) 95 (compr)	Injection mold, Extrusion, machining	Thermoplastic Low cost, thermally stable, rigid
Cyclic olefin copolymer (COC)[11]	0.17-0.18		75-170 (0.46MPa) 60-162 (1.82MPa)	65-180	80-155		6-8*10^{-5}	0.01-0.4%	Transparent n = 1.51-1.54	Dry food applications		10$^{10-10^{14}}$	0.940-1.12	1250-5490		1.5-140	36-77 (tensile)	Injection mold, little info on machining	
Polyether ether ketone (PEEK)[12]	0.25	1.273 (77C) 1.439 (127C)	160 (1.81MPa)	137-152	335-333	1% (120C, 1000hr)	1.61*10^{-4} (30-150C)	0.15% (24hr)	n = 1.671	Biocompatible. Medical implants, etc.		4.9*10^{16}	1.263-1.401	3560 (tensile) ~3000 (100C)		42-150	92 (tensile 23C) 50 (tensile (100C)	Molding, Machining	Excellent in all respects Superb electrical insulator More difficult to machine than polyimides?
Tefflon (PTFE)[13]	0.386-0.434 (0-100C)	1.4 (20C) 1.3 (150C)	132 (0.46MPa) 60 (1.82MPa)		314	1% (3.4MPa, 100hr, 23C) 1% (3.4MPa, 100hr, 100C)	2*10^{-4} (0C) 1.2*10^{-4} (100C)	0%		Biocompatible, medical implants, etc.	Hydrophobic	10^{17}	2.0-2.344	340 (23C, tensile) 69 (100C, tensile)		100-200% (23C)	7-28 (25C)	Molding, Machining	Super inert Difficult to machine
Polyoxymethylene/Acetal (Delrin)[14]	0.3-0.37	0.35 (-18-100C)	136 (1.82MPa) 172 (0.45MPa)	-75	165-175	Creep modulus 1.6GPa (1000hr)	7.5* 10^{-5}(-40-30C)	0.25% (24Hr) 0.9-1.4% (eq)				10$^{12-13}$	1.41-1.533	2825-3100 (23C)		23-75	60.6-68.9 (tensile)	Molding, Machining easier than Aluminum or brass	Susceptible to chlorine attack, degradation in hot water. Susceptible to catastrophic failure.
FormLabs High Temp resin[15]	Assumed PMMA-like, cross-linked polyacrylate-base	Assumed PMMA-like, polyacrylate-based	120 (0.45MPa) 78 (1.8MPa) Postcured 60min --- 238 (0.45MPa) 101 (1.8MPa) Postcured 80min @80C, lab oven 180min 120C	-	Cross-linked material, does not melt. Burns	Assumed PMMA-like, cross-linked polyacrylate-base	7.96*10^{-5} postcured 60min (0-150° C)	<1% (24hr)	Translucent orange	Highly cross-linked, proprietary composition but likely similar to FormLabs Clear which is bioinert with DNA samples in the lab		Assumed PMMA-like, cross-linked polyacrylate-base	Assumed PMMA-like, cross-linked polyacrylate-base	2800	LOW, brittle material	3.3	58.3 (tensile)	SLA 3D print	Thermoset, UV crosslinked Full cure properties appear in line with what we would want to try for cell prototyping

1.http://www.mit.edu/~6.777/matprops/pdms.htm; Johnston, I. D., McCluskey, D. K., Tan, C. K. L., & Tracey, M. C. (2014). Mechanical characterization of bulk Sylgard 184 for microfluidics and microengineering. Journal of Micromechanics and Microengineering, 24(3), 035017.; Polymer Data Handbook (1999) - PDMS

2.Polymer Data Handbook (1999) - PMMA, http://www.tangram.co.uk/TI-Polymer-PMMA.html; http://www.mit.edu/~6.777/matprops/pmma.htm; http://www.matweb.com/search/DataSheet.aspx?MatGUID=3cb08da2a0054447a3790015b7214d07

3.Averages from SciGlass DB https://en.wikipedia.org/wiki/List_of_physical_properties_of_glass; https://www.azom.com/article.aspx?ArticleID=4765; https://za.dedietrich.com/products-solutions/borosilicate-glass-properties

4.Polymer Data Handbook (1999) - Polyimide (PAI); http://www.matweb.com/search/DataSheet.aspx?MatGUID=1ca9588da84640d199959da7c00a6083; http://www.goodfellow.com/E/Polyamide-imide.html; https://www.solvayultrapolymers.com/en/binaries/Torlon-PAI-Design-Guide_EN-227547.pdf

5.Polymer Data Handbook (1999) - Polyimide (PEI); http://www.matweb.com/search/DataSheet.aspx?MatGUID=de1238d98afa4eafb937266edba99fa3; https://www.azom.com/article.aspx?ArticleID=1883; https://www.protolabs.com/media/1014801/ultem-1000-im.pdf;

6.Polymer Data Handbook (1999) - Polyimide (ODA-PMDA); http://readingplastic.com/vespel-vs-peek/; Escalas et al 1976; Dupont Vespel SP1 MSDS;

7.Polymer Data Handbook (1999) - Polyimide (Parylene); http://www.parylene.com/pdfs/PTC-Parylene_Properties_Chart.pdf; http://www.paryleneengineering.com/thermal_properties_of_parylene.htm

8.Polymer Data Handbook (1999) - Polypropylene; http://www.matweb.com/search/DataSheet.aspx?MatGUID=08fb0f47ef7e454fbf7092517b2264b2&ckck=1; Patti & Acierno, 2018; https://www.engineeringtoolbox.com/specific-heat-capacity-d_391.html; Bakonyi & vas, 2013; https://www.zeusinc.com/wp-content/uploads/2014/03/RESINATE-SE-Biocompatibility-of-Plastics.pdf;

9.Polymer Data Handbook (1999) - PET; https://www.sd3d.com/wp-content/uploads/2017/06/MaterialTDS-PETG_01.pdf;

10.Polymer Data Handbook (1999) - Polystyrene; https://www.engineeringtoolbox.com/specific-heat-capacity-d_391.html; http://www.matweb.com/reference/deflection-temperature.aspx; http://www.matweb.com/search/DataSheet.aspx?MatGUID=df6b1ef50ce84e7995bdd1f6fd1b04c9&ckck=1
11.http://www.matweb.com/search/DataSheet.aspx?MatGUID=c47e16ad84a047798fc4d1f6172e48f7; https://topas.com/sites/default/files/files/TOPAS_Brochure_E_2014_06(1).pdf
12.Polymer Data Handbook (1999) - PEEK; [Kurtz, 2012] Peek Biomaterials Handbook; https://www.victrex.com/~/media/literature/en/victrex_automotive_brochure_en.pdf
13.Polymer Data Handbook (1999) - PTFE; Dupont PTFE Handbook;
14.Polymer Data Handbook (1999) - Polymethyene oxide; http://www2.dupont.com/Plastics/en_US/assets/downloads/design/DELDGe.pdf; [Fister et al. 1985]; ASTM Corrosion and Degradation of Implant Materials;
15. https://archive-media.formlabs.com/upload/HighTemp-DataSheet.pdf
16. https://formlabs-media.formlabs.com/datasheets/Flexible_Technical.pdf

Sample material selection matrix is presented on the following page.

Table 0.1. Fluidic cell material selection matrix.

Material	High Thermal conductivity (2)	Low specific heat Cp (2)	High heat deflection T (3)	Glass transition T (1)	High melting T (3)	Low creep (2)	Low thermal expansion (1)	Low swelling (3)	High biocompat. (3)	High electrical resistivity (4)	High Yng Modulus (2)	Low elongation (2)	High UTS (1)	Ease of manufacturing (5)	Weighted Score
Cured PDMS	+	++	n/a +++++	n/a +++++	n/a +++++	++	+	++++	+++++	++	+	+	+	+	66
PMMA (acrylic)	+	++	++	+++	+++++	+++	++	+++	++++	+++	+++	+++	++++	++++	78
Glass (borosilicate)	+++++	+++++	+++++	+++++	+++++	+++++	++++	n/a +++++	+++++	+++	+++++	+++++	+	+	100
Polyimide (PAI, Torlon)	+++	+++	+++++	+++++	? (+++)	++++	+++	+++	++++	++	++++	+++	+++++	+++	85
Polyimide (PEI, Ultem 1000)	+	+	+++++	+++++	? (+++)	+++++	+++	++++	++++	++++	++++	+++	+++++	+++	88
Polyimide (ODA-PMDA, Vespel)	+++	+++	+++++	+++++	? (+++)	+++++	+++	++++	+++	++++	+++	+++	++++	+++	89
Polypropelene (PP, isotactic)	+	+	++	+	+++++	++	++	+++++	+++++	+++++	+++	++	+++	+	73
PETG	+++	+++	+	+++	+++++	+++	++	+++++	+++	++	+++	++	+++	++++	77
Polystyrene (solid not styrofoam)	+	++	+	++++	+++++	+++	+++	+++++	++++	+++++	++++	++++	++++	+++	87
Cyclic olefin copolymer (COC)	+	? (+)	+++	++++	++	? (+)	+++	+++++	++	++	++++	++	+++	+++	64
Polyether ether ketone (PEEK)	++	++	+++++	+++++	+++++	+++++	++	+++++	+++++	+++++	++++	+++	+++++	++	98
Tefllon (PTFE)	++++	++	+++	? (+)	+++++	+++++	++	+++++	+++++	+++++	++	++	++	+	83
Polyoxymethylene / Acetal (Delrin)	+++	+++++	+++++	+	++++	++++	+++	+++	++++	+++	++++	+++	+++++	+++	94
FormLabs High Temp resin	? (+)	? (+)	++++	n/a +++++	n/a +++++	? (+++)	+++	++++	? (+)	? (+++)	++++	++++	+++++	+++++	86

Appendix C – Fluidic cell barrier cap casting system

Cap casting system is a convenience accessory designed to produce barrier caps. Mann Ease Release 200 silicone-based mold release agent is applied prior to casting silicone into the mold.

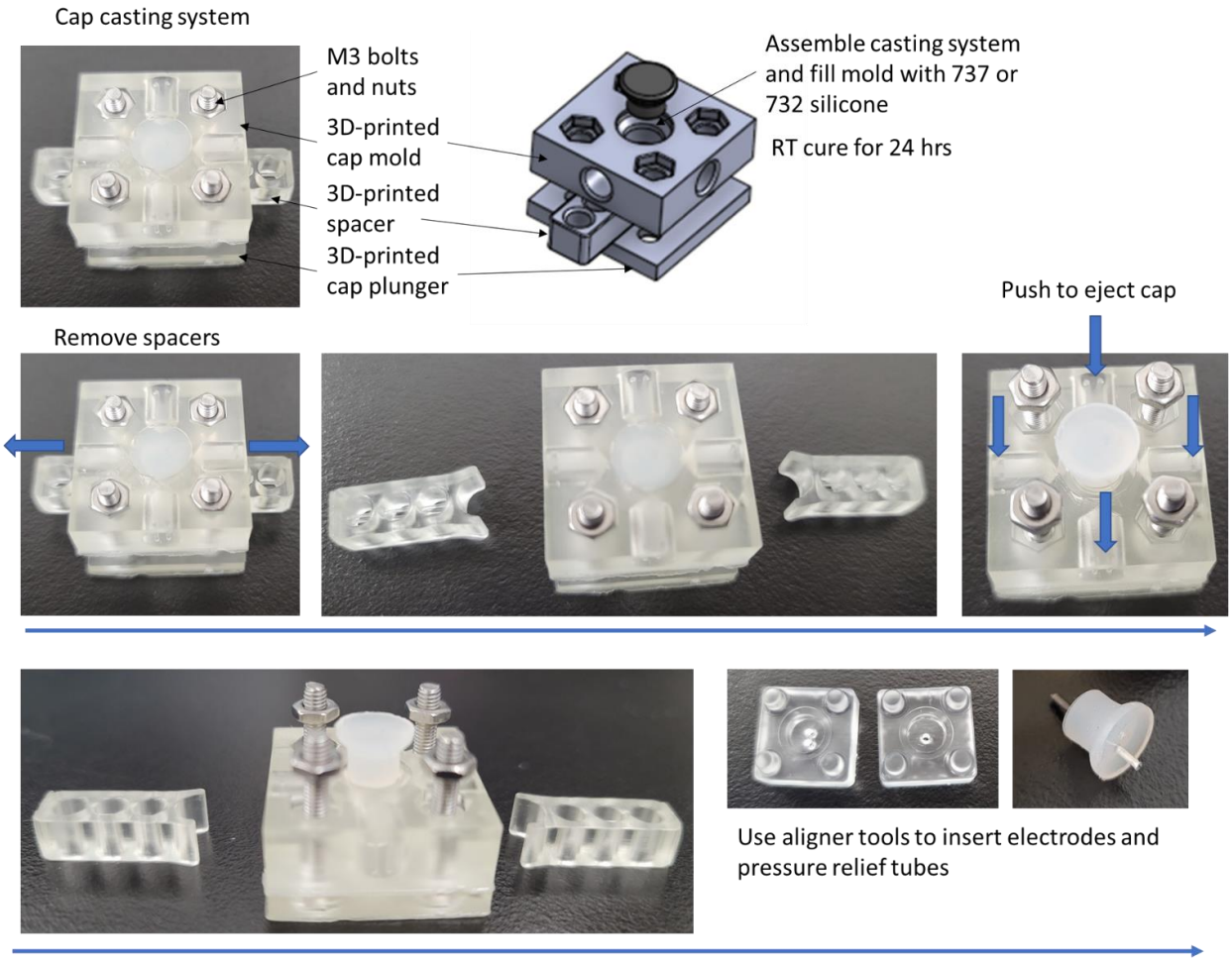

Updated cap casters feature smooth top for easer leveling of silicone

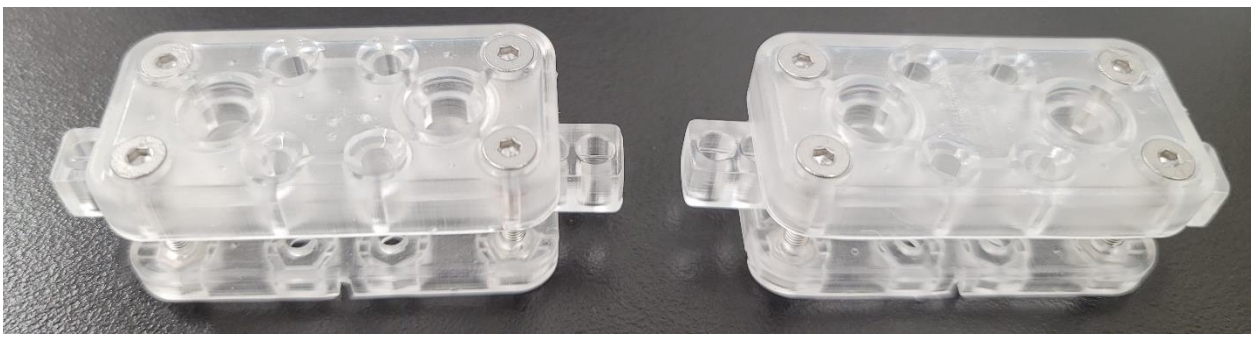

Appendix D – Elements of mixing fluid heater design

Ideal requirements for the heater power are approximated using a simple thermodynamic energy balance. Parameters are taken at average bath temperature $T_m = (T_{in} + T_{out})/2$. Highlighted are the heater requirements for the highest design setpoint temperature required. Contaner heat losses are estimated from a simple isothermal cylinder model as well as Solidworks FVA. Heat requirements are specified for different input fluid temperatures for steady state heat transfer. Maximum heat requirements are specified for the ambient temperature fluid input at different HT fluid flow rates.

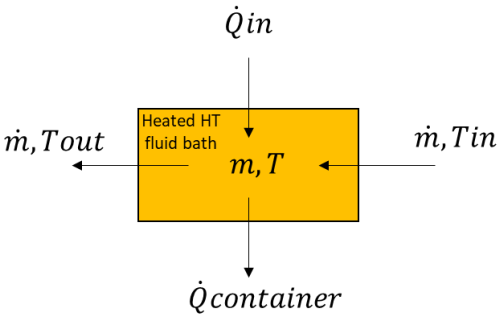

$$\dot{Q}_{in} = \rho(T)\dot{V}Cp(T)(T_{out} - T_{in}) + \dot{Q}_{container}$$

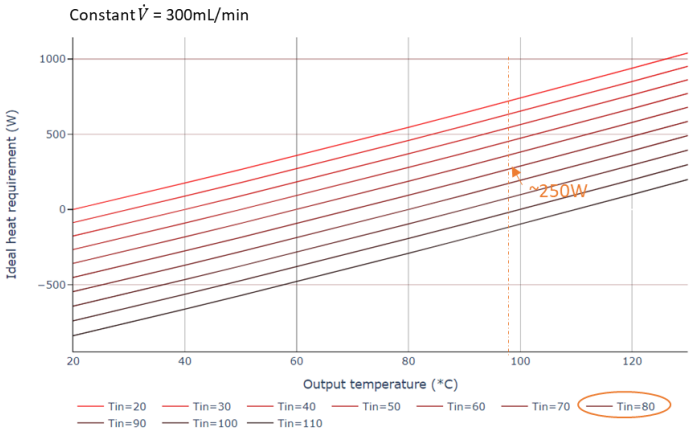

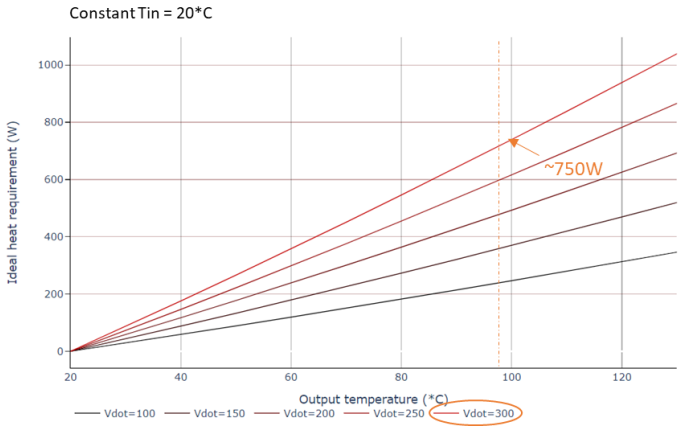

Both the heat loss model from the container, as well as the thermal step control of the fluidic cell temperature rely on fluid staying at approximately uniform temperature within the

heated container. As such, a fluidic mixer is required to ensure the thermal uniformity of the container fluid.

Mixed reactor design is well-described in [308]–[312]. In brief, design steps involve:

1. Standard industrial dimensioning relationships
    - define impeller and baffle dimensions and spacing
2. Design threshold for 95% mixing of all fluid in the tank (assumed within 5.2s)
    - determine the Power, Flow and Reynolds numbers for turbulent regime
    - compute required impeller speed
3. Performance characteristics for an impeller of choice (45° 4x pitched blade impeller selected)
    - compute force, power, and torque requirements
    - estimate mechanical and pumping efficiency

Results computed using an extensive Python script:

- Pitched blade, 45°, x4 blades
- 60mm < impeller D < 120mm
- 480rpm < impeller speed <2000rpm
- For a 61mm impeller at 467rpm:
    - 1.51N axial bearing
    - 22mNm shaft torque
    - 1.1W mechanical power

Design was also simulated in Solidworks 2020 flow simulation to verify and visualize expected flow patterns and thermal profiles in the heater. Geometry of the Ace Glass Instatherm 9601-18 heated glass bath along with the designed mixer was used.

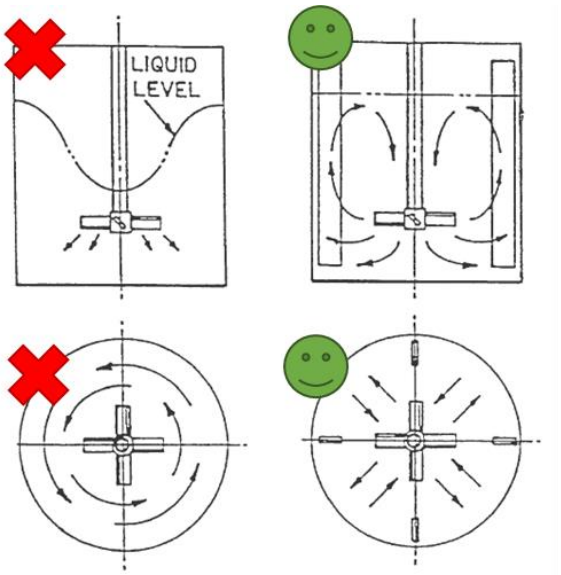

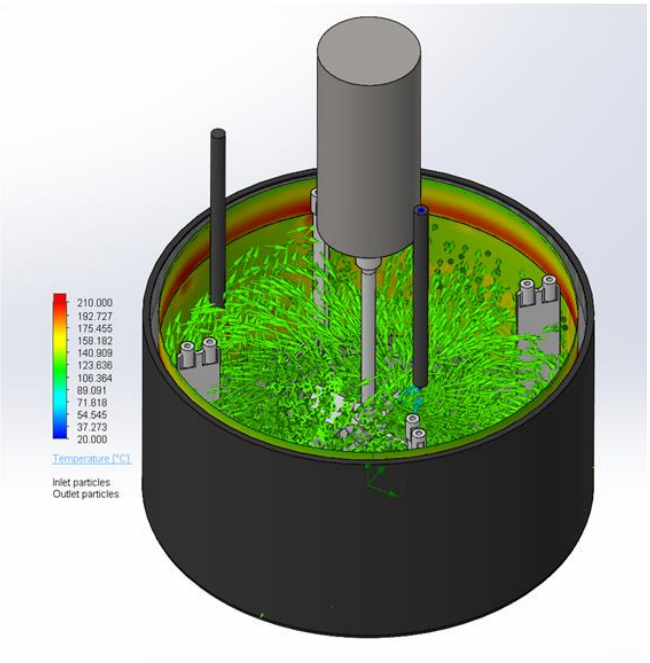

A well-designed fluid mixing system to facilitate temperature uniformity of container HT fluid results in a vertical compartmentalized motion of the fluid, which has been achieved in both the flow simulation model and fabricated prototype.

Appendix E – A few notes on pinch valve design

Dual-pinch-valve design notes:

- All components are heavily oversized d/t availability and affordability
    - E.g. clevis pin comes in minimum 8 mm size, while we could do with <3 mm (mostly to minimize deflection as opposed to stresses)
    - E.g. simple Oilite sleeve bearing is way over spec (1000N @ 120rpm), but that is what is available on the cheap
- No rated capacity available for bearings used or cam-follower – no lifetime estimate; keep lubricated and observe surface condition
    - No issues during compression set testing of Formlabs Tough 1500 cams – fully recovered from 4kg x 24hrs room temperature compression
    - No issues for over a year of operation with hot Viton tubing at the end of the pin

Cam dynamics simulation results from Python analysis script:

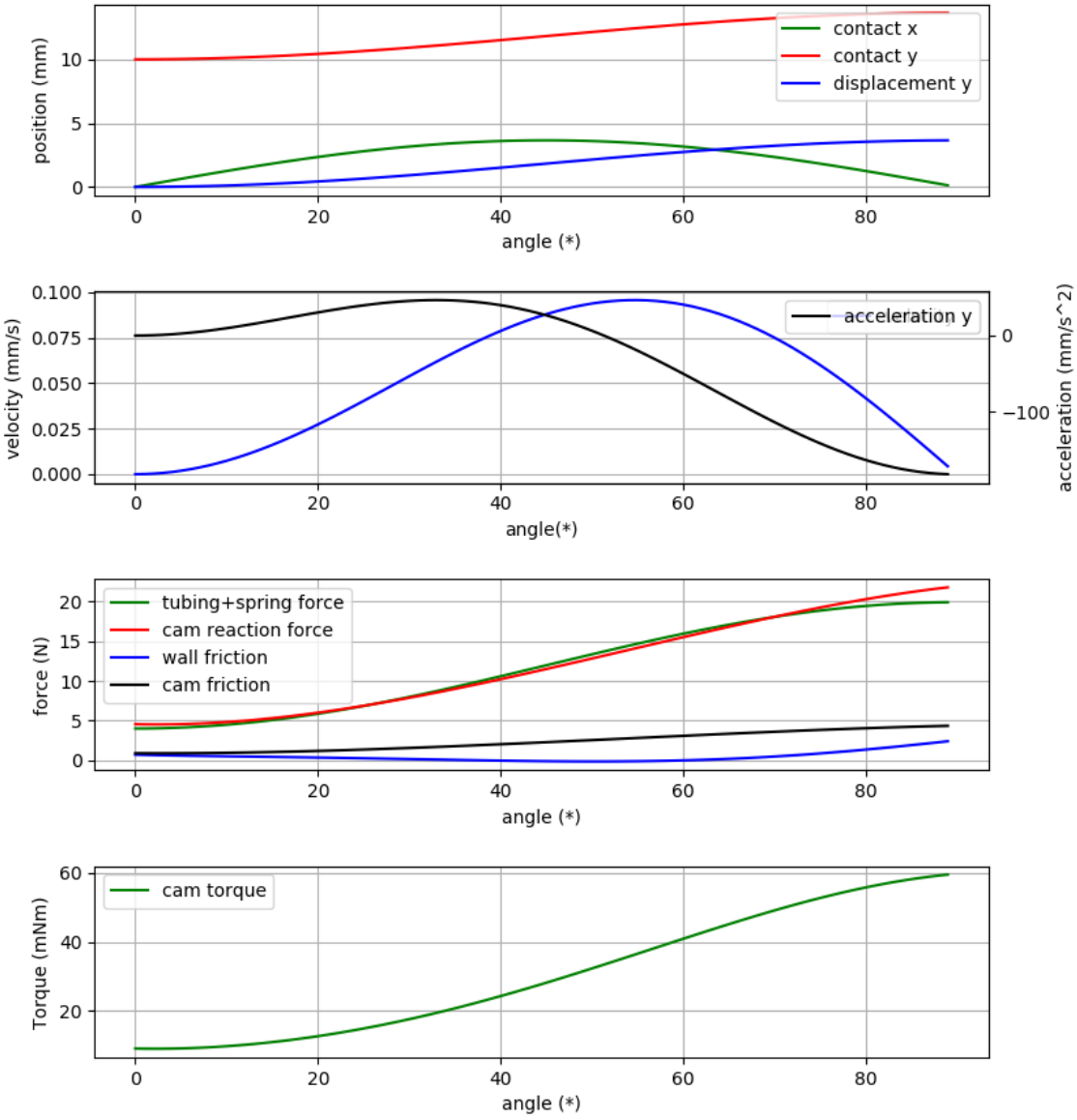
position (mm)
contact x
contact y
displacement y
angle (*)
velocity (mm/s)
acceleration y
acceleration (mm/s^2)
angle(*)
force (N)
tubing+spring force
cam reaction force
wall friction
cam friction
angle (*)
Torque (mNm)
cam torque
angle (*)

Appendix F – Analysis of thermal step response data

Step response of the fluidic cell analyte temperature next to the nanopore chip was assessed for input HT fluid temperatures ranging from 25 to 95 °C. Trials were ran 'in order' to save a significant amount of time (> 1hr per trial) on heating/cooling the oil bath that would be required for randomized analysis. As a consequence, thermal history effects can confound temperature trends:

- Sequentially increasing hot setpoint may introduce bias to time constants that appear smaller for higher temperatures. Possible pre-heating effects on material properties.
- Previous cycling of cold reservoir with some hot fluid can increase room temperature reservoir temperature, increasing variation of initial temperatures

Trials were conducted over 3 days, replicating each temperature condition 3 times. An automated thermal cycling program was implemented to step a 'hot' temperature setpoint for 1200s, followed by a room temperature setpoint for 1200s while recording data.

Initial temperature was determined from the initial section of each trial dataset (~60s). Drift was fitted as a linear function $ax + b$ with a confidence interval. Single trial analysis:

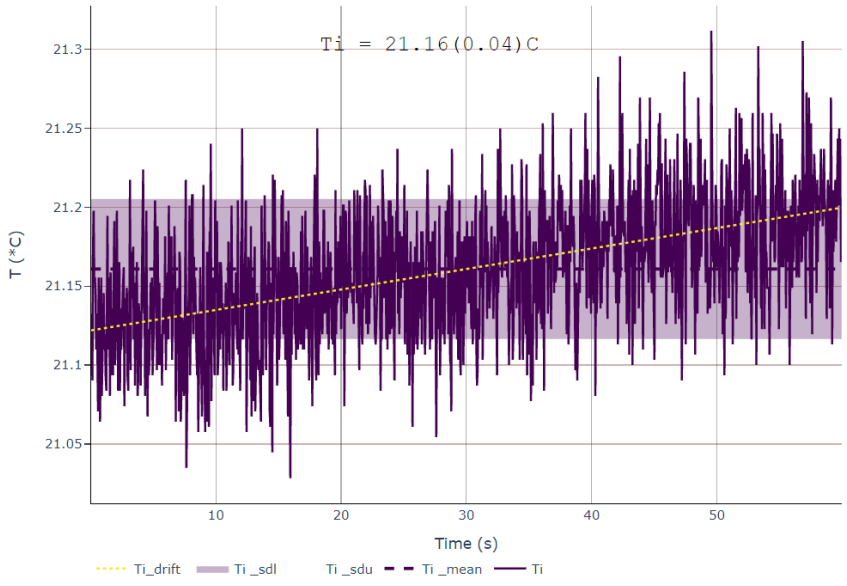

Trace plots for all trials:

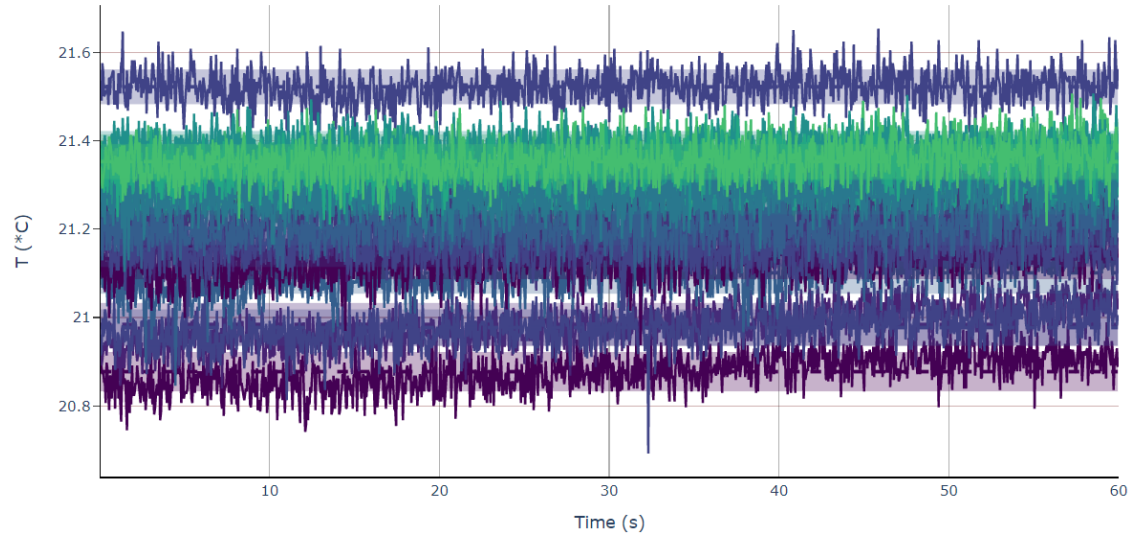

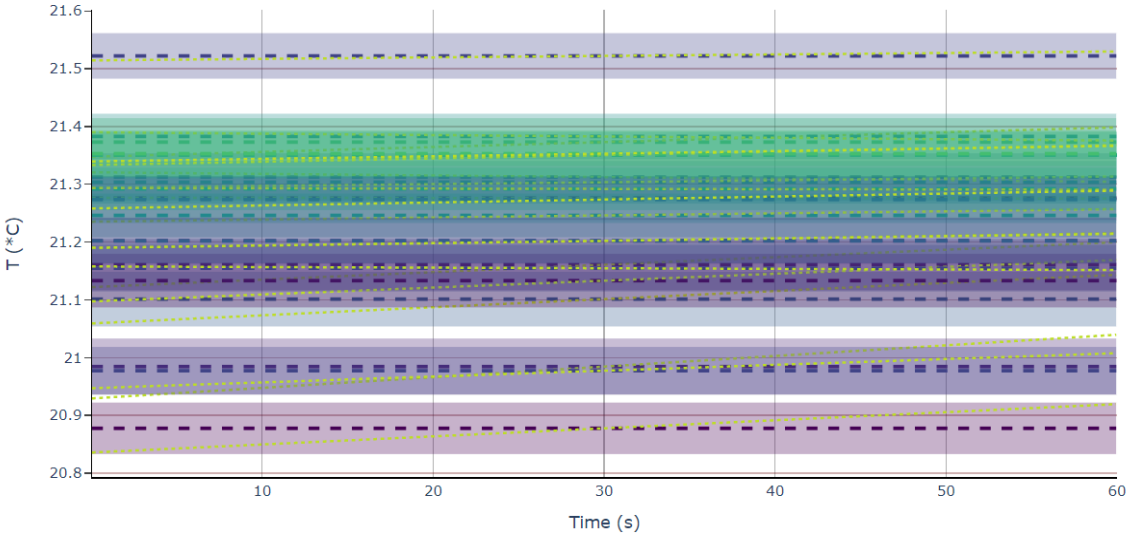

System dead time was computed by filtering temperature data (1d uniform, 100-pt averaging window, ~4s) and taking a time point where temperature is away from average by 1.96SD + drift value:

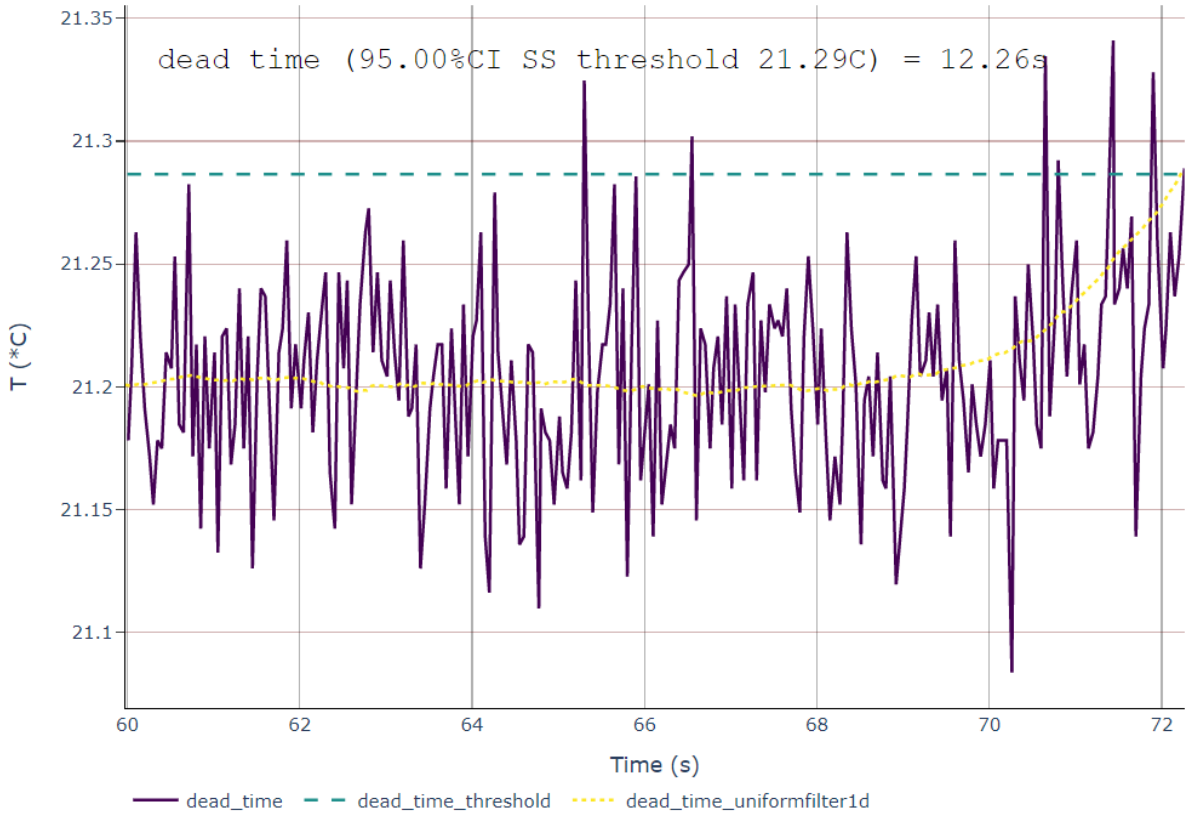
dead time (95.00%CI SS threshold 21.29C) = 12.26s
T (*C)
Time (s)
dead_time
dead_time_threshold
dead_time_uniformfilter1d

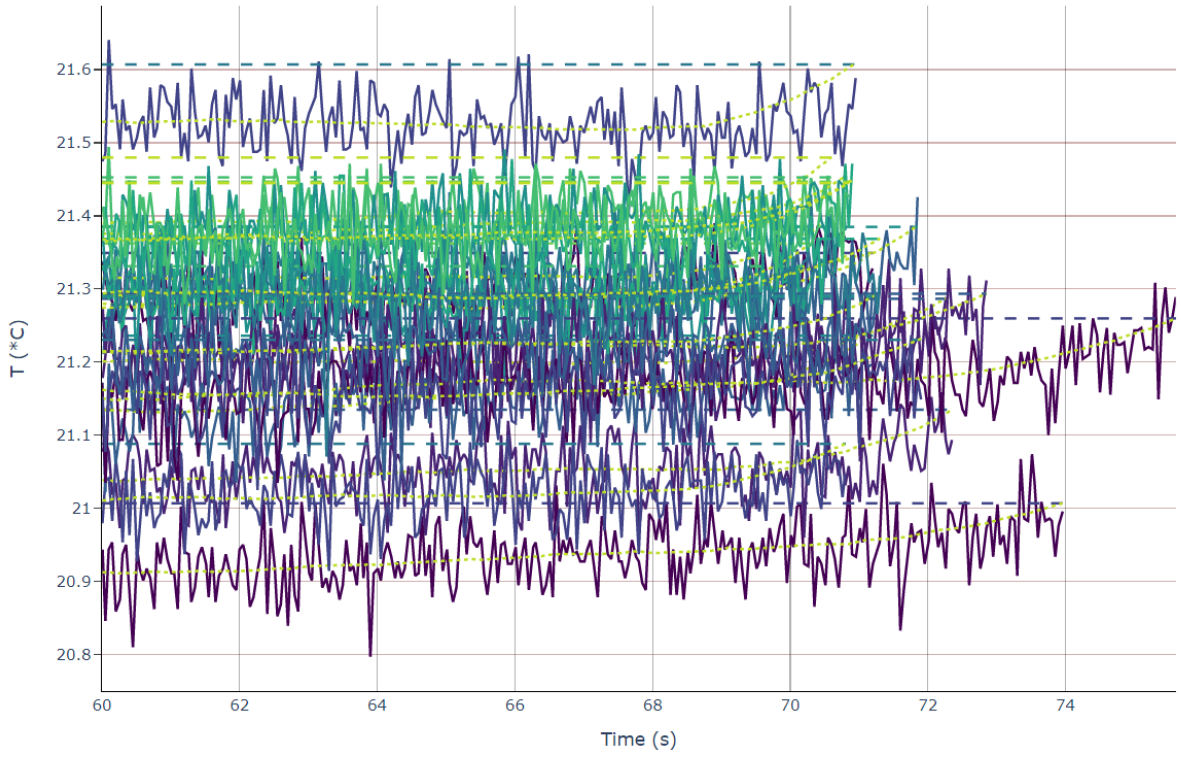
T (*C)
Time (s)

Main section of the step response include the temperature rise and steady state, shown for all trials in the following plot:

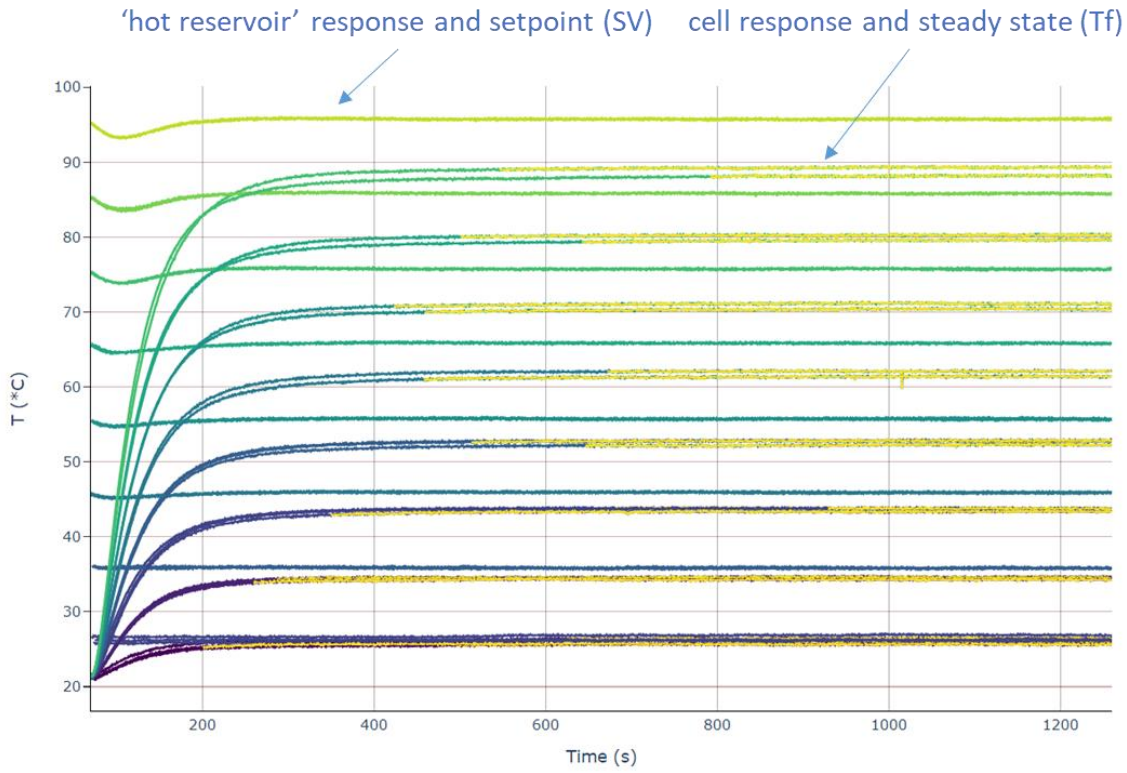

1st order response is fit for each trial using the initial and final (steady-state) temperature states:

$$T(t) = T_f - \Delta T e^{\left(\frac{-t}{\tau}\right)}$$

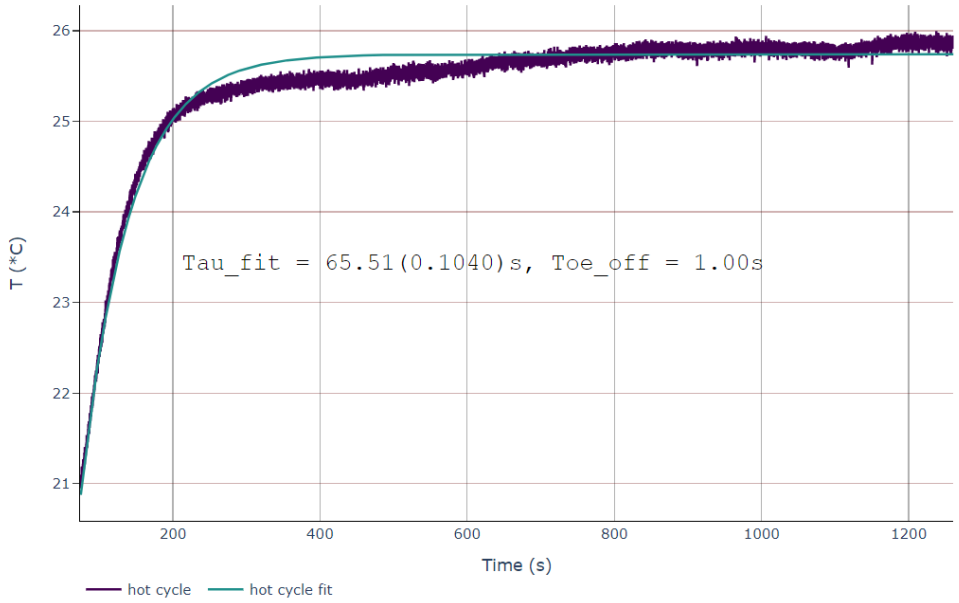

Steady state temperature was determined using a Cumulative Sum (CUSUM) algorithm from the Python *detecta* library – Duarte, M. (2020) detecta: A Python module to detect events in data. GitHub: https://github.com/demotu/detecta. Module is based on:

- Michèle Basseville and Igor V. Nikiforov (1993). Detection of Abrupt Changes: Theory and Application. Prentice-Hall.
- Fredrik Gustafsson (2000) Adaptive Filtering and Change Detection. Wiley.

and features peak, onset, CUSUM, and sequence detection.

CUSUM algorithm is typically used for detecting abrupt changes in a trace, but can be used on slower ramping data. The idea is that the algorithm accumulates changes in signal (sum) until threshold is tripped:

change in value

data drift compensation

cumulative sums for positive or negative changes

$$\begin{cases} s[t] = x[t] - x[t-1] \\ g^+[t] = max\left(g^+[t-1] + s[t] - drift,\ 0\right) \\ g^-[t] = max\left(g^-[t-1] - s[t] - drift,\ 0\right) \end{cases}$$

$$if \quad g^+[t] > threshold \quad or \quad g^-[t] > threshold:$$

Alarm upon reaching threshold and reset sums

$$\begin{cases} t_{talarm} = t \\ g^+[t] = 0 \\ g^-[t] = 0 \end{cases}$$

Following plot shows a typical response curve with CUSUM threshold trip points:

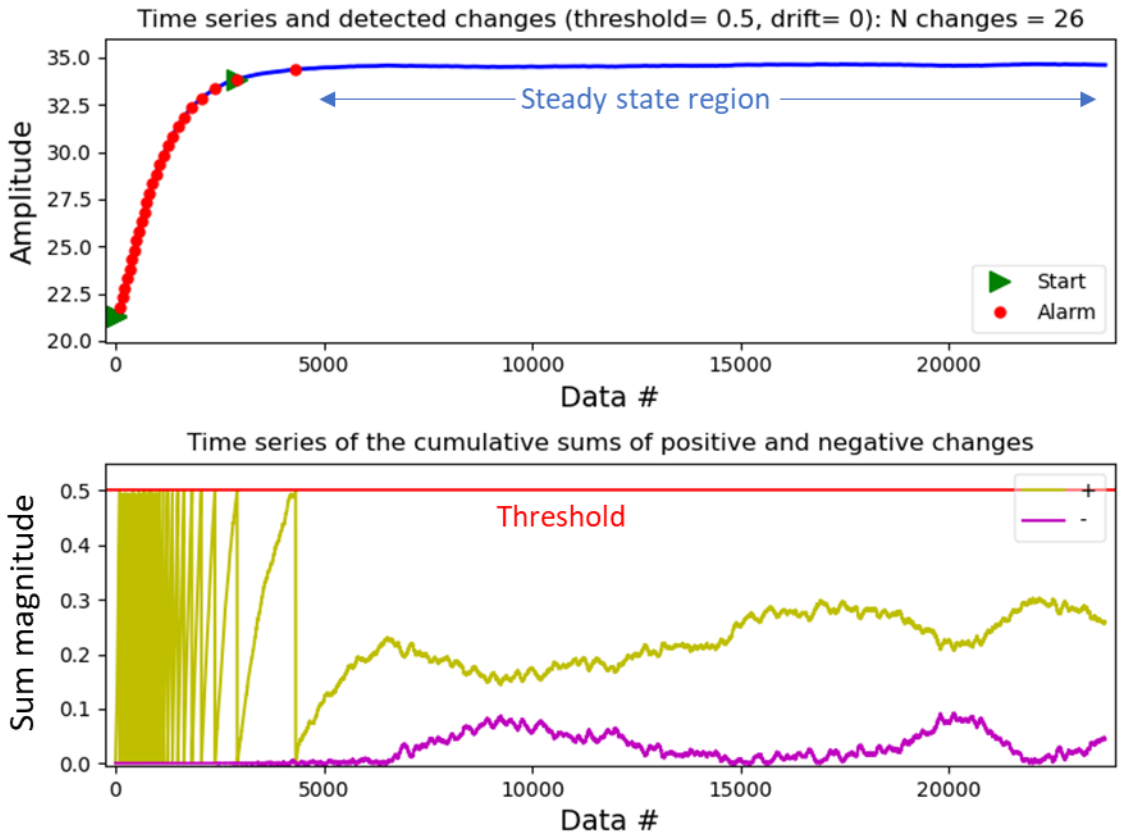

Steady state is achieved when cumulative sum of value changes stays under the threshold. Signal distortions and extremes can also be filtered out by considering means of segments that trip the threshold and doing a comparison:

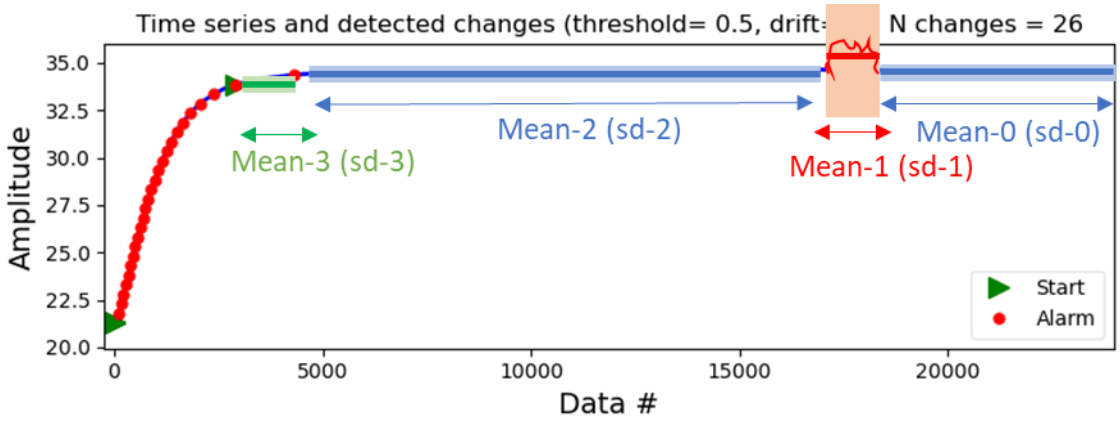

Segments that are not different from each other can be considered the same steady state value, while extraneous segments are thrown out with assumption they are noise. Algorithm loop:

$$if\ |mean_n - mean_{n-s}| < k\sigma_n :$$

$$Data_n = Data_n \cup Data_{n-s}$$

$$mean_n = mean(Data_n)$$

$$\sigma_n = std(Data_n)$$

$$s \in [1, n-1]$$

where s is the segment number, σ is the standard deviation, k is some threshold. Example of artificially noisy data:

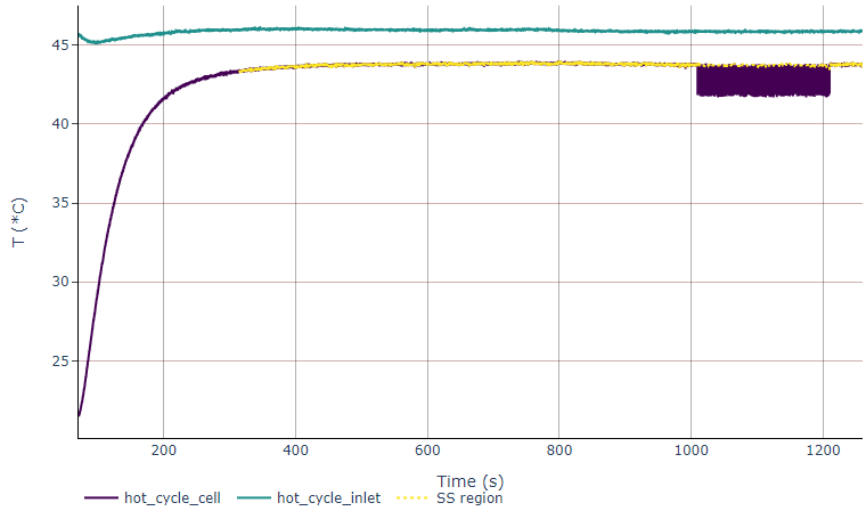

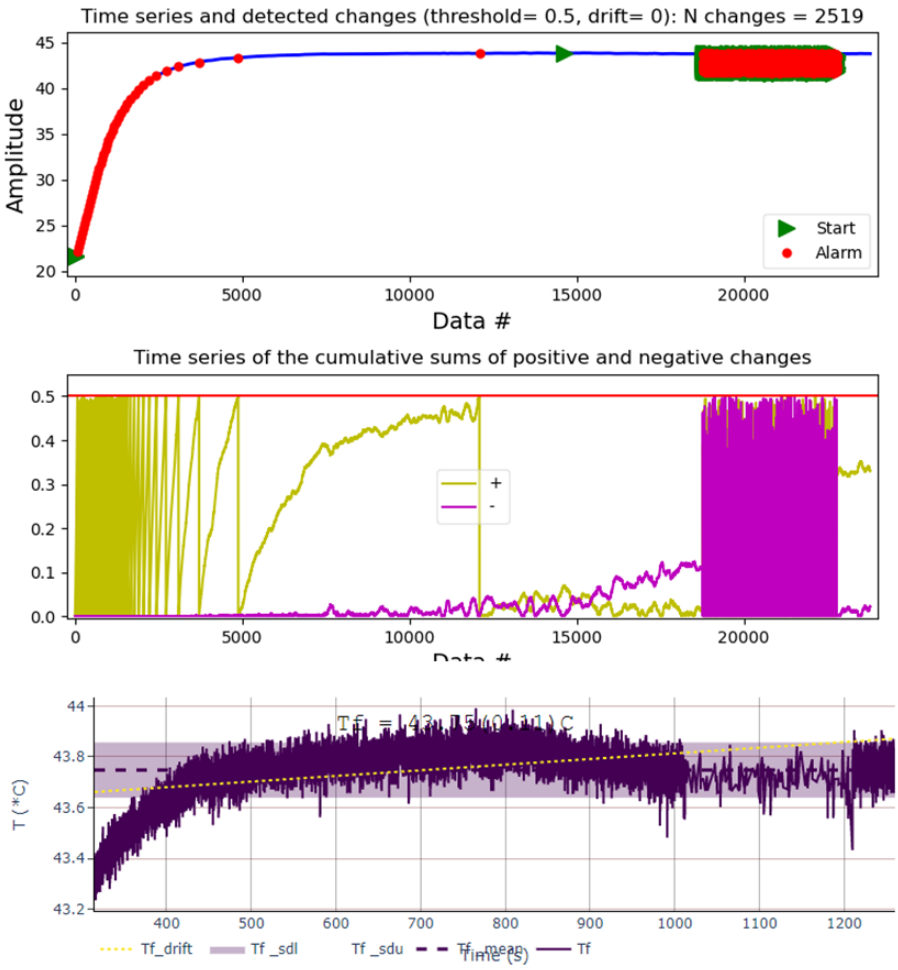

Time constant fits are improved by fitting real data with offsets that minimize fit variance:

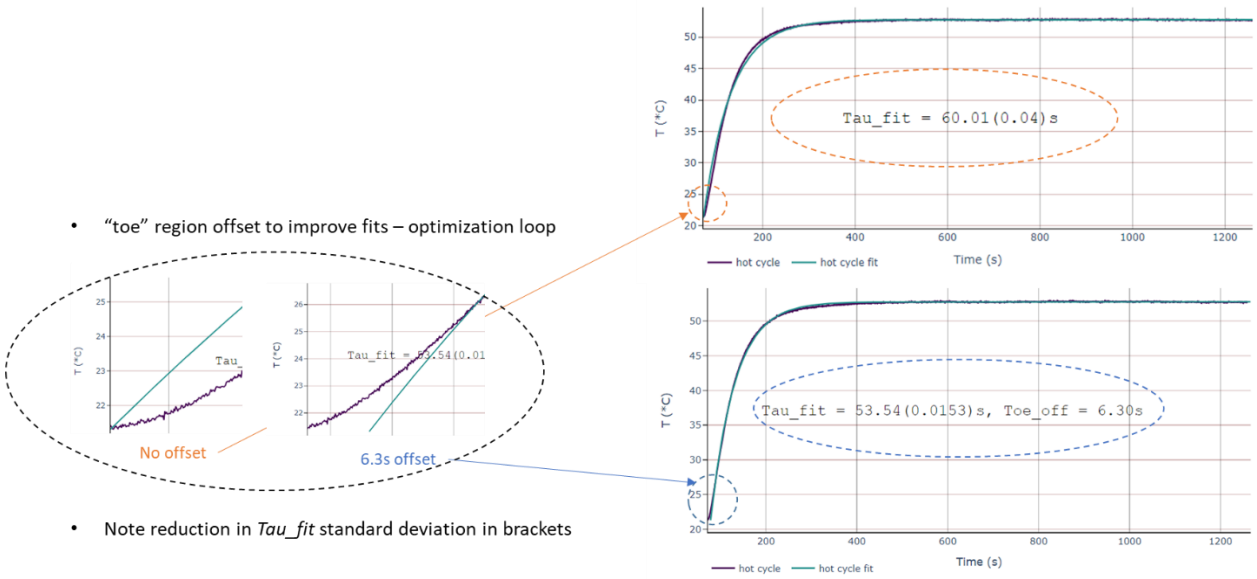

Appendix G – Safety systems

Multiple safety systems have been implemented to ensure user safety. Some can be improved, with improvement tracking in the following table:

ID	System	Status	Implementation details
0	Software overpressure protection	Operational	• Main commands prevent user from blocking off both valves simultaneously. • Pump is turned off if channel switch is requested. • Pump is not started unless channels have switched. • Channel switching or pump starting commands can not be started unless previous command has finished running. • Special commands available for hardware testing which can allow unsafe situations – TODO: make only accessible in special maintenance mode.
1	Hardware overpressure protection	Operational	• Forward pumping overpressure branch protected by overpressure jar with valve. Jar contents can be emptied by opening a luer lock port and pumping fluid out of the main tube. • While prohibited and fairly inconvenient to do, pump direction can be reversed by flicking a switch on the pump. Can result in reverse overpressure if valves are closed – TODO: consider using directional valves on forward and reverse branches connected to overpressure protection device
2	Software oil bath overheat protection	Operational	• SOLO4848 controller has alarm and disables output above 150*C (tP-H setting) • Alarm is also triggered at 135*C (AL1H setting) • Disconnection of thermocouple results in alarm and disabling of output. • Software sends signal to turn off bath if overtemperature or thermocouple disconnect detected. • Under consideration: redundant software protection using a secondary sensor system • TODO: Case of thermocouple being taken out of the hot bath while system running. Software to disable controller output if output is high (> 50%) and temperature rise not detected within 30 s.
3	Hardware oil bath overheat protection	Under consideration	• Direct power disconnect if bath temperature in the heater exceeds a threshold. • Secondary level of protection in case of software fault.
4	Hardware overcurrent protection	Operational	• Overcurrent, motor stall, and short circuit protection fuses implemented. • 12V line 3A fuse, 5V line 1A fuse.
5	Spill protection	Operational	• Easy to wipe plastic mat on the steel table. • Cold reservoir jar stand has a shallow tray. Added a wide and shallow petri dish under the jar for spills during maintenance activities. • Overpressure device within a separate beaker if overfills and starts leaking from the valve

6	Power system protection and certification	Operational	• Replaced open PSU with an enclosed, CSA certified PSU (ENP-240-12) • Has power switch, short circuit, overload, overvoltage, overtemperature protection.
7	Fan safety	Operational	• Durable material nets over fans to prevent wires or fingers coming in. • Fans do not have enough power to cut off fingers. • TODO: Oil bath fan has the less-accessible side open which may need another net.
8	Flow switch servo motor safety	Under development	• Flow switch located far from commonly used areas. • Prevent deliberate fingers and other objects from obstructing the flow switches. • Mount general enclosure, likely of plexiglass.
9	Bath stirrer safety	Operational	• Shaft guard prevents easy access to the rotating shaft. • Oil bath splash guard prevent access to the impeller.
10	Hot fluid safety	Operational	• Oil bath splash guard prevents fingers from going into the fluid, and prevents hot fluid splashes. • Tubing and fittings designed for >130*C spec. • Quick disconnect fittings seem secure after months of operation. Tubing and fittings don't burn fingers upon accidental contact.
10	Heating element isolation	Operational	• Thermocouple wires fixed to tubing or supports, should not contact heating element. • Tubing fixed in supports, should not contact heating element. • Heating element frame should not go above 70*C, frame is isolated from bath via 2mm Pyrogel insulation. • TODO: Need HOT warning signs. Mount general system enclosure, likely of plexiglass.
11	Reservoir fluid level feedback	Under consideration	• Allow automated checks of fluid levels
11	Valve position feedback	Under consideration	• Allow checks of valve position if servomotors fail

Appendix H – Custom control software UI

Custom control and temperature data acquisition software was programmed in Python. It includes a backend responsible for multithreaded interactions with the heardware, and a front end to improve user experience. Main interface allows individual control over flow direction, pump operation, HT fluid container stirrer, and bath temperature control. However, a simpler control scheme has been overlaid for automated operation. These include Auto Start and Auto Shutdown functions that use best default values for operation. Automated control of fluidic cell temperature is also available as long as all components are operational. It only requires specifying the type of control and the desired temperature.

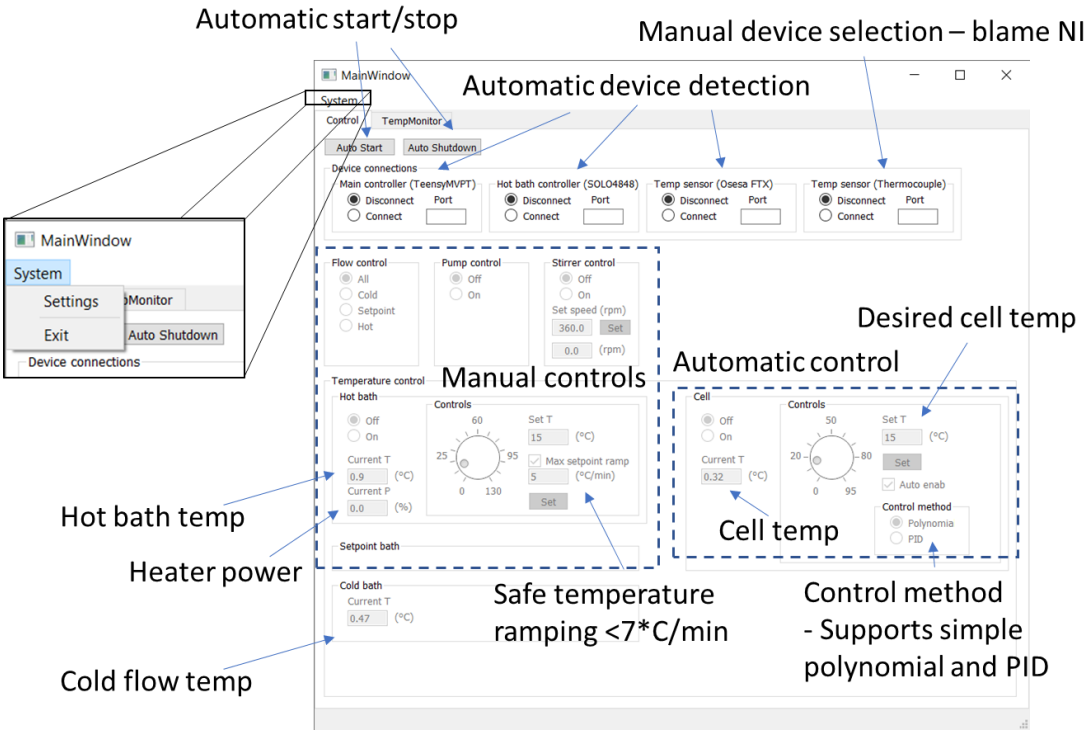

Data logging interface shows presently enabled thermometers and allows saving the data for subsequent analysis using MVPT analysis scripts. MVPT analysis scripts are based on Kyle Briggs Chimera VC100 .mat/.log format readers and signal filtering scripts. Temperature data is

added to the analysis and synchronized via the save time stamps. Automatic file naming and database creation allows MVPT scripts to read the data for a specific experiment.